The front-cover picture is an AB_2-type alloy after hydrogenation cycles, while the back-cover picture is a zoom of a ZrO_2 found in the microstructure of an AB_2-type alloy. Both taken during this thesis

TiMn$_2$ BASED METAL HYDRIDES FOR HYDROGEN COMPRESSION APPLICATIONS: NUMERICAL AND EXPERIMENTAL APPROACH

Tesis doctoral presentada por:
Andrés Ricardo Galvis Escobar

Madrid, España
Junio de 2018

Memoria de tesis presentada por:

Andrés Ricardo Galvis Escobar
Para optar al grado de: **Doctorado en Materiales avanzados y Nanotecnología**

Director de Tesis:
Prof. José Francisco Fernández Ríos

Madrid, Junio 2018

"If I have seen further it is by standing on the shoulders of Giants"
Issac Newton

"Success teaches us nothing; only failure teaches."
Hyman G. Rickover

Agradecimientos / Acknowledgements / Remerciements

Mi familia es lo primero, y no tengo duda que nada de lo que he conseguido en mi vida, sea profesional o personal, lo habría podido lograr sin su ayuda, guía y soporte en todo momento, especialmente, gracias al apoyo de mis padres Ricardo y Marina, y el de mi hermana Diana. Asimismo, a toda mi familia por estar presente con su aliento.

Sin duda, no tengo palabras suficientes para contar todo lo que debo agradecer a mi amiga y compañera de vida, Andrea, a la que agradezco mi camino actual y mi fortaleza para poder caminarlo desde el primer día, siempre junto a ella. A Stella y Milton por su apoyo y entendimiento en los momentos más críticos.

Igualmente, en mi experiencia como estudiante de doctorado he aprendido enormemente del conocimiento y sabiduría de toda la gente alrededor mío. Es más que necesario comenzar con mi director de tesis, Paco, al que no solo debo su guía en horas de obscuridad conceptual, sino también su paciencia y apoyo en todo lo que necesite para culminar en buen término la tesis, es sin duda un excelente profesor, y aun mejor, una de las mejores personas que conozco. A Julio le agradezco por ayudarme a reencontrarme con la programación y sus enseñanzas en Matlab, Labview, además de sus pláticas sobre política y Messi. Carlos siempre me sorprendió enormemente por sus conocimientos en muchos ámbitos científicos, además de su constancia y sus conversaciones de historia, aprendí mucho de diversos temas hablando con él. Isabel siempre brindo un gran apoyo no solo a mí, sino a todo el grupo con su liderazgo y gestión de responsabilidades que sin duda otros no podríamos realizar. Xoxe, eres una gran parte del pilar que sostiene el laboratorio y agradezco mucho el conocimiento y ejemplo que me has dado, espero que puedas seguir haciendo lo que te gusta por mucho tiempo. Fabrice te agradezco las conversaciones sobre varios temas tanto de la tesis como de muchos otros tópicos, pero aún más la buena actitud y el soporte en muchos aspectos tanto profesionales como personales. Fer el laboratorio casi que se abrió contigo dentro, y sé que seguirás por mucho tiempo más, sin duda tu preocupación por la gente te hace especial no solo para el laboratorio sino para los que te conocen, te quiero agradecer por tu apoyo en muchas etapas de mi doctorado además de esa preocupación conmigo y mis allegados. Edu, viva México, mi compañero y amigo durante muchos años de trabajo arduo, gracias por mostrarme más claramente el valor de ayudar a otros y las ayudas técnicas con los ordenadores, te deseo lo mejor. Clama, muchas gracias por las experiencias y consejos profesionales que me has dado, han sido valiosos para tomar distintas decisiones a lo largo de mi tesis.

A Mariam y Sato, aunque no se encuentren ahora en el laboratorio, les agradezco mucho el acogerme desde el comienzo de este proceso con su ánimo y buena actitud. A Marine, le quiero agradecer encarecidamente, no solo por ayudarme a conseguir mi estancia en Grenoble, sino por apoyarme y soportarme durante esos meses que compartimos allá. A Ricardo y Dani les agradezco por la amistad, las conversaciones, risas y por ser un gran soporte en momentos de incertidumbre existencial. A Mikel y Laura por hacerme participe de sus vidas durante todo el tiempo que pudimos compartir en la facultad y en las salidas casuales, les deseo lo mejor. Finalmente, por parte de la UAM, me gustaría destacar y agradecer la ayuda de Kike, Esperanza, Mario y Noemi por todas las medidas que tuve que realizar en los laboratorios del SIDI durante el transcurso de la tesis.

J'ai eu la chance de travailler avec des gens magnifiques pendant tous mes stages de recherche en France. C'est la raison pour laquelle j'ai l'honneur de remercier plusieurs personnes qui ont contribué au travail réalisé. Tout d'abord, à l'équipe du CAE à Grenoble. A Olivier, le responsable du LHS, une personne unique et incroyable, musicien à qui je dois le partage de son expertise au quotidien, tant en ingénierie qu'en sciences. J'espère qu'il va très bien et qu'il

continuera à profiter de la vie avec ses passions et sa famille. De la même façon, à Albin, aussi un grand musicien qui avec sa générosité et son talent professionnel m'a énormément aidé pour tout ce dont j'ai pu avoir besoin, tant pour mes mesures dans le projet que pour m'apporter des idées pour ma thèse. Vasile, un collègue exemplaire avec qui je pouvais parler de n'importe quel sujet dans les congrès et les conférences, merci pour tous les moments où nous avons ri et pour les conversations si agréables. En vous souhaitant que vous et votre famille alliez très bien.

Ensuite, je tiens à remercier et féliciter tous les employés du CIMPE-CRNS à Thiais-Paris, pour l'admirable travail que vous faites tous les jours, c'est vraiment remarquable. En premier, je me dois de remercier Fermin, une des meilleures personnes que j'ai pu rencontrer et un excellent professeur qui m'a, en plus, accueilli deux fois au sein de sa famille. Je vous souhaite la meilleure des chances. Michelle, la grande chef et respectueuse membre de la communauté scientifique. Il me manquera toujours des mots pour vous remercier de l'opportunité d'être dans votre laboratoire, de m'avoir intégré au sein de votre équipe. J'ai pu apprendre beaucoup grâce à vous. En grand merci à Jean-Marc d'avoir pris le temps de voyager en Colombie, d'avoir partagé des moments avec ma famille et surtout de m'avoir fourni un élément très précieux pour ma recherche : son modèle EOS. A Yunxian, merci pour les bons moments passés ensemble, pour les conseils si pertinents et d'avoir eu la gentillesse de prendre les mesures dont j'avais besoin pour mon projet. De la même façon, j'espère que votre programme aura du succès. Je tiens aussi à remercier vivement Pavel pour son aide. Il fut d'un accompagnement précieux pendant ma période d'apprentissage dans le laboratoire. Je lui souhaite des très bons résultats avec sa thèse aussi. Pour Encarni, ma chère ex-voisine, je te remercie pour la compagnie et le fous-rires partagés. Bonne continuation avec ton nouveau poste au laboratoire. Je remercie aussi Nicolas pour son temps et les moments où nous nous sommes autant amusés. Je lui souhaite d'exceller dans son projet de thèse. Enfin, Jean-Claude, Claudia, Fabrice, Valérie L., Benjamin, Valérie P., Olivier, Éric L. et Dominique, merci à tous pour votre aide et votre accueil au sein du laboratoire. Je vous souhaite le meilleur à tous.

Por último, quiero agradecer al Departamento Administrativo de Ciencia, Tecnología e Innovación – Colciencias- en Colombia, por haberme concedido el crédito-condonable bajo la convocatoria 568, ya que sin el no habría podido realizar esta tesis. Asimismo, destacar su apoyo logístico y administrativo.

Resumen

Se ha diseñado, modelado y estudiado un sistema de compresor de hidrógeno de tres etapas a partir de hidruros metálicos de tipo AB$_2$, considerando aproximaciones tanto experimentales como numéricas. Se utilizó un programa de selección para evaluar varios tipos de aleaciones de la literatura a través de la implementación de restricciones de operación del sistema del compresor y de la termodinámica básica de los hidruros. A partir de las aleaciones seleccionadas, se han utilizado métodos de síntesis y caracterización experimental (composicional, estructural, morfológica, termodinámica y cinética) sobre estos materiales, para analizar el comportamiento de estas aleaciones y también para utilizar estos datos como entrada de las simulaciones. Asimismo, se estudiaron las propiedades mecánicas de uno de los hidruros seleccionados, obteniendo parámetros fundamentales para el diseño del sistema como la porosidad, el factor de empaquetamiento en estado hidrogenado y la interacción de las partículas con el reactor. Se desarrolló un algoritmo en Matlab® considerando ecuaciones de estado reales del H$_2$ gas, los modelos termodinámicos y también los datos experimentales termodinámicos de los materiales seleccionados. Finalmente, se ensambló, configuró y utilizo un sistema de medición para la compresión de H$_2$ gas en tres etapas, con el fin de realizar experimentos de compresión, estudiar en detalle el comportamiento de estos sistemas y comparar los valores experimentales obtenidos con los simulados.

Abstract

A three stage Metal Hydride Hydrogen Compressor system based on AB$_2$-type alloys have been designed, modelled and studied, on the basis of both experimental and numerical approaches. A selection program was used to evaluate several types of alloys from literature through the implementation of MHHC operation restrictions and basic thermodynamics of the hydrides. From the alloys selected, the synthesis methods and a complete experimental characterization (compositional, structural, morphological, thermodynamic and kinetic) has been developed to understand the behavior of the alloys and also use this data as an input of the simulations. Furthermore, the mechanical properties of one of the alloys selected was studied, obtaining key parameters for the design of the system, such as, porosity, hydrogenated packing fraction and the interaction between the particles and the reactor. A further algorithm was developed in Matlab® considering suitable real H$_2$ gas EOS, thermodynamic models and also the thermodynamic experimental data from the materials selected. Finally, a three stage MHHC measurement system was assemble, set-up and used to perform compression experiments, study in detailed the behavior of these systems and compare the experimental values obtained with the simulated ones.

If possible, please consider print this page for a proper reading of the document

Nomenclature

@: at, only used in equations and figures

BSE: Back-Scattered electrons

C: hydrogen composition in the hydride

CEA: Commissariat à l'énergie atomique et aux énergies alternatives

CNRS: Centre National de la Recherche Scientifique

Cp: Specific heat capacity, J/ Kg* K (If not, it will be stablished)

CR: Compression ratio, ln (Pdes @Th/Pabs @Tl)

Container = vessel = reactor

e.g.: "exempli gratia" = for example

Ea: Activation energy, kJ/mol*K

EOS: Equation of State

F(α): Reacted fraction of hydrogen in the hydride

ƒ(F(α)): Reacted fraction models, [References 31-32, chapter 3] =
D1: one-dimensional diffusion, **D2:** two-dimensional diffusion,
D3: three-dimensional diffusion (Jander), **D4:** three-dimensional diffusion (Ginstling-Braunshtein equation), **F1:** First-order reaction, **R2:** Two-dimensional phase boundary, **R3:** Three-dimensional phase boundary, **Z0:** Zero order, **A2:** Avrami-Erofe´ev with n=2, **A3:** Avrami-Erofe´ev with n=3.

FEM: Finite Element Method

g(P,Peq): Driving force models [Reference 33, chapter 3] = **g(P,Peq)$_1$:** Normalize pressure dependence method, **g(P,Peq)$_2$:** Pressure dependence related to a diffusion process, **g(P,Peq)$_3$:** Pressure dependence related to a phase transformation process

GtCO$_2$: giga tonnes of CO_2 = 1×10^{12} g of CO_2

H$_2$: Diatomic Hydrogen

ΔH: Enthalpy, kJ/ mol

HTF: Heat transfer fluid

HR: Heating rate

Hydralloy C0: $TiMn_{1.5}V_{0.45}Fe_{0.1}$, [Reference 35, chapter 1]

Hydralloy C2: $Ti_{0.98}Zr_{0.02}Mn_{1.46}V_{0.41}Cr_{0.05}Fe_{0.08}$, [Reference 25, chapter 2]

Hys: Hysteresis, ln(Pabs/Pdes)

ICMPE: Institut de Chimie et des Materiaux Paris-Est- Umr 7182

i.e.: "id est"= That is

K: Permeability, m²

k: Reaction rate constant, 1/ s

k$_0$: Pre-exponential Arrhenius rate constant, 1/ s

m: Mass, g

M: Metal = alloy

MH: Metal hydride

MHHC: Metal hydride hydrogen compressor

Mm: Molar mass, g/mol

Mtoe: Millions tonnes of oil equivalent = 11630 kWh.

n: moles

NIST: National Institute of Standards and Technology

NS: Not shown

O&M: Operation and maintenance

O.P.: Operational point(s)

P: Pressure, bar (If not, it will be stablished)

P-c-I: Pressure-composition Isotherm(s)

Q: Heat, Wh (If not, it will be stablished)

R: Gas constant, (it will be stablished each time)

RT: Room temperature, ºC (If not, it will be stablished)

ΔS: Entropy, J/ mol*K

SE: Secondary electrons

S.G.: Space group

Slp: Slope of the plateau region, d ln(P) / d (C)

St: Stage

t: Time, s (If not, it will be stablished)

T: Temperature, ºC (If not, it will be stablished)

TS: Technology stage

V: Volume, cm³

wt: Weight percentage, %

Greeks:

ϰ: Thermal conductivity, W/ m*K

μ: dynamic viscosity, kg /m*K

β: Beta phase

η: efficiency

α: Alpha phase solid solution

θ: Theta, degrees º

ε: Porosity

ρ: Crystallographic density, g/cm3 (If not, it will be stablished)

λ: Lambda

Subscripts:

abs: Absorption

c: compressed

des: Desorption

e: Effective

eq: equilibrium

ext: External

fr: Free

g: Gas

h: High

hs: Heat source

hd: Hydrogenated

in: Inlet

l: Low

m: Medium

max: Maximum

min: Minimum

mol: Molar

ms: Mass source

p: Plateau

r: Reservoir

re: Reaction

rev: Reversible

s: Solid

Superscripts:

Tr: Transpose

-Any other nomenclature not define in this table, will be described in the proper section.

-Through the whole document the numbers in parenthesis stand for errors in the last digit

Contents

Chapter 1. Introduction

1.1. General outlook of the problem and description of the study

Energy was, is and will be a need of society. Nowadays, the world's demand for energy is constantly increasing [1] (Fig. 1a), but unfortunately, it is also mainly produced by fossil fuels that yield emissions of CO_2 (Fig. 1b) and produce well-known environmental consequences [2]. Moreover, the renewable energy sources are slowly growing in importance and application, but, one major drawback to their full and efficient implementation is the lack of a proper energy storage technology [3].
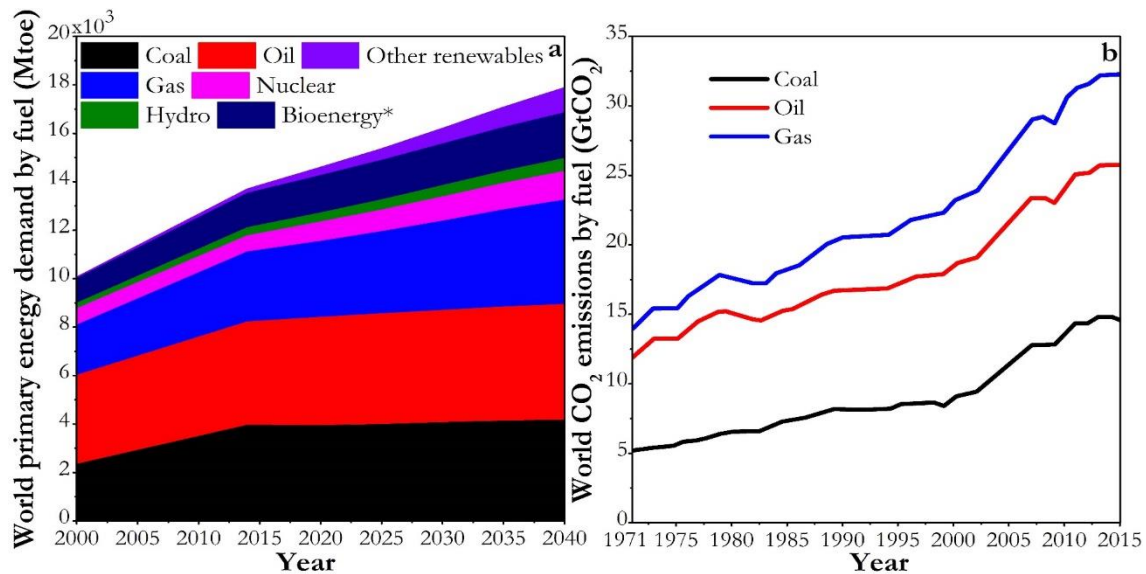
Fig.1. Energy consumption and related CO_2 generation. a) World primary energy demand by fuel in a new policy scenario. b) World CO_2 emission by fuel combustion. *Bioenergy: solid biomass and modern bioenergy. Adapted from references [2, 4].

In general, storage is a problem of all sources of energy. Several storage technologies have been used for different applications considering mainly the quantity of energy they can store and the discharge time for this energy (Fig. 2).
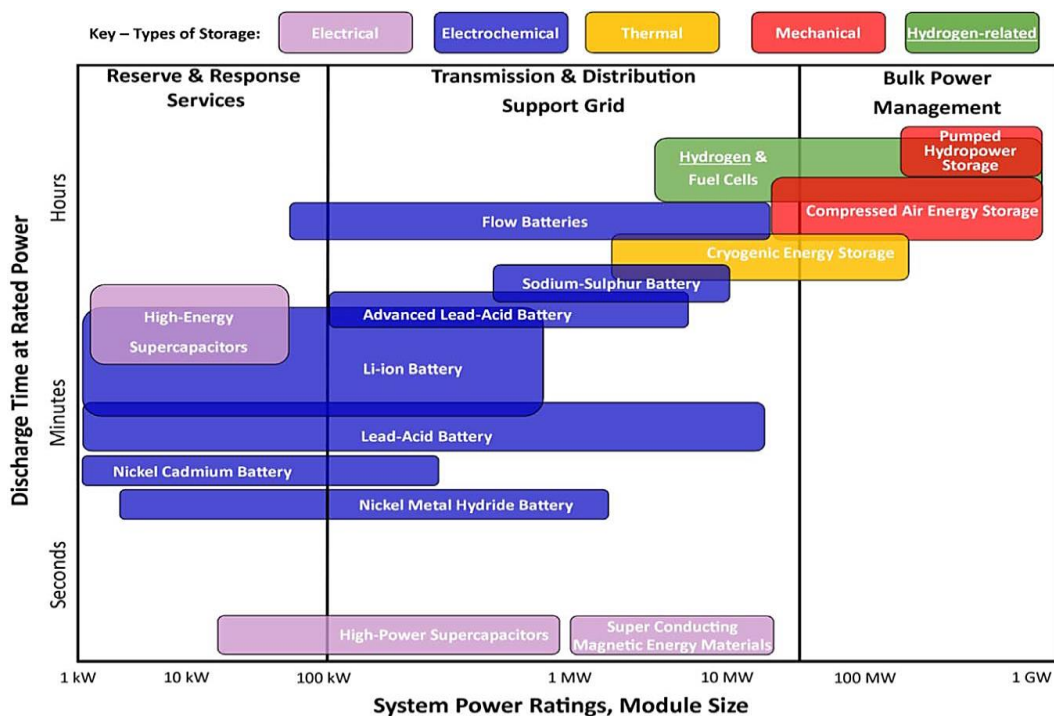
Fig.2. Technologies to store energy on the discharge time for different system power ratings [5].

Among all, hydrogen storage gives a high-power scalability and a longer storage in time, which can position this technology as a big reservoir of energy [5]. As part of the well-known hydrogen economy (cycle), storage is one of the cornerstones that has been studied for several years, gathering methods such as pressurize H_2 gas in cylinders ($350 - 700$ bars), liquid hydrogen in cryogenic tanks, physisorption of H_2, chemisorption of H_2 in metal, complex and chemical hydrides [6, 7]. Furthermore, extensive research has been done on hydrogen storage alloys, considering that in the last years a higher amount of hydrogen per unit volume than high pressure tanks and liquid hydrogen has been achieved [8, 9].
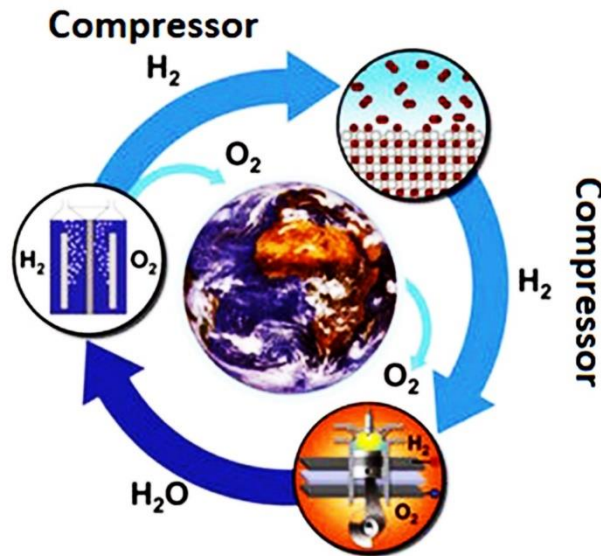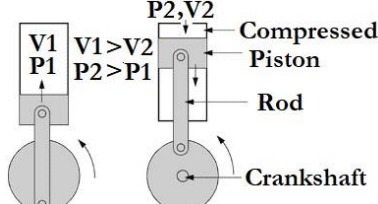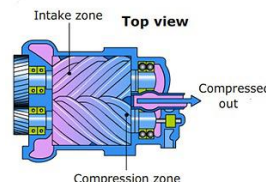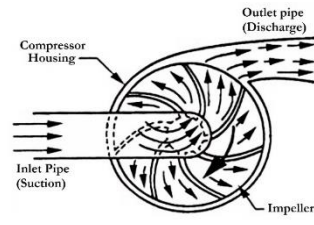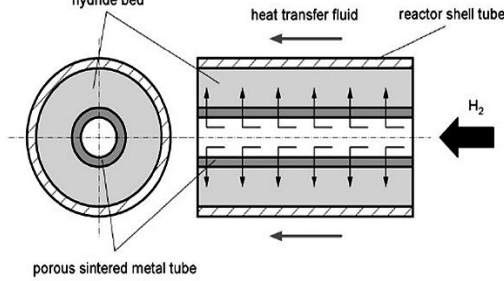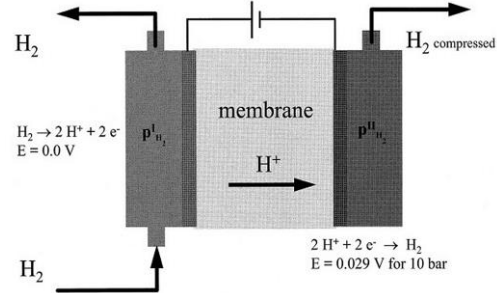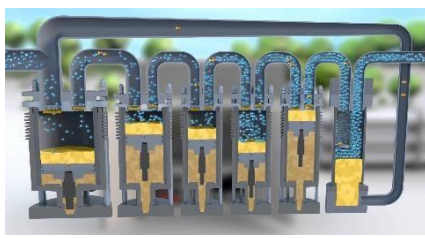
Fig.3. Hydrogen cycle showing the possible links of the hydrogen compressor with other key areas. Adapted from [6].

Likewise, in order to link the storage with the rest of the main areas of the hydrogen cycle (Fig.3.), some technologies have been implemented. One of the most significant in the field is the hydrogen compressor technology, which connects sectors of the hydrogen cycle like the production with storage and the storage with the consumption or energy-transforming technologies [6, 10, 11].

Some technologies have been developed to achieve the compression of hydrogen in different areas. Their most significant classification is mainly in mechanical (or conventional) and non-mechanical (or unconventional) compressors. Table 1 exhibits the most significant types of compressors with their basic operations and a comparison between them in terms of key parameters such as technology stage, compression ratio, H_2 rate, safety, and, operation and maintenance. At the end of the table some important aspects are defined.

Table 1. Basic operation and comparison between hydrogen compressing technologies

	Scheme of the system	Basic Operation	Comparative features
Conventional	**Positive displacement** **Reciprocating type [12, 13]** **Rotatory-Screw type [14]** 	H_2 delivered intermittently by packages with a motion element that constantly reduces the available volume, increasing the pressure	**TS:** Mature [+] **CR:** Low - High, depending on pressure rates [+] **H_2 rate:** High [+] **Safety:** Low, high permeation and leakage through seals [-] **O&M:** High, in valves, rider bands, piston rings, between other seals. [-]
	Centrifugal [15, 16] 	H_2 delivered continuously, increasing its pressure by passing through an impeller	**TS:** Mature [+] **CR:** Low – High. Depends on pressure rates [+] **H_2 rate:** High [+] **Safety:** Low. High permeation and leakage through seals [-] **O&M:** High in blades and moving parts [-]
Unconventional	**MHHC [13, 17]** 	Uses the thermodynamics of hydrides to increase the pressure, that is, the hydrogen stored in the alloys gets released by changing the system temperature, rising the pressure.	**TS:** R&D [+/-] **CR:** Low – High. Depends on materials [+] **H_2 rate:** Low -High. Depends on system design [+/-] **Safety:** High. No moving parts, compact system [+] **O&M:** Low. No moving parts, simple operation [+]
	Electrochemical [13] 	A membrane with a catalyst dissociates the molecular hydrogen and with the imposition of a voltage between electrodes, the crossover of hydrogen increases, rising the pressure afterwards	**TS:** R&D [+/-] **CR:** Medium-High. Depends on voltage, temperature applied [+/-] **H_2 rate:** Low -High. Depends on system design [+/-] **Safety:** High. No moving parts, compact system [+] **O&M:** Medium. Mainly the membranes [+]
	Liquid ionic [18-20] 	Like a reciprocating type. An ionic fluid displaces and compresses the H_2, like a piston, and reduces the leaks through the seals	**TS:** R&D [+ / -] **CR:** High [+] **H_2 rate:** High [+] **Safety:** Possible leakage in stand-by mode [+/-] **O&M:** Medium. Mostly corrosion inspection and liquid ionic change [+/-]

Positive = [+]; Intermediate = [+/-]; Negative = [-]

In general, mechanical compressors come to mind first. These solutions are currently well developed, though, show some drawbacks when used with H_2. In particular, the need for pure H_2 in fuel cells put some question marks to the use of mechanical compressors, as the presence of oil is always a source of contamination not advisable for fuel cells. Furthermore, H_2 compressors based on metal hydrides present other advantages compared with the mechanical ones: the absence of mechanical parts and noise, the safer and cleaner operation provided by these MH systems and the possibility to use waste heat for the energy demands of these equipment [17]. This method allows for clean, efficient and reliable transformation of H_2 produced at 1 bar pressure into compressed H_2 at a higher pressure, and for instance, it would be a fundamental part of a photochemical H_2 production system that generates this gas at atmospheric pressure. Between the compressor technologies in research stage, the MHHC exhibit equal or better parameters than the other ones, making them attractive for studies in basic research and technology development. In the following section the technology operation, advantages, disadvantages and recent studies will be described in detail.

1.2. Metal Hydride Hydrogen Compressors
1.2.1. Detailed operation

Firstly, since the main operation of this technology relays on the thermodynamics of MH [21], some concepts should be explained. The basic reaction that takes place when the H_2 interacts with the alloy is [17]:

$$M(s) + \frac{x}{2}H_2(g) \underset{absorption}{\overset{desorption}{\rightleftarrows}} MH_x(s) \pm Q \qquad (1)$$
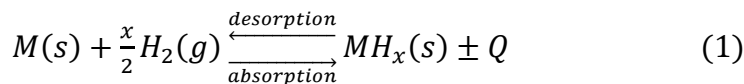
This reaction is very complex, involving a number of different phenomena. Fig.4a describes schematically the modifications taken place in the metal during MH formation.
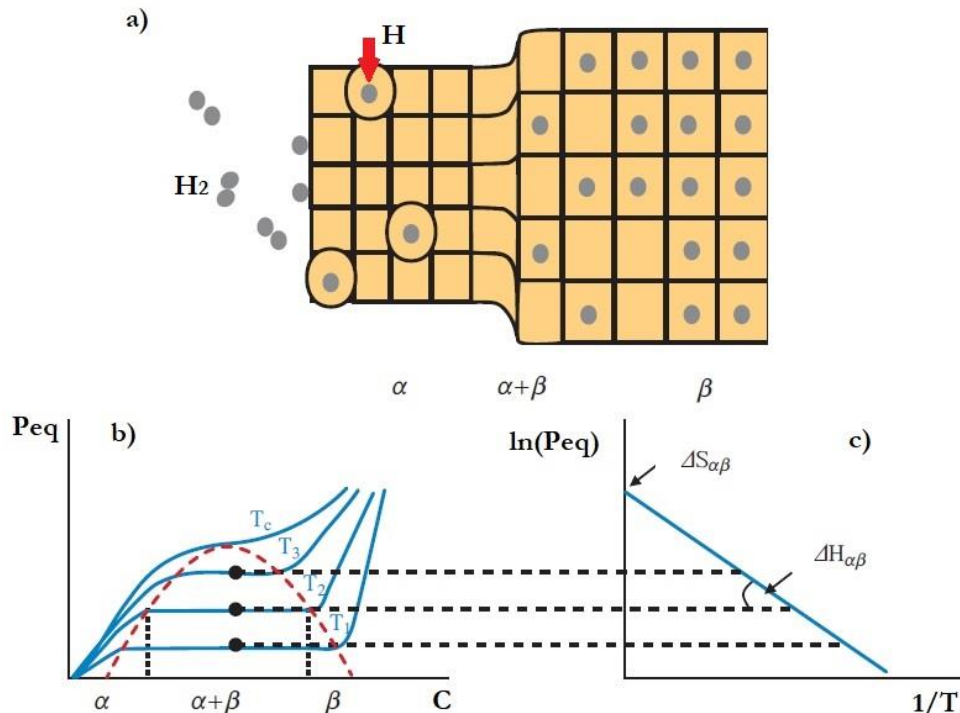
Fig.4. Thermodynamics of MH, a) scheme of the hydride formation, b) Ideal P-c-I scheme at different temperatures and P_P (black points), c) Van´t Hoff plot scheme. Adapted from [22].

During the absorption, the alloy interacts with the hydrogen in gas phase (H_2), originating a solid solution (α) that with a pressure increase, will produce a phase transition from the metal structure to the MH (α-β). During this process an abrupt expansion of the crystallographic matrix occurs. The MH formation is an exothermic process and thus an increase of sample temperature would be expected during hydrogen absorption. As pressure increases, the final MH (β) is achieved. At desorption, heat or a pressure change is applied to destabilize the hydride and release the atomic hydrogen (H) confined, then, the path followed is the opposite as in the absorption stage. In Fig.4b an ideal P-c-I curve of a hydride is shown. A P-c-I curve provides the equilibrium pressure as a function of hydrogen concentration for a metal hydride. As pressure increases at a certain temperature, the absorption-desorption processes follow the path described from (α) to (β), creating a pressure composition curve at an isothermal condition that describes the quantity of hydrogen stored in the hydride at the equilibrium conditions stablished. Ideally, the phase transition (α-β) will occur at a constant P_p (Fig.4b, black points) that can vary with temperature. This P_p is closely link to the chemical potential of the hydrogen in the gas and solid phases, as it is properly described by the Van´t hoff plot (Fig.4c) and the equation [17, 22, 23]:

$$ln\left(\frac{P_p}{P_0}\right) = \frac{\Delta H_{\alpha\beta}}{R * T} - \frac{\Delta S_{\alpha\beta}}{R} \qquad (2)$$

Where P_0=1atm =1.013 bar, $\Delta H_{\alpha\beta}$ and $\Delta S_{\alpha\beta}$ are the enthalpy and entropy of reaction for hydride formation respectively. It is important to highlight that the fact that P_p increase with temperature is what makes that a MH can compress hydrogen without any moving part [17, 24].

Specifically, a one-stage MHHC works ideally as follows:
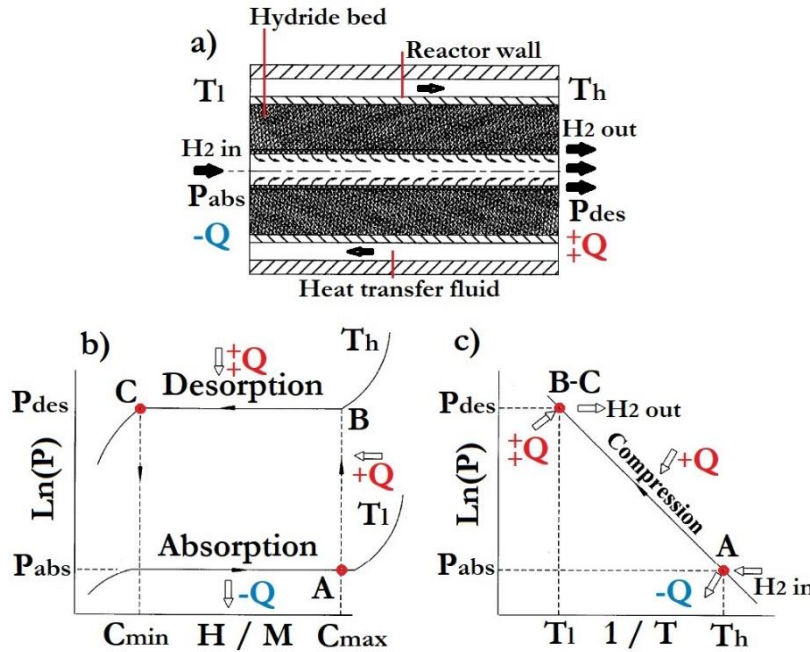
Fig.5. One-Stage MHHC working operation scheme, a) compressor scheme and main parameters, b) ideal P-c-I, c) Van´t Hoff plot. Adapted from [25].

First of all, H_2 at a P_{abs} is applied to achieve a quantity of stored hydrogen (C_{max} and point A), maintaining a T_l during all this hydrogenation process in order to remove the heat generated (-Q) (Fig.5b). Then, a sensible heating process is gradually applied (+Q to ++Q) up to the point where the hydride desorbs (point B to C) at T_h and a final quantity of released hydrogen

7

is reached at a final hydride composition (C_{min}), increasing the pressure of the system (P_{des}). This final pressure can be designed to fulfil directly the requirement of pressure and H_2 rate of a consuming system (e.g. fuel cell) or to couple it with a second stage, in which case, this P_{des} should be greater than the P_{abs} of the second stage at T_l. The process is repeated to attain a higher pressure with the hydride in the second stage. It has to be highlighted that in a normal metal-hydrogen system, the thermodynamics evidence features like sloping plateau and hysteresis that will have an effect on the performance of the MHHC [17, 24, 25].

On the other hand, for the real operation of a MHHC and any other system that uses metal hydrides (e.g. storage, thermal systems), the H_2 flux rate at which the gas is delivered is important to maintain a constant supply for any system that requires it. In general, for MH systems the time length of the hydrogenation cycles and therefore their dynamic performances depend on the rates (or kinetics) of the absorption and desorption reactions (equation (1)) [17, 24]. Likewise, intrinsic hydride kinetic mechanisms relay on complicated time- and space-related factors, such as temperature, hydrogen pressure, catalysis, morphology, as well as the change of the driving force (due to the P_p variation with temperature) [26]. However, generally in the overall system the parameter that slows down the kinetics (rate determine step) is the heat transfer between the MH and the thermal management system, since temperature changes in the exothermic-endothermic hydrogenation reactions have an influence on both the chemical activation and the driving force [27-30].

Moreover, a MHHC is a heat engine that is restricted by the Carnot efficiency. However, the efficiency of the real engine is reduced by some factors that can be divided in two main groups [17, 31]: 1. intrinsic features that characterize the physical-chemical behavior of H_2 with the hydride forming materials such as reversible hydrogen sorption capacity, plateau slope, hysteresis, intrinsic hydride kinetics and lattice expansion during hydrogenation. From the improvement of these parameters a better CR and a high cycle stability can be achieved. 2. The design and technological performance of the MHHC and its components. Especially, design parameters of the MH containers like the rates of heat exchange between the MH bed and the MHHC thermal management system, which will determine the productivity of the system since their overall kinetics is mainly control by the heat transfer [29, 32, 33, 34]. Also, the dead space volume, the MH bed swelling behavior in the container, and, the material consumption in the MH container throughout hydrogenation cycling.

In the last years, these parameters have been considered by several authors to understand and enhance this technology.

1.2.2. State of the art

The works performed by several authors will be discussed, to summarize the key elements to consider for this technology in all of the aspects needed.

As a first approach, several experimental studies and prototypes have been developed. **Hagström et al.** [35] studied the alloys $TiCrMn_{1-3x}Fe_{2x}V_x$ (X=0, 0.05, 0.1, 0.15, 0.2), $T_{1-y}Zr_y(Cr_zMn_{1-z})_2$, Hydralloy C2 and hydralloy C0, to tailor their thermodynamic properties through the changes in chemical composition, specifically, to achieve high capacity and low hysteresis at high pressures and narrow temperatures ranges. It was found that when optimizing the composition of the materials, it was very difficult to remove the hysteresis and maintain a high capacity at the same time, also, that in the AB_2-type alloys it is possible to tailor easily the thermodynamic properties within a narrow temperature interval. For instance, using a coupling of Hydralloy C2 - Hydralloy C0 and ($TiCrMn_{0.55}Fe_{0.33}V_{0.15}$), the

pressure can increase from 20 to 200 bar with 20 to 60ºC. Afterwards, **Vanhanen et al.** [36] analyzed the feasibility of combined MHHC and heat pump through the combination of the same AB_2-type alloys described by Hagström. The selected alloys for both compression and heat pump were the Hydralloy C2, Hydralloy C0 and the $TiCrMn_{0.55}Fe_{0.33}V_{0.15}$ for the first, second and third stage, respectively. For the heat pump application, heat transfer was the key to enhance the kinetics of its complete cycle.

Park et al. [37] developed a compressor-driven metal hydride heat pump system to generate higher cooling power than with conventional metal hydride heat pumps. A $Zr_{0.9}Ti_{0.1}Cr_{0.55}Fe_{1.45}$ Laves phase metal hydride was selected to operate in a pressure range from 1 to 18 atm, achieving a maximum cooling power with this system of 251 kcal/(kg alloy *h).

Wang et al. [38] studied the thermodynamic properties of AB_5-type $(Mm_{0.8-x}Ca_{0.2}La_x)(NiAl)_5$ (x=0-0.7) alloys and AB_2 type $Ti_{1+x}(CrMnV)_2$ (x=0 – 0.2) alloys by tailoring their chemical composition and with the purpose of using them as stages of a MHHC. A $Mm_{0.7}Ca_{0.2}La_{0.1}(Ni_{4.95}Al_{0.05})$ was selected as the material for the single-stage and the pair $Mm_{0.2}La_{0.6}Ca_{0.2}Ni_5/Ti_{1.1}Cr_{1.5}Mn_{0.4}V_{0.1}$ for the double-stage MHHC, both systems were designed and built. The single-stage can compress from 40 to 450 bar with hot oil at a T_h=170ºC, while the double-stage can achieve the same 450 bar but just with hot water. Then, **Wang et al.** [39, 40] developed a two-stage 700 bar compressor by using two different coupling alloys to achieve the final pressure. The composition of several AB_5-type and AB_2-type alloys were tailored for this purpose. In the first system studied, a $La_{0.35}Ce_{0.45}Ca_{0.2}Ni_{4.95}Al_{0.05}$ alloy was employed, compressing from 50 bar at 298 K to 385 bar at 423 K, while for the second stage a $Ti_{0.8}Zr_{0.2}Cr_{0.95}Fe_{0.95}V_{0.1}$ was selected to couple with the first stage at 298 K and compress the H_2 to 700 bar at 423 K. For the other system, a $Ti_{0.95}Zr_{0.05}Cr_{0.8}Mn_{0.8}V_{0.2}Ni_{0.2}$ and $Ti_{0.8}Zr_{0.2}Cr_{0.95}Fe_{0.95}V_{0.1}$ were selected for the first and second stage of the 700 bar MHHC, respectively. The inlet pressure was 40 bar at 298 K and the desorption pressure of the first stage was of 300 bar at 423K, while the desorption pressure of the second stage was of 700 bar at 423 K.

Laurencelle et al. [41, 42], designed a three-stage AB_5-type MHHC prototype for a hydrogen production facility using a low-pressure alkaline electrolyzer. The materials selected for the system were $LaNi_{4.8}Sn_{0.2}$, $LaNi_5$ and $MmNi_{4.7}Al_{0.3}$ for the first, second and third stage respectively, where it performs a thermal cycling between 20 and 80 °C with a flow rate that reaches about 20 L (NTP) of hydrogen per hour and achieves a CR of 20. Also, several experiments were performed on the system, encountering some issues. It is imperative to reduce the dead volume that is affected directly by thermal cycling, and, have a better thermal management system that would allow to achieve a closer intrinsic kinetics to the one that the AB_5-type hydrides exhibit during the experiments.

Dehouche et al. [43] investigated the thermodynamic and kinetic effect of changing several elements in a Ti-Zr-V-Mn system to be used as a first-stage MHHC. From the materials studied at 23ºC, the $Ti_{0.95}Zr_{0.05}V_{0.2}Mn_{1.3}$ exhibit the best plateau region needed for the reversible thermal compressor, a proper hydrogen absorption capacity of 1.6 wt.%, high stability during cycling and small enhancement in hydrogen discharge rate. Then, **Dehouche et al.** [44] employed three AB_5-type alloys for a triple-stage MHHC. The three alloys $LaNi_{4.8}Sn_{0.2}$, $LmNi_{4.9}Sn_{0.1}$ and $MmNi_{4.7}Al_{0.3}$ were studied thermodynamically (P-c-I, specific heats, and effective thermal conductivities) and kinetically at several temperatures, and, they were couple as a MHHC considering their real thermodynamic behavior (Fig.6). The absorption pressure of the system at 1 atm and 23ºC was compressed until 20 atm at 80ºC.
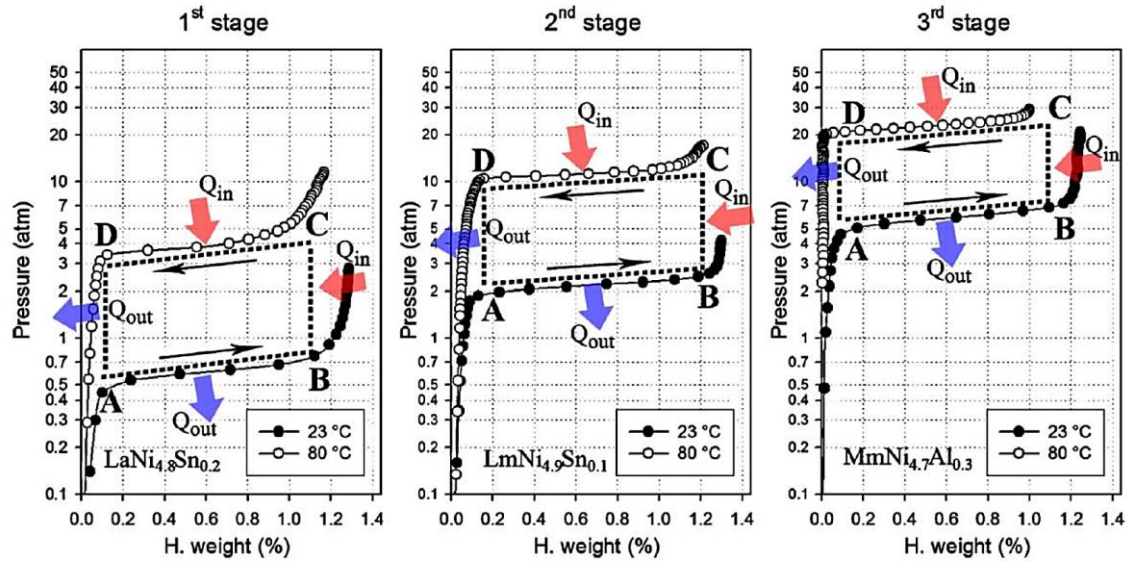
Fig.6. Thermodynamically coupled triple-stage MHHC system [44].

Talagañis et al. [45] developed a double-stage MHHC by measuring the thermodynamic properties of two different AB_5–type alloys. In the first stage a $LaNi_5$ absorbs 5.75 bar at 25ºC and compressed it to 13.65 bar at 90ºC, while a $La_{0.67}Ce_{0.19}Nd_{0.08}Pr_{0.06}Ni_5$ was implemented as the second stage to achieve a final pressure of 21 bar at 90ºC and to obtain a CR of 3.65.

Koultoukis et al. [46] investigated the thermodynamic properties of four Zr-based AB_2-type alloys, in order to use them in a MHHC. From the alloys analyzed, the $Zr_{0.5}Ti_{0.5}Fe_{1.2}Ni_{0.4}V_{0.4}$ and $Zr_{0.75}Ti_{0.25}Fe_{1.0}Ni_{0.8}V_{0.2}$ were selected for the first and second stages, respectively. The absorption of the first container was of 10 bar at 20ºC and its desorption pressure 40 bar at 90ºC, while the final desorption pressure with the second alloy could achieved more than 100 bar at 90ºC.

Bhuiya et al. [47] made an experiment-driven design procedure to optimize the combination of stages in a double-stage hydrogen compressor and thus enhance its final compression ratio. Three different combinations of single-stage reactors were studied separately, $LaNi_5$, $Ca_{0.6}Mm_{0.4}Ni_5$ and $Ca_{0.2}Mm_{0.8}Ni_5$. It was found that compression ratios were similar for low supply pressure conditions, which improved significantly for high supply pressure conditions in single stage experiments. Also, design aspects and selection of metal hydride have a great influence on the performance of double-stage MHHC (e.g. minimizing pressure drop between stages by efficient design, enhances the compression ratio significantly). A final double-stage compressor system with $LaNi_5$ and $Ca_{0.2}Mm_{0.8}Ni_5$ in the first- and second stage was proposed based on single stage results, achieving a 53% higher compression ratio.

Muthukumar et al. [48] performed experimental tests on a $MmNi_{4.6}Al_{0.4}$ based hydrogen compressor by varying operating parameters such as supply pressure and heating temperature, under constant and variable delivery pressures with different storage volumes. Hydrogen storage pressure increases with a rise in the supply pressure and heating temperature, but, the former has a negative effect on the efficiency. In the best conditions studied, with a variable H_2 delivery a maximum isentropic efficiency of 7.3% is obtained at a CR of 8.8 (43.8/5 bar) and 95ºC hot fluid temperature, while with a constant delivery, the corresponding efficiency is 14.2%, the CR is 3 (30/10 bar) and the hot fluid is at 85ºC.

Kim et al. [49] examined the performance of a single-stage compressor by using porous metal hydride compacts with high thermal conductivity of two different AB5-type alloys,

LaNi$_5$ and LaNi$_{4.75}$Al$_{0.25}$. Two cooling (20 and 30ºC) and four heating (60, 70, 80, and 90 ºC) temperatures were employed while transient temperature distributions and compressed pressures were monitored to find the maximum work and efficiency. Results showed that LaNi$_{4.75}$Al$_{0.25}$ had a faster absorption rate than LaNi$_5$, especially for the lowest cooling temperature. In addition, the compression ratio was found to be primarily dependent on the temperature difference between cooling and heating. At a cooling temperature of 20ºC and heating temperature of 90ºC, the maximum work (2.44 kJ) and efficiency (5.91%) occurred with the LaNi$_5$ alloy.

Beside the experimental studies reviewed and others [50, 51], several prototypes have been developed, as resume by [17]:

Table.2. Resume of MHHC prototypes. Adapted from [17]

Year	Operation*	Alloy (number of containers per stage; mass)	T$_l$ (ºC)	P$_l$ (bar)	T$_h$ (ºC)	P$_h$ (bar)	Developers ; important features
1970	Periodic	TiFe (1; 60 g)	20	35	137	255	US Atomic Energy Commission ; electric heating, convective cooling
1971	Periodic	VH$_x$ (1; 100 g)	18	7	50	24	Brookhaven NL (US); water heating/cooling
1979	Continuous	LaNi$_5$ (2; 700 g)	20	2.5	80	20	National Chemical Laboratory for Industry (JP) ; water heating/cooling, 28 W mechanical power output
1980	Periodic	LaNi$_{4.63}$Al$_{0.37}$ (1; 1.5 kg)	23	1.2	68	2.1-3.3	Sandia NL (US) ; water heating /cooling, water pump:/15 L per cycle
1983	Periodic	LaNi$_5$ (19; 0.91 kg)	27	3	90	18	Tsukuba Research Centre (JP) ; used for desalination by reverse osmosis, water heating/ cooling (30 L/min)
1990	Continuous	AB$_5$ (NS; NS)	25	1-4	85	40-200	Ergenics Inc (US) ; commercial series, 20 years life time
1993	Continuous	TiFe + 2 wt.% Mm (3; 1 kg)	20	10	250	100	Universidade Estadual de Campinas (BR) ; water cooling/ electric heating
1995	Periodic	LaNi$_5$ (3; 1.5 kg)	25	10	370	150	Inst. Probl. Mech. Eng. (UA) ; electric heating (3 kW in total), convective cooling; 106 dm^3 volume; 46 kg weight
1995	Periodic	LaNi$_5$ (7; 1.4 kg)	25	10	370	300	Inst. Probl. Mech. Eng. (UA) ; electric heating (8 kW in total), convective cooling; 170 dm^3 volume; 142 kg weight
1996	Periodic	1.ZrNi (1; 0.225 kg) 2.LaNi$_{4.8}$Sn$_{0.2}$ (1; 0.92 kg) 3.LaNi$_{4.8}$Sn$_{0.2}$ (1; 1.5 kg)	25	0.001	1-280 2-95 3-240	1-1 2-3 3-103	NASA-JPL. (US) ; Electric heating (245 W), radiator cooling. hydride beds mass 57 kg
1998	Continuous	1. LaNi$_{4.5}$Mn$_{0.5}$ (30; 1.33 kg) 2. LaNi$_5$ (30; 1.33 kg)	25	3	250	150	Inst. Probl. Mech. Eng. (UA) ; electric heating, forced air cooling (27 kW in total).

Year	Operation*	Alloy (number of containers per stage; mass)	T_l (°C)	P_l (bar)	T_h (°C)	P_h (bar)	Developers ; important features
1999	Periodic	$MmNi_5$ (1 ; 1.6 kg)	15	25	327	400	Inst. Probl. Mech. Eng. (UA) ; electric heating (1kW), air cooling
2001	Periodic	VH_x (NS)	20	100	527	5000	Russian Federal Nuclear Center ; air cooling/ electric heating; research facility for H_2 and D_2 compression
2001	Continuous	AB_5 (NS)	25	20	400	345	Ergenics Inc (US) ; air cooling/ electric heating.
2002	Continuous	$LaNi_{4.78}Sn_{0.22}$ (6 ; 615 g)	-7	0.6	197	50	NASA-JPL (US) ; chiller plate cooling/electric heating (410W). Used for the cryo-cooling on-board of Planck spacecraft. Lifetime 20,000 cycles
2005	Periodic	$MmNi_{4.6}Al_{0.4}$ (1 ; 0.4 kg)	20	5	95	43.8	Indian Inst. of Technology ; liquid heating/cooling (1×10^3 L/min)
2009	Continuous	1.$(La,Ce)Ni_5$ (1 ; 160 g) 2.$(Ti,Zr)(Fe,Mn,Cr,Ni)_2$ (4 ; 120 g)	15	7	110	200	Univ. Western Cape(ZA); electric heating (400 W), water cooling
2009	Periodic	1.$LaNi_{4.25}Al_{0.75}$ (1; 3.5 kg) 2.$LaNi_{4.8}Sn_{0.2}$ (1; 45 kg)	50	16	175	33	Tech. Univ. of Lodz (PL); oil heating/cooling.
2009	Periodic	1.$LaNi_{4.85}Al_{0.15}$, (1; 120 g) 2.$LaNi_{4.9}Cu_{0.1}$, (1; 120 g) 3.$MmNi_{4.05}Fe_{0.95}$; (1; 120 g)	20	2	80	56	Nat. Inst. for R&D of Isotopic and Molecular Technologies (RO); water heating/cooling
2011	Periodic	1.$LaNi_5$, $Ca_{0.6}Mm_{0.4}Ni_5$, $Ca_{0.2}Mm_{0.8}Ni_5$. (3; NS)	10	13-40	90	100-150	Joint US-KR team ; water heating/ Cooling. MH: compacts of Cu-encapsulated IMC particles (5/3 g) with Sn binder (0.5/0.3 g), 170-200 bar compacting pressure.
		1.$LaNi_5$ (1; NS) 2.$LaNi_5$, $Ca_{0.6}Mm_{0.4}Ni_5$, $Ca_{0.2}Mm_{0.8}Ni_5$. (3; NS)	10	7	125	100-160	
2012	Continuous	1.$LaNi_5$ (6; 14 kg); 2.$La_{0.5}Ce_{0.5}Ni_5$ (6; 10 kg)	10-15	2-5	150	150-160	Russian Acad. Sci; Spec. Design & Engineering Bureau in Electrochemistry (RU); water cooling, steam heating
2012	Continuous	1. $(La,Ce)Ni_5$ (2; 15 kg); 2.$(Ti,Zr)(Fe,Mn,Cr,Ni)_2$ (2; 12 kg)	20	10	120	200	Univ. Western Cape (ZA); water cooling, steam or overheated water heating.
2012	Periodic	1.$La_{0.4}Y_{0.6}Ni_{4.8}Al_{0.2}$ (1; 594 g) 2.$V/LaNi_5$ (1; 594 g)	20/80	20	95/175	350/380	Inst. of Refrigeration and Cryogenics Eng., Shanghai Jiaotong Univ. (CN) ; water cooling, water/ oil heating
2012	Continuous	1.AB_5 (1; NS) 2.AB_2 (1; NS)	50	160	190	600	Univ. of Birmingham (UK); oil heating, water cooling
2013	Continuous	1.AB_5 (3; NS) 2.AB_2 (3; NS)	30	10-30	120	200	HYSTORSYS AS (NO); oil heating/cooling

*Continuous: the flux of H_2 is not interrupted after each full compressing cycle (e.g. from first to last stage)
Periodic: the flux of H_2 is interrupted after each full compressing cycle

Several aspects can be inferred from the studies and prototypes described. A few studies work with inlet pressures close or lower than 1 atm, which reduces the opportunity of using this technology with low pressure H_2 generation techniques, e.g. a photoelectrochemical cell. Most of the materials employed in a single-, double- and/or triple-stage MHHC are basically of the AB_2-type and AB_5-type type alloys. Also, the tailoring of the chemical composition to enhance the thermodynamic and intrinsic kinetic properties of the alloys is important to achieve an optimal operation in a MHHC system. Simulations can be performed with the thermodynamic properties of the alloys as an approach to design MHHC´s, for instance to improve the CR [17]. In addition, the implementation of just experimental measurements and set-ups to test different combination of materials can be a limitation, since not all the materials could be assessed to be considered for a MHHC system.

Although the thermodynamic properties are important for the design of a MHHC, the thermal management and/or design of the system are also key features for the performance of the entire kinetics, affecting the final productivity and efficiency of the compressor. Also, as previously addressed by some authors, an enhancement of the thermal management can be achieved through the implementation of proper equipment (heating/cooling type and coupling with respect to MH vessel, e.g. external electric heating), the increase of the thermal conductivity of the MH with its container (type and layout, e.g. fins, metal foams, compacts, etc) and/or the geometry optimization of the container to reduce its thermal resistance (e.g. small diameters and wall thicknesses) [52, 53-55].

Thus, a proper design of a MHHC have to account for several variables like thermodynamics, intrinsic kinetics, heat and mass transport, gas velocity, and, integrity of the system, resulting in a complex issue to be addressed just by experimentation. As a result, a numerical modelling approach is a useful instrument to identify and predict the hydrogenation state of the MH, as well as, to determine the relationship between the different factors mentioned, finding the best performance of MHHC´s and MH storage in general [17, 56].

The simulations of MHHC and MH containers mostly relay in the coupling of the mass and heat transfer processes. The mass transfer process is ruled by parameters like instant H_2 pressure, P_{eq} (function of temperature), hydride bed temperature and hydrogen concentration in the hydride. Also, the hydride temperature is the result of the heat transfer process between the hydride bed and the heating-cooling fluid, resulting in a mutual influence between both processes [57]. Considering these parameters, several numerical and analytical approximations have been done on MH storage vessels and MHHC´s. In Table 3, the most important aspects to consider from some simulation studies on MH and MHHC are resumed. Specially the main assumptions of the model (as will be mentioned in table 3: 1. H_2 behaves as an ideal gas; 2. Thermal conductivity and specific heat of the hydrides are assumed to be constant; 3. radiative heat transfer is negligible; 4. The bed void fraction remains constant and uniform 5. local thermal equilibrium is instantly achieved between the gas and the hydride; 6. The effect of pressure variation (heat transfer by mass convection) in the tank is negligible; 7. the dependence of equilibrium pressure on hydrogen concentration can be neglected), the parameters that were optimized or analyzed, the material (s) used and the final results are briefly described.

Table 3. Numerical and analytical studies on MH and MHHC

MH				
Material (s)	**Main assumptions of the model[+]**	**Parameters optimized / analyzed**	**Final outcome[++]/ important aspects analyzed**	**Reference**
Two couple alloys: 1.MmNi$_{4.5}$Al$_{0.5}$ 2.MmNi$_{4.2}$Al$_{0.1}$Fe$_{0.7}$	*1; 3 *1-D model *First order rate equation	*Three dynamic subsystems and 1 complete coupled system analyzed *Analyzed the duration of the total time process and the solving time step *Internal Heat exchanger	Transient behavior of: *H$_2$ flow rate *H$_2$ transferred amount, pressure and temperature. *temperature of the hydrides and the HTF *heat flow rates *amount of heat transferred	[57]
MmNi$_{4.5}$Al$_{0.5}$	*1; 3 *1-D model *H$_2$ is supplied by a reservoir vessel and finally deliver to a receiver container *All pressure drops are neglected *Pressure and temperature of H$_2$ in the reservoir / receiver vessels are assumed to vary with time only.	*Different external HTF temperatures *Model account for the effects of hysteresis, plateau slope and variation in bed pressure	*The thermal conductivity of the MH bed should be improved *Pressure drop and thermal mass of the MH container. There is some discrepancy in the bed temperatures due to the thermal mass of the reactor and the pressure drop. Hence, these effects have to be taken into account for an accurate performance prediction of hydride beds.	[58]
Ti$_{0.98}$Zr$_{0.02}$V$_{0.43}$Fe$_{0.09}$Cr$_{0.05}$Mn$_{1.5}$	*1; 2; 3; 4 *2-D, temperature and H$_2$ concentration vary along the radial and axial direction. *H$_2$ is supplied to the tank at a known constant pressure.	*Analyzed the effects of: -Internal H$_2$ supply pressure -External cooling fluid temperature -Overall heat transfer coefficient -Height to the radius ratio of the tank (H/R)	*With a higher supply pressure, it was achieved: -Lower cooling fluid temperature needed -Better overall heat transfer coefficient -Larger rate of hydride formation. *Lower H/R values means less time to full absorption *The time to hydride saturation increases with H/R value till H/R =2, larger than this, a reverse trend is observed.	[59]
LaNi$_5$	*1; 3; 5; 6 *1-D model *Thermal and physical properties are considered independent of bed temperature and concentration.	*Quantity of internal aluminum (Al) foam *Aspect ratio of the cylindrical tank (radius/height) *Natural convection vs external active cooling (forced convection)	*Effect of tank aspect ratio on the filling rate/time: -becomes strong when the effective thermal conductivity of the metal hydride powder is small (less aluminum foam in the tank). -Stronger when the heat removal rate is high (larger convection coefficient). *Hydride bed can reach a higher saturation with hydrogen in under active cooling (h = 2500 W/m²-K), without Al foam. *When filling time is limited to several minutes, a 30% of Al foam is required to maximize hydrogen absorption with natural convection, while with active cooling just a 10% is needed.	[54]

LaNi$_5$	*1; 3; 5; 6 *1-D model *Thermo-physical properties are considered independent of bed temperature and concentration	*Different MH vessel designs analyzed: -Case 1: a cylindrical tank that exchanges heat through its surrounding surfaces at a constant temperature. -Case 2: a cylindrical tank equipped with fins on its external lateral surface. -Case 3: Similar to case 1, with the addition of an internal heat exchanger tube without fins and filled with flowing cooling fluid. - Case 4: Similar to case 3, with the addition of fin attached to the internal heat exchanger tube. *Steel and brass reactor walls were tested	*Heat transfer is controlled by the poor conductivity of the hydride bed. Therefore, the hydrogen storage time is nearly the same for the two wall-metals analyzed, even with their significant difference in thermal conductivity. *An almost 80% improvement of the storage time can be achieved when the design includes a concentric heat exchanger tube equipped with fins and filled with flowing cooling fluid	[60]
LaNi$_5$	*1;2;3;4;5;6 *3-D model *the powdery metal hydride vessel is treated as an isotropic and homogeneous porous medium characterized by uniform porous properties, such as the porosity, permeability, and tortuosity. *The volumetric expansion of the metal hydride during hydrogen absorption is negligible.	*Effects of considering P$_{eq}$ (With and without) *Effects of the metal hydride vessel design: -3 different shapes *Effects of the hydrogen inlet pressure	*Better agreement is achieved under consideration of the equilibrium pressure as a function of both the dissipation temperature and the quantity of hydrogen absorbed (H/M). It was concluded that the effect of P$_{eq}$ can't be overlooked. *Higher hydrogen feed pressure improves the kinetics of the hydrogen absorption process and consequently leads not only to a rapid hydrogen charging performance but also to a reduction in the cooling load of the vessel. *Due to the effect of temperature on the P$_{eq}$, at the beginning of the absorption, the sorption velocity is higher closer to the wall, where the cooling system is applied, but then it increases towards the center. * A higher contact area per volume of the hydride bed with the cooling fluid will enhance the time at which the hydride completely hydrogenates (e.g. A/V=0.155)	[61]

MHHC				
Material (s)	**Main assumptions of the model[+]**	**Parameters optimized / analyzed**	**Final outcome[++] / important aspects analyzed**	**Reference**
St1:LaNi$_5$ St2:MmNi$_{4.6}$Al$_{0.4}$ St3:Ti$_{0.99}$Zr$_{0.01}$V$_{0.43}$Fe$_{0.99}$Cr$_{0.05}$Mn$_{1.5}$	*1;2; 3; 5 *1-D model *Viscous dissipation is negligible. *There is no heat transfer through the porous filter. *The medium is isotropic	*Effect of changing in all the three stages: -Different supply pressures -Desorption temperatures (T$_h$) -Absorption temperatures (T$_l$)	*Lower absorption temperatures yield higher storage pressures and correspondingly desorb larger amount of hydrogen *When the supply pressure is increased (e.g. from 5 bar to 10 bar), the storage pressure increases only a small amount but the efficiency of the compressor decreases considerably. *Due to the poor thermal conductivity of the hydride bed, the generated amount of heat during the rapid absorption process is not being transferred from the hydride bed to the heat transfer fluid, resulting in a sudden rise in the bed temperature. Also, during the initial stage of desorption process, the required amount of heat is not being transferred from the heat transfer fluid to the hydride bed and hence, the required amount of heat is taken from the bed itself, resulting in sudden fall in the bed temperature. *Sensible heating increases the equilibrium pressures of the reactor, which provides a favorable condition for the stage-coupled desorption and absorption processes	[62]
MmNi$_{4.6}$Al$_{0.4}$	*1; 3; 5; 6 *1-D model	*Varying operating parameters: -Supply pressure -Heat source temperature	*Hydrogen storage pressure increases with an increment of supply pressure and heat source temperature. * the system efficiency increases with hot fluid temperature but by a small amount *For a stablished desorption temperature, the increase of supply pressure will have a negative effect on the system efficiency, since the CR is reduced. *Maximum efficiency of 7.3% is obtained with pressure ratio of 8.8 (43.8/5.0) at 95 °C hot fluid temperature. *Compressor efficiency improves at higher heat source temperatures	[63]

St1: LaNi5 St2: Ca0.6Mm0.4Ni5.	*1; 3; 6; 7 *1-D model *The double-stage reactor is modeled as two single stage reactors of the same size in series * All of the hydrogen absorbed by the metal hydrides would be desorbed	*Cooling reservoir temperature *The simulation use experimental parameters measured	*The final output pressures and compression ratios follow an upward trend when increasing the heating bath temperatures. *A final CR of approximately 12 when using cooling and heating temperatures of 10ºC and 90ºC, respectively *Large differences in the energy requirements for the absorption and desorption processes of the $Ca_{0.6}Mm_{0.4}Ni_5$ may be due to environmental losses in combination with hysteresis.	[64]
St1:$LaNi_5$ St2:$MmNi_{4.6}Al_{0.4}$ St3:$Ti_{0.99}Zr_{0.01}V_{0.43}Fe_{0.99}Cr_{0.05}Mn_{1.5}$.	*1; 3; 5; 6 *1-D model	*Analyzed the effect of constant Th= 100ºC for desorption and Tl=20ºC for absorption at every stage	*A final pressure of 115 bar is achieved, which provides a compression ratio 23. * the generated amount of heat is not being transferred properly from the external heater to the bed due to the poor thermal conductivity of the hydride.	[65]
St1:$LaNi_5$ or $MmNi4.6Al0.4$ St2: Zr–V–Mn–Nb (AB2-type) or Hydralloy C5)	*1; 2; 3; 5; *1-D model *Initially the temperature and pressure profiles are uniform.	*Different alloys for the first and second stages and 4 different combinations: -Case 1: $LaNi_5$ and Zr–V–Mn–Nb -Case 2: $MmNi_{4.6}Al_{0.4}$ and Zr–V–Mn–Nb -Case 3: $LaNi_5$ and Hydralloy C5 -Case 4: $MmNi_{4.6}Al_{0.4}$ and Hydralloy C5	*With case 1 a final CR of 22 was achieved at a temperature range between 20ºC (hydrogenation) and 130ºC (dehydrogenation) and an inlet pressure of 15 bar *For case 2 and 4 (St1=$MmNi_{4.6}Al_{0.4}$) the CR was of 12 and 11, respectively, working between 20 and 100 ºC, however, the cycling time was faster and the energy consumption lower	[66]
Materials for a St1: $LaNi_5$ AB2-type (Ti-Zr-Mn based)	*1; 2; 3; 4; 5 *3-D model *Initially the temperature and pressure profiles are uniform. *The characteristics, e.g. the kinetics and thermal properties, of the bed are unaffected by the number of loading and unloading cycles, i.e. bed aging is neglected. *The bed fills the entire volume of the space between the fins and tubes.	Three different heat management scenarios: 1. use of a different number of plain cooling/heating tubes embedded in the reactor 2. different number of transverse Al surfaces extending along the cooling/heating tubes 3. different number of longitudinal Al extended surfaces along the cooling/heating tubes	*In terms of hydrogenation time: -the optimized geometries for the finned tube geometries and the optimum geometry for the transverse finned tubes is the combination of 30 fins (between the fins 9.8 mm) with radius 8 mm and thickness 2 mm. Tthe optimum geometry for the longitudinal finned tubes is the combination of 12 fins with each fin height 5 mm and thickness 0.5 mm. *Just in the case of the longitudinal fins the AB2-type presented a much faster response than $LaNi_5$ (4.5 min for the 12 finned tubes and 5 min for the 16 finned tubes configuration),	[67]

++Validated with experimental results

17

From these investigations and others [68-73], it can be implied that a model that successfully resembles the experimental behavior of a system, requires the implementation of appropriate physical-thermodynamic governing equations. In general, a system of differential equations of energy, mass and momentum conservation have to be simultaneously solved. Also, to simplify the resolution of these equations, several assumptions are taken (e.g. the common ones in many studies are mention in Table 3) [52, 56, 65].

Several parameters have a significant effect on the performance of MHHC. The hydride alloys that are used in each stage have a direct effect on the performance of the compressor, especially for the CR and H_2 rate, depending on their thermodynamics and intrinsic kinetics. The heat management (in all of its arrangements) is essential to account for sensible heating of the system and the change in P_{eq} due to the exothermic/endothermic reaction of the hydride in absorption/desorption, respectively. Also, the poor thermal conductivity of the MH bed should be improved, and/or, a reduction of the thermal resistance of the system should be considered, where in the latter an optimized aspect ratio can be a close solution to enhance the performance. The dead volume of the system is important since the higher the it is, the lower quantity of hydrogen can be store and compress afterwards [17], as a result, it would be better to have a lower dead volume of plumbing parts of the system and a higher quantity of MH in the tank. However, if also the thermal resistance of the reactor is reduced by decreasing the diameter and wall thickness, then an integrity issue in the vessel can be attained [74]. Thus, the optimized quantity of hydride in the container is a key parameter to consider.

In resume, as described by [17], the main target to attain with MHHC systems are:

- a high compression ratio (small slope of the isotherms, low hysteresis and appropriate thermodynamics of the metal-hydrogen system);
- high productivity and efficiency (low number of compressions steps, fast kinetics of hydrogen exchange, efficient heat transfer, low transient heat losses);
- long and reliable operation (high cycle stability of metal hydride materials at the operating conditions, efficient system design).

One suitable approach to these targets relays on using simulations with realistic features that account for the experimental behavior of each proper material to be used. From the studies and parameters researched, a scope of the work to be developed in the thesis can be defined.

1.3. Objective and scope of the thesis

Considering the problematic described, the present study has the main objective of developing an algorithm that accounts for thermodynamics and kinetics of metal hydrides in order to design properly a metal hydride hydrogen compressor through the implementation of numerical models linked to experimental measurements, approaching the real behavior of this system. The results of this program would serve as a basis to construct a real three stage MHHC.

As a result, each chapter will describe specific objectives to be achieved in order to fulfill the aim of the thesis:

Chapter 2: Describes the whole methodology applied through the thesis, the thermodynamic, and kinetic models applied, and the experimental procedures used. Also, a

basic material selection program is described, accounting for basic thermodynamics and operational parameters of the compressor.

Chapter 3: The materials selected are synthesized and characterized structurally, compositionally, morphologically, thermodynamically and kinetically by the experimental techniques and models described. The purpose of this objective is to verify the materials synthesized and to obtain the experimental measurements to properly validate the simulations in the next chapters.

Chapter 4: The mechanical properties of previously selected low pressure AB_2-type alloy are studied, specifically, the hydride breathing in terms of the porosity evolution throughout hydrogenation cycles. These measurements will determine how the powder bed interact inside a reactor while its absorbing/desorbing and will provide a value of the porosity that will be part of the model developed.

Chapter 5: A thermodynamic simulation algorithm is developed using real H_2 gas EOS and realistic thermodynamic models to account for an accurate behavior of the materials selected while they are simulated at different temperatures, optimizing the system to achieve a high CR as a first approach to design a MHHC. Also, a simulation of the real operation of a three stage MHHC system is studied.

Chapter 6: A Sieverts-type MHHC measurement system is assembled, set up and employed as a measurement equipment to test MHHC system from vacuum to 250 bar. The calibration and set up will be described using the thermodynamic properties of the materials selected. A final experiment of the entire system, preparation and the phenomena happening, will be described and discussed.

Finally, the final resume of achievements, conclusions of the whole thesis and future work is shown.

1.4. References

[1]   International Energy Agency, "Key world energy statistics 2017," IEA, Paris, France, 2017.

[2]   International Energy Agency, "CO2 Emissions From Fuel Combustion Highlights 2017," IEA, Paris, France, 2017.

[3]   R. C. Armstrong *et al.*, "The frontiers of energy," *Nat. Energy*, vol. 1, no. 1, p. 15020, Jan. 2016.

[4]   International Energy Agency, "World Energy Outlook 2016," IEA, Paris, France, 2016.

[5]   K. T. Møller, T. R. Jensen, E. Akiba, and H. Li, "Hydrogen - A sustainable energy carrier," *Prog. Nat. Sci. Mater. Int.*, vol. 27, no. 1, pp. 34–40, Feb. 2017.

[6]   B. Elvers, Ed., *Handbook of fuels: energy sources for transportation*. Weinheim: Wiley-VCH, 2008.

[7]   R. Mohtadi and S. Orimo, "The renaissance of hydrides as energy materials," *Nat. Rev. Mater.*, vol. 2, no. 3, p. 16091, Dec. 2016.

[8]   J. Kurtz, C. Ainscough, L. Simpson, and M. Caton, "Hydrogen storage needs for early motive fuel cell markets," National Renewable Energy Laboratory (NREL), Golden, CO., 2012.

[9]   A. Züttel, "Materials for hydrogen storage," *Mater. Today*, vol. 6, no. 9, pp. 24–33, 2003.

[10] S. Pique, B. Weinberger, V. De-Dianous, and B. Debray, "Comparative study of regulations, codes and standards and practices on hydrogen fuelling stations," *Int. J. Hydrog. Energy*, vol. 42, no. 11, pp. 7429–7439, Mar. 2017.

[11] J. Alazemi and J. Andrews, "Automotive hydrogen fuelling stations: An international review," *Renew. Sustain. Energy Rev.*, vol. 48, pp. 483–499, Aug. 2015.

[12] ESC, "Major categories of compressors." Taken from: http://aircompressor.org/technology/air-compressors/.

[13] S. Makridis, "Hydrogen storage and compression," *ArXiv Prepr. ArXiv170206015*, 2017.

[14] GHS VINA CO., "KINDS OF AIR COMPRESSORS." Taken from: http://ghsvina.com/en/kind-of-air-compressor.pd/kinds-of-air-compressors.html.

[15] Engineering 360, "Refrigeration Compressors and Air Conditioning Compressors Information." Taken from: https://www.globalspec.com/learnmore/building_construction/hvac/ventilation/refrigeration_compressors_air_conditioning_compressors.

[16] O. of E. E. and R. E. DOE, "Gaseous Hydrogen Compression." Taken from: https://energy.gov/eere/fuelcells/gaseous-hydrogen-compression.

[17] M. V. Lototskyy, V. A. Yartys, B. G. Pollet, and R. C. Bowman, "Metal hydride hydrogen compressors: A review," *Int. J. Hydrog. Energy*, vol. 39, no. 11, pp. 5818–5851, Apr. 2014.

[18] Linde, "Linde standard hydrogen filling station with IC90 compressor." Taken from: https://www.youtube.com/watch?v=usaQrCDORFY&ab_channel=Linde.

[19] M. Beckman, "Linde Hydrogen Fueling Overview," Washington D.C., 18-Nov-2014.

[20] N. A. Kermani, I. Petrushina, A. Nikiforov, J. O. Jensen, and M. Rokni, "Corrosion behavior of construction materials for ionic liquid hydrogen compressor," *Int. J. Hydrog. Energy*, vol. 41, no. 38, pp. 16688–16695, Oct. 2016.

[21] J. F. Lynch, A. J. Maeland, and G. G. Libowitz, "HYDROGEN COMPRESSION BY METAL HYDRIDES," Advances in Hydrogen Energy, 1, 1984.

[22] A. Fernández *et al.*, "Hidruros sólidos como acumuladores de hidrógeno," *Rev. Esp. Física*, vol. 24, no. 1, pp. 63–67, 2010.

[23] M. Dornheim, "Thermodynamics of metal hydrides: tailoring reaction enthalpies of hydrogen storage materials," in *Thermodynamics-Interaction Studies-Solids, Liquids and Gases*, InTech, 2011.

[24] V. A. Yartys *et al.*, "Metal hydride hydrogen compression: recent advances and future prospects," *Appl. Phys. A*, vol. 122, no. 4, Apr. 2016.

[25] P. Muthukumar, M. Prakash Maiya, and S. Srinivasa Murthy, "Parametric studies on a metal hydride based single stage hydrogen compressor," *Int. J. Hydrog. Energy*, vol. 27, no. 10, pp. 1083–1092, 2002.

[26] Y. Pang and Q. Li, "A review on kinetic models and corresponding analysis methods for hydrogen storage materials," *Int. J. Hydrog. Energy*, vol. 41, no. 40, pp. 18072–18087, Oct. 2016.

[27] F. S. Yang, G. X. Wang, Z. X. Zhang, X. Y. Meng, and V. Rudolph, "Design of the metal hydride reactors – A review on the key technical issues," *Int. J. Hydrog. Energy*, vol. 35, no. 8, pp. 3832–3840, Apr. 2010.

[28] P. D. Goodell, G. D. Sandrock, and E. L. Huston, "Kinetic and dynamic aspects of rechargeable metal hydrides," *J. Common Met.*, vol. 73, no. 1, pp. 135–142, 1980.

[29] P. D. Goodell, "Thermal conductivity of hydriding alloy powders and comparisons of reactor systems," *J. Common Met.*, vol. 74, no. 1, pp. 175–184, 1980.

[30] S. S. Murthy, "Heat and mass transfer in solid state hydrogen storage: a review," *J. Heat Transf.*, vol. 134, no. 3, p. 031020, 2012.

[31] G. Sandrock, "A panoramic overview of hydrogen storage alloys from a gas reaction point of view," *J. Alloys Compd.*, vol. 293, pp. 877–888, 1999.

[32] T. Forde, J. Maehlen, V. Yartys, M. Lototsky, and H. Uchida, "Influence of intrinsic hydrogenation/dehydrogenation kinetics on the dynamic behaviour of metal hydrides: A semi-empirical model and its verification," *Int. J. Hydrog. Energy*, vol. 32, no. 8, pp. 1041–1049, Jun. 2007.

[33] J. Bloch and M. H. Mintz, "Kinetics and mechanisms of metal hydrides formation—a review," *J. Alloys Compd.*, vol. 253, pp. 529–541, 1997.

[34] P. Dantzer and E. Orgaz, "Hydriding kinetics: the role of thermal transfer," *J. Common Met.*, vol. 147, no. 1, pp. 27–39, 1989.

[35] M. T. Hagstrom, J. P. Vanhanen, and P. D. Lund, "AB2 metal hydrides for high-pressure and narrow temperature interval applications," *Int. J. Hydrog. Energy*, vol. 269, no. 1–2, pp. 288–293, 1998.

[36] J. P. Vanhanen, M. T. Hagström, and P. D. Lund, "Combined hydrogen compressing and heat transforming through metal hydrides," *Int. J. Hydrog. Energy*, vol. 24, no. 5, pp. 441–448, 1999.

[37] J.-G. Park, K.-J. Jang, P. S. Lee, and J.-Y. Lee, "The operating characteristics of the compressor-driven metal hydride heat pump system," *Int. J. Hydrog. Energy*, vol. 26, no. 7, pp. 701–706, 2001.

[38] X. Wang *et al.*, "Investigation on high-pressure metal hydride hydrogen compressors," *Int. J. Hydrog. Energy*, vol. 32, no. 16, pp. 4011–4015, Nov. 2007.

[39] X. Wang, H. Liu, and H. Li, "A 70 MPa hydrogen-compression system using metal hydrides," *Int. J. Hydrog. Energy*, vol. 36, no. 15, pp. 9079–9085, Jul. 2011.

[40] H. Li, X. Wang, Z. Dong, L. Xu, and C. Chen, "A study on 70MPa metal hydride hydrogen compressor," *J. Alloys Compd.*, vol. 502, no. 2, pp. 503–507, Jul. 2010.

[41] F. Laurencelle, Z. Dehouche, J. Goyette, and T. Bose, "Integrated electrolyser—metal hydride compression system," *Int. J. Hydrog. Energy*, vol. 31, no. 6, pp. 762–768, May 2006.

[42] F. Laurencelle, Z. Dehouche, F. Morin, and J. Goyette, "Experimental study on a metal hydride based hydrogen compressor," *J. Alloys Compd.*, vol. 475, no. 1–2, pp. 810–816, May 2009.

[43] Z. Dehouche, M. Savard, F. Laurencelle, and J. Goyette, "Ti–V–Mn based alloys for hydrogen compression system," *J. Alloys Compd.*, vol. 400, no. 1–2, pp. 276–280, Sep. 2005.

[44] Z. Dehouche, N. Grimard, F. Laurencelle, J. Goyette, and T. K. Bose, "Hydride alloys properties investigations for hydrogen sorption compressor," *J. Alloys Compd.*, vol. 399, no. 1–2, pp. 224–236, Aug. 2005.

[45] B. A. Talagañis, M. R. Esquivel, and G. Meyer, "A two-stage hydrogen compressor based on (La,Ce,Nd,Pr)Ni5 intermetallics obtained by low energy mechanical alloying – Low temperature annealing treatment," *Int. J. Hydrog. Energy*, vol. 34, no. 4, pp. 2062–2068, Feb. 2009.

[46] E. D. Koultoukis, E. I Gkanas, S. S. Makridis, C. N. Christodoulou, D. Fruchart, and A. K. Stubos, "High-temperature activated AB $_2$ nanopowders for metal hydride hydrogen compression: Metal hydride technology in hydrogen compression," *Int. J. Energy Res.*, vol. 38, no. 4, pp. 477–486, Mar. 2014.

[47] M. M. H. Bhuiya *et al.*, "Experimentally tuned dual stage hydrogen compressor for improved compression ratio," *Int. J. Hydrog. Energy*, vol. 39, no. 24, pp. 12924–12933, Aug. 2014.

[48] P. Muthukumar, M. Prakashmaiya, and S. Srinivasamurthy, "Performance tests on a thermally operated hydrogen compressor," *Int. J. Hydrog. Energy*, vol. 33, no. 1, pp. 463–469, Jan. 2008.

[49] J. Kim, "A hydrogen-compression system using porous metal hydride pellets of LaNi5-xAlxLaNi5-xAlx," *Int. J. Hydrog. Energy*, vol. 33, no. 2, pp. 870–877, Jan. 2008.

[50] X. Guo *et al.*, "Laves phase hydrogen storage alloys for super-high-pressure metal hydride hydrogen compressors," *Rare Met.*, vol. 30, no. 3, pp. 227–231, Jun. 2011.

[51] A. Züttel, "Demonstration eines Metallhydrid Speichers in einem mit Wasserstoff angetriebenen Pistenfahrzeug," Swiss Federal Office of Energy SFOE and Universität Fribourg, Fribourg, 250046, Apr. 2004.

[52] M. Afzal, R. Mane, and P. Sharma, "Heat transfer techniques in metal hydride hydrogen storage: A review," *Int. J. Hydrog. Energy*, vol. 42, no. 52, pp. 30661–30682, Dec. 2017.

[53] P. Muthukumar and M. Groll, "Metal hydride based heating and cooling systems: A review," *Int. J. Hydrog. Energy*, vol. 35, no. 8, pp. 3817–3831, Apr. 2010.

[54] H. Wang, A. K. Prasad, and S. G. Advani, "Hydrogen storage systems based on hydride materials with enhanced thermal conductivity," *Int. J. Hydrog. Energy*, vol. 37, no. 1, pp. 290–298, Jan. 2012.

[55] M.-L. Tsai and T.-S. Yang, "On the selection of metal foam volume fraction for hydriding time minimization of metal hydride reactors," *Int. J. Hydrog. Energy*, vol. 35, no. 20, pp. 11052–11063, Oct. 2010.

[56] S. S. Mohammadshahi, E. M. Gray, and C. J. Webb, "A review of mathematical modelling of metal-hydride systems for hydrogen storage applications," *Int. J. Hydrog. Energy*, vol. 41, no. 5, pp. 3470–3484, Feb. 2016.

[57] M. Gambini, "Metal hydride energy systems performance evaluation. Part A: dynamic analysis model of heat and mass transfer," *Int. J. Hydrog. Energy*, vol. 19, no. 1, pp. 67–80, 1994.

[58] M. R. Gopal and S. S. Murthy, "Studies on heat and mass transfer in metal hydride beds," *Int. J. Hydrog. Energy*, vol. 20, no. 11, pp. 911–917, 1995.

[59] J. Ye, L. Jiang, Z. Li, X. Liu, S. Wang, and X. Li, "Numerical analysis of heat and mass transfer during absorption of hydrogen in metal hydride based hydrogen storage tanks," *Int. J. Hydrog. Energy*, vol. 35, no. 15, pp. 8216–8224, Aug. 2010.

[60] F. Askri, M. Bensalah, A. Jemni, and S. Bennasrallah, "Optimization of hydrogen storage in metal-hydride tanks," *Int. J. Hydrog. Energy*, vol. 34, no. 2, pp. 897–905, Jan. 2009.

[61] J. Nam, J. Ko, and H. Ju, "Three-dimensional modeling and simulation of hydrogen absorption in metal hydride hydrogen storage vessels," *Appl. Energy*, vol. 89, no. 1, pp. 164–175, Jan. 2012.

[62] P. Muthukumar, K. Singh Patel, P. Sachan, and N. Singhal, "Computational study on metal hydride based three-stage hydrogen compressor," *Int. J. Hydrog. Energy*, vol. 37, no. 4, pp. 3797–3806, Feb. 2012.

[63] P. Muthukumar, M. Prakashmaiya, and S. Srinivasamurthy, "Experiments on a metal hydride based hydrogen compressor," *Int. J. Hydrog. Energy*, vol. 30, no. 8, pp. 879–892, Jul. 2005.

[64] R. R. Hopkins and K. J. Kim, "Hydrogen compression characteristics of a dual stage thermal compressor system utilizing LaNi5 and Ca0.6Mm0.4Ni5 as the working metal hydrides," *Int. J. Hydrog. Energy*, vol. 35, no. 11, pp. 5693–5702, Jun. 2010.

[65] E. I. Gkanas, S. S. Makridis, and A. K. Stubos, "Modeling and simulation for absorption-desorption cyclic process on a three-stage metal hydride hydrogen compressor," in *Computer Aided Chemical Engineering*, vol. 32, Elsevier, 2013, pp. 379–384.

[66] E. I. Gkanas *et al.*, "Numerical study on a two-stage Metal Hydride Hydrogen Compression system," *J. Alloys Compd.*, vol. 645, pp. S18–S22, Oct. 2015.

[67] E. I. Gkanas, D. M. Grant, M. Khzouz, A. D. Stuart, K. Manickam, and G. S. Walker, "Efficient hydrogen storage in up-scale metal hydride tanks as possible metal hydride compression agents equipped with aluminium extended surfaces," *Int. J. Hydrog. Energy*, vol. 41, no. 25, pp. 10795–10810, Jul. 2016.

[68]   G. Karagiorgis *et al.*, "Design, development, construction and operation of a novel metal hydride compressor," *Int. J. Hydrog. Energy*, vol. 42, no. 17, pp. 12364–12374, Apr. 2017.

[69]   Y. Wang *et al.*, "Simulation study on the reaction process based single stage metal hydride thermal compressor," *Int. J. Hydrog. Energy*, vol. 35, no. 1, pp. 321–328, Jan. 2010.

[70]   S. Mellouli, F. Askri, H. Dhaou, A. Jemni, and S. Ben Nasrallah, "Numerical simulation of heat and mass transfer in metal hydride hydrogen storage tanks for fuel cell vehicles," *Int. J. Hydrog. Energy*, vol. 35, no. 4, pp. 1693–1705, Feb. 2010.

[71]   B. Satya Sekhar, M. Lototskyy, A. Kolesnikov, M. L. Moropeng, B. P. Tarasov, and B. G. Pollet, "Performance analysis of cylindrical metal hydride beds with various heat exchange options," *J. Alloys Compd.*, vol. 645, pp. S89–S95, Oct. 2015.

[72]   S. L. Garrison *et al.*, "Optimization of internal heat exchangers for hydrogen storage tanks utilizing metal hydrides," *Int. J. Hydrog. Energy*, vol. 37, no. 3, pp. 2850–2861, Feb. 2012.

[73]   B. A. Talagañis, G. O. Meyer, and P. A. Aguirre, "Modeling and simulation of absorption–desorption cyclic processes for hydrogen storage-compression using metal hydrides," *Int. J. Hydrog. Energy*, vol. 36, no. 21, pp. 13621–13631, Oct. 2011.

[74]   B. Charlas, A. Chaise, O. Gillia, P. Doremus, and D. Imbault, "Investigation of hydride powder bed swelling and shrinking during hydrogen absorption/desorption cycles under different compressive stresses," *J. Alloys Compd.*, vol. 580, pp. S149–S152, Dec. 2013.

Chapter 2. Materials selection, simulations and experimental techniques

2.1. Introduction

This chapter is aimed to describe the methodology followed to develop the compressor program properly. Therefore, as a first approach a material selection program was implemented in Microsoft Excel® using literature, some restrictions defined for the operation of the compressor and basic thermodynamics of hydrides. From the alloys selected, the synthesis methods and several experimental techniques employed to characterize them are described, where the experimental parameters measured will be used in the simulations. A further algorithm was developed in Matlab® considering suitable real H_2 gas EOS, thermodynamic models and also the thermodynamic experimental data from the materials selected, from which the basic design of a three stage MHHC measurement system was developed.

2.2. Material Selection program

Considering that most of the materials use in MHHC systems are of the AB_2-type, AB-type, AB_5-type, most of the literature research for the selection program was based on these alloys. Specifically, several materials reviewed in [1, 2] and other literature works [3-25] have been used to develop a single data base of over 200 materials with their thermodynamic data, which are the main input of an excel algorithm generated in this work. Then, to select the materials for the different stage of the compressor, several considerations and parameter constraints were taken into account in the algorithm:

Table 4. Resume of considerations and parameter constraints imposed to the selection algorithm

Thermodynamic considerations	Operational parameters
-Available Entropy and Enthalpy of hydride formation / dissociation in literature	-Working temperatures (between RT≈23ºC and 150 °C)
-Single plateau alloys	-Inlet pressure of the compressor system ≈1 bar <2 bar
-Van´t Hoff curve determined from enthalpy, entropy and operational temperatures	-P_{in} @RT ≈ 1 bar <2 bar and P_{des} @T_h as high as possible in the 1 stage
-Constant Hysteresis	-P_{des} @T_h <150ºC as high as possible in the 3 stage
	-P_{des} @T_h in 2 stage ≥ P_{abs} @RT in the 3 stage
-The possibility of tuning the thermodynamic properties of the hydrides by modifying slightly their chemical composition	-P_{des} @T_h in 1 stage ≥ P_{abs} @RT in the 2 stage
	-CR > 8 between coupling stages, e.g. first and second

The considerations and parameters evidence in Table 4 were considered as follows:

1. The first selection of the algorithm is made by comparing for each hydride included in the database [1, 25] created, the temperatures of operation and related plateau pressures with the established range at which the compressor works.
2. For the first selected compounds in the data base, the published enthalpy and entropy of formation are employed to generate Van´t Hoff plots (determined with Eq.2) both for absorption and desorption. For materials which data is only provided in absorption or desorption, a constant average value of hysteresis is applied [1] depending on the hydride type (Hys(AB)=0.4, Hys(AB_2)=0.4, Hys(AB_5)=0.2) to obtain the respective absorption/desorption Van´t Hoff plots. Also, the hysteresis values found in literature for some materials were used.
3. Several alloys were selected for the first stage based on one of the operational parameters, which stated that the inlet pressure at RT should be around 1 bar (below 2 bar) (Fig.7 a)

and its desorption pressure at 80°C should be as high as possible, resulting in the first selection of materials. Similarly, for the third stage, alloys with the highest desorption pressures (Fig.7 b) achievable at temperatures < 80°C were identified.
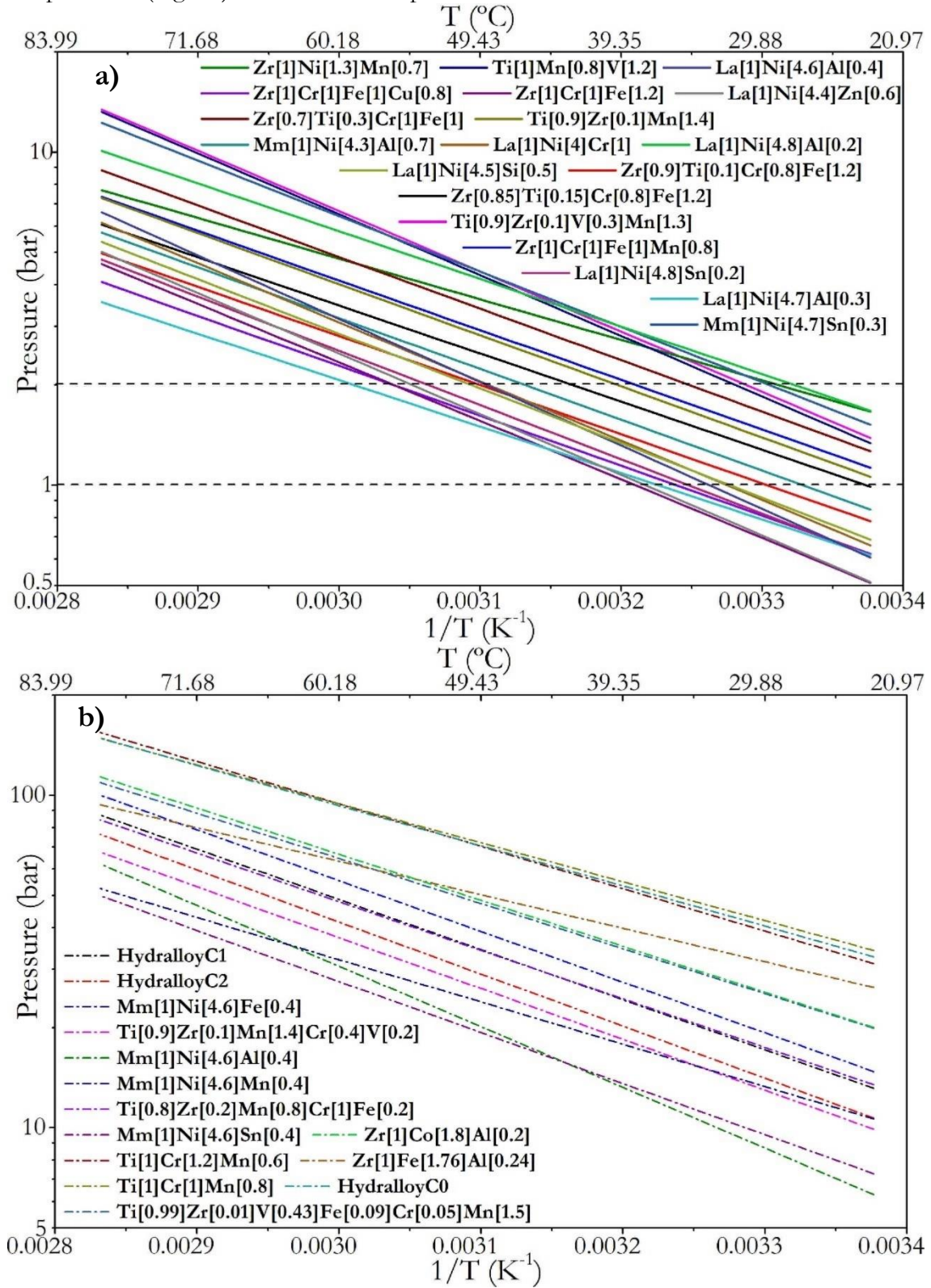

Fig.7. Van´t Hofft plots, a) alloys of the 1 stage that absorb at a P_{in}@RT close to 1 bar (black dash line), b) alloys of the 3 stage that desorb at a high pressure@80°C. Hydralloy C1: $Ti_{0.99}Zr_{0.01}V_{0.43}Fe_{0.09}Cr_{0.05}Mn_{1.5}$ [26, 27]

4. The coupling of the second stage alloy will aid to select the best hydride combination, hence the alloy from this stage must accomplish that its desorption pressure at high temperature should be equal or greater than the absorption pressure of the third alloy at RT. Since the kinetics are not considered in this thermodynamic analysis, it can be assumed that even with close pressures a driving force will create a desorption / absorption process. Likewise, the desorption pressure of the first stage have to be equal or greater than the absorption pressure of the second alloy at RT. Several reduced combinations of alloys fulfilling these conditions were found and resume (table Annex 1).

5. The final selection was taken by choosing alloys of close chemical composition, so that the final thermodynamic properties can be properly modified by tuning a small quantity of their constituting elements. As a result, three compounds of the AB_2-type – $TiMn_2$ family, a low pressure (A-P_l), a medium pressure (A-P_m) and a high pressure (A-P_h) hydrides were selected as the ideal final combination of alloys that achieves all of the requirements proposed above. Another P_l alloy was selected for comparison reasons, an AB_5-type, considering the higher resistance to impurities that this material exhibit in comparison with AB_2-type alloys in general, though, it is not a priority for the development of the thesis.
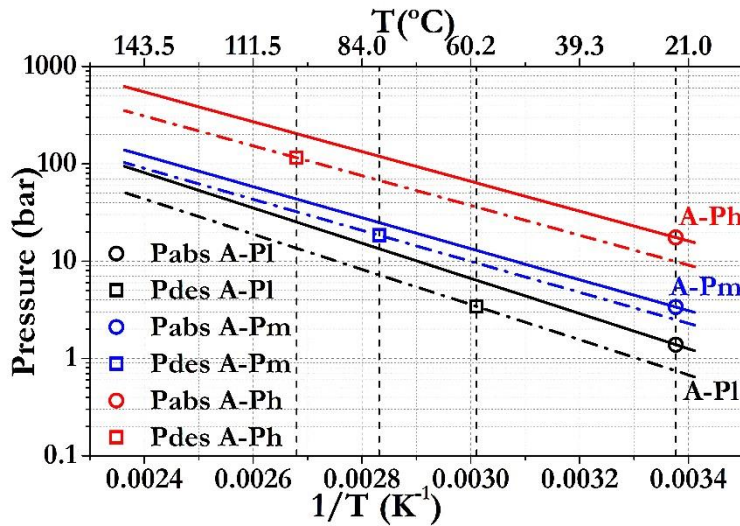
Fig.8. Alloys selected for the three stages. The open-circle points indicate the P_{abs} at RT, while the open-square ones are the P_{des} at the respective T_h of each stage. Adapted from [28]

Fig.8 presents the Van´t Hoff plot from the final hydrides selected and the operational points of the three stages. The materials selected by the algorithm were the $Ti_{0.9}Zr_{0.1}Mn_{1.3}V_{0.3}$ (A-P_l), the $Ti_{0.8}Zr_{0.2}Mn_{1.2}Cr_{0.6}V_{0.2}$ (A-P_m) and the $Ti_{0.9}Zr_{0.1}Mn_{1.4}Cr_{0.4}V_{0.2}$ (A-P_h). The values of the pressures and temperatures achieved with the combination of alloys selected can be seen in Table 5.

Table 5. Main results found by the selection algorithm for the three alloys. Adapted from [28]

Stage / material	Absorption pressure @ 23ºC (bar)	Desorption pressure (bar)	Desorption temperature (ºC)	CR between stages
1 / A-P_l	1.4	3.4	59	1-2: 13.1
2 / A-P_m	3.3	18.4	80	2-3: 34.9
3 / A-P_h	17.5	115.4	100	1-3: 82.4

For each alloy the desorption pressure at high temperature (open squares Fig.8) matches with the absorption pressure at 23ºC (open circles Fig.8) of the alloy used in the subsequent stage. This ideally couples the first to the second, and, the second to the third stages. The CR achieved between stages is always greater than 8, as stablished before. Something to highlight is that the three alloys are $TiMn_2$-based, for which small compositional changes give rise to strong modifications of the Van´t Hoff plots (Fig.8). The combination of these alloys fulfills all of the parameter constraints established previously.

2.3. Experimental techniques

The experimental measurements applied in this thesis has two main aims. First, to help on the design and building of a three stage MHHC, and second to validate and give a more accurate approximation of the simulations to reality. For the materials selected, the synthesis and further characterization was done by the following techniques.

2.3.1. Synthesis of the alloys

The synthesis of the alloys selected and the AB_5-type alloy ($LaNi_{4.8}Sn_{0.2}$) was made by a combination of the raw materials shown and described in Fig.9. For all the AB_2-type alloys and excess between 5-10% of Mn was used to maintain the stoichiometry of the final ingot, considering that this element has a low vapor pressure and thus it sublimates easily during the melting process. The AB_5-type alloy was prepared taking care of the fast oxidation of La pieces by preparing them in an Ar atmosphere and putting them promptly in the arc furnace.
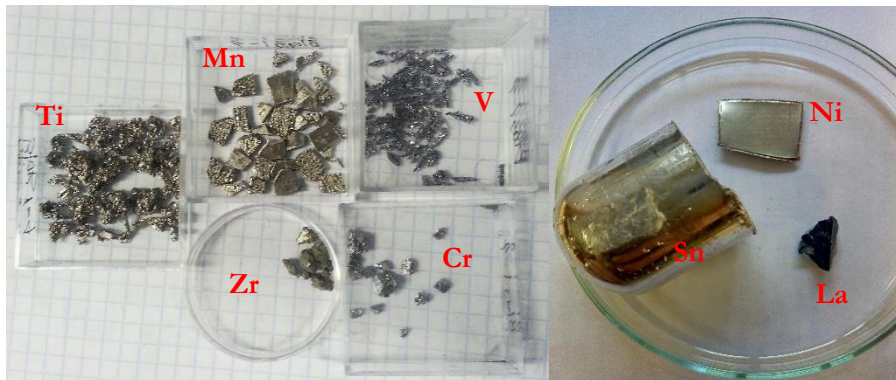
Fig.9. Raw materials for the alloys studied. Ti granules (dendrites) 99,99% ALFA AESAR, Zr sponge pieces 99,9% JMC, Mn chips 99,9% JMC, Cr pieces 99,2% ALFA AESAR, V granules (dendrites) 99,7 % ALFA AESAR, La pieces 99.99% ALFA AESAR, Ni foil 99.5 % JMC , Sn rod 99.9% Alfa AESAR

Two different processes were used during the investigation: arc melting and induction melting.

With the arc melting process (Fig.10 a and b), the raw materials were set in a Cu crucible that allow 5 – 7 gr of final ingot. Once the elements were in the fusion chamber a purging process began: a vacuum of $9*10^{-3}$ mbar is imposed, and a further Ar pressure of 500-900 mbar is applied, the process is repeated 5 times. Then the fusion method was as follows:

1. An Ar pressure between 750-900 mbar is set and remains steady during the melting. Then the DC voltage source is turn on, and a starting current of 20 A is employed to create the first spark (i.e. by touching the W-electrode with the W-primer (Fig.10 b)).
2. The current is increased up to 70 A until the sample starts melting down and with the steel bar a circular movement is applied constantly to homogenize the sample (red circle in Fig.10 b) for a minute.
3. The current is reduced gradually as: 40 A for 20 s, 20 A for 10 s, 10 A for 5 s, and off.
4. To homogenize the sample, the ingot is turn over and re-melted. This is repeated 5 times
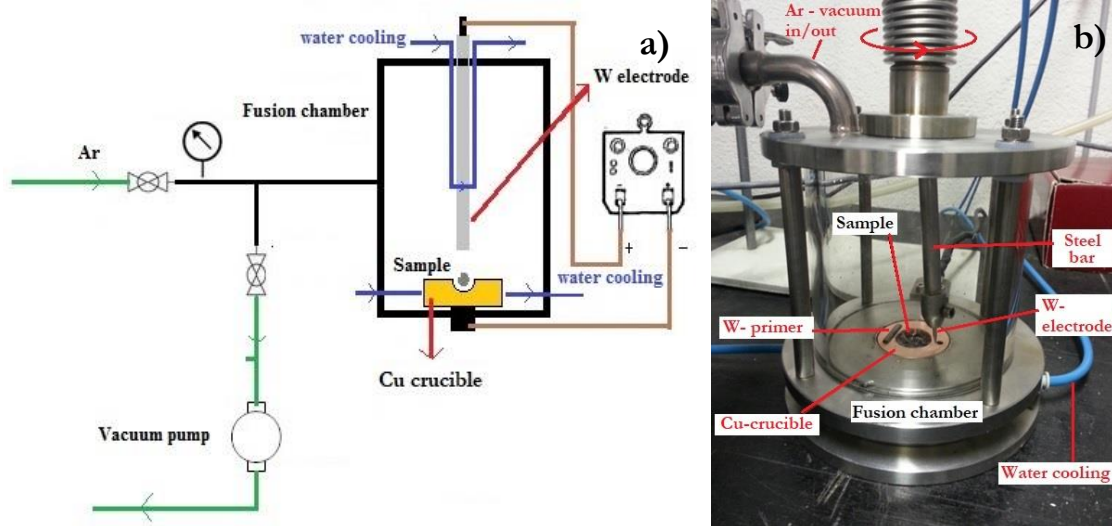
Fig.10. Synthesis by arc melting furnace. a) scheme of the system, b) fusion chamber

Fig.11. Cu crucible of the induction furnace [29]

For the induction furnace (Fig. 11), the material is placed in a Cu crucible and purge 2 times, then a constant flux of Ar at a pressure of 1 bar is applied. In this case the power of the equipment was increased gradually up to the point where the sample melted. The ingot remained levitating and spinning in the crucible for two minutes and then the power was reduced every two minutes until it was off. With this method the sample was melted just once.

From both processes the ingots obtained can be seen in Fig.12.
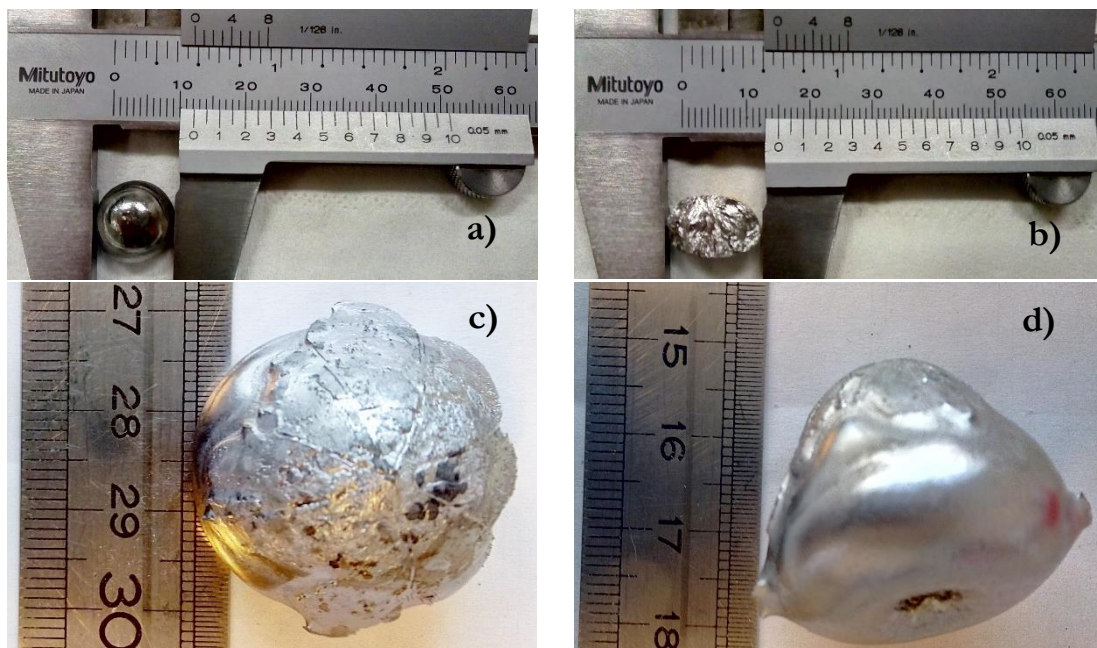
Fig.12. Ingots obtained by the synthesis methods, a) Top view arc melting, b) cross section view arc melting, c) Top view induction melting, d) lateral view induction melting

2.3.2. Annealing process

Usually as-cast alloys present heterogeneities in the microstructure, as a result, an annealing process can be a solution to homogenize the composition and the morphology(ies) related to it.

Fig.13. Open annealing sample holder. Adapted from [30]

For the AB_2-type alloys, the samples were pieces of the as-cast ingots that were placed in a stainless steel container with 1 bar of Ar atmosphere (Fig. 13), and then sealed. This procedure is needed due to the low vapor pressure of Mn in the AB_2-type alloys. The sample holder is put inside of a furnace under the same Ar pressure and at different temperatures, depending on the material used. Also, for the AB_5-type alloy, the samples were annealed in the furnace without the use of a special sealed chamber. For the AB_5-type alloy, a temperature of 950ºC for 120 h was applied as it has been stablished in previous works [31, 32], while for the AB_2-type alloys a temperature of 950ºC for 17 h was employed, considering the possible Mn loss, and the conditions employed in other works [33-35].

2.3.3. Characterization techniques

For the samples synthesized, several measurements were performed by different characterization techniques.

2.3.3.1. Compositional and morphological characterization

Know the real composition of the ingots is essential not only to verified that the synthesized alloy is close to what was expected, but also as an input of the structural characterization. Also, the identification of the morphology(ies) in the main matrix of the material is important to understand the possible changes in other properties (e.g. thermodynamic or kinetic)

2.3.3.1.1. Scanning Electron Microscopy (SEM) and Energy Dispersive X-ray spectroscopy (EDX)

These techniques are commonly coupled and are mostly employed to characterize the composition of a sample and identify the morphologies shown in the material [36]. To do the measurements, the samples had to be prepared as follows:

1. The samples were cut transversely and embed in a resin (combination of EpoFix Resin and EpoFix Hardener (Struers), 100/14 ml ratio)
2. As the resin hardened, a first coarse polishing procedure is applied, by using grinding papers of 180, 340, 600, 1000 and 1200 mesh.
3. A fine polishing procedure is applied, using diamond pastes (Metadi II, Buehler) of 9, 6, 3, 1 μm, and then a colloidal Alumina suspension of 0.3 μm (OP-S Suspension, Struers). Once finished the sample should look mirror like finish (Fig.14 a)
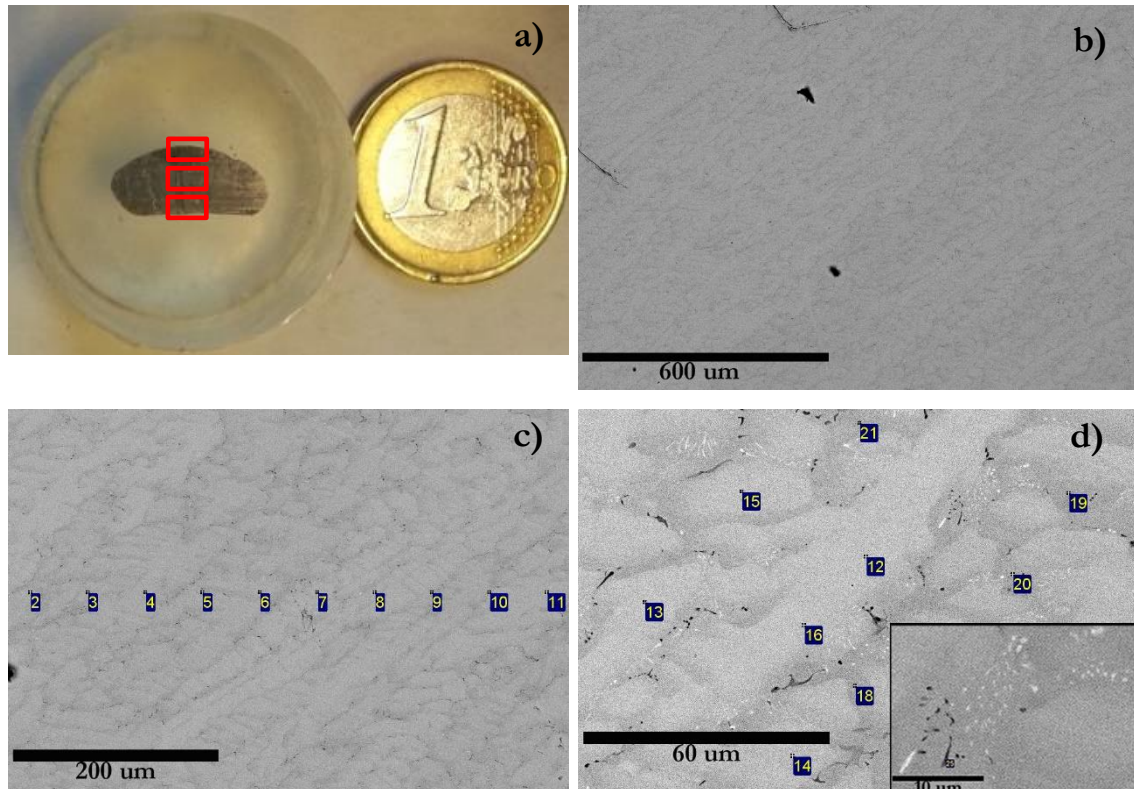
Fig.14. Sample compositional measurements with back-scatter electron detector (BSE), a) embed polished sample with the main measurement zones, b) general window, c) line scan, d) dark and light zones (inset picture shows secondary precipitates)

Three zones were taken for each sample, top, middle and bottom (red squares Fig.14 a), were at each of these areas the measurements were performed at 20 KeV in a SEM Hitachi S-3000N. A typical analysis comprises the following:

1. General composition using a full window 100x (fig.14 b)

2. Line scan to see the variability of the samples in a smaller range and identify possible heterogeneities in the main matrix (fig.14 c)

3. Distinctive secondary phases were measured by scatter points (fig.14 d)

4. Photographs of the main zones and particularities presented in the alloys were taken at different zooms

5. An image analysis of the secondary precipitates found in the AB_2-type samples was performed by using an open source program (ImageJ [37]). The analysis was done at the three different zones described and with several images taken at these zones, where the secondary phases were counted, and a density of these morphologies was obtained in comparison with the area of analysis. A density average value of the three zones was the final outcome.

2.3.3.1.2. Electron Probe Micro Analyzer (EPMA)

The equipment used for this technique (Electronic microprobe CAMECA SX100) uses a couple analysis with a Silicon Drift Detector (SDD) and a Wavelength Dispersive Spectrometer (WDS), giving a higher resolution in the quantitative measurements of elements compositions in the samples than a SEM-EDS instrument [38]. In this case, the samples were embedded with a low melting point alloy and polished also with a coarse and fine procedure.
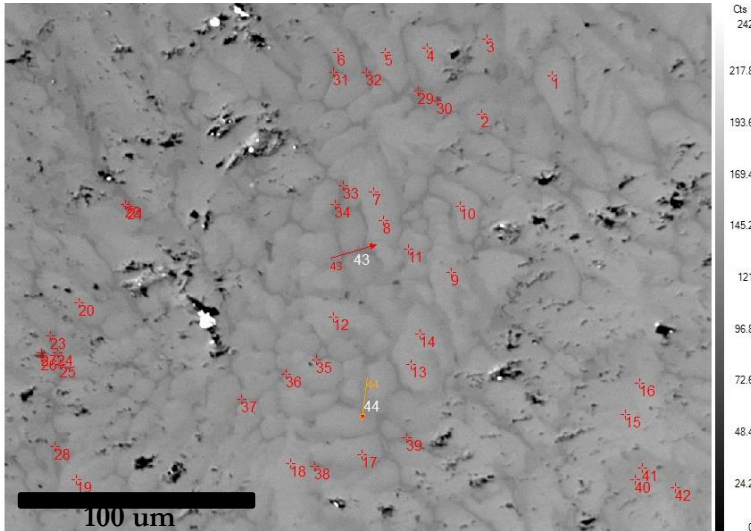
Fig.15. EPMA measurements. BSE micrograph

At different random zones of the sample, several measurement points were taken, looking for the composition in some heterogeneities of the alloy matrix.

2.3.3.1.3. Inductively coupled plasma optical emission spectrometry (ICP-OES)

This is a global destructive elemental analysis technique that allows the simultaneous analysis of many elements of the periodic table with a good accuracy. An Axial Detection System provides a detection limit threshold of the order of μg / L. This procedure is an ideal tool for analyzing composition of major elements but also elements with trace concentrations of a few ppm or ppb. It can be complementary to EPMA and / or EDX. The instrument use for the measurements is a ICP-OES Varian VistaPro [39]. The samples were prepared with a concentrated HCl solution and diluted in a volumetric flask with ultra-pure water. The final solution passes through a chamber where constant Ar flux maintain the plasma once it is generated, producing an emission that is quantified.

2.3.3.2. Structural characterization

The main purpose of this analysis is to identify the main phases and to obtain the lattice parameters and densities of the alloys

2.3.3.2.1. X-ray powder diffraction (XRPD)

Powder XRD (X-ray Diffraction) is perhaps the most widely used X-ray diffraction technique for characterizing materials. As the name suggests, the sample is usually in a powdery form, consisting of fine grains compose of several single crystalline materials to be studied. Its principles are widely known [40].

Fig.16. XRPD sample preparation, a) agate mortar and pestle, b) sieve of 45 μm, c) sample prepared on a quartz plate

For the measurements the following procedure was applied:

1. To prepare the samples an Agate mortar and pestle (Fig. 16 a) is employed to crush the material. Then it is sieved below 45 μm (Fig. 16 b).
2. The powder is spread on a quartz plate that have an adhesive element to attach the powder (Fig.16 c)
3. The sample is placed in a X-Ray diffractometer, which for most of the alloys measured, was a PANALYTICAL X'pert PRO equipment with a Johansson monochromator for K alpha1 with λ[Å]=1.5405, and were measured with the following conditions: Bragg-Brentano θ-2θ geometry, sample time=100 s, step angle= 0.0167°, RT. However, for samples synthesized in the CEA and ICMPE institutes, the radiation is composed of both K alpha1 with λ[Å]=1.5405 and K alpha2 with λ[Å]=1.544330.
4. The resulted diffractogram was analyzed with a X-pert Highscore Plus PRO and also a Rietveld refine was performed with the program Fullprof [41]. In the latter, the chemical composition measured previously by EDX, EPMA or ICP-OES is used as input. Also, a Thomson-Cox-Hastings pseudo-Voigt profile shape function was used for the refinement, which considers the peak profile as a weighted sum of a Gaussian and a Lorentzian. The final refinement considers the compatibility of the experimental diffractogram and its refinement (difference curve)(Fig.17.), and the optimization of other statistical parameters [42, 43].
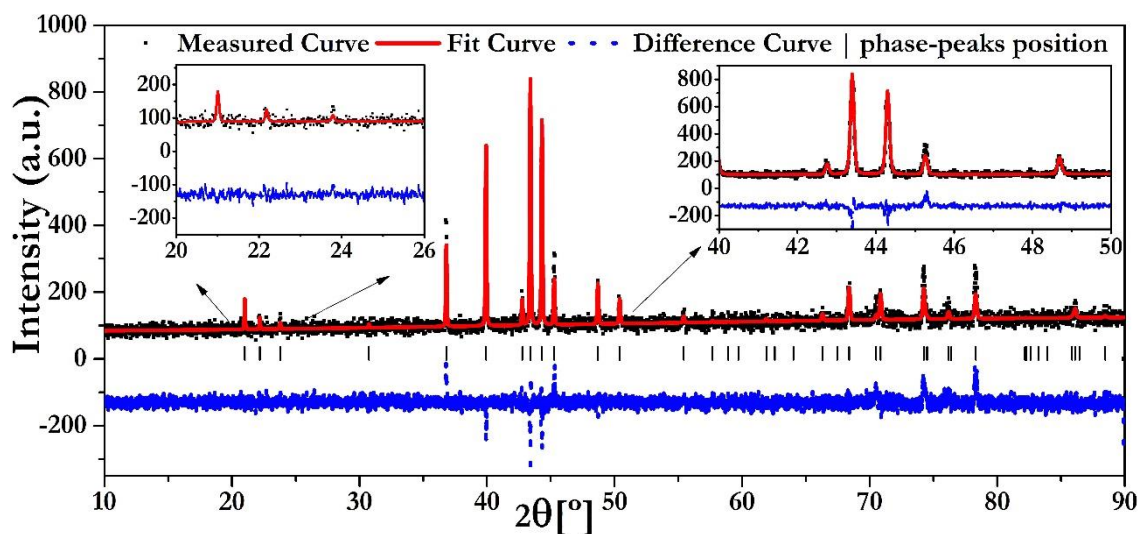
Fig. 17. Rietveld refined of a XRPD sample and its main features

2.3.3.3. Thermodynamic and kinetic characterization

The thermodynamic properties of hydrides can be quantified by the measurement and determination of the P-c-I. For this purpose, a manometric method that use a Sieverts-type reactor is employed [44]. This apparatus also allows for kinetic measurements by measuring the reacted fraction as a function of time. These measurements can be performed using adequate thermal systems like thermal baths, to maintain the temperature as stable as possible. In Fig.18, the schemes of the Sievert reactors employed in this investigation can be seen, where Vr is the main reservoir volume, the R1 and R2 are storage reservoir volumes, H_2, Ar and D_2 are the inlet for these gases, vacuum and atmosphere are the respective outlets and reactor is the volume of the sample container. A relevant difference between both apparatus is that the one in Fig.18a is inmersed in a thermostatic bath (±0.2 temperature) while the one in Fig 18b is enclosed in a room thermally controlled (±1°C).

33
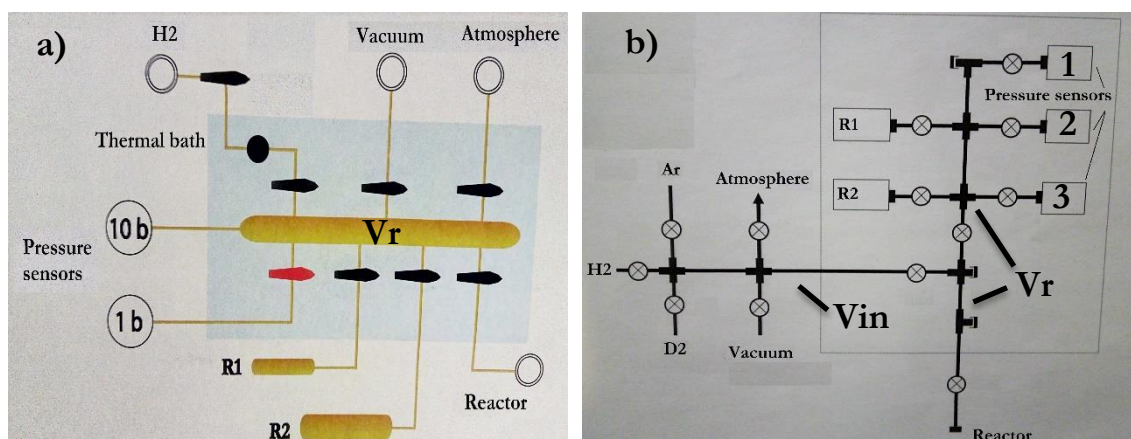
Fig.18. Sieverts type reactor schemes, a) system in thermal bath (black and red shapes stand for valves, 1 b is a special volume for systems with a pressure sensor up to 1 bar), b) system in a room thermally controlled (circles with an X in, stands for valves)

From the two schemes shown in Fig.18., the calibrated volumes of each system can be evidence in Table 6.

Table.6. Calibrated volumes of the sieverts-types reactors used, all volumes in cm³

System with thermal bath						
Vr	R1	R2	1 b			
8.0(3) – 12.0(4)	40.0(8) – 50(1)	76(1) – 150(2)	2.5(1) – 3.5(2)			
System in thermal control room						
Vr	R1	R2	1	2	3	Vin
23.4(1.1)	149.8(4.1)	53.4(1.6)	4.9(2)	12.36(44)	13.2	8.9(1.6)

For the thermally control room system, the values of the volumes are exactly the ones shown in Table.6, while in the case of the thermal bath systems a range of the volumes is given, since several units were used. However, real values of each volume were taken at the experiment and determination of the P-c-I.

Fig. 19. Top view of Sieverts reactor and filter

The samples for the P-c-I and the kinetic measurements were prepared as follows:

1. The alloy is crushed with an agate mortar (like for XRPD samples) in a globe box with Ar atmosphere.
2. The powder is poured inside the reactor (Fig.19) and weighted to know the mass of the sample (0.5 - 1 gr). Then, is sealed with the rest of the reactor (tubes, valve, connections, others) and a filter inside, in Ar atmosphere.
3. The reactor is assembled to the rest of the system, which is in vacuum, and tested for leaks with Ar
4. The free volume of the reactor (V_{fr}) is measured with Ar expansions, where the regular values were in the range of 3 – 6 cm³
5. A test for small leaks with H_2 is performed, then the activation of the sample is done 3 times for all the alloys measured. To fully desorb the samples between each activation, a vacuum pressure at a higher temperature is applied.
6. Pressures are measured and the corresponding P-c-I determined at different temperatures for absorption and desorption by using real H_2 gas EOS [45, 46]. In the system that resembles the scheme shown in Fig.18b, the effective temperature of the gas is measured for other temperatures that RT, while for the systems based on the scheme

in Fig.18a the thermostatic control of temperature in the volumes employed is constrained enough to assure that a change of temperature in the gas inside each volume would be regulated to the controlled temperature assigned.

7. With the P-c-I´s determined, a kinetic experiment is performed between the operational points of the MHHC, and, at the same temperatures used for the P-c-I experiments. To reduce pressure and temperature changes during these experiments, small pressure drops were taken by using higher reservoir volumes.

8. To take out the sample in hydrogenated state (just for the lower P_{eq} hydrides), the samples were passivated by giving small quantities of oxygen (5%) combined with Ar at the hydrogenated O.P.$_{abs}$ (P_{abs} to achieve β_{min} composition), and without the presence of more H_2 gas. For the rest of the samples a vacuum process was performed.

An important factor in these experiments is the identification of error sources, which can be of different types, and the accuracy of the measurements relay on reducing them [44] [47-49]:

* The instruments and equipment calibration must be performed before each measurement.
* Monitor and control temperature in the system. This variable becomes more difficult to control as measurement temperatures are further away from RT, due to thermal gradients throughout the apparatus. Therefore, two options for accounting this issue are: to have a compact system where all of the respective volumes are with a control temperature, or, measure an effective temperature for the experimental set up that will be use in the experiment at T_h. The type K thermocouple error in the systems described is of ±1°C.
* Reduce accumulative errors during volumetric uptake by recalibrating the system before each measurement or considering for the previous errors. The instrumental error in the pressure measurements is of 14 mbar in the system in Fig.18b, except when thermal fluctuation in the room produce a larger pressure variation (Fig.20), in which case, the value of this change is taken.
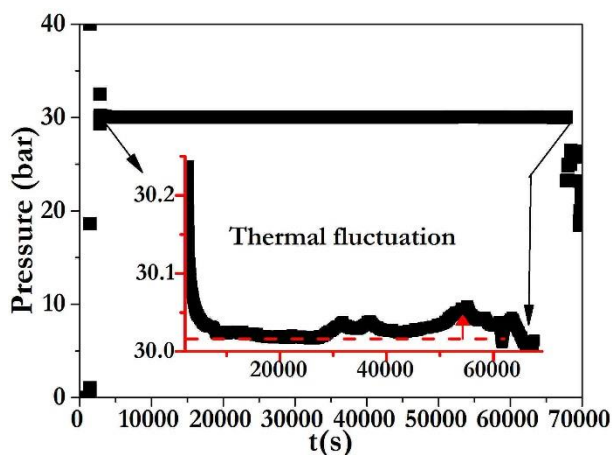
Fig.20. Effect of thermal fluctuation on pressure in an absorption stage.

* Reduce the time of experimentation to control the temperature shifts during an experiment day, or/and account the temperature fluctuations that the room suffer and affect a possible experiment in progress, especially during day-night change. Fig.20. evidence a higher-pressure error than the instrumental one, due to thermal fluctuation during the night period.

* The sample and reactor size should be appropriate so that the equipment being used can sense clearly the changes in the experimental variables.
* Before experimentation begin, a careful gas leak search should be performed, because any small gas leak could be confused as sorption by the material.
* The real behavior of the gas should be considered by implementing real EOS to prevent accumulative errors from occurring during the P-c-I determination. This becomes more significant as the pressure during a measurement increases.
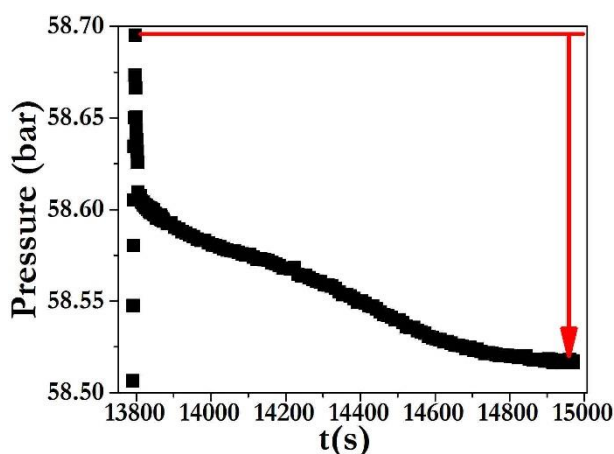
Fig.21. H₂ thermalization effect after a throttling process (passing through a small volume)

* When filling the gas reservoir, sufficient time should be allowed for the gas to come to thermal equilibrium with the tubing and vessels before a pressure reading is taken [50], this is due to an isenthalpic thermal expansion of the gas that generates an increased in temperature during the relaxation of the gas in a restriction, which for H_2, He or Ne at RT is the opposite to other real gases, and that in a throttling process (e.g. passing through a valve from and to a bigger volumes) generate a thermalization of the gas [51]. Fig.21. exhibits the time that the thermal control room system can last for the gas to reach thermal equilibrium with the rest of the system, this measurement was taken with an expansion from V_{in} at 58.68 bar to V_r at vacuum, to fill the reservoir volume before beginning. This effect is more critical with higher pressures and with systems that do not have a fast response thermal management system that can regulate this thermalization.

2.3.3.4. Differential Scanning Calorimetry (DSC)

This technique measures the difference in the amount of heat that should be added/removed to the sample (S) and an inert reference material (R) considering that both are simultaneously heated with individual heaters that aid to control any unbalance in the temperature between the sample and the reference [52]. The recorded heat flow can be associated to thermodynamic parameters such as Specific heat (Cp).
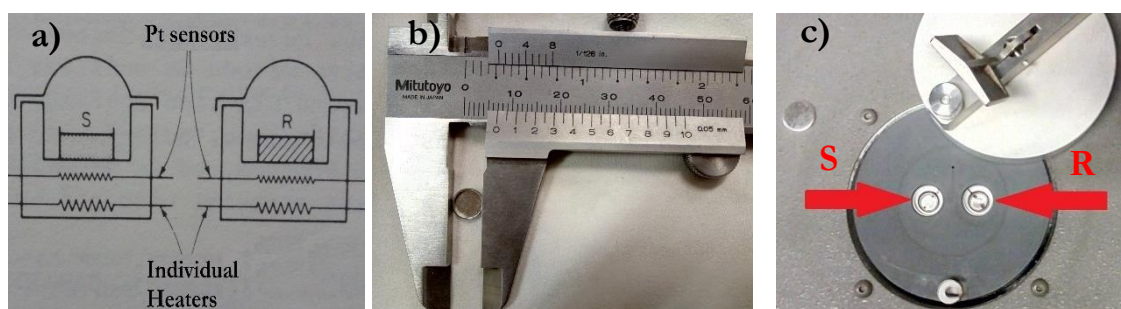
Fig.22. DSC, a) scheme (Adapted from [52]), b) Al sample holder, c) individual heaters for the sample holders.

For this experiment, 22.87(1) mg of sample are introduced in an Al sample holder (fig.22 b) and placed in a PERKIN-ELMER DSC-4 (red arrows Fig.22 c). The temperature and the heat were calibrated with Indium. For the reference material an empty Al sample holder was used (Fig.22b). The heat flow and temperature are recorded as a function of time during heating and cooling, with ramps between 50 and 200 °C at a constant heating rate of 20 °C/min and a sensitivity of 5 mcal/s. A baseline was measured in the same experimental conditions with an empty crucible before each experiment.

2.3.3.5. Thermal conductivity with thermal Van Der Pauw Method

These measurements were performed in a system developed in the MIRE group at the Universidad Autónoma de Madrid and is based on the thermal Van Der Pauw technique [53, 54].

Fig.23. Thermal conductivity system. The inset picture of the left is the compressed sample, while the inset picture of the rigth is a zoom of the sample in the vacumm chamber with all the thermo-resistances (T-1, T-2, T-3, T-4)

First, the powder of the P_1 AB_2-type alloy after hydrogenation cycles was compressed at 9 Ton of force to generate the sample (left inset figure in Fig.23.). The sample is placed in a heat sink (T-1, Cu bar with clamps) and connected to other three thermal resistances (Pt-1000) that can heat and also serve as temperature sensors, everything in a chamber at high vacuum (<1e-4 mbar).

In this case, a heat flow imposed between T-1 and T-2 (the thermo-resistance through which the current is passing would be T-2) generates a temperature difference measurement between points T-3 and T-4, likewise, putting a heat flow imposed between T-1 and T-3 will create a temperature difference between T-2 and T-4. By having both measurements and the sample thickness, then the thermal conductivity is determined by applying the formula described in [54].

2.3.3.6. Mechanical properties characterization
2.3.3.6.1. Hydride breathing

This technique is employed to measure the mechanical properties of hydrides, specifically how the powder bed interacts with its containing vessel during sorption cycling. This method and its general test bench assembly (COMEDHY) has been described in [55] [56]. Firstly, a special design for the inner parts of the test bench instrument is developed to fulfill that the experiments can be done with low quantity of material, and most importantly, that different stresses could be apply on the sample to measure its response during hydrogenation cycles. In Fig. 24, the scheme of the design developed can be observed.
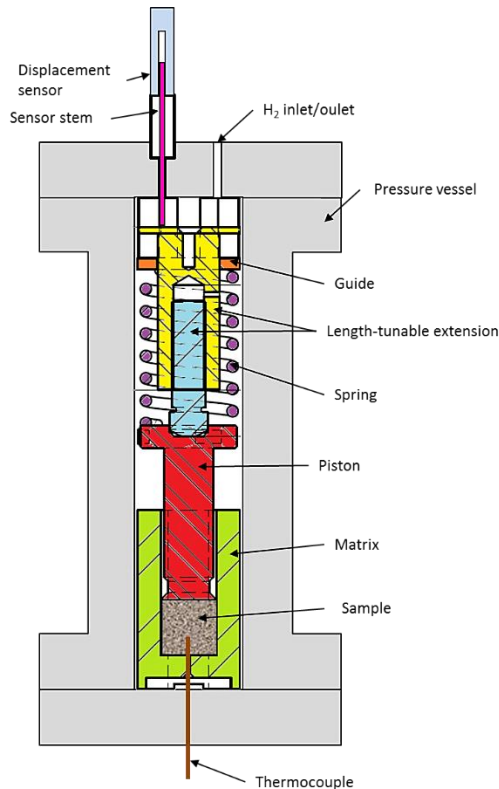
Fig.24. Scheme of the assembly with the inner parts designed for the COMEDHY test cell

In the system, a Linear Variable differential transformer (LVDT) sensor is employed to measure the vertical displacement generated by the volume expansion in the test cell while a control flux of hydrogen is getting in and out of the cell [57]. Moreover, for the temperature measurement a thermocouple is set in direct contact with the sample that is confined in a matrix with a diameter of 25 mm and a height of 25(1) mm (defined by the quantity of alloy). As mentioned, for the experiments the inner layout of the test cell was designed to admit lower quantities of material and also to apply the three levels of stress through springs with different calculated and calibrated stiffness.

In the scheme, the moving piston applied directly on the upper surface of the sample a constant force generated by the helical spring compression and the weight of the rest of the parts. The inlet and outlet H_2 flows were measured and regulated with calibrated mass flow controllers. The pressure was measured inside the vessel, and the temperature was measured inside the sample and on the surface of the vessel, were a thermal resistance was used to heat the system to 83(1) ºC in the test cell, where this temperature was determined with the thermodynamic properties of the alloy as will be described in chapter 4.

2.3.3.6.2. Laser Granulometry

This technique was employed to measure the average size distribution of the grains before and after the hydrogenation cycling of the Hydride breathing experiment. The samples before and after hydrogenation were submitted to ultrasound during 2 min. The powder is submerged in a Malvern Mastersizer 2000 instrument with ethanol dispersant and then a red light He-Ne laser with a wavelength of 466 nm passes through creating a scatter light pattern that is recorded and with analytical relationships, it calculates the size of particles that created that pattern [58].

2.4. Algorithm for the thermodynamic design of a MHHC

An algorithm in Matlab was implemented to simulate different operational variables of the compressor. As described previously, to resemble the real experimental behavior of a compressor, either thermodynamically or kinetically, the algorithm to be implemented need real models that can approach to this aim. First, the implementation of real H_2 gas EOS is a priority to account the compressibility of the gas, as described before. Likewise, the implementation of realistic P-c-I models that can predict the behavior of the material in absorption and desorption is extremely important, since not considering the real thermodynamics of the alloys can generate huge errors in the simulations at different temperatures [59, 60].

2.4.1. Real H$_2$ Gas EOS

In several applications, the H$_2$ EOS developed by Leachman et al. [61] is widely applied, since it is the one implemented by the NIST [62] for its H$_2$ calculation and modelling. Also, several works [63, 64] have pointed out that most of the EOS attempted to enhance the Van der Waals model by improving from its base equation, parameters such as the temperature dependence, molar volume, and others. From these studies, models like the one developed by Hemmes et al. [45], clearly improve its accuracy in determine the compressibility of the H$_2$ gas by fitting several experimental data. Also, other models attempt to resemble the accuracy of the Hemmes model with an easier analytical approach, like in the case of Wolverton et al. [65] that fitted the Hemmes equation with a 5th grade polynomial. Other model that attempted to simplify the analytical complexity of the Van der Waals and therefore the Hemmes model, is the one developed by Joubert [46], which is based on an analytical description of the Gibbs energy as a function of pressure at room and higher temperatures, and also is compatible with the CALPHAD method.

In light of these investigations, it was studied the difference of the models developed by Hemmes et al., Leachman et al., Joubert, Wolverton et al. with respect to their accuracy and easy implementation in further simulations in a range of temperature between RT and 150°C and pressure up to 1000 bar. Firstly, the definitions and ranges of these models can be seeing as follows:

The Leachman model was derived from the Helmholtz free energy, where the H$_2$ EOS developed is:

$$\alpha(\tau, \delta) = \alpha^r(\tau, \delta) + \alpha^0(\tau, \delta) \qquad (3)$$

Where

$$\alpha^0(\tau, \delta) = \ln(\delta) + 1.5 \ln(\tau) + a_1 + a_2\tau + \sum_{k=3}^{g} a_k ln[1 - \exp(b_k\tau)] \qquad (4)$$

$$\alpha^r(\tau, \delta) = \sum_{i=1}^{l} N_i\delta^{d_i}\tau^{t_i} + \sum_{i=l+1}^{m} N_i\delta^{d_i}\tau^{t_i}(-\delta^{p_i})$$
$$+ \sum_{i=m+1}^{n} N_i\delta^{d_i}\tau^{t_i} * exp[\varphi_i(\delta - D_i)^2 + \beta_i(\tau - \gamma_i)^2] \qquad (5)$$

The α^0 is the ideal contribution and the α^r is the residual contribution to the whole Helmholtz energy, while δ and τ are the reduced density ($\rho/\rho_{critical}$) and the reduced inverse temperature ($T_{critical}/T$), respectively, also g=7, l=7, m=9 and n=14. The other parameters mention (a_k, b_k, β_i, ϕ_i, D_i, N_i, d_i, t_i, p_i) in equations (4) and (5) are coefficients tabulated in [62]. The relationships to find the compressibility factor and other thermodynamic parameters from equation (3) can be observed in [66]. Nevertheless, this equation is complicated enough to manage and resolve, and thus, a reduced EOS just for the compressibility factor (Z) was also developed by Lemmon et al. [67] in the temperature range between 150-1000K and to pressures up to 2000 bar:

$$Z(p, T) = \frac{p}{\rho RT} = 1 + \sum_{i=1}^{9} a_i \left(\frac{100K}{T}\right)^{b_i} \left(\frac{p}{1MPa}\right)^{c_i} \qquad (6)$$

The coefficients for these equations are tabulated in [67].

The Hemmes model is defined between 1 bar to 1 Mbar of pressure and between 100 to 1000K, and its main equation is defined as [45]:

$$\left(P + \frac{a(P)}{\left(\frac{V}{n}\right)^{\alpha}}\right)\left(\frac{V}{n} - b(P)\right) = RT \qquad (7)$$

From this main equation the variables depending on the pressure a(P) and b(P) are defined between some ranges as:

$$a(P) = exp(a1 + a2 * ln(P) - exp(a3 + a4 * ln(P)) \quad P > 1bar \qquad (8)$$

$$b(P) = \begin{cases} \sum_{i=0}^{8} b_i * \ln(P)^i \quad (P \geq 100bar) \\ b(100) \qquad (P < 100bar) \end{cases} \qquad (9)$$

The coefficients of a, b and α are given in [45]. Also, the temperature dependence parameter α(T) is defined as:

$$\alpha(T) = \alpha_0 + \alpha_1 * T + \alpha_2 * T^2 \quad < 300K \qquad (10)$$
$$\alpha(T) = \alpha(300) \quad > 300K \qquad (11)$$

As it can be implied by the complexity of this model, the need of a programing tool is imperative. However, the approach of Wolverton et al. attempted to achieved the level of accuracy from Hemmes model with an easier equation [65], and in a reduced range of temperature (200 – 1000K) and pressure (1-500 bar). Specifically, the compressibility factor (Z) (Eq.12) was derived fitting the molar volume from the Hemmes EOS, acheiveing a 5th order bivariable polynomial:

$$n = \frac{PV}{ZRT} \qquad (12) \qquad ; \qquad Z(P, T) = \sum_{j=0}^{5}\sum_{i=0}^{5} c_{ij}P^i T^j \qquad (13)$$

The 21 c_{ij} coefficients of equation (13) can be seen in [65]. Finally, the Joubert model used a procedure that it is compatible with CALPHAD method, to describe the molar volume in terms of a single analytical equation of the pressure (Eq.14) that works between 298-1000K and 0-1Mbar. The coefficients a, b and c can be found in [46] (the temperature dependence of the non-ideal part was neglected).

$$V_{mol} = \frac{\partial G}{\partial P} = \frac{RT}{P} + a_1 * \exp\left(-\frac{p}{b_1}\right) + a_2 * \exp\left(-\frac{p}{b_2}\right) + a_3 * \exp\left(-\frac{p}{b_3}\right) + a_4 * \exp\left(-\frac{p}{b_4}\right)$$
$$+ a_5 * \exp\left(-\frac{p}{b_5}\right) + C \qquad (14)$$

One way to compare the contribution of the real part of the EOS is by separating the molar volume into two parts, the ideal EOS and the one obtained by a real one [46]. As a result, Fig.25, evidence the difference between each real EOS molar volume and the ideal one while experimental values from Vargaftik [68] are also included to validate the results.
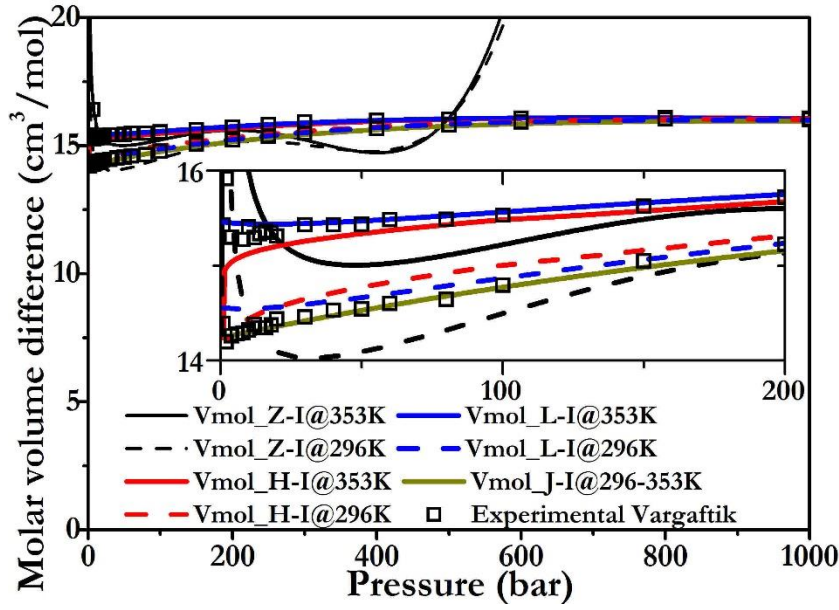
Fig.25. Molar volume difference between the real models and the ideal one and their comparison with experimental values, at 296 and 353K. Vmol_Z-I, Vmol_H-I, Vmol_J-I and Vmol_L-I are the molar volume differences of the Wolverton, Hemmes, Joubert and Leachman models, respectively. Adapted from [60]

As observed in Fig.25. all of the real EOS models are close to each other, as some authors also discussed [64]. However, it is also plausible that the Joubert, Leachman and Hemmes EOS fit better the experimental results of Vargaftik and with a larger range than in the case of the Wolverton model [60]. Also, the Joubert model in this analysis doesn't exhibit a representation in at 353K, because its temperature dependence is based in the ideal contribution of the equation, which in the graph is subtracted. Then, by analyzing the implementation of the EOS, the simplicity and assessment of the real behavior of H_2 gas [69] by the Joubert equation can be an advantage in the modelling of thermodynamic and kinetic phenomena of hydrides, and therefore it was taken for the simulations.

2.4.2. P-c-I models

Likewise, the application of non-ideal P-c-I models will aid to simulate the thermodynamic and kinetic behavior, accounting for the variability of the P_{eq} as temperature changes in hydrogenation cycles [70] by considering features like sloping plateau and hysteresis, making more accurate predictions in the behavior of the compressor [59]. Some widely used models just consider the plateau region (α-β) with a hysteresis factor and sloping plateau factor and constant coefficients [71-74]. However, the equation used in that works does not fit the phase boundaries like other models [70]. The approaches of Lacher-Lotosky [75], Jemni [76], and Fang-Zhou [77] can represent the P-c-I curves properly and accounting the temperature dependence of the P_{eq}. Some works that compare some of these models found that the Fang-Zhou model gave more accurate fits than the Lacher-Lotosky and the Jemni approaches [78]. Also, the equation of Fang-Zhou is easier to implement and only two P-c-I at different temperatures are needed for an appropriate fit, which aids to optimize the experiment time and energy. As a result, the Fang-Zhou model was used for the P-c-I fit and the further modelling of the isotherms at different temperatures.

The Fang-Zhou model is composed by two main equations that consider temperature variations and represents the plateau zone (α-β) and the single-phase zones (α) and (β). The plateau region is described by the equation:

$$\ln(P) = -\frac{\Delta H}{RT} + \frac{\Delta S}{R} + [(f_s)_{298} - 298 * k](C - C_m) + kT(C - C_m) \qquad (15)$$

41

$$f_s = \frac{\ln(P) - \ln(P_m)}{C - C_m} \qquad ; \qquad f_s = (f_s)_{298} + k(T - 298)$$

Where fs is the slope factor and $(f_s)_{298}$ is the slope factor at 298K, also Pm and Cm are the pressure and hydrogen concentration at the middle of the plateau region and k is the variation rate of the slope factor with temperature. Likewise, the equation that models the (α) and (β) zones is:

$$C_{\alpha//\beta} = x_1 * P^{x2}/_2 * \exp\left[-\frac{x_2 * x_3 * P}{RT}\right] * \exp\left[-\frac{x_2 * x_4}{RT}\right] \qquad (16)$$

Where x_1, x_2, x_3 and x_4 are mathematical coefficients that are found for each material tested and remain the same value for different temperatures.

Then, with the main thermodynamic equations stablished, an algorithm that simulates the thermodynamic behavior of the MHHC at the different stages was developed. The main input to the program could be either experimental and/or simulated P-c-I curves at the selected temperatures for the MHHC operation. Simulation of P-c-I curves uses the Fang-Zhou model described. The scheme of the MHHC system studied can be seen in Fig.27.
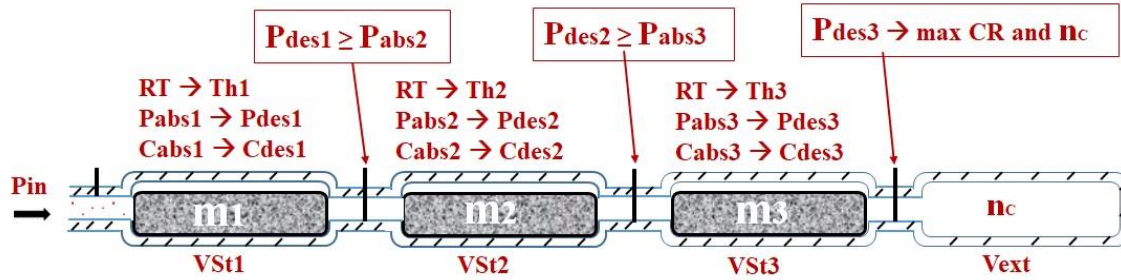
Fig.26. MHHC design scheme. Numbers indicate each consecutive stage up to V_{ext}. Adapted from [28]

In Fig.26, all of the parameters to consider in the design of the MHHC can be observed. At each stage a vessel volume (VSt1, VSt2 and VSt3) and a mass of alloy (m1, m2 and m3) are found by iterating mainly V_{ext} and the T_h at each stage to fulfill some operational constrains and considerations and finally achieve the highest quantity of H_2 moles compressed (n_c) and highest CR. Then, in Table 7 the operational constrains and considerations for the design of the compressor can be evidence.

Table 7. Operational constrains and considerations in the design of the MHHC. Adapted from [28]

Constrains	Considerations
*The P_{in} and P_{abs} at each stage generates directly the minimum concentration in the beta phase (β_{min}) in each hydride at RT.	*A 65% of packing fraction of the hydrogenated material is used considering our studies (presented in chapter 4) on these type of materials [57].
*The desorption point (O.P.$_{des}$= (C_{des}, P_{des}) in the P-c-I) at each stage and its corresponding iterative T_h, will be the one to achieve the maximum concentration in the alpha phase (α_{max}), and a P_{des} that have to be equal or greater than the P_{abs} of the following stage at RT.	*the mass and volume of the reactor at each stage are also linked to V_{ext} where the H_2 will be compressed, hence, this volume will be another parameter to vary in order to observe its effect in the quantity of mass and reactor volumes at each stage.
*The final desorption point, at the third stage, will determine the optimum (T_h) value that enhances the CR and final number of H_2 moles compressed (n_C).	*A dead volume was considered at each stage due to connection tubes, valves and others of ≈15.4 cm³ (this volume was assumed by calculating the inner volume of a system with plumbing parts from Swagelok®).
	*A real H_2 gas EOS is also implemented.
	* Experimental and/or simulated P-c-I curves are inputs to the algorithm.

From the scheme and the operation parameters mentioned, the algorithm implemented uses different steps as evidence in its flow diagram (Annex 2). The general process of the program can be described as:

1. With the implementation of the Fang-Zhou model, a mean squared error minimization was employed to find the proper mathematical and physical coefficients that described equations 15 and 16 for different temperatures.
2. These coefficients are the input of a subroutine where several O.P.$_{des}$ are found to fulfil the constraints described (Table 7) by iterating T$_h$ in each stage.
3. The operational points and the optimum T$_h$ found for each stage, are the input of the final subroutine where the V$_{ext}$ is iterated to find the final mass of alloy and reactor volume at each stage considering all the constrains and considerations mentioned (Table 7).

The optimized parameters were T$_h$ of each stage and V$_{ext}$. With these variables the CR, n$_c$, and O.P., mass and volumes of each stage were found taking into account the fixed considerations described in Table 7. Most of the parameters optimized with the algorithm will be employ as input of the future heat and mass simulations.

2.4.3. Kinetics

As described, the kinetics of the MHHC system relay on the intrinsic kinetics of the alloys and on the heat and mass transfer of the system. The optimization of geometry and heat and mass transfer parameters are highly relevant for the global behavior of the system, and they will be analyzed in a future work, however, the understanding of the parameters use in these simulations have to be consider to implement them properly. In particular, equilibrium properties and intrinsic reaction kinetics of hydrides, and, the heat and mass balance have to be accounted.

1. Equilibrium properties and intrinsic reaction kinetics of hydrides

The reaction rate and equilibrium properties of the hydrides vary depending on each material. In a kinetic experiment the reacted fraction (e.g. the amount of metal that becomes hydride in absorption and of hydride that becomes metal for desorption) is measured as a function of t, P, T and for different sample shapes. The relation between these parameters can take the form [79]:

$$f(F(\alpha)) = k(P,T,r) * t \quad (17)$$

Where F(α) is the reacted fraction, k is the constant that determines the reaction rate that is dependent on the P, T and shape of the sample, r. Also, the k can be express as:

$$k(P,T,r) = a(r) * g(P,P_{eq}) * h(T) \quad (18)$$

Where the function a(r) is related to the sample geometry, g(P, P$_{eq}$) is the driving force for the reaction that can have different models approaches to considering it [79, 80], and, the h(T) is the reaction dependency on temperature, which is based on the Arrehnius equation:

$$h(T) = k_0 * \exp\left(\frac{-E_a}{R * T}\right) \quad (19)$$

Also, several models ($f(F(\alpha))$) in the literature describe the kinetics of isothermal solid-state reactions [81-83], from which, all of them depends on the controlling mechanism of the reaction and derived into different functional forms of the reacted fraction $F(\alpha)$.

Then to know the reaction rate, the final equation will consider the determination of the reaction rate constant (Eq.18) and the derivative of the reaction fraction function $F(\alpha)$ that is taken from the models mentioned.

$$\frac{\partial f(F(\alpha))}{\partial F(\alpha)} * \frac{\partial F(\alpha)}{\partial t} = k(P,T,r) \implies \frac{\partial F(\alpha)}{\partial t}$$
$$= \left(a(r) * k_0 \exp\left(\frac{E_a}{R*T}\right) * g(P, P_{eq}) \right) / \left(\frac{\partial f(F(\alpha))}{\partial F(\alpha)} \right) \quad (20)$$

This reaction rate can be different between absorption and desorption, depending on the parameters that define each function (i.e. the P_{eq} difference between the absorption and the desorption due to a hysteresis effect, the activation energy or the k_o parameter). Likewise, through hydrogen composition, considering the dependence of the P_{eq} on this parameter. Therefore, the use of the Fang-Zhou model described before to account the realistic features of the P-c-I, would be needed for a proper consideration of the kinetics effects.

2. Heat flow equation

The heat equation that links the temperature and gas velocity fields can be written as:

$$(\rho C_p)_e \frac{\partial T}{\partial t} = \kappa_e \nabla^2 T - \rho_g C_{pg} \vec{v} \cdot \nabla T + Q_{hs} \qquad (21)$$

Where, the hydride is considered as a porous media and therefore the effective density, heat capacity and thermal conductivity are:

$$\left(\rho C_p \right)_e = \varepsilon \rho_g C_{pg} + (1+\varepsilon)\rho_s C_{ps} \qquad (22) \quad ; \quad \kappa_e = \varepsilon \kappa_g + (1+\varepsilon)\kappa_s \qquad (23)$$

And the heat source term Q_{hs} is directly related with the hydrogenation-dehydrogenation reaction rate, and can adopted the following form [84]:

$$Q_{hs} = \frac{\partial F(\alpha)}{\partial t} * \left(\frac{wt_{max}}{1-wt_{max}} \right) * \rho_s * (1-\varepsilon) * \frac{\Delta H_{re}}{M_m} \qquad (24)$$

Where wt_{max} is determined between the operational points defines (O.P.$_{abs}$ and O.P.$_{des}$ at each stage). In the case of the initial point at absorption, the wt_{max} is considered from the beginning of the hydrogenation.

3. Mass balance

To know the hydrogen concentration distribution in the MH bed and its evolution with time, a mass balance must be considered. Two main equations have to be couple in order to know the gas behavior in the system, the mass conservation represented by the equation of continuity, and the momentum equation that considers the diffusion of the gas in the hydride and through the rest of the system. The mass conservation for the gas and the hydride can be observed in equations 25 and 26, respectively. The hydride is considered as a mass source (Q_{ms}) that is also related to the hydrogenation reaction rate [70].

$$\frac{\partial \rho}{\partial t} + \nabla \cdot (\rho v) = 0 \qquad (25) \qquad ; \qquad \frac{\partial(\varepsilon \rho)}{\partial t} + \nabla \cdot (\rho v) = Q_{ms} \qquad (26)$$

Also, the momentum equation of the gas (Eq.27) and solid (Eq.28) can be described as:

$$\rho \frac{\partial v}{\partial t} + \rho v(v \cdot \nabla) = -\nabla \cdot P - \nabla \cdot \vec{\bar{\tau}} \qquad (27)$$

$$\frac{\rho}{\varepsilon}\left(\frac{\partial v}{\partial t} + \frac{v}{\varepsilon}(v \cdot \nabla)\right) = -\nabla \cdot P - \nabla \cdot \frac{\vec{\bar{\tau}}}{\varepsilon} - v\left(\frac{\mu}{K} + \frac{Q_{ms}}{\varepsilon^2}\right) \quad (28)$$

Where the viscous stress tensor ($\vec{\bar{\tau}}$) and the mass source would be:

$$\vec{\bar{\tau}} = \mu(\nabla v + (\nabla v)^{Tr}) - \frac{2}{3}\mu(\nabla \cdot v) \qquad (29)$$

$$Q_{ms} = \frac{\partial F(\alpha)}{\partial t} * \left(\frac{wt_{max}}{1 - wt_{max}}\right) * \rho_s * (1 - \varepsilon) \qquad (30)$$

Finally, the modelling of the intrinsic kinetics of the alloys will be developed using the methodology defined, while the main parameters to be considered in a future heat and mass transfer simulation were described and measured through the development of this work, i.e. heat capacity, heat conductivity, porosity, density, intrinsic kinetics, ΔH.

2.5. References

[1] T. G. Voskuilen, E. L. Waters, and T. L. Pourpoint, "A comprehensive approach for alloy selection in metal hydride thermal systems," *Int. J. Hydrog. Energy*, vol. 39, no. 25, pp. 13240–13254, Aug. 2014.

[2] University of Purdue, "Purdue Metal Hydride Toolbox." University of Purdue. Taken from: https://github.com/PurdueH2Lab/MetalHydrideToolbox, 2014.

[3] M. T. Hagstrom, P. D. Lund, J. P. Vanhanen, and others, "Metal hydride hydrogen storage for near-ambient temperature and atmospheric pressure applications, a PDSC study," *Int. J. Hydrog. Energy*, vol. 20, no. 11, pp. 897–909, 1995.

[4] G. Capurso *et al.*, "Development of a modular room-temperature hydride storage system for vehicular applications," *Appl. Phys. A*, vol. 122, no. 3, Mar. 2016.

[5] T. Huang, Z. Wu, G. Sun, and N. Xu, "Microstructure and hydrogen storage characteristics of TiMn2−XVX alloys," *Intermetallics*, vol. 15, no. 4, pp. 593–598, Apr. 2007.

[6] T. A. Zotov, I. A. Romanov, S. V. Mitrokhin, V. N. Verbetsky, and O. A. Pertii, "Electrochemical And Hydrogen Sorption Properties of Ab5—Type Alloys Where A—La, Ce; B—Ni, Co, Mn, Fe, Cu, Cr, Al," in *Carbon Nanomaterials in Clean Energy Hydrogen Systems*, Springer, 2008, pp. 523–532.

[7] Z. Dehouche, N. Grimard, F. Laurencelle, J. Goyette, and T. K. Bose, "Hydride alloys properties investigations for hydrogen sorption compressor," *J. Alloys Compd.*, vol. 399, no. 1–2, pp. 224–236, Aug. 2005.

[8] V. Iosub, M. Latroche, J.-M. Joubert, and A. Percheron-Guégan, "Optimisation of MmNi5−xSnx (Mm=La, Ce, Nd and Pr, 0.27<x<0.5) compositions as hydrogen storage materials," *Int. J. Hydrog. Energy*, vol. 31, no. 1, pp. 101–108, 2006.

[9] B. Rożdżyńska-Kiełbik, W. Iwasieczko, H. Drulis, V. . Pavlyuk, and H. Bala, "Hydrogenation equilibria characteristics of LaNi5-xZnx intermetallics," *J. Alloys Compd.*, vol. 298, no. 1, pp. 237–243, 2000.

[10] M. Bereznitsky, I. Jacob, J. Bloch, and M. . Mintz, "Thermodynamic and structural aspects of hydrogen absorption in the Zr(AlxCo1-x)2 system," *J. Alloys Compd.*, vol. 346, no. 1, pp. 217–221, 2002.

[11] M. Bereznitsky, I. Jacob, J. Bloch, and M. . Mintz, "Thermodynamic and structural aspects of hydrogen absorption in the Zr(AlxFe1-x)2 system," *J. Alloys Compd.*, vol. 351, no. 1, pp. 180–183, 2003.

[12] L. Lijun *et al.*, "Structures and Hydrogen Storage Properties of La1-xMgxNi4.25Al0.75 (x=0.0, 0.1, 0.2, 0.3) Alloys," *Rare Met. Mater. Eng.*, vol. 45, no. 1, pp. 56–61, 2016.

[13] P. Dantzer, "Static, dynamic and cycling studies on hydrogen in the intermetallics LaNi5 and LaNi4. 77Al0. 22," *J. Common Met.*, vol. 131, no. 1–2, pp. 349–363, 1987.

[14] E. M. Borzone, A. Baruj, M. V. Blanco, and G. O. Meyer, "Dynamic measurements of hydrogen reaction with LaNi5−xSnx alloys," *Int. J. Hydrog. Energy*, vol. 38, no. 18, pp. 7335–7343, Jun. 2013.

[15] L. Pickering, D. Reed, A. I. Bevan, and D. Book, "Ti–V–Mn based metal hydrides for hydrogen compression applications," *J. Alloys Compd.*, vol. 645, pp. S400–S403, Oct. 2015.

[16] V. Kumar, D. Pukazhselvan, A. K. Tyagi, and S. K. Singh, "Hydrogen absorption/desorption characteristics of room temperature ZrMn2–xNix system (x= 1· 25–1· 50)," *Bull. Mater. Sci.*, vol. 37, no. 3, pp. 655–660, 2014.

[17] S. V. Mitrokhin, T. N. Bezuglaya, and V. N. Verbetsky, "Structure and hydrogen sorption properties of (Ti, Zr)–Mn–V alloys," *J. Alloys Compd.*, vol. 330, pp. 146–151, 2002.

[18] W. E. Wallace and F. Pourarian, "Hydrogen storage materials of hyperstoichiometric alloys," US4512965A, 1985.

[19]   M. V. Lototsky, V. A. Yartys, and I. Y. Zavaliy, "Vanadium-based BCC alloys: phase-structural characteristics and hydrogen sorption properties," *J. Alloys Compd.*, vol. 404–406, pp. 421–426, Dec. 2005.

[20]   J. Kapischke and J. Hapke, "Measurement of the pressure-composition isotherms of high temperature and low-temperature metal hydrides," *Exp. Therm. Fluid Sci.*, vol. 18, no. 1, pp. 70–81, 1998.

[21]   X. Guo *et al.*, "Laves phase hydrogen storage alloys for super-high-pressure metal hydride hydrogen compressors," *Rare Met.*, vol. 30, no. 3, pp. 227–231, Jun. 2011.

[22]   E. Y. Anikina and V. N. Verbetsky, "Investigation of the hydrogen interaction with Ti0.9Zr0.1Mn1.3V0.7 by means of the calorimetric method," *Int. J. Hydrog. Energy*, vol. 41, no. 27, pp. 11520–11525, Jul. 2016.

[23]   J.-M. Park and J.-Y. Lee, "Hydrogenation characteristics of the Zr1-xTixCr1-yFe1+y laves phase alloys," *J. Common Met.*, vol. 160, no. 2, pp. 259–271, 1990.

[24]   M. H. MENDELSOHN, D. M. GRUEN, and A. E. DWIGHT, "LaNi5-xAlx is a versatile alloy system for metal hydride applications," *Nature*, vol. 269, pp. 45–47, Sep. 1977.

[25]   V. M. Skripnyuk and M. Ron, "Hydrogen desorption kinetics in intermetallic compounds C2, C51 and C52 with Laves phase structure," *Int. J. Hydrog. Energy*, vol. 28, no. 3, pp. 303–309, 2003.

[26]   J. Payá, M. Linder, R. Mertz, and J. M. Corberán, "Analysis and optimization of a metal hydride cooling system," *Int. J. Hydrog. Energy*, vol. 36, no. 1, pp. 920–930, Jan. 2011.

[27]   K. Meier, C. Kurtz, C. Weckerle, M. Hubner, and I. Bürger, "Air-conditioning system for vehicles with on-board hydrogen," *Appl. Therm. Eng.*, vol. 129, pp. 1150–1159, Jan. 2018.

[28]   A. R. Galvis E, F. Leardini, J. R. Ares, F. Cuevas, and J. F. Fernandez, "Simulation and design of a three-stage metal hydride hydrogen compressor based on experimental thermodynamic data," *Int. J. Hydrog. Energy*, Mar. 2018.

[29]   ICMPE, "Alloy melting using induction heating." INSTITUT DE CHIMIE ET DES MATERIAUX PARIS-EST- UMR 7182. Taken from: http://www.icmpe.cnrs.fr/spip.php?article1648&lang=en.

[30]   M. Ponthieu, "Novel Mg-rich materials for hydrogen storage: bulk and nanoconfined Mg6Pd1 xTMx (TM= Ni, Ag, Cu) compounds and MgH2-TiH2 nanocomposites," 2013.

[31]   J.-M. Joubert, M. Latroche, R. Černỳ, R. C. Bowman Jr, A. Percheron-Guégan, and K. Yvon, "Crystallographic study of LaNi5- xSnx (0.2≤ x≤ 0.5) compounds and their hydrides," *J. Alloys Compd.*, vol. 293, pp. 124–129, 1999.

[32]   S. Luo, J. D. Clewley, T. B. Flanagan, R. C. Bowman Jr, and L. A. Wade, "Further studies of the isotherms of LaNi5- xSnx–H for x= 0–0.5," *J. Alloys Compd.*, vol. 267, no. 1–2, pp. 171–181, 1998.

[33]   B. Villeroy, F. Cuevas, J. Bettembourg, P. Olier, and M. Latroche, "Influence of the Ti/Zr ratio and the synthesis route on hydrogen absorbing properties of (Ti1−xZrx)Mn1.5V0.5 alloys," *J. Phys. Chem. Solids*, vol. 67, no. 5–6, pp. 1281–1285, May 2006.

[34]   Z. Dehouche, M. Savard, F. Laurencelle, and J. Goyette, "Ti–V–Mn based alloys for hydrogen compression system," *J. Alloys Compd.*, vol. 400, no. 1–2, pp. 276–280, Sep. 2005.

[35]   J.-G. Park, H.-Y. Jang, S.-C. Han, P. S. Lee, and J.-Y. Lee, "The thermodynamic properties of Ti–Zr–Cr–Mn laves phase alloys," *J. Alloys Compd.*, vol. 325, no. 1–2, pp. 293–298, 2001.

[36]   Servicio de Investigación Interdepartamental (SIdI), "Scanning Electron Microscopy and Energy Dispersive X ray Laboratory." Universidad Autonoma de Madrid. Taken from: http://uam.es/ss/Satellite?c=UAM_Laboratorio_FA&cid=1242668922067&language=en&pagename=Universidad AutonomaMadrid%2FUAM_Laboratorio_FA%2FUAM_laboratorio&pid=1242690542525&title=Scanning+Electron+Microscopy+and+Energy+Dispersive+X+ray+Laboratory.

[37]   "ImageJ an open source Java image processing program." Taken from: https://imagej.net/ImageJ.

[38]   ICMPE, "MICROSONDE ELECTRONIQUE." INSTITUT DE CHIMIE ET DES MATERIAUX PARIS-EST- UMR 7182. Taken from: http://www.icmpe.cnrs.fr/spip.php?article148&lang=fr.

[39]   ICMPE, "Chemical analysis: ICP-OES Varian Vista Pro." INSTITUT DE CHIMIE ET DES MATERIAUX PARIS-EST- UMR 7182. Taken from: http://www.icmpe.cnrs.fr/spip.php?article1880&lang=en.

[40]   Servicio de Investigación Interdepartamental (SIdI), "X-Ray Powder Diffraction Laboratory." Universidad Autonoma de Madrid. Taken from: http://uam.es/ss/Satellite/en/1242690538615/1242668923592/UAM_Laboratorio_FA/laboratorio/X-Ray_Powder_Diffraction_Laboratory.htm.

[41]   J. Rodríguez-Carvajal, "An introduction to the program," *Full Prof*, 2000.

[42]   L. B. McCusker, R. B. Von Dreele, D. E. Cox, D. Louer, and P. Scardi, "Rietveld refinement guidelines," *J. Appl. Crystallogr.*, vol. 32, pp. 36–50, 1990.

[43]   B. H. Toby, "R factors in Rietveld analysis: How good is good enough?," *Powder Diffr.*, vol. 21, no. 01, pp. 67–70, Mar. 2006.

[44]   D. P. Broom, *Hydrogen Storage Materials*. London: Springer London, 2011.

[45]   H. Hemmes, A. Driessen, and R. Griessen, "Thermodynamic properties of hydrogen at pressures up to 1 Mbar and temperatures between 100 and 1000K," *J. Phys. C Solid State Phys.*, vol. 19, no. 19, p. 3571, 1986.

[46]   J.-M. Joubert, "A Calphad-type equation of state for hydrogen gas and its application to the assessment of Rh–H system," *Int. J. Hydrog. Energy*, vol. 35, no. 5, pp. 2104–2111, Mar. 2010.

[47]   D. P. Broom and C. J. Webb, "Pitfalls in the characterisation of the hydrogen sorption properties of materials," *Int. J. Hydrog. Energy*, vol. 42, no. 49, pp. 29320–29343, Dec. 2017.

[48]   C. J. Webb and E. M. Gray, "The effect of inaccurate volume calibrations on hydrogen uptake measured by the Sieverts method," *Int. J. Hydrog. Energy*, vol. 39, no. 5, pp. 2168–2174, Feb. 2014.

[49]   T. P. Blach and E. M. Gray, "Sieverts apparatus and methodology for accurate determination of hydrogen uptake by light-atom hosts," *J. Alloys Compd.*, vol. 446–447, pp. 692–697, Oct. 2007.

[50]   K. J. Gross and K. Russel Carrington, "Recommended Best Practices for the Characterization of Storage Properties of Hydrogen Storage Materials." Office of Energy Efficiency and Renewable Energy (EERE), 2008.

[51]   M. Hirscher, Ed., *Handbook of hydrogen storage: new materials for future energy storage*. Weinheim: Wiley-VCH, 2010.

[52] J. L. McNaughton and C. T. Mortimer, *Calorimetria Diferencial de Barrido*, vol. 10. Butterworths, 1975.

[53] J. de Boor and V. Schmidt, "Complete Characterization of Thermoelectric Materials by a Combined van der Pauw Approach," *Adv. Mater.*, vol. 22, no. 38, pp. 4303–4307, Oct. 2010.

[54] C. Morales *et al.*, "On the van der Pauw's method applied to the measurement of low thermal conductivity materials," *Rev. Sci. Instrum.*, vol. 87, no. 8, p. 084902, Aug. 2016.

[55] B. Charlas, A. Chaise, O. Gillia, P. Doremus, and D. Imbault, "Investigation of hydride powder bed swelling and shrinking during hydrogen absorption/desorption cycles under different compressive stresses," *J. Alloys Compd.*, vol. 580, pp. S149–S152, Dec. 2013.

[56] B. Charlas, O. Gillia, P. Doremus, and D. Imbault, "Experimental investigation of the swelling/shrinkage of a hydride bed in a cell during hydrogen absorption/desorption cycles," *Int. J. Hydrog. Energy*, vol. 37, no. 21, pp. 16031–16041, Nov. 2012.

[57] A. R. Galvis Escobar, A. Chaise, V. Iosub, B. Salque, J. F. Fernandez, and O. Gillia, "Stress effect on the swelling/shrinking behavior of an AB2 alloy during hydrogenation cycles," *Int. J. Hydrog. Energy*, vol. 42, no. 35, pp. 22422–22431, Aug. 2017.

[58] MALVERN Instruments, "Mastersizer 2000 user manual." Taken from: https://www.labmakelaar.com/fjc_documents/mastersizer-2000-2000e-manual-eng1.pdf, 2007.

[59] M. V. Lototskyy, V. A. Yartys, B. G. Pollet, and R. C. Bowman, "Metal hydride hydrogen compressors: A review," *Int. J. Hydrog. Energy*, vol. 39, no. 11, pp. 5818–5851, Apr. 2014.

[60] A. R. Galvis E., F. Leardini, J. Bodega, J. R. Ares, and J. F. Fernandez, "Realistic simulation in a single stage hydrogen compressor based on AB2 alloys," *Int. J. Hydrog. Energy*, vol. 41, no. 23, pp. 9780–9788, Jun. 2016.

[61] J. R. Travis, D. Piccioni Koch, J. Xiao, and Z. Xu, "Real-gas Equations-of-State for the GASFLOW CFD code," *Int. J. Hydrog. Energy*, vol. 38, no. 19, pp. 8132–8140, Jun. 2013.

[62] J. W. Leachman, R. T. Jacobsen, S. G. Penoncello, and E. W. Lemmon, "Fundamental Equations of State for Parahydrogen, Normal Hydrogen, and Orthohydrogen," *J. Phys. Chem. Ref. Data*, vol. 38, no. 3, pp. 721–748, Sep. 2009.

[63] H. Chen, J. Zheng, P. Xu, L. Li, Y. Liu, and H. Bie, "Study on real-gas equations of high pressure hydrogen," *Int. J. Hydrog. Energy*, vol. 35, no. 7, pp. 3100–3104, Apr. 2010.

[64] K. Nasrifar, "Comparative study of eleven equations of state in predicting the thermodynamic properties of hydrogen," *Int. J. Hydrog. Energy*, vol. 35, no. 8, pp. 3802–3811, Apr. 2010.

[65] M. J. Wolverton, G. K. Kannarpady, and A. Bhattacharyya, "A TEMPERATURE DIFFERENTIAL MODEL–BASED SIEVERTS APPARATUS," *Instrum. Sci. Technol.*, vol. 39, no. 2, pp. 173–197, Mar. 2011.

[66] E. W. Lemmon and R. T. Jacobsen, "A New Functional Form and New Fitting Techniques for Equations of State with Application to Pentafluoroethane (HFC-125)," *J. Phys. Chem. Ref. Data*, vol. 34, no. 1, pp. 69–108, Mar. 2005.

[67] E. W. Lemmon, M. L. Huber, and J. W. Leachman, "Revised standardized equation for hydrogen gas densities for fuel consumption applications," *J. Res. Natl. Inst. Stand. Technol.*, vol. 113, no. 6, p. 341, 2008.

[68] N. Vargaftik, *Tables on the thermophysical properties of liquids and gases*, 2nd ed. New York: John Wiley & Sons, Inc, 1975.

[69] P. L. Hagelstein, "Equation of State and Fugacity Models for H2 and for D2," *J. Condense Matter Nucl. Sci.*, vol. 16, pp. 23–45, 2015.

[70] S. S. Mohammadshahi, E. M. Gray, and C. J. Webb, "A review of mathematical modelling of metal-hydride systems for hydrogen storage applications," *Int. J. Hydrog. Energy*, vol. 41, no. 5, pp. 3470–3484, Feb. 2016.

[71] T. Nishizaki, K. Miyamoto, and K. Yoshida, "Coefficients of performance of hydride heat pumps," *J. Common Met.*, vol. 89, no. 2, pp. 559–566, 1983.

[72] V. A. Yartys *et al.*, "Metal hydride hydrogen compression: recent advances and future prospects," *Appl. Phys. A*, vol. 122, no. 4, Apr. 2016.

[73] E. I. Gkanas *et al.*, "Numerical study on a two-stage Metal Hydride Hydrogen Compression system," *J. Alloys Compd.*, vol. 645, pp. S18–S22, Oct. 2015.

[74] P. Muthukumar, K. Singh Patel, P. Sachan, and N. Singhal, "Computational study on metal hydride based three-stage hydrogen compressor," *Int. J. Hydrog. Energy*, vol. 37, no. 4, pp. 3797–3806, Feb. 2012.

[75] M. V. Lototsky, V. A. Yartys, V. S. Marinin, and N. M. Lototsky, "Modelling of phase equilibria in metal–hydrogen systems," *J. Alloys Compd.*, vol. 356–357, pp. 27–31, 2003.

[76] A. Jemni and S. B. Nasrallah, "Study of two-dimensional heat and mass transfer during absorption in a metal-hydrogen reactor," *Int. J. Hydrog. Energy*, vol. 20, no. 1, pp. 43–52, 1995.

[77] Fang, S., Zhou, Z., Zhang, J., Yao, M., Feng, F., and Northwood, D.O., "The application of mathematical models to the calculation of selected hydrogen storage properties (formation enthalpy and hysteresis) of AB2-type alloys," *Int. J. Hydrog. Energy*, vol. 25, no. 2, pp. 143–149, 2000.

[78] J. Payá, M. Linder, E. Laurien, and J. M. Corberán, "Mathematical models for the P–C–T characterization of hydrogen absorbing alloys," *J. Alloys Compd.*, vol. 484, no. 1–2, pp. 190–195, Sep. 2009.

[79] J. F. Fernandez and C. R. Sanchez, "Rate determining step in the absorption and desorption of hydrogen by magnesium," *J. Alloys Compd.*, vol. 340, no. 1–2, pp. 189–198, 2002.

[80] M. Ron, "The normalized pressure dependence method for the evaluation of kinetic rates of metal hydride formation/decomposition," *J. Alloys Compd.*, vol. 283, no. 1–2, pp. 178–191, 1999.

[81] J. H. Sharp, G. W. Brindley, and B. N. Narahari Achar, "Numerical Data for Some Commonly Used Solid State Reaction Equations," *J. Am. Ceram. Soc.*, vol. 49, no. 7, pp. 379–382, 1965.

[82] J. D. Hancock and J. H. Sharp, "Method of comparing solid-state kinetic data and its application to the decomposition of kaolinite, brucite, and BaCO3," *J. Am. Ceram. Soc.*, vol. 55, no. 2, pp. 74–77, 1972.

[83] L. F. Jones, D. Dollimore, and T. Nicklin, "Comparison of experimental kinetic decomposition data with master data using a linear plot method," *Thermochim. Acta*, vol. 13, no. 2, pp. 240–245, 1975.

[84]   A. Chaise, P. Marty, P. de Rango, and D. Fruchart, "A simple criterion for estimating the effect of pressure gradients during hydrogen absorption in a hydride reactor," *Int. J. Heat Mass Transf.*, vol. 52, no. 19–20, pp. 4564–4572, Sep. 2009.

Chapter 3. Compressor Alloys: Compositional, morphological, structural, thermodynamic and kinetic characterization

3.1. Introduction

In this chapter the experimental measurements required for the proper characterization and further simulation of the MHHC are performed and analyzed. For the measurements, two types of materials were studied: three AB_2-type alloys that were chosen as a first option by a selection algorithm (see section 2.2), and, an AB_5-type alloy that is used to compare its performance with the first stage AB_2-type alloy. The morphological, compositional, structural, thermodynamic and kinetic characterization of the AB_2-type and AB_5-type alloys are presented separately, highlighting the key features that each type of alloys evidence. Also, the comparison between them and a discussion on the possible factors that define which of both types of materials have to be in the first stage of the MHHC are included. A resume with all the measurements performed in all the samples and their designation can be seen in the following table:

Table 8. Resume of all the experimental characterization measurements performed to the alloys tested

		Annealed	XRPD / XRPD hydrogenated	EDX 100x / ICP-OES	EDX linescan	EDX Dark-light zones	SEM	P-c-I	Kinetic
P_l alloys	BN1-1	-	X	X	X	X	X		-
	BN1-2	-	-	-	-	-	-	-	-
	BN1-2-2	-	X	X	X	X	X	-	-
	BN1-2-3	-	X	X	X	X	X	-	-
	BN1-2-4	-	X	X	X	X	X	-	-
	BN1-2-5	X	X	X	X	X	X	X	X
	BN1-2-6	-	X	X	-	-	X	-	-
	BNI1	-	X / X	X	X	X	X	X	-
	BNI2	-	X	X	X	X	X	X	-
	BNIC1	-	X	ICP-OES	-	EPMA	X	X	-
	BNIC2	-	X	ICP-OES	-	EPMA	X	X	-
	LaNiSn	X	X	X	-	X	X	X	X
P_m alloys	BN2	X	X	X	X	X	X	X	X
	BN2IC	-	X	ICP-OES	-	EPMA	-	X	-
	BN2IC2	-	X	ICP-OES	-	EPMA	-	X	-
P_h alloys	B1	-	X	X	X	X	X	-	-
	B2	-	-	-	-	-	-	-	-
	B3	-	X	X	X	X	X	-	-
	B4	-	X	X	X	X	X	-	-
	B1-2	-	X	X	X	X	X	-	-
	B1-3	-	X	X	X	-	X	-	-
	B1-4	-	X	X	X	X	X	-	-
	B1-5	-	X	X	X	X	X	-	-
	B1-6	-	X	X	X	-	X	-	-
	B7	-	X	X	X	X	X	-	-
	B8	-	X	X	X	X	X	-	-
	B9	X	X	X	X	X	X	X	X
	BI1	-	X	X	X	X	X	X	-
	BI2	-	X	X	X	X	X	X	-
	BIC	-	X	ICP-OES	EPMA	EPMA	X	X	-
	BIC2	-	X	ICP-OES	EPMA	EPMA	X	X	-

For the first stage (P_l alloy, white in Table 8) two theoretical compositions were evaluated, considering the composition, structure and thermodynamic properties. The first alloy researched labeled as BN1-1, had a composition of: $Ti_{0.9}Zr_{0.1}Mn_{1.34}V_{0.3}$ and the second one (BN1-2) of: $Ti_{0.85}Zr_{0.15}Mn_{1.33}V_{0.3}$, in both cases the alloys were non-stoichiometric. The $LaNi_{4.8}Sn_{0.2}$ and the P_m alloys (BN2, light grey) were completely characterized and the P_h alloy

(B, dark grey) was the one with a higher number of characterizations, since it was the first one to be studied and also due to a previous know-how on this material. Also, the samples highlighted in red were oxidized and therefore dismissed from the rest of the analysis. The samples with the label EPMA and ICP-OES are the ones using these techniques for the compositional characterization, as described in chapter 2.

3.2. AB$_2$-type alloys
3.2.1. General aspects of the three alloys

As mention in chapter 2, in all the AB$_2$ alloys an excess of 5-10% of Mn has been taken, considering previous experience of the melting systems used, arc and induction. As a result of this excess of Mn, the composition of the final ingot can vary. Therefore, the compositional, morphological and structural characterization are important to analyze the effect of the synthesize method and its considerations. From the different types of measurements described for EDX (chapter 2) a first observation was made in relation to the results obtained with the different alloys, especially with the linescan measurement, as it can be observed in Fig.27.
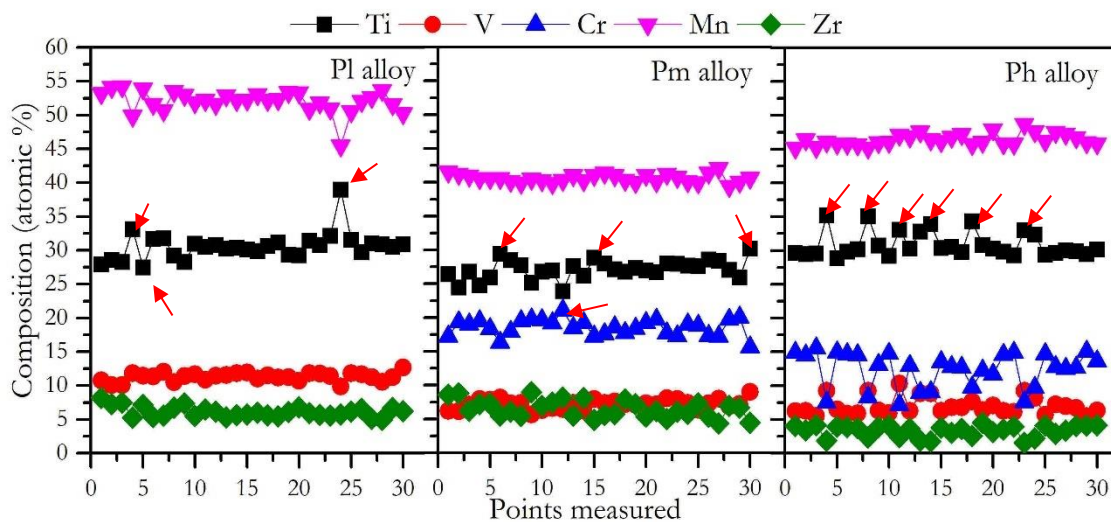
Fig.27. Linescan measurements of three samples with the different compositions. Red arrows indicate measurement points with variability in their composition

It was found in the linescan measurements, the presence of more than one phase in the main matrix, as indicated by the simultaneous modifications of atomic composition for some of the elements (red arrows in Fig.27). To analyze in detail the composition of the samples the method described previously (chapter 2) was adopted. As a result, the compositional measurements (100x and light and dark zones described) were performed to have a detail stoichiometry of the alloy, and an average composition between a dark and a light zones founded. For comparison purposes some of the alloys of each material will be presented for the different types of measurements

3.2.2. Compositional, morphological and structural characterization

In table 9, the global composition found by EDX at 100X or ICP-OES, the light and dark zones (EDX or EPMA) and the average between these zones are compared with the nominal stoichiometry used in the synthesis of each alloy. The compositional and structural results of all the samples used can be observed in Annex 3. The "A" letter in some alloys stand for an annealing process implemented in these samples.

Table 9. Stoichiometry measured for the different comparable alloys

		Light zone (at/f.u.)	Dark zone (at/f.u.)	Light-dark average (at/f.u.)	Global stoichiometry -100x / ICP-OES - (at/f.u.)	Nominal Stoichiometry (at/f.u.)
BN1-2-5	Ti	0.80(1)	0.87(1)	0.84(2)	0.85(1)	0.85
	Zr	0.20(1)	0.13(1)	0.16(2)	0.15(1)	0.15
	Mn	1.53(1)	1.27(1)	1.40(2)	1.40(1)	1.33
	V	0.30(1)	0.30(1)	0.30(2)	0.31(1)	0.3
BNI2	Ti	0.81(2)	0.88(2)	0.85(4)	0.85(1)	0.849
	Zr	0.18(1)	0.12(1)	0.15(2)	0.15(1)	0.15
	Mn	1.46(1)	1.23(1)	1.35(2)	1.25(1)	1.33
	V	0.31(1)	0.29(1)	0.30(2)	0.28(1)	0.301
BNIC2	Ti	0.82(2)	0.88(3)	0.85(5)	0.85(1)	0.85
	Zr	0.18(1)	0.12(1)	0.15(2)	0.15(1)	0.15
	Mn	1.50(2)	1.28(4)	1.39(6)	1.41(1)	1.33
	V	0.33(1)	0.32(1)	0.33(2)	0.31(1)	0.3
BN125A	Ti	0.80(1)	0.88(1)	0.84(1)	0.85(1)	0.85
	Zr	0.20(1)	0.12(1)	0.16(1)	0.15(1)	0.15
	Mn	1.39(1)	1.42(1)	1.40(1)	1.35(1)	1.33
	V	0.30(1)	0.31(1)	0.31(1)	0.31(1)	0.3
BN2	Ti	0.73(1)	0.84(1)	0.79(1)	0.80(1)	0.8
	Zr	0.27(1)	0.16(1)	0.21(1)	0.20(1)	0.2
	Mn	1.16(1)	1.19(1)	1.18(1)	1.20(1)	1.2
	Cr	0.62(1)	0.51(1)	0.56(1)	0.56(1)	0.6
	V	0.17(1)	0.22(1)	0.20(1)	0.20(1)	0.2
BN2IC	Ti	0.74(1)	0.88(5)	0.81(6)	0.80(1)	0.8
	Zr	0.26(2)	0.14(3)	0.19(5)	0.20(1)	0.2
	Mn	1.17(1)	1.22(2)	1.20(3)	1.28(1)	1.2
	Cr	0.67(1)	0.52(2)	0.60(3)	0.60(1)	0.6
	V	0.17(1)	0.26(4)	0.21(5)	0.20(1)	0.2
BN2A	Ti	0.74(1)	0.85(1)	0.80(1)	0.80(1)	0.8
	Zr	0.26(1)	0.15(1)	0.20(1)	0.20(1)	0.2
	Mn	1.16(1)	1.20(1)	1.18(1)	1.18(1)	1.2
	Cr	0.58(1)	0.50(1)	0.54(1)	0.55(1)	0.6
	V	0.18(1)	0.22(1)	0.20(1)	0.20(1)	0.2
B9	Ti	0.88(1)	0.94(1)	0.91(2)	0.90(1)	0.9
	Zr	0.12(1)	0.06(1)	0.09(2)	0.10(1)	0.1
	Mn	1.37(1)	1.38(1)	1.38(2)	1.35(1)	1.4
	Cr	0.44(1)	0.28(1)	0.36(2)	0.35(1)	0.4
	V	0.18(1)	0.25(1)	0.22(1)	0.20(1)	0.2
BIC1	Ti	0.89(1)	0.93(1)	0.91(2)	0.90(1)	0.9
	Zr	0.11(1)	0.07(1)	0.09(2)	0.10(1)	0.1
	Mn	1.41(1)	1.42(1)	1.42(2)	1.48(1)	1.4
	Cr	0.42(1)	0.31(1)	0.37(2)	0.40(1)	0.4
	V	0.19(1)	0.25(1)	0.22(2)	0.20(1)	0.2
B9A	Ti	0.88(1)	0.93(1)	0.91(1)	0.90(1)	0.90
	Zr	0.12(1)	0.07(1)	0.09(1)	0.10(1)	0.10
	Mn	1.36(1)	1.39(1)	1.38(1)	1.37(1)	1.35
	Cr	0.43(1)	0.36(1)	0.39(1)	0.40(1)	0.35
	V	0.18(1)	0.22(1)	0.20(1)	0.20(1)	0.20

Considering the values found in Table 9 several aspects should be highlighted. The global composition found and the average one between light and dark zones are close to each other, however, some values change due to the nature of the measurements, in other words, in the general composition not only the main matrix is measured but also the quantification of some secondary phases are also included. The desired nominal composition was mainly achieved for all samples, though, difficulties on the Mn-composition adjustment are evident. The uncertainty on the amount of Mn lost due to evaporation is on the basis of such problems. For P_m and P_h alloys, the two areas have close Mn content. However, for A-type elements, the light area exhibits higher Zr and lower Ti content than the nominal one.

Similarly, for B-type elements, the light area has higher Cr and lower V than the nominal value. As for P_l alloys, the content of A-type elements Zr and Ti follow the same tendency as in P_m and P_h. However, the light area displays a high content of Mn leading to over stoichiometry in B-type elements as compared to the nominal value. Likewise, the anneal samples (BN125A, BN2A, B9A) did not exhibit a relevant change in composition compared to the original ones (BN1-2-5, BN2, B9). Additionally, in Fig. 28 these heterogeneities in the main matrix of the alloy and also the presence of secondary phases were evidenced.
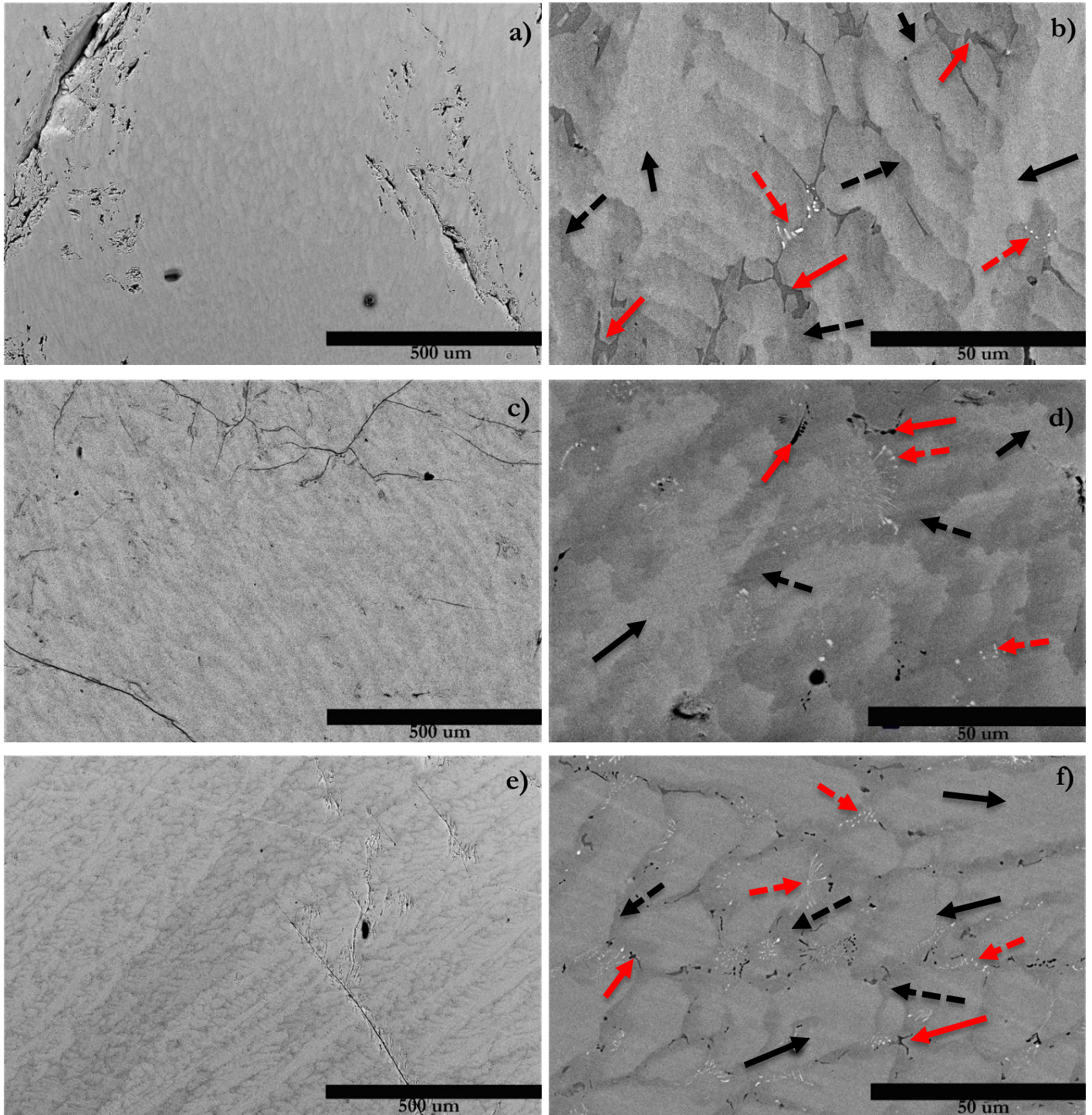

Fig.28. BSE Micrographs of the different alloys, a-b) P_l-type alloy, c-d) P_m-type alloy, e-f) P_h-type alloy

54

First, the three alloys show that the grains formed during the synthesis process have a dendritic morphology (Fig. 28 a, c, e), which is common in this type of synthesis process. Then, the light zones are the dendrites itself, while the dark zones are basically the inter-dendritic areas of the alloy. In the magnification of the general micrographs (Fig. 28 b, d, f), the light area in all the samples is shown as solid black arrows, while the dark area is with dash black arrows, also, secondary phases like ZrO_2 (red dash line) and a precipitate identified by EDX as an AB-type composition (solid red line) can be observed. The chemical composition of the AB precipitate found by EDX for P_l alloys is $Ti_{0.985(6)}Zr_{0.104(4)}Mn_{0.817(6)}V_{0.191(4)}$, while for the P_m and P_h alloys it is $Ti_{0.94(4)}Zr_{0.06(4)}Mn_{0.50(6)}Cr_{0.15(6)}V_{0.093(4)}$ [1]. Then, in Fig.29 the annealed samples did no exhibit any relevant change in the heterogeneity between light and dark zones evidenced in the original alloys (Fig.28).
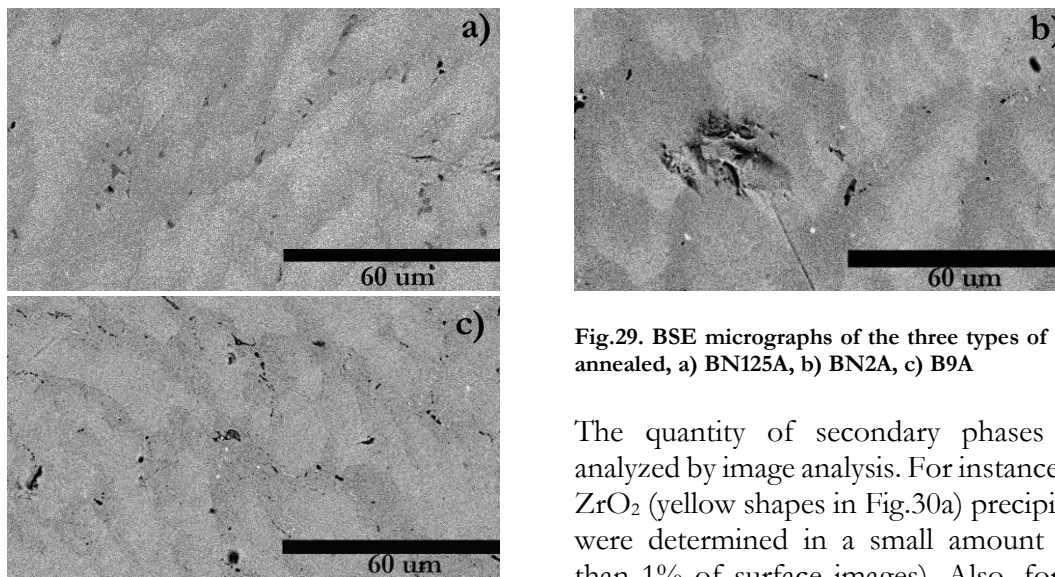
Fig.29. BSE micrographs of the three types of alloys annealed, a) BN125A, b) BN2A, c) B9A

The quantity of secondary phases was analyzed by image analysis. For instance, the ZrO_2 (yellow shapes in Fig.30a) precipitates were determined in a small amount (less than 1% of surface images). Also, for the AB-type precipitate found by EDX, a low amount (<1%) was found.
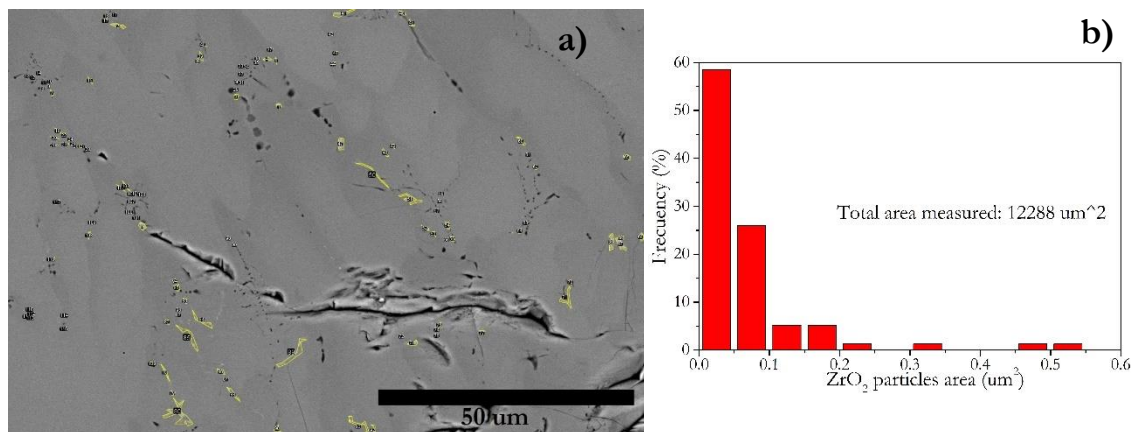
Fig.30. Image analysis of the ZrO_2, a) image of the area analyzed and the places where the precipitates were found (yellow shapes), b) Histogram with the particle distribution in the whole area analyzed.

In the structural analysis, it was important to see if these heterogeneities in the alloys could be evidenced, specially, the secondary phases that in the image analysis seem to be small in quantity in comparison with the rest of the material. Also, if the annealed sample exhibit a variation in comparison with its original state. Then, a comparison of the XRPD from the different type of alloys can be observed in Fig.31. Some vertical lines were put as a guide to

evidence the shift in the peaks that each type of alloy could have, considering a C14 laves phase refinement from the P_l alloys, which are shown as small bars at the bottom of Fig.31.

Fig.31. X-ray diffractograms from representative samples of all the materials. Bars at the bottom stand for the C14 laves phase peak position obtained from the refinement of the low-pressure alloys. The intensities were adapted to evidence the difference in the positions of the peaks between materials. • AB-type composition found. The P_l alloys are the BN1 samples, the P_m alloys are the BN2 samples and the P_h alloys are the B samples
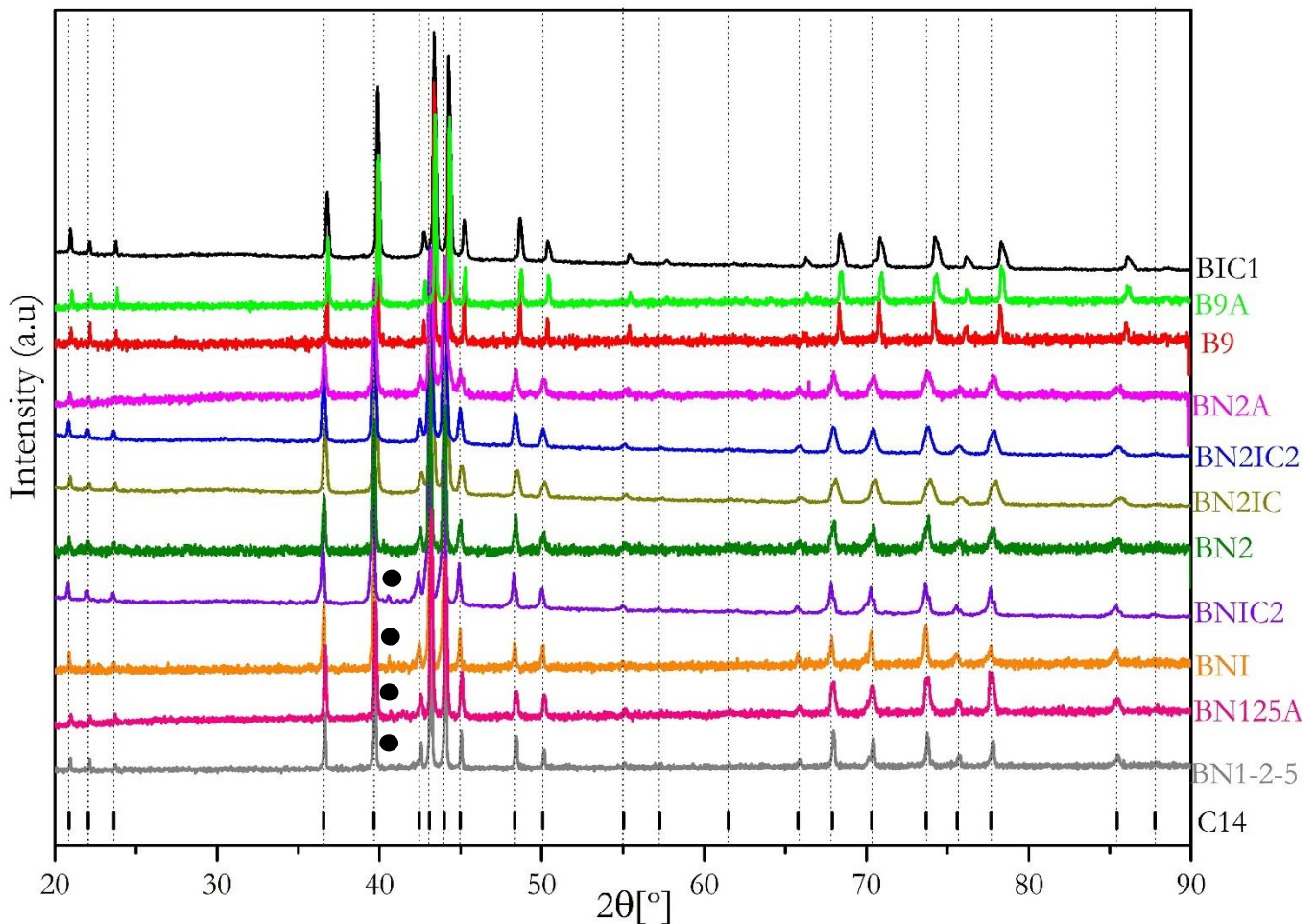
A small peak was found in the P_l alloys (• in Fig.31.), which could be related to the AB-type composition found in the EDX analysis. Also, all the alloys exhibit the characteristic C14 laves phase (S.G. p63/mmm; No. 194) (Fig.32) [2-5]. The difference between the annealed samples and their original ones is scarce, like the tendency observed in the compositional and morphological analysis. Then, by considering the peaks of the refined P_l alloys as base line, the movement of the other material´s peaks is clear, which implies a reduction in the volume of the unit cell as these peaks move to the right in comparison to this base line (a comparison of all the materials can be seen in Annex 4). This variation is more evident by accounting the Rietveld refined performed on these samples and the parameters found with this method. First, the average composition between the light and dark zones was used as an input of the XRPD refinement, considering that a clear difference of the main phase in the peaks of the diffractograms could not be evidence (Fig.31). For instance, the Rietveld refinement performed in the samples BN1-2-5, BN2 and B9 can be seen in Fig.32.
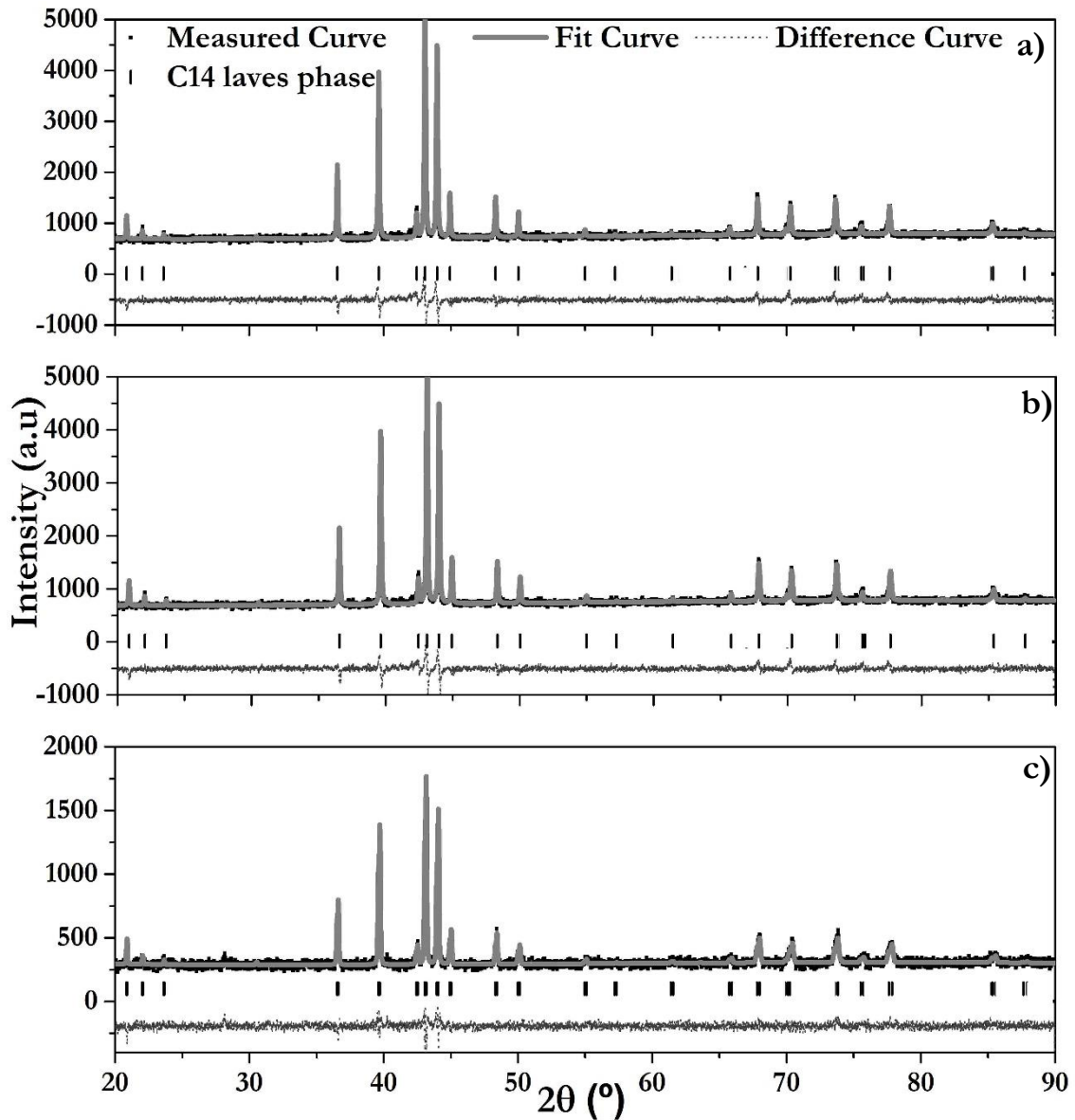
Fig.32. Rietveld refinement of the three types of alloys, a) BN1-2-5, b) BN2, c) B9 [1]

Using the average of the light and dark zones composition a reasonable refinement of the peaks in each sample was achieved. The parameters found with the refinement of the samples shown in Fig.32 can be observed in Table 10 (all the refined parameters are in Annex 3).

Table.10. Refined parameters of the three types of alloys

	a(Å)	c(Å)	V (Å³)	ρ (g/cm³)	χ2	Rb (%)
BN1-2-5	4.9139(1)	8.0629(1)	168.56(1)	6.45(1)	2.29	10.4
BNI2	4.9212(1)	8.0696(1)	169.25(1)	6.41(1)	1.81	13.5
BNIC2	4.9164(2)	8.0640(3)	168.80(1)	6.42(1)	21.9	7.83
BN125A	4.9134(1)	8.0622(1)	168.55(1)	6.45(1)	6.85	24
BN2	4.9030(1)	8.0470(1)	167.58(1)	6.54(1)	3.83	10.4
BN2IC	4.9021(1)	8.0471(1)	167.47(1)	6.50(1)	5.58	5.10
BN2A	4.9035(1)	8.0475(1)	167.57(1)	6.54(1)	3.37	24.5
B9	4.8828(1)	8.0143(2)	165.48(1)	6.44(1)	1.22	12.2
BIC1	4.8766(1)	8.0038(2)	164.84(1)	6.44(1)	12	9.16
B9A	4.8806(1)	8.0114(1)	165.27(1)	6.44(1)	3.93	25.9

First, the average of the densities in these alloys is 6.4±0.2 g/cm³. Then, as observed with the other characterization techniques, the annealing process did not change the structural parameters of the original alloys treated. Also, as observed in Fig.31. with the movement of the peaks, the cell volume in the three types of alloys exhibits a decreasing trend, $VP_l > VP_m > VP_h$ that is correlated to the decrease in stability of the hydrides. This tendency can be analyzed in detail comparing these results with their thermodynamic properties.

3.2.3. Thermodynamic characterization

In Fig.33, the three activations of samples BN1-2-5, BN2 and B9 can be observed.
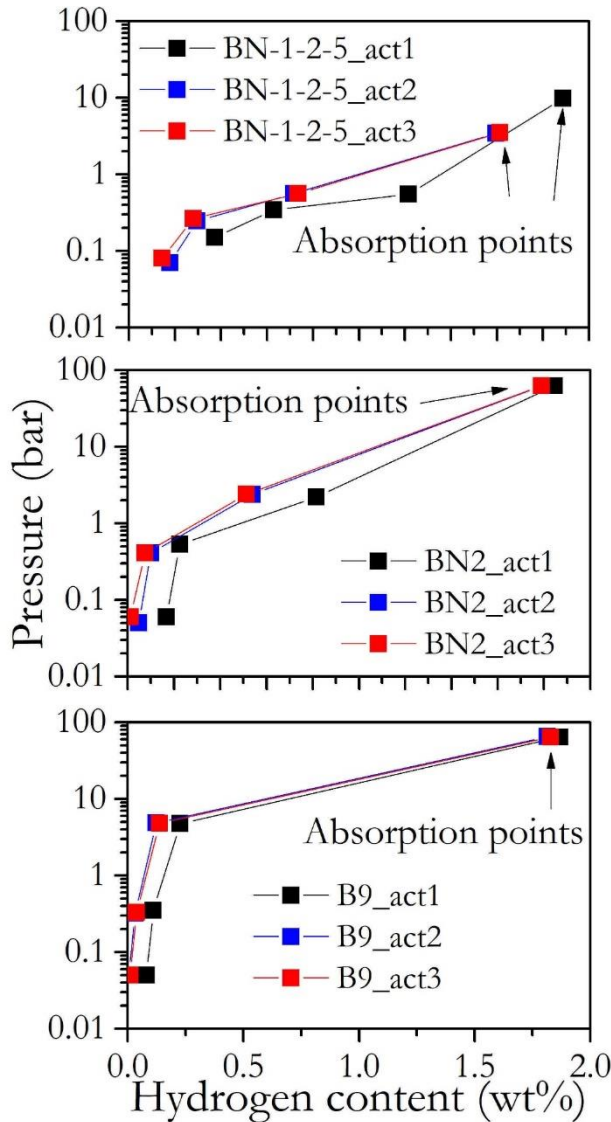
Fig. 33. Example of activation from the three different types of samples, a) BN1-2-5, b) BN2, c) B9.

It can be seen that from the second activation (act2), the length of the absorption is almost the same while the rest of desorption points return almost to zero. Both absorption and desorption behaviors verify that the samples have been activated and further experiments can be performed.

One of these experimental procedures is the thermodynamic characterization through the corresponding P-c-I curves. For the alloys described in table 10 (except annealed ones), these curves can be observed in Fig.34 in absorption and desorption at 23°C for all the materials, and, at 50°C and/or 80°C in some cases. The maximum sum of uncertainty considered by the different sources described in chapter 2 was of 0.008 wt% for the samples measured in the Sieverts system described in Fig.18a of chapter 2 (BN-1-2-5, BNIC2, BN2, BN2IC, B9, BIC1), while for the samples measured in the Sieverts system described in Fig.18b of chapter 2 (BNI2), this added uncertainty was of 0.16 wt%.
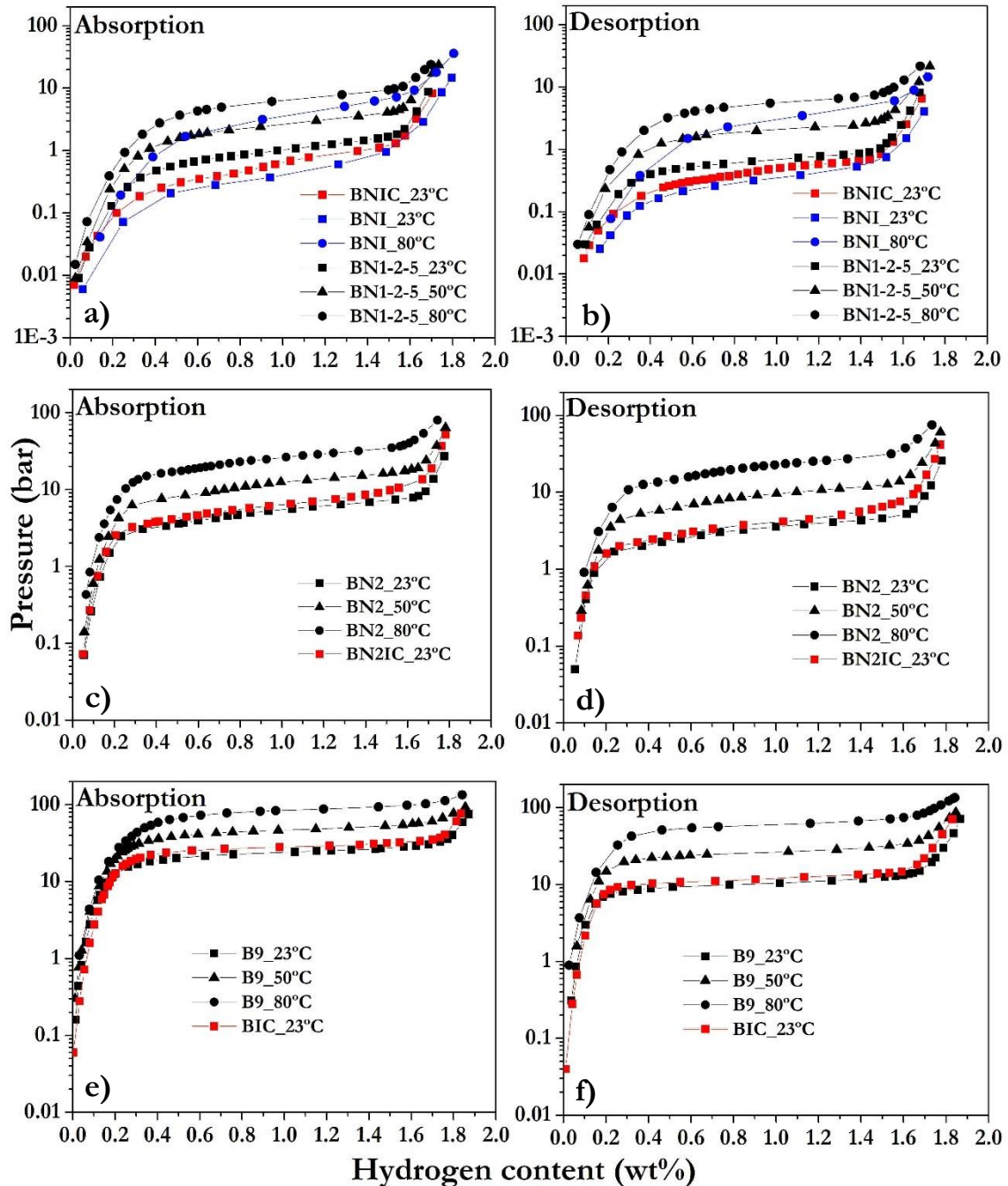
Fig.34. P-c-I curves of the distinct types of alloys. a-b) P_l alloys, c-d) P_m alloys, e-f) P_h alloys

The P_l alloys exhibit an absorption pressure around 1 bar (<2 bar) that generates a β_{min} composition as stated in the selection program. Also, the P_h alloys have a higher P_{eq} than P_m and P_l alloys, which confirms the trend mentioned in section 3.2.1 and enables to couple these materials with the appropriate thermodynamic conditions. From the materials that were measured at three different temperatures (BN1-2-5, BN2 and B9), the enthalpy ΔH and entropy ΔS of absorption and desorption were determined by implementing the Van´t Hoff plot that can be observed in Fig.35.
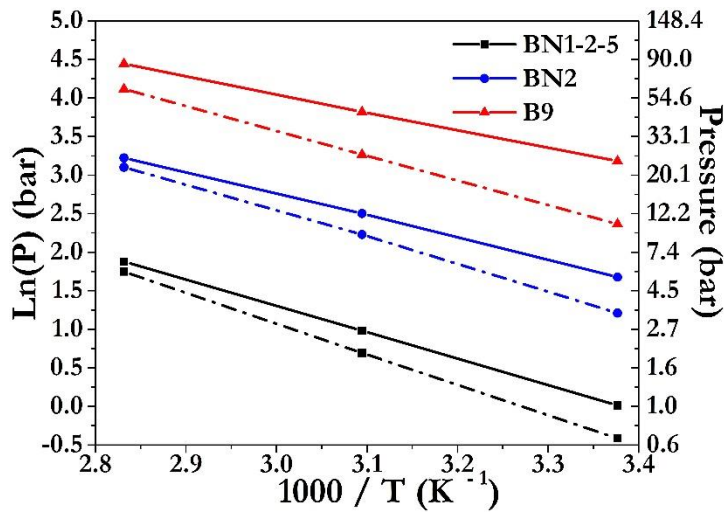
Fig.35. Van´t Hoff plot from experimental data of each type of alloy. The P_p were taken at ≈1wt% of composition from the alloys BN-1-2-5 (black), BN2 (blue) and B9 (red). The solid line is the absorption while the dash line is the desorption. Adapted from [1]

In addition to the resulting values of the enthalpy and entropy for alloys described, the sloping plateau and hysteresis values can also be seen in Table 11, for all the alloys measured in Fig.34 at the different temperatures used.

Table 11. Experimental thermodynamic parameters obtained from the different types of alloys. Adapted from [1]

|	Hys @ ≈1wt%			Slp@absorption			Slp@desorption			ΔH_{abs} (kJ/mol)	ΔS_{abs} (J/mol*K)	ΔH_{des} (kJ/mol)	ΔS_{des} (J/mol*K)
	23ºC	50ºC	80ºC	23ºC	50ºC	80ºC	23ºC	50ºC	80ºC				
BN1-2-5	0.39	0.26	0.14	1.03	0.89	0.83	0.59	0.60	0.60	28(2)	96(2)	-33(1)	-107.8(0.1)
BN2	0.44	0.28	0.14	0.69	0.68	0.67	0.68	0.73	0.75	24(1)	94(1)	-29(1)	-108(3)
B9	0.80	0.54	0.31	0.28	0.27	0.27	0.29	0.27	0.26	19.3(0.5)	91.3(0.2)	-27(1)	-110(2)
BNI	0.16	--	0.13	1.32	--	1.35	1.05	--	1.21	--	--	--	--
BNIC	0.30	--	--	1.53	--	--	1.44	--	--	--	--	--	--
BN2IC	0.44	--	--	0.79	--	--	0.94	--	--	--	--	--	--
BIC	0.84	--	--	0.26	--	--	0.3	--	--	--	--	--	--

The values of enthalpy and entropy found for the BN-1-2-5, BN2 and B9 are between the ranges of similar types of alloys [6-8]. In the special case of the BNI hydrogenated sample, an XRPD analysis was performed in order to measure the lattice parameters of the hydride phase, since these values are a key element of the mechanical properties analysis in chapter 4. As for the rest of the alloys, these hydrogenated parameters were not measured, considering that for the rest of the P_l alloys the volume expansion and therefore the lattice parameters associated to this hydride formation, are close to each other and won't change drastically, also, this effect can be applied to the P_m and P_h alloys [9].
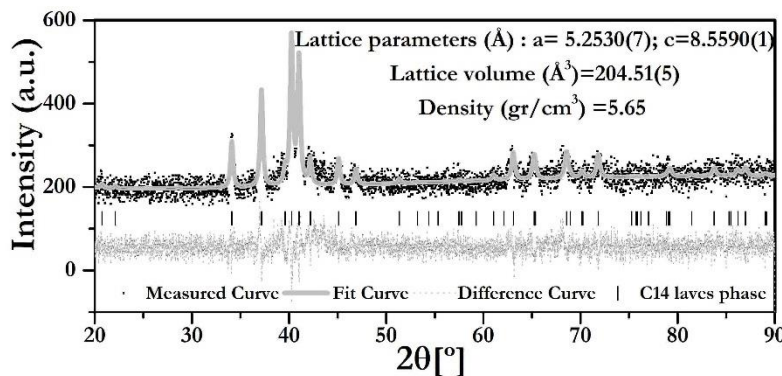
Fig.36. Rietveld refinement of the hydrogenated BNI sample and the structural parameters found

As observed in Fig.36, the lattice parameters found in the hydrogenated state at a pressure of 1 bar in RT, are larger than the ones from the alloy without hydrogen (Table 10). Also, an expansion coefficient was found from these two states, where the volume expansion was about 20.8% of the unit cell volume between the alloy and the hydride state.

3.2.4. Comparison between compositional, structural and thermodynamic measurements

Several aspects should be discussed regarding the different characterizations described. First, as observed through the EDX and SEM analysis, the main heterogeneities in the matrix are dendritic morphologies (light zones) and inter-dendritic ones (dark zones), which have a close composition as described before. However, the higher Mn content in the light zone observed in the B-type elements of the P_l alloys (Table 9.) seem to be driven by the lack of Cr, which on the contrary is in the P_m and P_h alloys that exhibit close Mn values between the light and dark zones [1]. Also, it must be highlighted that despite of the different composition between the light and dark zones, both phases crystallize in C14 laves phase with close lattice parameters as evidenced by the XRPD analysis (Fig.31), which concurs with previous studies showing that $TiMn_2$ AB_2-type alloys can accommodate between a wide stoichiometric ratio ($1.2 \leq B/A \leq 2$) without changing their structural order [10-13]. Also as mentioned, the annealed process applied to the samples (BN1-2-5, BN2, B9) did not provide the homogeneous effect in the matrix of the alloys as it would be expected, which can be explained by considering that the main elements that control the light and dark zones are the Zr and Cr (in the alloys that have it) and the temperature employed for this process was evidently not enough to diffuse these elements homogeneously between the two zones while keeping the Mn content constant. This clearly evidence the difficulty to homogenize this type of alloys, as it has been observed in previous works with similar $TiMn_2$ based alloys [14, 15]. It has to be consider, that a higher temperature produces a higher evaporation of the Mn that is not easy to control, even within a close chamber.

In the case of the secondary phases evidenced, it was found in the P_l alloys an AB composition through EDX analysis and a peak that did not correspond to the C14 laves phase (● in Fig.31.), which was not completely identify experimentally, but two options were considered from the literature. On the one hand, for comparable alloys, some authors have found an AB composition [3, 14] that resembles the one described for the P_l alloys, and also exhibit a peak close to the same angle found, while other authors [15, 16] described this peak for a $TiMn_2$ as an AB phase (β-TiMn) that takes after the morphology found in the P_l alloys, as it can be observed in Fig.37.
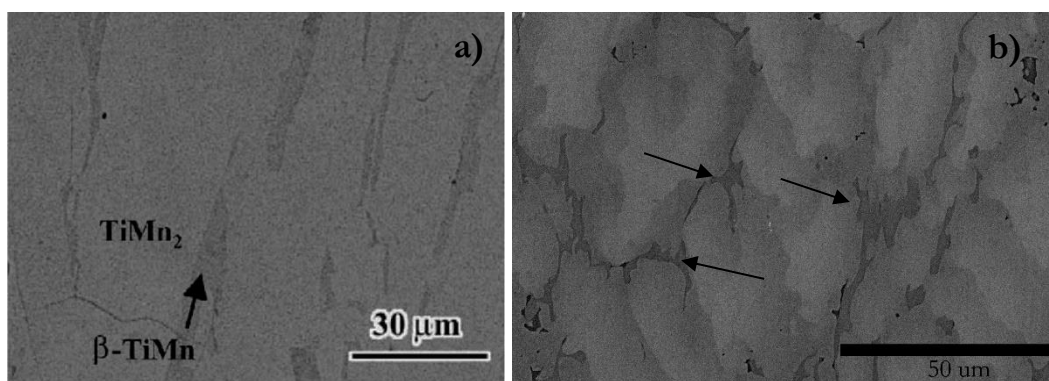
Fig.37. Secondary phases in $TiMn_2$-based alloys, a) $TiMn_2$ (adapted from [16]), b) BN1-2-5

However, several authors [13, 14] found through different characterization techniques that this peak is related to a Zr_3V_3O-type structure (FCC structure; S.G. Fd3m; No.227), even if by EDX or EPMA the composition measured was an AB one (e.g. $(Zr_{0.75}Ti_{0.25})_3(MnV)_3O$), the final composition is related to this carbide-type oxide that can be present in alloys containing Zr and V elements simultaneously [13]. Also, these secondary phases don't appear in large quantities through the alloys, and their repercussion in other properties (i.e.

thermodynamic) is neglected compared to the effect of compositional changes in the alloy matrix (i.e. light and dark zones). On the other hand, the cell volume between the different alloys clearly decreases in a tendency $VP_l > VP_m > VP_h$ (Table 10), which can partially be explained by the variation in the composition of the alloys. First, since the P_l alloy is non-stoichiometric, the Mn (covalent radii R = 1.29 Å [17]) sites of the B-type elements can be substituted by V atoms (R = 1.44 Å) and also by A-type elements like Ti atoms (R = 1.48 Å) that follow the same tendency and aid to increase the cell volume [12, 18]. Then, between the P_m and P_h alloys the variation of the Zr (R= 1.64 Å) in the A-type elements and of Cr (R= 1.3 Å) in the B-type elements originates a change in the cell volume in these two alloys that are composed of the same elements but with slightly modified composition. Specifically, an increase of the Zr in the P_m alloy will enlarge the cell volume, considering its higher size in comparison with the Ti. Also, in a lower scale for the same alloy, a substitution of Mn by Cr creates the same enlarging effect in the volume cell, since there will be less V substituting Mn [3, 7].
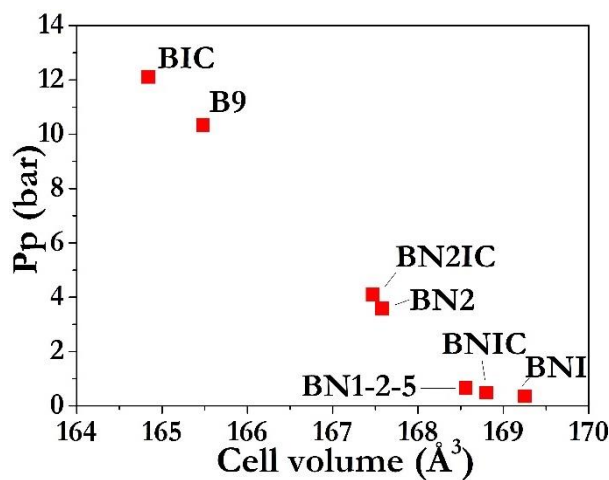
Fig.38. Plateau pressure in desorption as a function of the cell volume

The cell volume changes due to the elements used in the alloys, induce a concomitant variation in the P_{eq} and the thermodynamic properties of the alloys. First, considering empirical geometric models like the hole size effect [19, 20], the increase of the cell volume will create also a decrease of the P_{eq} of the system (Fig. 38), in which case, the increase of Zr, Cr and V will also point out in this direction [7]. Also, the enthalpy and related entropy in desorption and absorption follow the same trend, i.e. a decrease in the cell volume indicates a lower enthalpy (lower stability). Likewise, an increment of Mn decreases the cell volume and thus increases the P_{eq} [12, 21, 22] as it was observed in comparable alloys (such as BN1-2-5 and BNIC, BN2 and BN2IC, and, B9 and BIC). Then, the hysteresis reduces as the cell volume increases (Table 11), considering that the lattice strain (i.e. the elastic energy barrier between metal and hydride phases) during absorption tends to reduce as the volume cell increases. However, this may be not the only explanation for this phenomenon [7, 23, 24, 25]. A hysteresis reduction is presented in all the cases with a temperature increase [26]. Finally, the sloping plateau decreased as $SlpP_l > SlpP_m > SlpP_h$, which is related to the lower stability mentioned. The most important aspect controlling the sloping plateau is the heterogeneity in the composition of the matrix (i.e. light and dark zones) that causes this heterogenous absorption/desorption in the transition from α to β phase [7, 14, 23, 27], and is not easy to homogenize as observed and discussed previously.

As the control of the synthesis process have a great influence in the final composition and characteristics of the alloys, an enhanced control process would be quite advisable, especially in the management of the cooling rates after the melting. These rates would have an effect in the whole solidification process of the dendrites, since with lower cooling temperatures a thinner dendrite with a faster dendrites growth solidifies [28] and thus a smaller micro-segregation of the compositions could be obtained [29].

Apart from the analysis performed, another characterization linked to the previous ones that is needed for the full understanding of the system and future heat and mass transfer simulations, is the determination of the intrinsic kinetics of each alloy, which is explain in the next section.

3.2.5. Intrinsic kinetics of the AB_2-type alloys

The kinetic experiments were developed between the operational points stablished in previous sections (composition for α_{max} and β_{min} in the P-c-I) for the alloys BN-1-2-5 and BN2 at 23, 50 and 80ºC, while for the P_h alloy (B9) the temperatures were 10, 23 and 50ºC, because at 80ºC the kinetics were too fast to be measured properly. The measurements were performed in the same Sieverts-type reactor with a thermostatic bath used for the determination of the respective P-c-I curves, except for the 10ºC P-c-I that was determined in the Sieverts-type MHHC test bench that is going to be explain in detail in chapter 6. For the experiments a change of pressure of less than 2 bar was stablished between P_{in} and P_{eq}, as it can be seen in Fig.39 for some experiment examples.
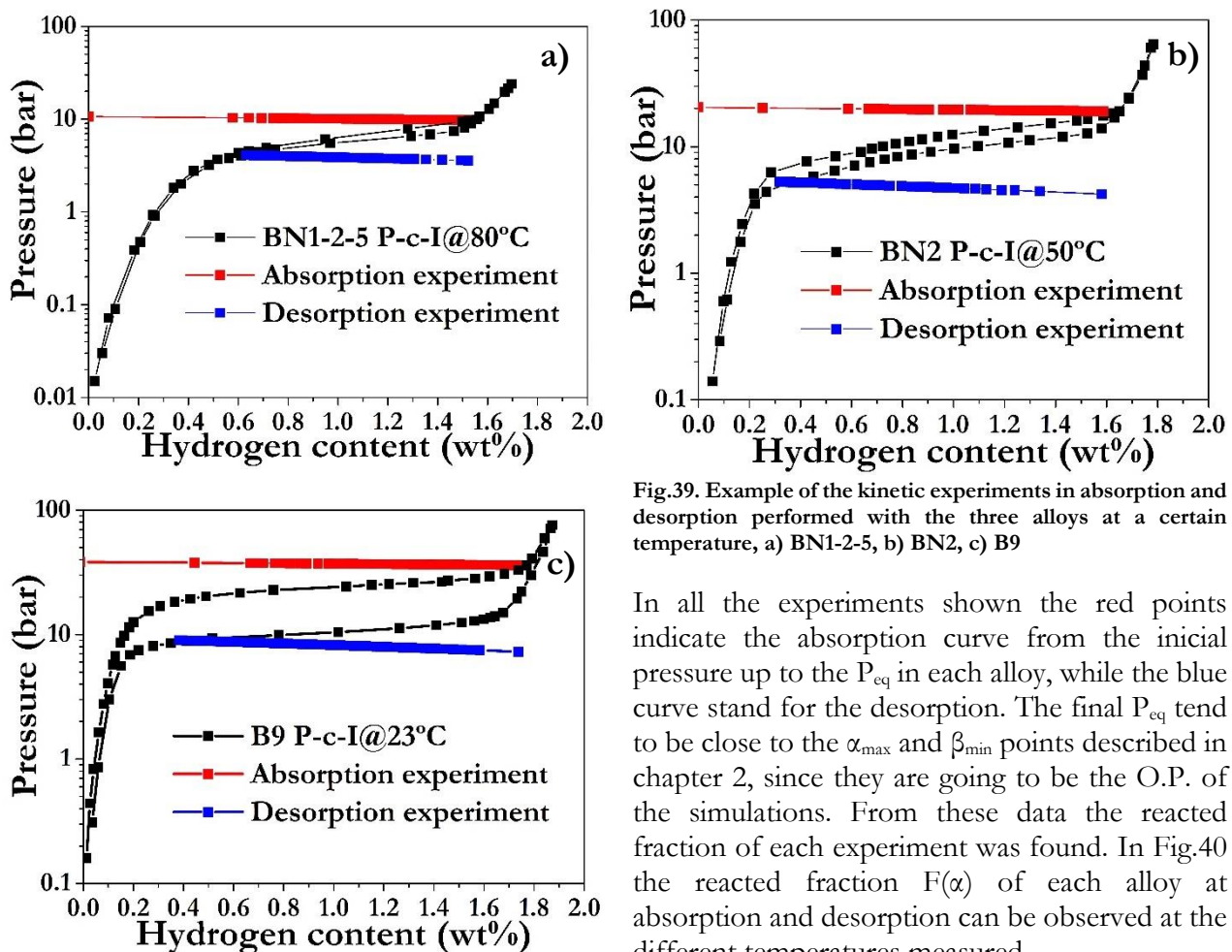
Fig.39. Example of the kinetic experiments in absorption and desorption performed with the three alloys at a certain temperature, a) BN1-2-5, b) BN2, c) B9

In all the experiments shown the red points indicate the absorption curve from the inicial pressure up to the P_{eq} in each alloy, while the blue curve stand for the desorption. The final P_{eq} tend to be close to the α_{max} and β_{min} points described in chapter 2, since they are going to be the O.P. of the simulations. From these data the reacted fraction of each experiment was found. In Fig.40 the reacted fraction $F(\alpha)$ of each alloy at absorption and desorption can be observed at the different temperatures measured.
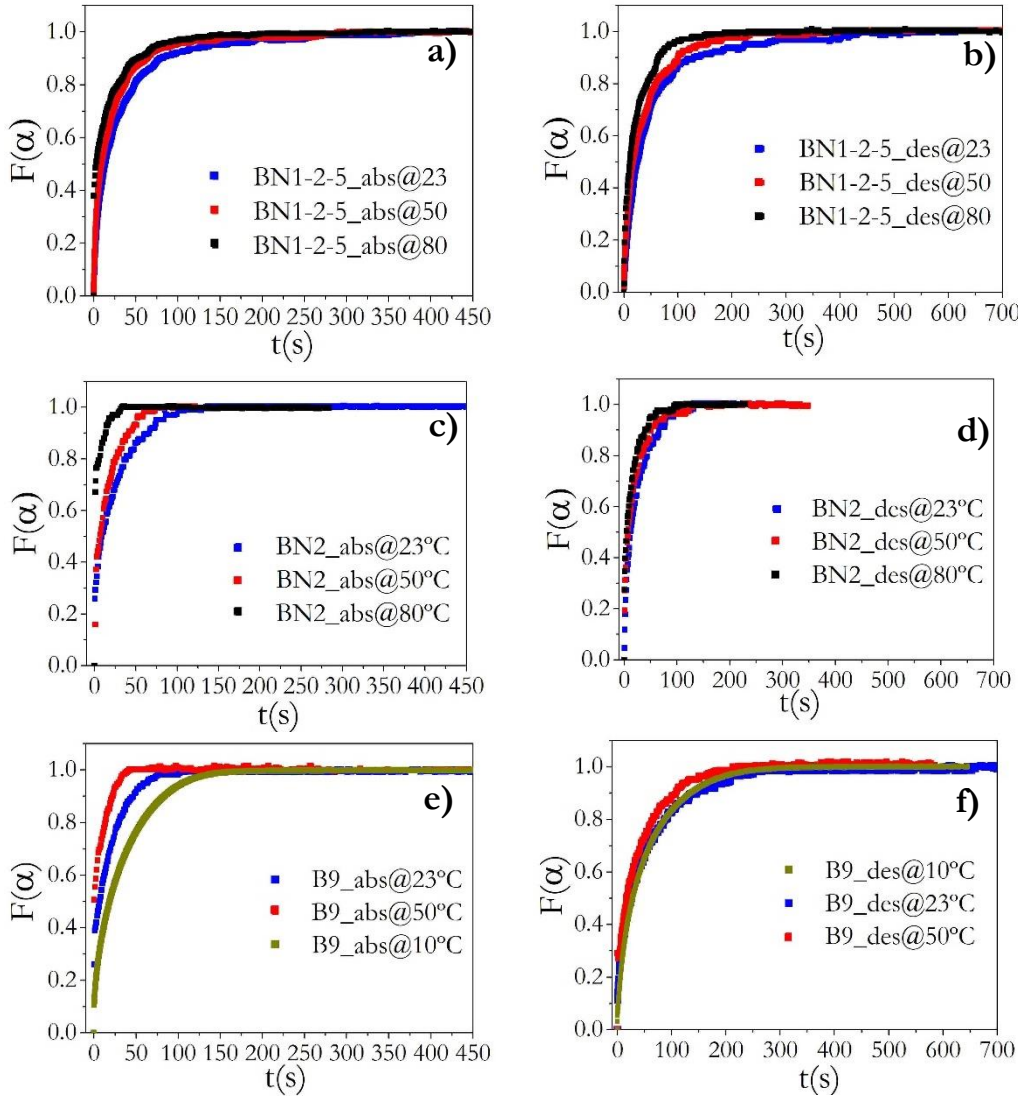
Fig.40. Reacted fraction F(α) as a function of time in absorption (abs) and desorption (des) for the three types of alloy, a-b) BN1-2-5, c-d) BN2, e-f) B9.

From Fig.40 some things can be highlighted. The absorption in all the samples is faster than its subsequent desorption. Also, in general all the alloys exhibit really good kinetics, achieving a 90% of reacted fraction below 200 s (≈3.3 min). Then, once the reacted fraction its been obtained some models have to be applied to analyze the kinetic behavoir of the alloys. As it was observed with the P-c-I curves (Fig.34 and 39), all of them exhibit sloping plateau that end up having a direct effect in the driving force and

in the hydrogenation and dehydrogenation state, as described in chapter 2. Thus, a method developed by Ron et al. [30] was used, considering that it accounts the dependency of the intrinsic kinetics of the alloys with the P_{eq}, without the need of several experiments at different starting pressures. Basically, the kinetic rate constant that considers the thermal ($h(T)$) and driving force ($g(P, P_{eq})$) effects can be obtained with the following equation:

$$\frac{f(F(\alpha))}{g(P, P_{eq})} = k(h(T)) * t \quad (31)$$

Where all the reacted fraction models ($f(F(\alpha))$) employed and driving force models ($g(P, P_{eq})$) can be observe in Annex 5. This basic equation gives a proper approximation for the kinetic analysis needed for the system design and future heat and mass transfer simulations, considering a comparison analysis of the models for the reaction fraction [31, 32] and the ones for the driving force [30, 33]. In Fig.41, the reacted fraction models at 23°C of each alloy are shown as example of the behavior at all the temperatures in absorption and desorption.
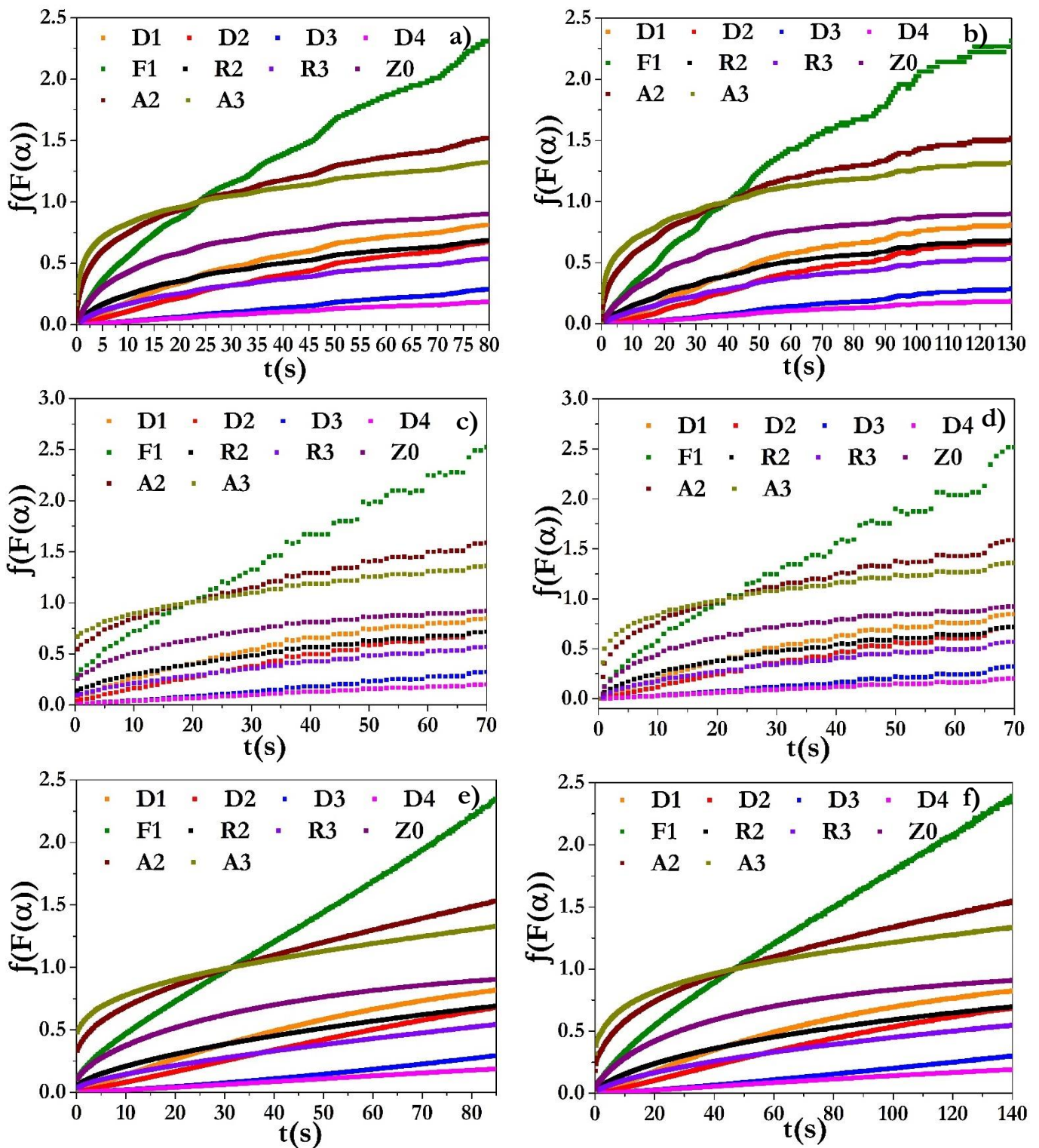
Fig.41. Reacted fraction models $f(F(\alpha))$ analyzed in absorption (left) and desorption (rigth) at a certain temperature, a-b) BN1-2-5 at 23ºC, c-d) BN2 at 23ºC, e-f) B9 at 10ºC. All models are displayed up to a reacted fraction of 90% (t_{90})

From all the models analyzed, the ones that have a closely linear relation with time are the F1, D2, D3, D4. However, since the dependency with the pressure has not been considered yet, an additional comparison using the methodology described was implemented. From this method the F1 model exhibit a better linear agreement with time than the other models

evaluated, once this reaction fraction function is normalized $(f(F(\alpha))/g(P,P_{eq}))$ by the different driving force models $(g(P,P_{eq})_1, g(P,P_{eq})_2, g(P,P_{eq})_3)$ and accounting a reacted fraction of 80% (t_{80}). Also, in Fig.42 it can be evidence the selected pair of the normalized models in absorption and desorption and at the respective temperatures of measurement.
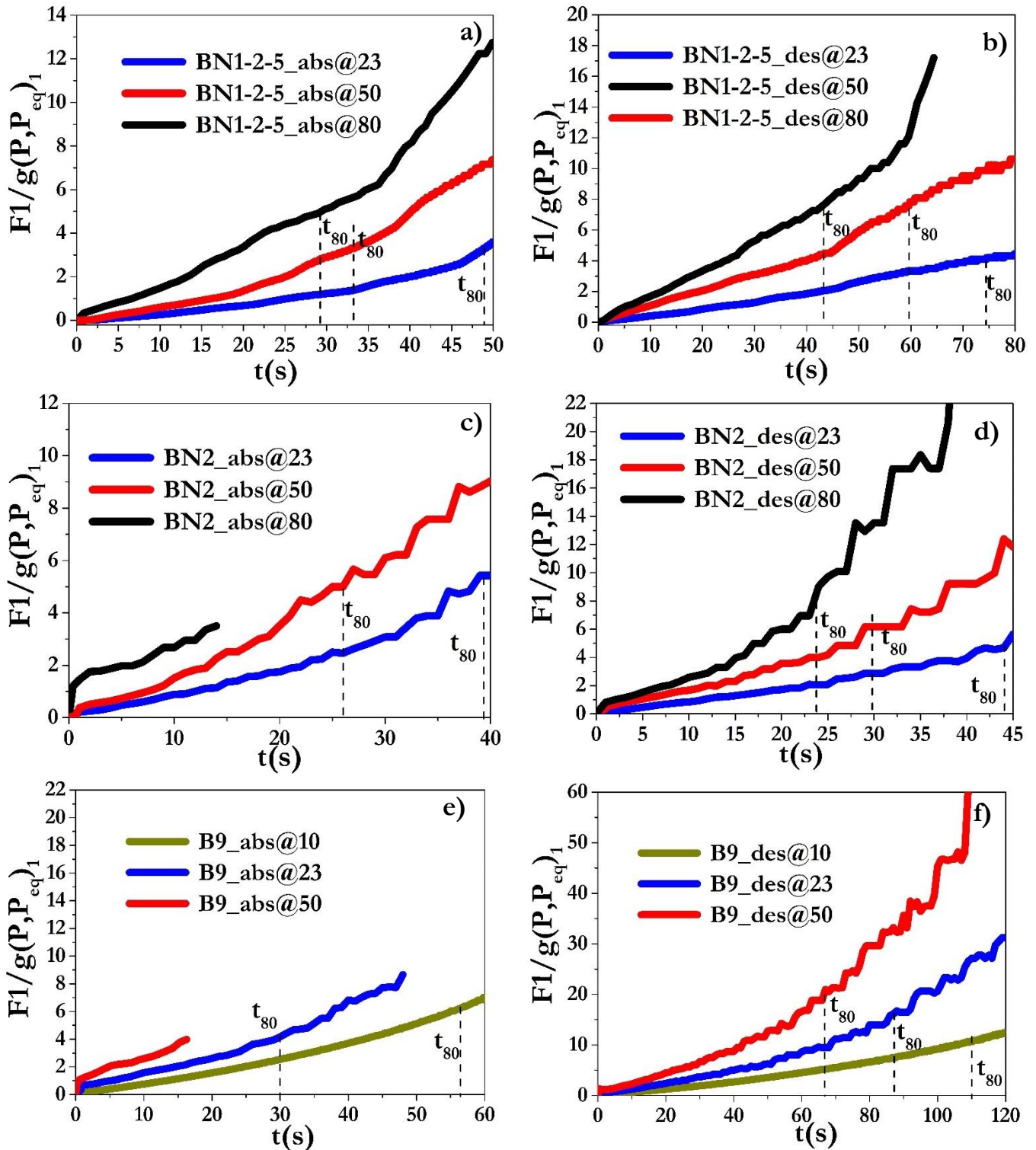
Fig. 42. Effect of the pressure dependence in the selected F1, F(α) model at absorption (left) and desorption (rigth), a-b) BN1-2-5, c-d) BN2, e-f) B9. All models where analized until a reacted fraction of 80% (t$_{80}$)

The reacted fraction model used was the F1 $(f(F(\alpha))=-Ln(1-F(\alpha))=kt)$, which is a nucleation and growth first–order kinetic model [31, 32]. The driving force model employed for the

experimental analysis was the $g(P,P_{eq})_1$, which is a normalized pressure dependence model [30]. This normalized model was chosen considering that its linear fit is better than the rest of the driving force models analyzed (Annex 5). In the absorption of the BN2 alloy at 80°C and the absorption of the B9 alloy at 50°C, the reaction was too fast and most of the absorption data could not be recorded ($F(\alpha)>50\%$) precluding to analyze this data properly, thus, these points were not considered. The slope of the curves will provide the intrinsic absorption-desorption rate at the different temperatures that will be use in an Arrhenius curve, to determine the activation energy, (E_a) and pre-exponential factor (k_o), as seen in Fig.43.
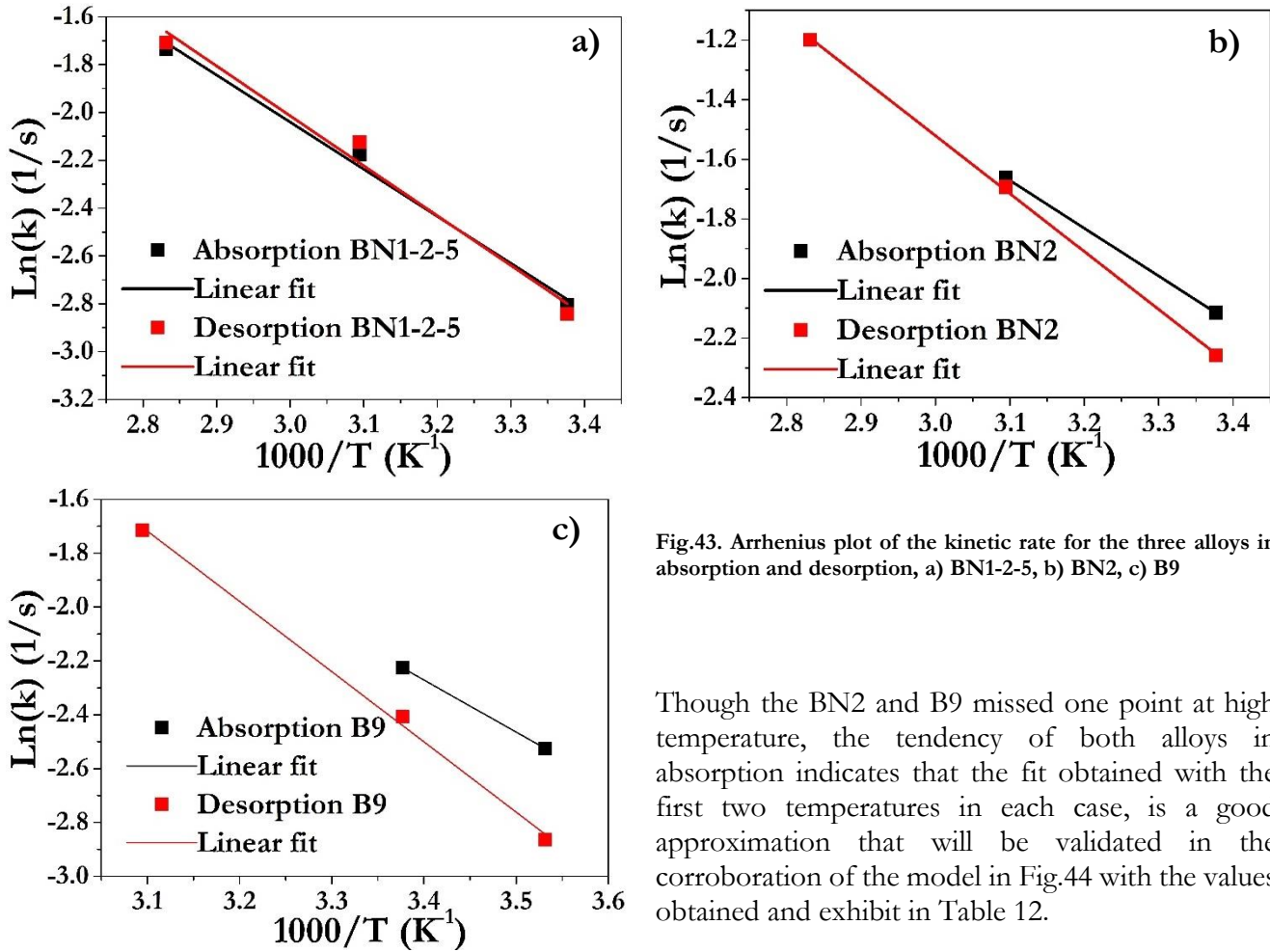
Fig.43. Arrhenius plot of the kinetic rate for the three alloys in absorption and desorption, a) BN1-2-5, b) BN2, c) B9

Though the BN2 and B9 missed one point at high temperature, the tendency of both alloys in absorption indicates that the fit obtained with the first two temperatures in each case, is a good approximation that will be validated in the corroboration of the model in Fig.44 with the values obtained and exhibit in Table 12.

Table 12. Final kinetic parameters obtained with the model implemented

	k_0(s^{-1})	E_a (kJ/mol)
BN1-2-5 absorption	47.6(1.6)	16.3(1)
BN1-2-5 desorption	69.5(2.4)	17.3(2)
BN2 absorption	27.3(2.1)	13.3(1)
BN2 desorption	74.3(1.1)	16.1(3)
B9 absorption	74.4 (2.1)	16.1(1)
B9 desorption	496.7(3.2)	21.7(1)

Finally, with the kinetic model implemented and the parameters found, a comparison of the experimental reacted fraction ($F(\alpha)$) and the one obtained with the model founded can be observe in Fig.44 for all the alloys in absorption and desorption.
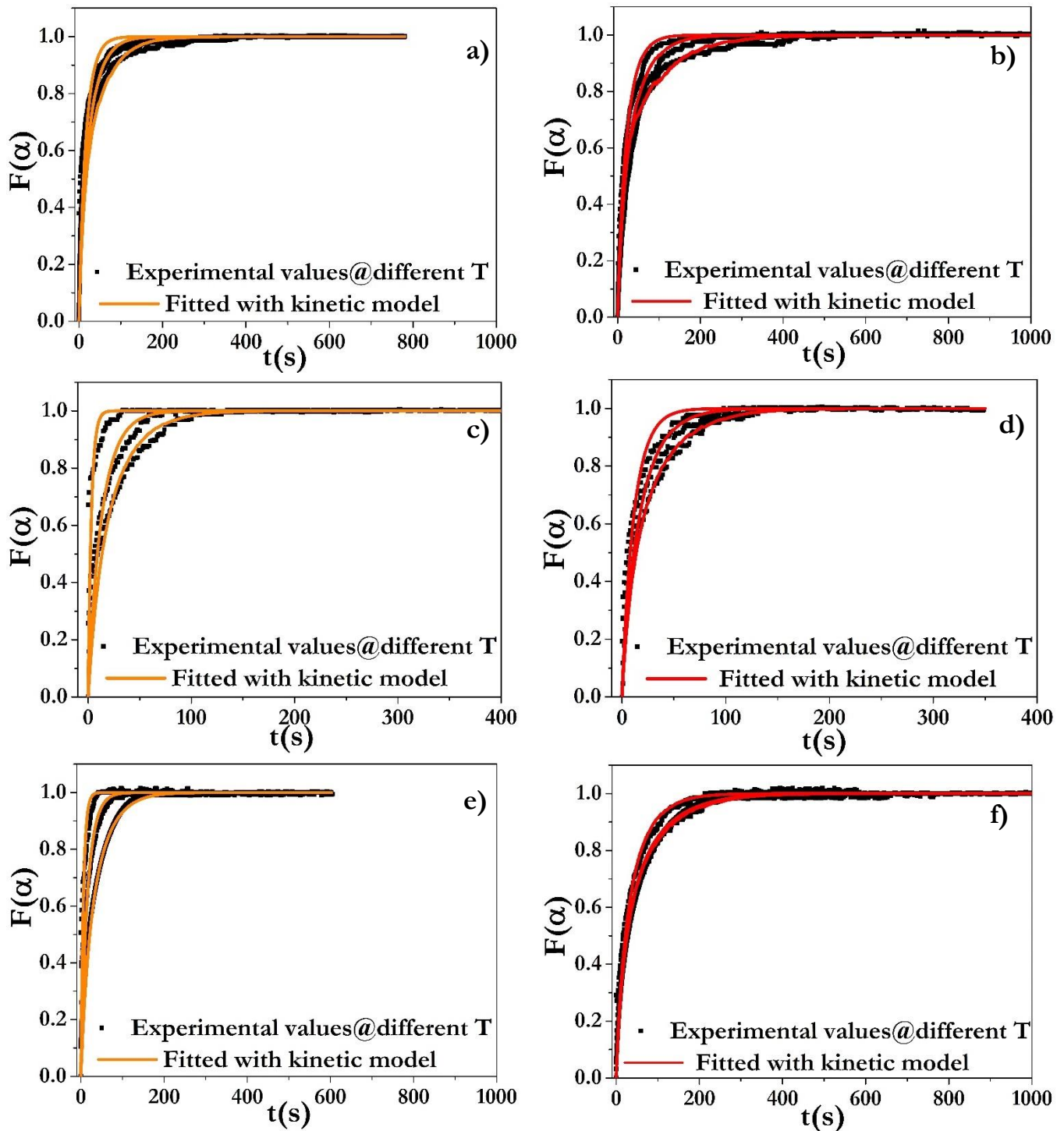
Fig.44. Validation of the kinetic model developed in absorption (left) and desorption (right), a-b) BN1-2-5, c-d) BN2, e-f) B9

The fit in each curve is close to the respective experimental points at least up to an 80% of reacted fraction. Also, it must be pointed out that those absorption curves that could not be analyzed and fit properly with the kinetic analysis performed (too fast kinetics of B9 and BN2 at high temperature), are well reproduced by the final selected model. These kinetic models allow to consider the intrinsic kinetics of each alloy in the design and performance of the MHHC system and will be very useful for future heat and mass transfer simulations.

3.2.6. Specific heat

A calibration factor (CF) must be found from the indium calibration (as described in chapter 2) to be use afterwards in the determination of the Cp. In Fig.45, the area of the indium calibration was found from the variation in time of the voltage generated from the heat applied.
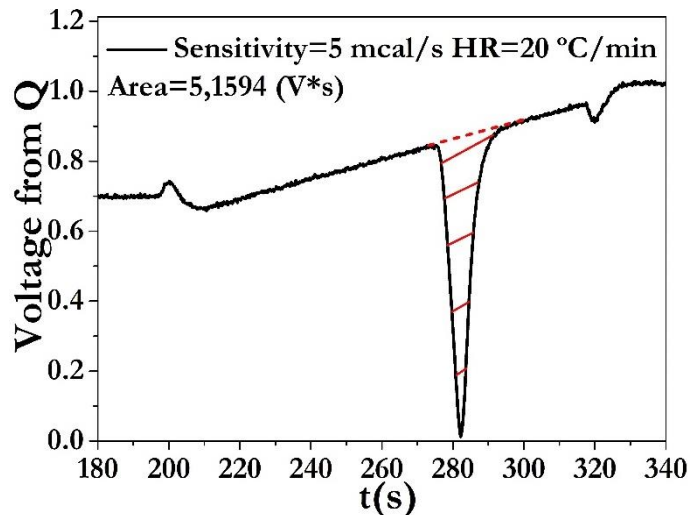
Fig.45. Indium calibration for the Cp determination

The mass of the indium used in the calibration was 4.24 g and its ΔH_{re}=6.8 cal/g. The calibration factor is found from this data and the area found in Fig.45 (area filled with crossed red lines). The equation for the calibration factor is:

$$CF = \frac{m * \Delta H}{area} = 5.5883 \frac{Cal}{V * s} \qquad (32)$$

Then, the measurement of the alloy and the reference was performed, and the results can be seen in Fig.46.
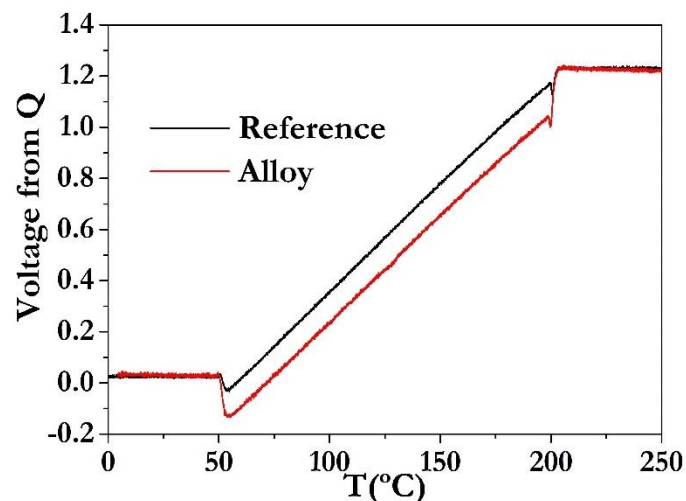
Fig.46. Comparison between the reference measurement and the alloy in a range of temperatures from 50 to 200ºC

From the difference between the reference and the alloy curves and the use of Eq.33, the Cp of the alloy was found. In Fig.47, the value obtained for a range of temperature between 50 and 200ºC can be observed. As it can be seen in Fig.47, a constant value of Cp=0.095(5) cal/(ºC*g) =0.40(2) J/(K*g) was taken from the curve, since the variation with temperature is not too large.

$$C_p = \frac{CF}{m * HR} \qquad (33)$$

69
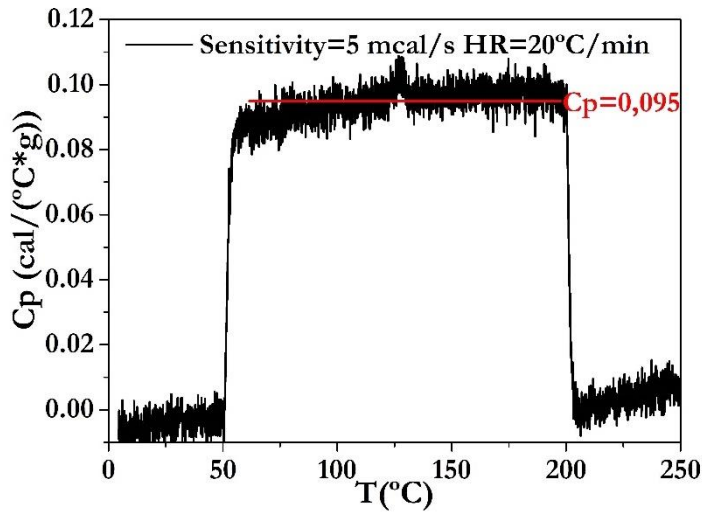
Fig.47. Cp values over a range of temperature from 50 to 200ºC

3.2.7. Thermal conductivity

As observed in the description of the technique in chapter 2, the samples have a thickness (tk) of 2 mm, also, for the measurements a current of 6 mA was employed. Then, the power input (Pw) to generate the heat flux between T-3 and T-4 was of 0.086(3)W while between T-2 and T-4 was of 0.078(3) W. The ΔT_{4-2} and ΔT_{4-3} can be obtained from the temperature change shown in Fig.48. Then, to calculate the $\varkappa$, the equation used was [34]:

$$1 = exp\left(-\pi * \varkappa * tk * \frac{\Delta T_{4-2}}{Pw_{2-1}}\right) + exp\left(-\pi * \varkappa * tk * \frac{\Delta T_{4-3}}{Pw_{3-1}}\right) \quad (34)$$
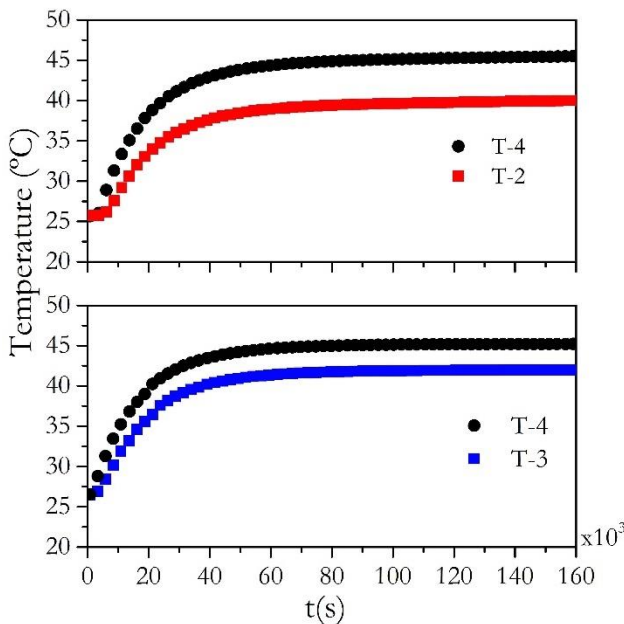
Fig.48. Variation of temperature during the experiment, a) ΔT_{4-2}, b) ΔT_{4-3}. Time scale multiplied by x10³.

The temperature values measured were ΔT_{4-2}=5.5ºC and ΔT_{4-3}=3.26ºC. Considering the parameters given and Eq. 34, a range of $\varkappa$ values from 0 to 80 w/ m*K was employed in order to generate the graph in Fig.49.
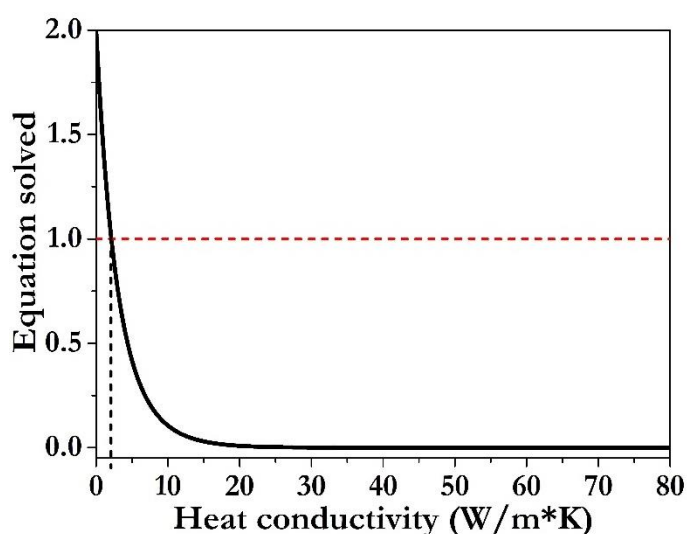
Fig.49. Van der Pauw equation solved as a function of $\varkappa$

As evidenced in Fig.49, the solution of equation 34 was obtained for a thermal conductivity, of ≈ 2.1 W/(m*K). However, considering the indications of the system [34], due to a low value of heat conductivity (<5 W/m*K) the systematic error is high enough to make this result not very accurate, but it gave the notion that is in the common range of powder conductivities [35, 36]. Therefore, the value of heat conductivity will be taken as ≈ 1 W/(m*K), accounting for previous studies on powder alloys of similar composition [36, 37].

3.3. AB$_5$-type alloy

Considering that the compressor could be couple to low pressure H$_2$ generation applications, such as a photo-electrochemical cell, a study of a material that could bear impurities or water vapor as the AB$_5$-type alloys was an option. A LaNi$_{4.8}$Sn$_{0.2}$ was characterized for this purpose, accounting that it was found with the selection program (section 2.2 in Chapter 2) as a first stage and in combination with the AB$_2$-type alloys described for the second and third stages (Annex 2).

3.3.1. Compositional, morphological and structural characterization

For this material an annealing process had to be performed to homogenize the structure, as described in chapter 2. The composition of the alloy before and after the annealing process can be observed in Table 13.

Table 13. Chemical composition of the as-cast and the annealed alloy

	Annealed	As-cast				
	Global stoichiometry - 100x (at/f.u.)	Global stoichiometry -100x (at/f.u.)	Main matrix Dark zone (at/f.u.)	Intermediate zone (at/f.u.)	Light zone (at/f.u.)	Nominal Stoichiometry (at/f.u.)
La	1.00(1)	1.00(1)	1.00(1)	1.00(1)	1.00(1)	1
Ni	4.81(3)	4.78(3)	4.94(3)	4.46(1)	3.43(1)	4.8
Sn	0.19(1)	0.22(1)	0.06(1)	0.54(1)	1.57(1)	0.2

Fig.50. BSE micrographs of the alloys before and after the annealing process, a-b) as-cast, c-d) annealed sample.

In Table 13 and Fig.50 a and b, three different distinct zones for the as-cast sample can be observed: a main dark matrix (solid red arrows), a light (solid black arrows) and an intermediate zone (dash black arrows). Each zone exhibits a composition that had to be homogenized by the annealing process (Table 13), though, the general stoichiometry (x100) found is close to the nominal one. However, the annealed sample (Fig. c and d) reveals a homogenous matrix with also a composition close to the nominal value. From these results it can be implied that the annealing process had a positive effect on the samples synthesized. Also, the Rietveld refinement of the annealed sample clearly indicates the homogeneous state of the sample, as expected.
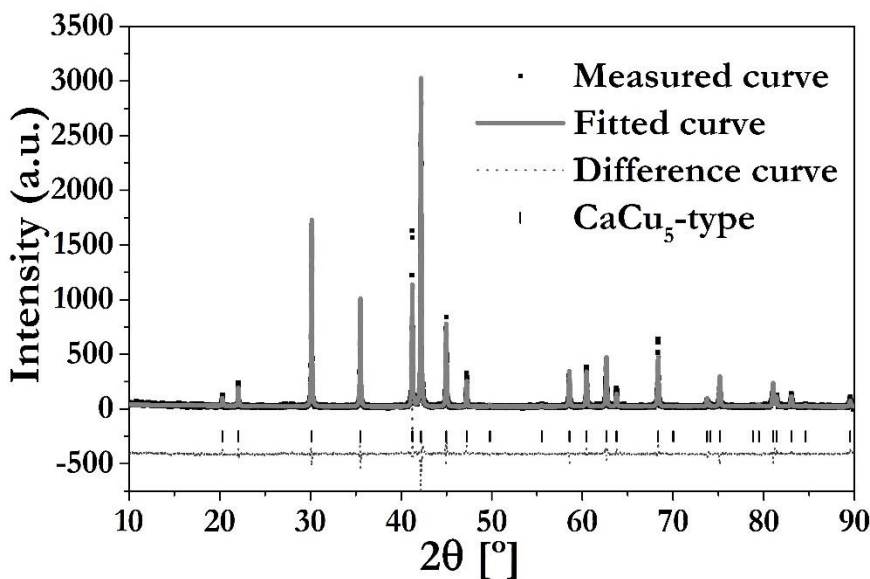
Fig.51. Rietveld refinement of the annealed LaNi$_{4.8}$Sn$_{0.2}$

The main phase is a hexagonal CaCu$_5$-type (S.G.=P6/mmm), which is the same evidenced in the LaNi$_5$ compound [38]. The lattice parameters found were: a=5.0523(1) Å, c=4.0281(1) Å, V=89.05(1) Å^3, (R$_b$=11.3, χ^2=2.2). Then, the thermodynamic properties of the annealed alloy were measured by the P-c-I determination.

3.3.2. Thermodynamic characterization

In Fig.52, the activation, P-c-I curves at 23, 50 and 80°C, and the Van´t Hoff plot of the LaNi$_{4.8}$Sn$_{0.2}$ can be observed.
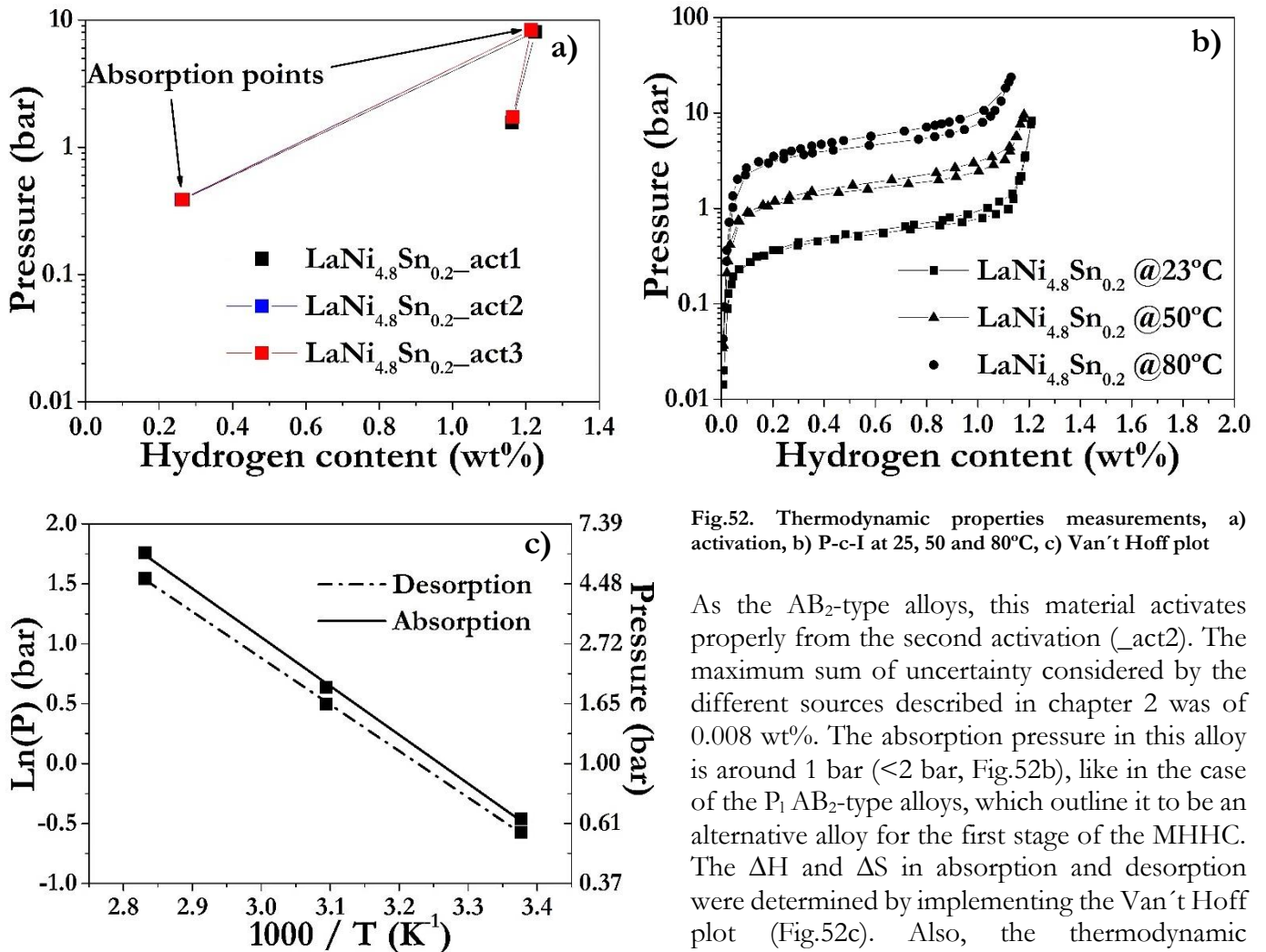
Fig.52. Thermodynamic properties measurements, a) activation, b) P-c-I at 25, 50 and 80°C, c) Van´t Hoff plot

As the AB$_2$-type alloys, this material activates properly from the second activation (_act2). The maximum sum of uncertainty considered by the different sources described in chapter 2 was of 0.008 wt%. The absorption pressure in this alloy is around 1 bar (<2 bar, Fig.52b), like in the case of the P$_1$ AB$_2$-type alloys, which outline it to be an alternative alloy for the first stage of the MHHC. The ΔH and ΔS in absorption and desorption were determined by implementing the Van´t Hoff plot (Fig.52c). Also, the thermodynamic parameters found can be seen in Table 14.

Table 14. Experimental thermodynamic parameters obtained from the annealed LaNi$_{4.8}$Sn$_{0.2}$ alloy

	Hys @ ≈1wt%			Slp@absorption			Slp@desorption			ΔH$_{abs}$ (kJ/mol)	ΔS$_{abs}$ (J/mol*K)	ΔH$_{des}$ (kJ/mol)	ΔS$_{des}$ (J/mol*K)
	23°C	50°C	80°C	23°C	50°C	80°C	23°C	50°C	80°C				
LaNi$_{4.8}$Sn$_{0.2}$	0.11	0.14	0.21	0.66	2.08	7.09	0.46	1.40	4.23	33.8(8)	110(2)	-32.2(5)	-104(1)

In Table 14, it can be observed that the values of enthalpy and entropy found are between the ranges of similar types of alloys [39, 40]. Also, some other interesting features can be observed and will be discuss in section 3.4. Then, the kinetic analysis performed with this alloy will be explain in the next section.

3.3.3. Intrinsic kinetics of the AB$_5$-type alloy

With this alloy the same methodology used for the AB$_2$-type alloys was employed. In Fig.53, it can be observed the F(α) and the models of f(F(α)) the implemented for the alloy in absorption and desorption.
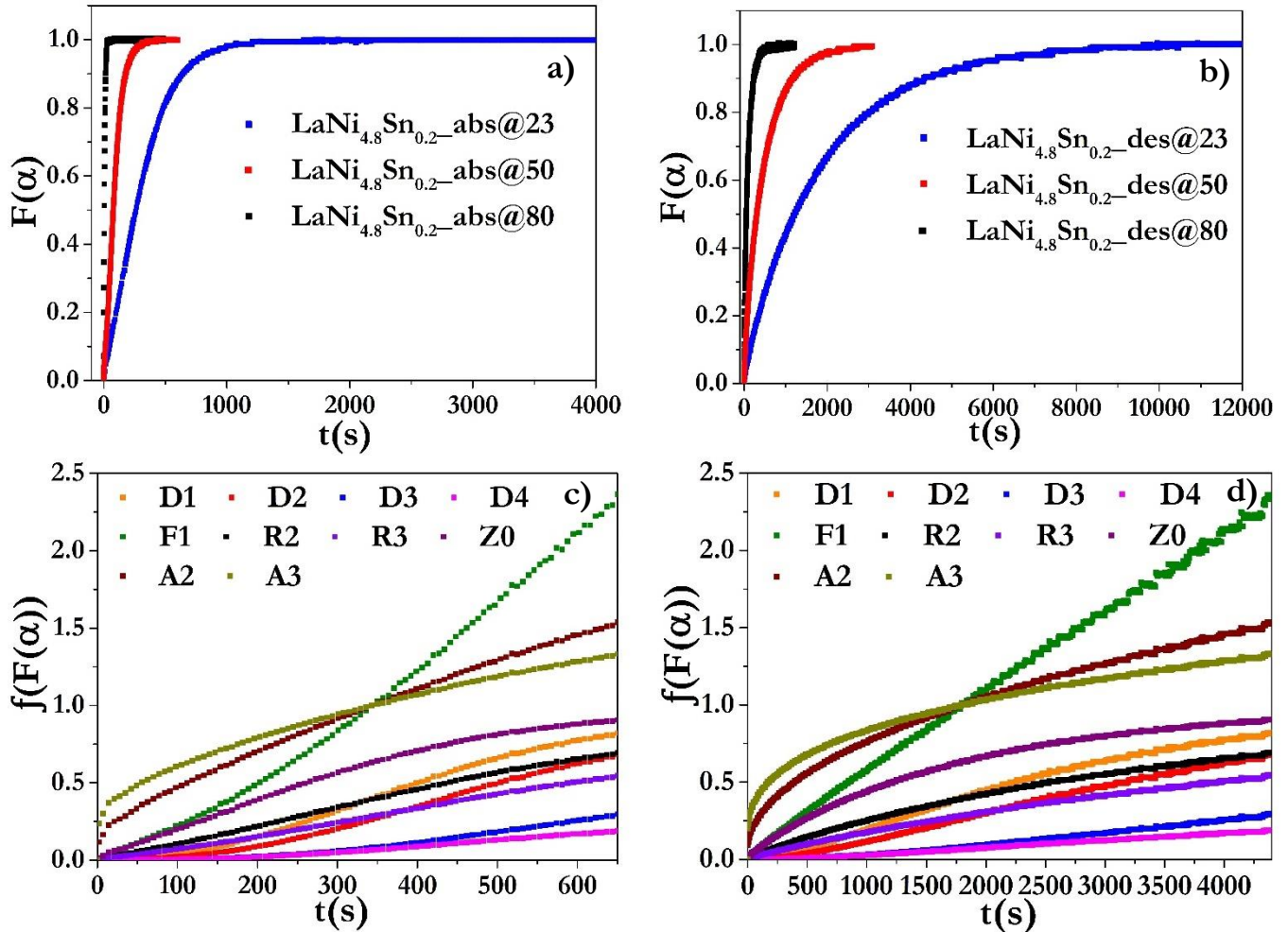
Fig.53. Reacted fraction F(α) versus time and their respective models f(F(α)) in absorption (left) and desorption (right), a-b) F(α), c-d) F(α) models at a 90% (t$_{90}$- full time scale)

From all the models analyzed, the ones that have a closely linear relation with time are the F1, D2, R3, D4. Using the methodology described and implemented before (Fig.42), it can be evidence the selected pair of normalized models (f(F(α))/g(P,P$_{eq}$)), for instance in desorption (Fig.54 a), at a reacted fraction of 80% (t$_{80}$) and at the respective temperatures of measurement, also, the Arrhenius plot in absorption and desorption generated (Fig.54 b) by the values found with the normalized models.
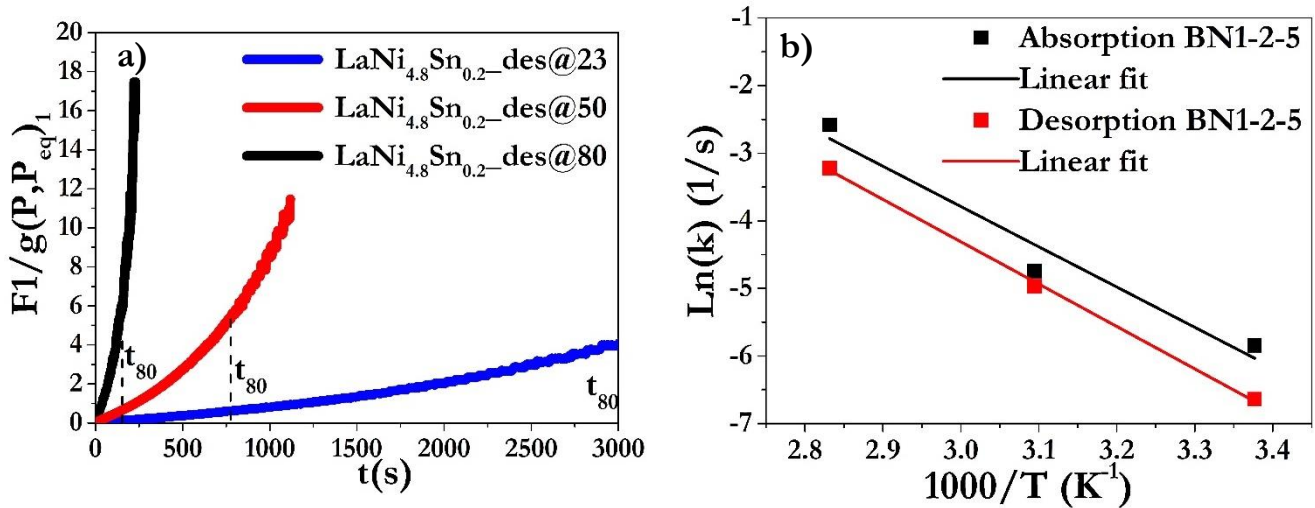
Fig.54. Kinetic model with pressure dependence, a) $f(F(\alpha))/g(P,P_{eq})_1$ in desorption, b) Arrhenius plot in absorption and desorption

With the fit found in the Arrhenius plot, the E_a and k_0 values were determined (Table 15), accounting the pressure dependence, reacted fraction and temperature. Also, the validation of the model with the parameters found can be observe in Fig.55.

Table 15. Final kinetic parameters obtained with the model implemented for the LaNi$_{4.8}$Sn$_{0.2}$

	k_0 (s^{-1})	E_a (kJ/mol)
LaNi$_{4.8}$Sn$_{0.2}$ absorption	1.31×10^6	50(1)
LaNi$_{4.8}$Sn$_{0.2}$ desorption	1.96×10^6	52(1)
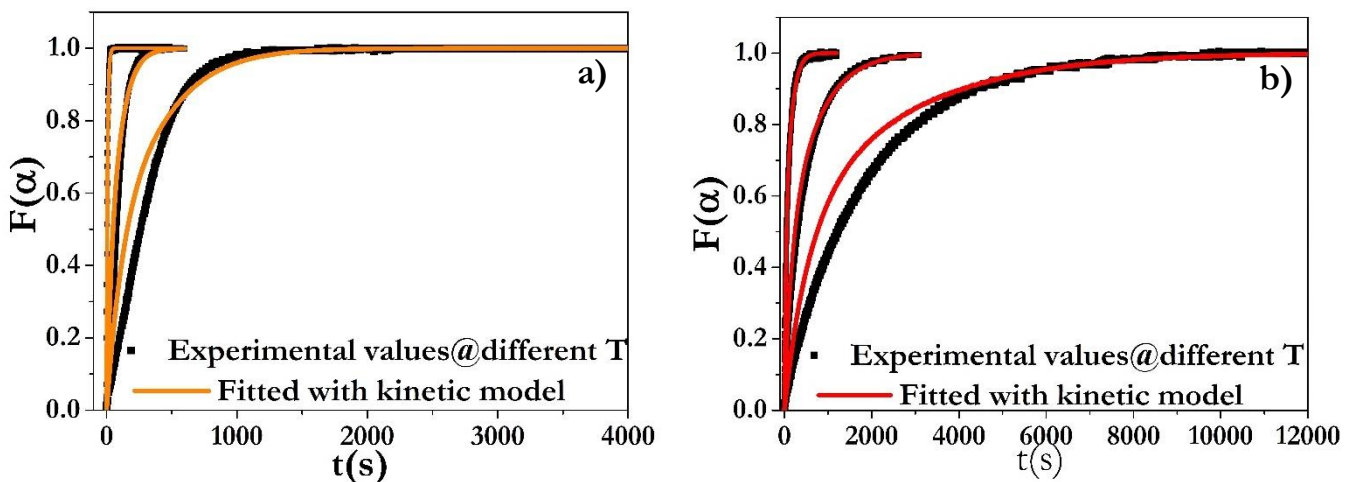
Fig.55. Validation of the LaNi$_{4.8}$Sn$_{0.2}$ model with the experimental values, a) absorption, b) desorption

The fitting curve is close to the respective experimental points, except at lower temperatures (23°C) where the fit is not that good, which can be attribute to a sluggish kinetics and a contrary fast-exponential nature of the F1 $f(F(\alpha))$ model employed. The rest have a similar behavior at least up to an 80% of reacted fraction, which is more than enough to account the intrinsic kinetics of each alloy and simulate the heat and mass transfer in a MHHC system.

3.4. General discussion

The final selection of the materials for the three stage compressor rely in a complete characterization of them, as the one presented through the development of this chapter.

First, the kinetics in the AB_2-type alloys reveal a fast response in all cases, especially in absorption, which corresponds with a possible determined step due to the growth of the α-β phases (F1 model) that slow the process at a high transformation stage ($F(\alpha) > 80\%$).
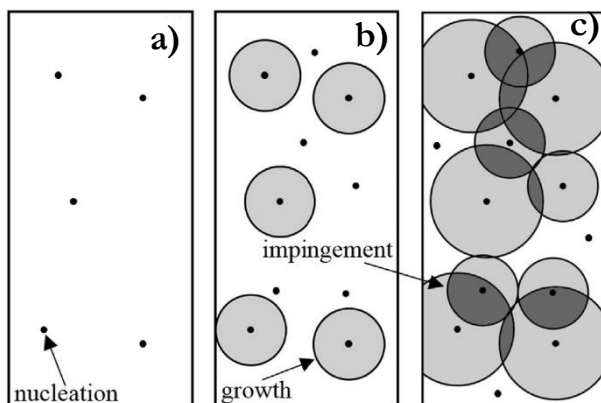
Fig.56. Scheme of the nucleation-grow-impingement models, a-c) the whole process step by step. Adapted from [41]

The reacted fraction ($F(\alpha)$) found with the kinetic model in all of the alloys analyzed reproduce closely the experimental data, especially in the case of AB_2-type alloys where the fit was more accurate through the whole experiments than the one of the $LaNi_{4.8}Sn_{0.2}$. The F1 model that best fit the experimental data for both, the AB_2-type and the AB_5-type compounds, correspond to a first order nucleation and growth model where both nucleation and the subsequent growing of the nuclei, are relevant to understand the kinetics (Fig.56) [41, 42]. In particular, a first order nucleation and growth process can be related to one in which the nucleation is fast and the determining step (growing and impingement) is mostly the phase grow. The better kinetic performance exhibited by the AB_2-type alloys, especially at lower temperatures can be related to the larger diffusion coefficient of this alloys compared to the AB_5-type ones [43]. Although, the model used in the kinetic analysis of all the alloys is accurate, to clearly identify the determined step of the kinetics in each alloy a further study has to be performed, however, for simulation purposes it is an effective model.

Other experimental parameters obtained highlighted the advantages of AB_2-type alloys over the AB_5-type. Firstly, as observed in the thermodynamic properties of each type of alloy, the reduction of the reversible capacity (C_{rev}) is evident between the AB_5-type and any of the AB_2-type alloys, this concurs with the normal thermodynamic behavior of both types of alloys [7, 44], but in terms of storage and also for further compression, results in a considerable decrease, reducing the CR and increasing the number of steps to hydrogenate the second and third stages, respectively [9]. Also, the $LaNi_{4.8}Sn_{0.2}$ exhibit a hysteresis and sloping plateau in contrast to similar alloys like the $LaNi_5$, which is mainly due to the effect of the tin in the structure [38, 45, 46]. Between P_1 alloys, the hysteresis in the AB_5-type slightly varies with temperature as also observed in previous works with similar alloys [39]. This behavior can be attribute to possible temperatures variations during the experiment that can change the behavior of the alloy, since the normal hysteresis tendency of this alloys is to decrease with temperature [44], like in the case of AB_2-type alloys that beneficially decreases as discussed previously.

Finally, it must be point out that a homogenization of the AB_5-type alloy is more plausible in comparison with that of all the AB_2-type ones, which is an advantage considering less sources of error to account in the analysis of the alloy behavior. Also, the resistance to impurities in the gas with this type of alloy is greater than the AB_2-type, which can be a big aid in coupled applications that could generate other types of gases besides H_2, e.g. a photo-electrochemical cell, though, the passivation due to impurities (e.g. oxygen and water vapor in a photo-electrochemical cell) can be reduced with special Pd membranes for cases with O_2 [47] or others like zeolites filters for water vapor [48].

In resume, considering the thermodynamic and kinetic properties, the BN1-2-5 is more suitable for an enhance operation of a first stage than the $LaNi_{4.8}Sn_{0.2}$, though, the use of a special filter like Zeolites can be applied.

3.5. Achievements and partial conclusions

1. A basic selection program was developed based on defined operational MHHC parameters and basic thermodynamics obtained from literature, which obtained two main combination of alloys suitable to become a MHHC system. The program analyzed a data base assembled from over 200 hydrides to select a combination of three hydrides. The two combinations of alloys experimentally studied can be couple in a MHHC considering its thermodynamic features.

2. The synthesis process have a great influence in the initial homogenization of AB_2-type alloys, and therefore, a better cooling control should be implemented to enhance the homogeneity.

3. Thermal homogenization of the main phase in the AB_2-type alloys is difficult and will not change properly thermodynamic features like sloping plateau and hysteresis, on the contrary, if the process is not well implemented it can degenerate the properties obtained due to a further loss of Mn during the process. On the other hand, an annealing process in AB_5-type alloys worked perfectly generating a homogenization of the main phase in the alloy.

4. From the experimental characterization results it was observed that the AB_2-type alloys studied exhibit several relevant properties for an MHHC system:
*All of the alloys exhibit a good reversible capacity close to the 2 wt%.
*The reduction of the hysteresis with temperature is an excellent fact that help to increase the compression ratio and therefore its productivity. However, the sloping plateau evident in all of the alloys goes in the opposite direction, though, it is a normal issue in these types of alloys that can be accounted with a proper design of the coupled alloys and the MHHC system at each stage, i.e. through simulations.
*Also, from the kinetic models implemented, it was concluded that these alloys exhibit excellent kinetics that can increase the productivity of the system at each stage.
*These $TiMn_2$-based alloys are suitable to variate their composition and tailor different properties such as structural, morphologic, thermodynamic and kinetic, from which a further design of the different stages of the MHHC can be more accurately performed.
*Although, these materials are not historically suited to resist gas impurities, solutions like zeolites or other types of membranes can be easily couple in the case of a couple application that generates non-purified gas.

5. The AB_5-type alloy have a required lower inlet pressure and like other material of its kind, have a good resistance to gas impurities, which is a good advantage for some applications. Although, the reduction of the reversible capacity, and slower kinetics than AB_2-type alloys make it a less desirable material to be applied in a first stage MHHC.

4. The kinetic models implemented are a useful tool for a future heat and mass transfer simulation, but it does not imply a full understanding of the kinetic mechanism involved in the absorption-desorption reaction in all the alloys. A further deep analysis is necessary.

3.6. References

[1]   A. R. Galvis E, F. Leardini, J. R. Ares, F. Cuevas, and J. F. Fernandez, "Simulation and design of a three-stage metal hydride hydrogen compressor based on experimental thermodynamic data," *Int. J. Hydrog. Energy*, vol. 43, no. 13, pp. 6666–6676, Mar. 2018.

[2]   Y. Morita, T. Gamo, and S. Kuranaka, "Effects of nonmetal addition on hydriding properties for Ti–Mn Laves phase alloys," *J. Alloys Compd.*, vol. 253, pp. 29 –33, 1997.

[3]   J.-L. Bobet, B. Chevalier, and B. Darriet, "Crystallographic and hydrogen sorption properties of TiMn2 based alloys," *Intermetallics*, vol. 8, no. 4, pp. 359–363, 2000.

[4]   P. Villars and L. D. Calvert, *Pearson's handbook of crystallographic data for intermetallic phases*, vol. 1–3, 3 vols. Metals Park. Ohio.: American Society for Metals., 1986.

[5]   J. L. Bobet and B. Darriet, "Relationship between hydrogen sorption properties and crystallography for TiMn2 based alloys," *Int. J. Hydrog. Energy*, vol. 25, no. 8, pp. 767–772, 2000.

[6]   E. Y. Anikina and V. N. Verbetsky, "Investigation of the hydrogen interaction with Ti0.9Zr0.1Mn1.3V0.7 by means of the calorimetric method," *Int. J. Hydrog. Energy*, vol. 41, no. 27, pp. 11520–11525, Jul. 2016.

[7]   B.-H. Liu, D.-M. Kim, K.-Y. Lee, and J.-Y. Lee, "Hydrogen storage properties of TiMn2-based alloys," *J. Alloys Compd.*, vol. 240, no. 1–2, pp. 214–218, 1996.

[8]   T. Gamo, Y. Moriwaki, N. Yanagihara, T. Yamashita, and T. Iwaki, "Formation and properties of titanium-manganese alloy hydrides," *Int. J. Hydrog. Energy*, vol. 10, no. 1, pp. 39–47, 1985.

[9]   M. V. Lototskyy, V. A. Yartys, B. G. Pollet, and R. C. Bowman, "Metal hydride hydrogen compressors: A review," *Int. J. Hydrog. Energy*, vol. 39, no. 11, pp. 5818–5851, Apr. 2014.

[10]   S. V. Mitrokhin, "Regularities of hydrogen interaction with multicomponent Ti(Zr)–Mn–V Laves phase alloys," *J. Alloys Compd.*, vol. 404–406, pp. 384–387, Dec. 2005.

[11]   F. Fang, Y. Li, Q. Zhang, L. Sun, Z. Shao, and D. Sun, "Hydrogen storage properties of TiMn1.5V0.2-based alloys for application to fuel cell system," *J. Power Sources*, vol. 195, no. 24, pp. 8215–8221, Dec. 2010.

[12]   S. V. Mitrokhin, T. N. Bezuglaya, and V. N. Verbetsky, "Structure and hydrogen sorption properties of (Ti, Zr)–Mn–V alloys," *J. Alloys Compd.*, vol. 330, pp. 146–151, 2002.

[13]   J. Hout, E. Akiba, and H. Iba, "Crystal structure and phase composition of alloys Zr1 − xTix(Mn1 − yVy)2," *J. Alloys Compd.*, vol. 228, no. 2, pp. 181–187, 1995.

[14]   F. Cuevas, B. Villeroy, E. Leroy, P. Olier, and M. Latroche, "Relationship between microstructure and hydrogenation properties of Ti0.85Zr0.15Mn1.5V0.5 alloy," *J. Alloys Compd.*, vol. 446–447, pp. 218–223, Oct. 2007.

[15]   B. Villeroy, F. Cuevas, J. Bettembourg, P. Olier, and M. Latroche, "Influence of the Ti/Zr ratio and the synthesis route on hydrogen absorbing properties of (Ti1−xZrx)Mn1.5V0.5 alloys," *J. Phys. Chem. Solids*, vol. 67, no. 5–6, pp. 1281–1285, May 2006.

[16]   S. Semboshi, N. Masahashi, T. J. Konno, M. Sakurai, and S. Hanada, "Composition dependence of hydrogen absorbing properties in melt quenched and annealed TiMn2 based alloys," *J. Alloys Compd.*, vol. 379, no. 1–2, pp. 290–297, Oct. 2004.

[17]   rsc, "Periodic Table." Royal Society of chemestry. taken from: http://www.rsc.org/periodic-table.

[18]   Y. L. Du, X. G. Yang, Y. Q. Lei, and M. S. Zhang, "Hydrogen storage properties of Zr0.8Ti0.2(Ni0.6Mn0.3−xV0.1+xCr0.05)2 (x=0.0,0.05,0.15,0.2) alloys," *Int. J. Hydrog. Energy*, vol. 27, no. 6, pp. 695–697.

[19]   C. E. Lundin, F. E. Lynch, and C. B. Magee, "A correlation between the interstitial hole sizes in intermetallic compounds and the thermodynamic properties of the hydrides formed from those compounds," *J. Common Met.*, vol. 56, no. 1, pp. 19–37, 1977.

[20]   C. B. Magee, J. Liu, and C. E. Lundin, "Relationships between intermetallic compound structure and hydride formation," *J. Common Met.*, vol. 78, no. 1, pp. 119–138, 1981.

[21]   Z. Dehouche, M. Savard, F. Laurencelle, and J. Goyette, "Ti–V–Mn based alloys for hydrogen compression system," *J. Alloys Compd.*, vol. 400, no. 1–2, pp. 276–280, Sep. 2005.

[22]   K. Morii and T. Shimizu, "Hydriding characteristics in (Ti, Zr)(Ni, Mn, X) 2 alloys," *J. Alloys Compd.*, vol. 231, no. 1–2, pp. 524–527, 1995.

[23]   D. G. Ivey and D. O. Northwood, "Storing Hydrogen in AB2 Laves-Type Compounds*," *Z. Für Phys. Chem.*, vol. 147, no. 1_2, pp. 191–209, 1986.

[24]   M. T. Hagström, S. N. Klyamkin, and P. D. Lund, "Effect of substitution on hysteresis in some high-pressure AB2 and AB5 metal hydrides," *J. Alloys Compd.*, vol. 293, pp. 67–73, 1999.

[25]   K. Young, T. Ouchi, and M. A. Fetcenko, "Pressure–composition–temperature hysteresis in C14 Laves phase alloys: Part 1. Simple ternary alloys," *J. Alloys Compd.*, vol. 480, no. 2, pp. 428–433, Jul. 2009.

[26]   S. Qian and D. O. Northwood, "Hysteresis in metal-hydrogen systems: a critical review of the experimental observations and theoretical models," *Int. J. Hydrog. Energy*, vol. 13, no. 1, pp. 25–35, 1988.

[27]   C.-N. Park, S. Luo, and T. B. Flanagan, "Analysis of sloping plateaux in alloys and intermetallic hydrides," *J. Alloys Compd.*, vol. 384, no. 1–2, pp. 203–207, Dec. 2004.

[28] R. D. Doherty, E. A. Feest, and K. Holm, "Dendritic solidification of Cu-Ni alloys: Part I. Initial growth of dendrite structure," *Metall. Mater. Trans. B*, vol. 4, pp. 115–124, 1973.

[29] Y. Shudo, T. Ebisawa, and H. Itoh, "Characterization of Ti–Zr–Mn–V-based Laves phase alloys for MH refrigeration system," *J. Alloys Compd.*, vol. 356, pp. 497–500, 2003.

[30] M. Ron, "The normalized pressure dependence method for the evaluation of kinetic rates of metal hydride formation/decomposition," *J. Alloys Compd.*, vol. 283, no. 1–2, pp. 178–191, 1999.

[31] J. D. Hancock and J. H. Sharp, "Method of comparing solid-state kinetic data and its application to the decomposition of kaolinite, brucite, and BaCO3," *J. Am. Ceram. Soc.*, vol. 55, no. 2, pp. 74–77, 1972.

[32] J. H. Sharp, G. W. Brindley, and B. N. Narahari Achar, "Numerical Data for Some Commonly Used Solid State Reaction Equations," *J. Am. Ceram. Soc.*, vol. 49, no. 7, pp. 379–382, 1965.

[33] T. Forde, J. Maehlen, V. Yartys, M. Lototsky, and H. Uchida, "Influence of intrinsic hydrogenation/dehydrogenation kinetics on the dynamic behaviour of metal hydrides: A semi-empirical model and its verification," *Int. J. Hydrog. Energy*, vol. 32, no. 8, pp. 1041–1049, Jun. 2007.

[34] C. Morales *et al.*, "On the van der Pauw's method applied to the measurement of low thermal conductivity materials," *Rev. Sci. Instrum.*, vol. 87, no. 8, p. 084902, Aug. 2016.

[35] M. R. Gopal and S. S. Murthy, "Studies on heat and mass transfer in metal hydride beds," *Int. J. Hydrog. Energy*, vol. 20, no. 11, pp. 911–917, 1995.

[36] S. S. Murthy, "Heat and mass transfer in solid state hydrogen storage: a review," *J. Heat Transf.*, vol. 134, no. 3, p. 031020, 2012.

[37] E. Suissa, I. Jacob, and Z. Hadari, "Experimental measurements and general conclusions on the effective thermal conductivity of powdered metal hydrides," *J. Common Met.*, vol. 104, no. 2, pp. 287–295, 1984.

[38] J.-M. Joubert, M. Latroche, R. Černỳ, R. C. Bowman Jr, A. Percheron-Guégan, and K. Yvon, "Crystallographic study of LaNi5- xSnx (0.2≤ x≤ 0.5) compounds and their hydrides," *J. Alloys Compd.*, vol. 293, pp. 124–129, 1999.

[39] V. Iosub, M. Latroche, J.-M. Joubert, and A. Percheron-Guégan, "Optimisation of MmNi5-xSnx (Mm=La, Ce, Nd and Pr, 0.27<x<0.5) compositions as hydrogen storage materials," *Int. J. Hydrog. Energy*, vol. 31, no. 1, pp. 101–108, 2006.

[40] S. Luo, W. Luo, J. D. Clewley, T. B. Flanagan, and L. A. Wade, "Thermodynamic studies of the LaNi5- xSnx-H system from x= 0 to 0.5," *J. Alloys Compd.*, vol. 231, no. 1–2, pp. 467–472, 1995.

[41] Y. Pang and Q. Li, "A review on kinetic models and corresponding analysis methods for hydrogen storage materials," *Int. J. Hydrog. Energy*, vol. 41, no. 40, pp. 18072–18087, Oct. 2016.

[42] J. F. Fernandez and C. R. Sanchez, "Rate determining step in the absorption and desorption of hydrogen by magnesium," *J. Alloys Compd.*, vol. 340, no. 1–2, pp. 189–198, 2002.

[43] D. Richter, R. Hempelmann, and R. C. Bowman, "Dynamics of hydrogen in intermetallic hydrides," in *Hydrogen in Intermetallic Compunds II*, Springer, 1992, pp. 97–163.

[44] S. Luo, W. Luo, J. D. Clewley, T. B. Flanagan, and R. C. Bowman Jr, "Thermodynamic and degradation studies of LaNi4. 8Sn0. 2-H using isotherms and calorimetry," *J. Alloys Compd.*, vol. 231, no. 1–2, pp. 473–478, 1995.

[45] R. C. Bowman, C. A. Lindensmith, S. Luo, T. B. Flanagan, and T. Vogt, "Degradation behavior of LaNi5−xSnxHz (x=0.20–0.25) at elevated temperatures," *J. Alloys Compd.*, vol. 330–332, pp. 271–275, 2002.

[46] S. Luo, J. D. Clewley, T. B. Flanagan, R. C. Bowman, and L. A. Wade, "Further studies of the isotherms of LaNi5−xSnx–H for x=0–0.5," *J. Alloys Compd.*, vol. 267, no. 1–2, pp. 171–181, 1998.

[47] M. R. Rahimpour, F. Samimi, A. Babapoor, T. Tohidian, and S. Mohebi, "Palladium membranes applications in reaction systems for hydrogen separation and purification: A review," *Chem. Eng. Process. Process Intensif.*, vol. 121, pp. 24–49, Nov. 2017.

[48] N. Kosinov, J. Gascon, F. Kapteijn, and E. J. M. Hensen, "Recent developments in zeolite membranes for gas separation," *J. Membr. Sci.*, vol. 499, pp. 65–79, Feb. 2016.

Chapter 4. Mechanical properties of a low pressure AB$_2$ C14 laves phase compound: Hydride breathing and particle size evolution

4.1. Introduction

In an optimal design of MHHC two key features to consider are the shape-optimization of the vessel to improve its heat exchange, and, the quantity of hydride that can be introduce in order to have a greater amount of hydrogen to compress and reduce the dead space [1, 2]. However, stresses have a major impact on the integrity of the system, specially, when a container is filled with a large quantity of hydride and the volume expansion due to hydrogenation creates stresses on the container, and/or, when the hydride powder bed have a slender geometry that could increase its stress at the bottom of the container vessel (e.g. a vertical container) [3-5]. As a result, it becomes extremely important to know beforehand the mechanical behavior of the hydride in order to design the optimal geometry and account for the quantity of mass that can be inside of an hydride container without causing any structural damage [1, 6, 7].

In this chapter the mechanical properties of a lower pressure AB_2-type hydride at three different levels of stress is experimentally studied. Specifically, to perform an analysis of the mechanical behavior of the hydride, an evolution of the relative swelling of the grains and of the powder bed should be developed. Hence, at each level of stress, several absorption-desorption hydrogenation cycles have been applied to the hydride until it reaches semi-stabilization in the change of the hydride volume. The variation in the volume will determine how is the global behavior of the powder bed with the vessel and how the powder grains rearrange in the stack.

4.2. Detail description of the mechanical experiments

The three mechanical experiments were done with a combination of the induction melted samples BNI described in chapter 3, considering that the quantity of mass need for all the experiments was more than 100 gr. In particular the samples used were BNI1 ($Ti_{0.83(2)}Zr_{0.17(2)}Mn_{1.48(4)}V_{0.31(2)}$) and BNI2 ($Ti_{0.85(2)}Zr_{0.15(2)}Mn_{1.35(2)}V_{0.30(2)}$) altogether in a mass proportion of 60% (BNI1) and 40% (BNI2), and with lattice parameters a= 4.9219(1) (Å), c=8.0684(2) (Å), V=169.27(1) (Å^3), and, a= 4.9211(1) (Å), c=8.0693(2) (Å), V=169.24(1) (Å^3), respectively. (specific values of each alloy for composition and lattice parameters are given in Annex 3).

Then the three samples were taken in order to measure, in each one, a different level of stress in hydrogenation and dehydrogenation stages. The samples were crushed and sieved below 1.25 mm from the mixture of the alloys mentioned. Then they were set in the cylindrical test cell, where the three springs were placed over to simulate the effect that a hydride in contact with its container walls can produce. The main parameters of each experiment can be seen at Table 16.

Table 16. Main parameters of the hydride breathing test [8]

Test sample	1	2	3
Spring stiffness [N/mm]	0.28(2)	1.96(4)	20.72(2)
Mean axial stress [MPa]	0.0325(1)	0.12(1)	0.84(1)
Mass (gr)	45.28(1)	45.08(1)	45.33(1)
Volume (powder mass + voids) in the cell (cm^3)	12.3(9)	12.0(9)	11.9(9)
Bulk density (Initial powder mass / Volume in the cell) (gr/ cm^3)	3.680(3)	3.762(3)	3.808(3)
Volume occupied by the solid mass in the cell (cm^3)	7.00(1)	6.97(1)	7.00(1)
Initial packing fraction (%)	57	58	59

The free volume of the whole test bench and the pressure vessel have been measured with no sample, by using the mass flow meters integration (respectively 0.194 l and 0.283 l). Then, the volume of the parts and the sample introduced in the vessel has been subtracted from the vessel volume. Hence, the mass of gas inside the test bench and the vessel can be deduced from the pressure measurement, using a real H_2 gas EOS [9].
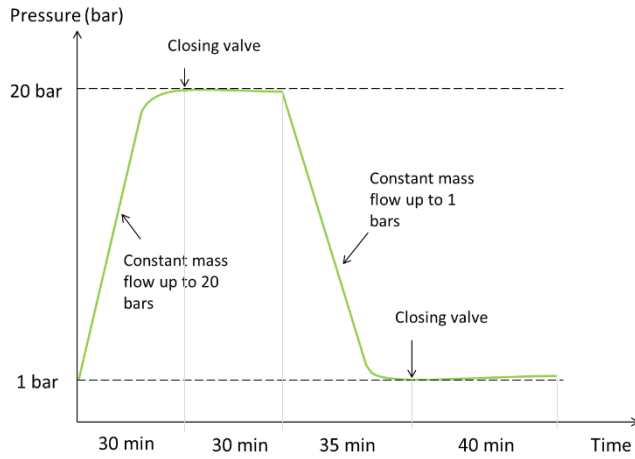
Fig.57. Time profile of each automatic complete cycle

Finally, the experiments were performed from the activation of the sample in the first cycle until approximately 100 cycles, where each cycle lasted 2.25 hours. Each cycle consisted in a hydrogenation step (up to 20 bar) for 60 minutes and a further dehydrogenation step (up to 1 bar) for 75 minutes. This desorption pressure was designated to avoid a vacuum inside the experimental cell that could change abruptly the position of the inner parts, also, the absorption pressure was designed to achieve the beta phase at the temperature define by the thermodynamics of the material.

Before the analysis of the different hydride breathing experiments, some operational parameters must be considered. Specifically, the thermodynamic behavior of the alloy was determined to design the temperature and absorption pressure of the experiments during cycling. Fig.58 shows the P-c-I obtained for the combination of the BNI samples
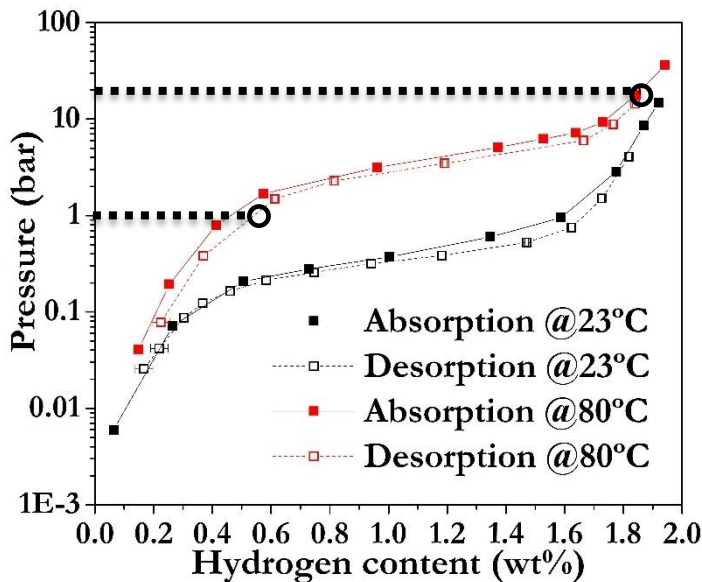
Fig.58. P-c-I of the BNI sample at 23 and 80°C

In the experiment, a temperature of 83(1)°C was finally used, based on the P-c-I at 80°C (Fig.58), were a desorption equilibrium pressure above 1 bar is reached, and also at this temperature, a pressure of 20 bar can achieve a composition in the β phase.

Likewise, the reversible capacity evolution between the absorption and desorption cycling points can be observed in Fig.59. for each experiment.
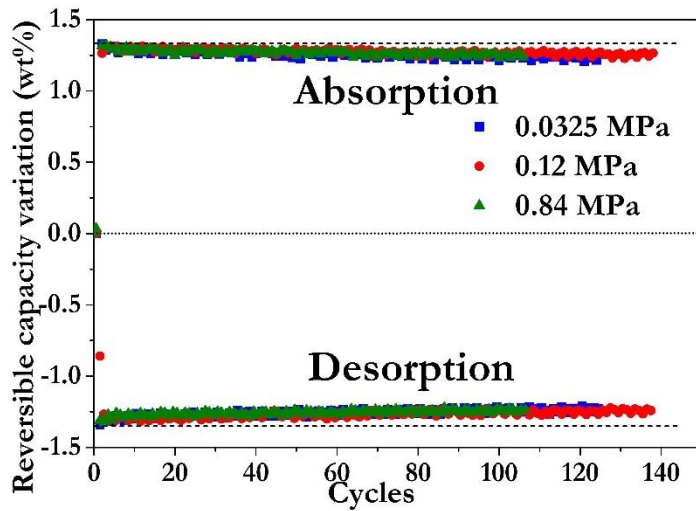
Fig.59. Hydrogen variation in the hydride through absorption and desorption cycles.

It can be observed that the reversible capacity for all the experiments have the same tendency, however it tends to diminish by 3% as cycles increases. This effect will be discussed afterwards with the development of the hydride breathing behavior.

4.3. Mechanical properties

To analyze the behavior and critical packing fraction that this material can evidence in the conditions of the experiments, first the variation of the axial stresses imposed to the MH bed have to be observed.
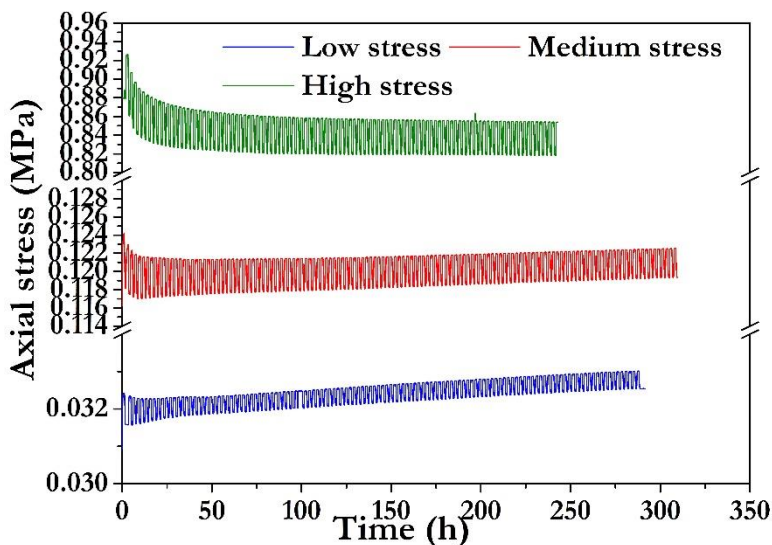
Fig.60. Axial stress evolution at each experiment

The axial stresses imposed on the contact surfaces of the MH beds have a constant value of 0.0325 MPa (blue), 0.12 MPa (red), and 0.84 MPa (green), for the lower-, medium- and high-pressure experiment, respectively. However, as observed in Fig.60, the variations in the general stress for each experiment depends also on the breathing behavior that the samples exhibit at the hydrogenation and dehydrogenation cycling. Also, the axial stresses are always larger during absorption. On the other hand, it is clear that as cycles increases the axial stress of the sample and their evolution are different for the three constant stresses applied. The next sections correlate those changes to aspects of the mechanical behavior of the hydride.

4.3.1. Change in the volume of the hydride

One of the main objectives of the study is to analyze the volume change that takes place in the hydride at the hydrogenation stages while the sample is subjected to different levels of stress. Therefore, in Fig.61 the volume change (Fig.61 a) and the volume variations (Fig.62 b, c and d) between absorption and desorption are presented for the different levels of axial stress (0.0325 MPa –blue-, 0.12 MPa –red-, and 0.84 MPa –green-), measured as a function

of the hydrogenation cycling. The volume variations ($\overline{\Delta Vr}$) were calculated as stated in [10, 11]:

$$\overline{\Delta Vr_{abs}} = \frac{V_H^i - V_D^i}{V_D^i} \qquad (35)$$

$$\overline{\Delta Vr_{des}} = \frac{V_H^i - V_D^{i+1}}{V_D^{i+1}} \qquad (36)$$

Where V_D^i is the volume at the beginning of the cycle just as absorption begins, V_H^i is the maximum volume of the cycle where absorption reached stabilization and V_D^{i+1} is the volume at the end of the cycle just as desorption finishes.
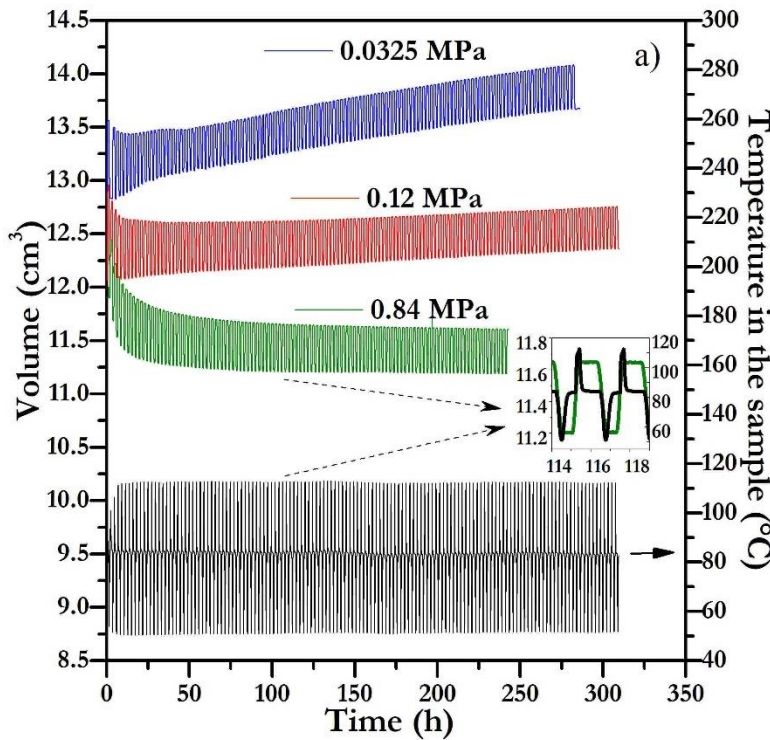
Fig.61. Volume and temperature change of the alloy during hydrogenation-dehydrogenation stages for the three levels of vertical stress: 0.0325 MPa (blue), 0.12 MPa (red), 0.84 MPa (green). Adapted from [8]

In Fig.61 it can be observed that the volume change of each sample is intrinsically associated to a temperature variation (Fig.61 bottom, black line and right vertical axis), which is as well related to the exothermic / endothermic reaction that takes place in the hydrogenation / dehydrogenation stages (inset graph in Fig.61). Furthermore, it is evident that the greater the stress applied to the sample, the lower the initial volume for a similar mass (Table 16), which is mainly due to a higher initial rearrangement of the powder bed as the initial axial stress rises. After that, different behaviors of the powder bed evolution can be observed at Fig.61. For the lower stress (0.0325 MPa), the tendency of the powder bed volume is to increase with time a 4.4 % in the hydride state. Similarly, for the medium stress (0.12 MPa), the volume of the powder bed is also swelling or increasing, but by a smaller amount, 0.4% after 308 cycles. Then, for the higher stress applied (0.84 MPa), the volume of the powder is clearly shrinking instead of swelling by a 6% in the hydride state.
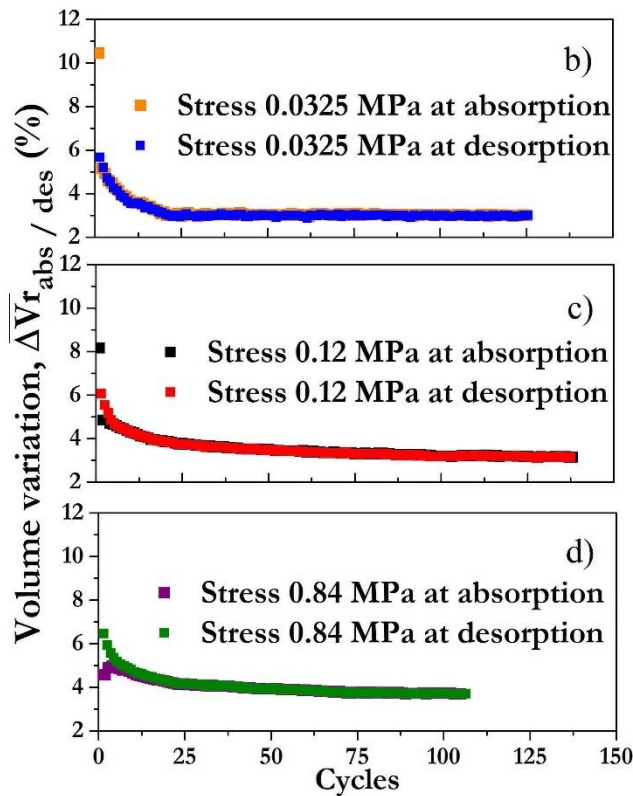
Fig.62. Volume variation between absorption and desorption ($\overline{\Delta Vr_{abs}}$ and $\overline{\Delta Vr_{des}}$) of the alloy as a function of hydrogen cycling for the stresses 0.0325 MPa (a), 0.12 MPa (b), and 0.84 MPa (c). Adapted from [8]

Fig. 62a, b and c evidence the volume variations at each cycle. For all the applied stresses, there is first a high decrease of the volume variation up to the 25th cycle (~50 h in Fig.61). This rapid evolution may be linked to the decrepitation process that is known to take place at early stages of cycling [12]. Similarly, in the case of the absorption, the initial volume variation tends to reduce as stresses increases (first cycle point of absorption in Fig.62 a-c), which can be explain by a greater initial rearrangement of the particles with a higher stress and also with a probable difficulty of these particles to expand easily during hydrogenation. For the second part of the evolution (after ~25 cycles), it is highly interesting that for the lower stress, the variations are quite constant, whereas for the medium and high applied stresses, the volume variation tends to decrease. This is remarkable, because on one hand, it has been checked that the absorption rate of hydrogen for each cycle is almost constant (Fig.59), meaning that the volume expansion of each particle remains also almost constant, while on the other hand, the volume variation of the bed keeps decreasing. As a result, it can be said that this particle volume variation finds a way to be more and more absorbed within the powder bed itself, i.e. particles find a better way to rearrange between other grains of the bed, specifically, within the volume occupied by porosity at each cycle. This kind of behavior has already been observed in [10].

These different behaviors may be explained by the several ways the powder grains can arrange under different applied stresses, considering that not only these pressures may restrain the mobility of the particle packing, but also that the decrepitation process seems to play a role in this evolution. The following part presents an analysis of the grain size distribution and the particle morphology.

4.3.2. Grain distribution

The grain distributions before and after the hydrogenation experiments with the three samples are shown in Fig.63a. Furthermore, Fig. 63b, c and d, evidence secondary (SE) and back scattered electron (BSE) images of the grains taken from the high stress sample after hydrogenation.
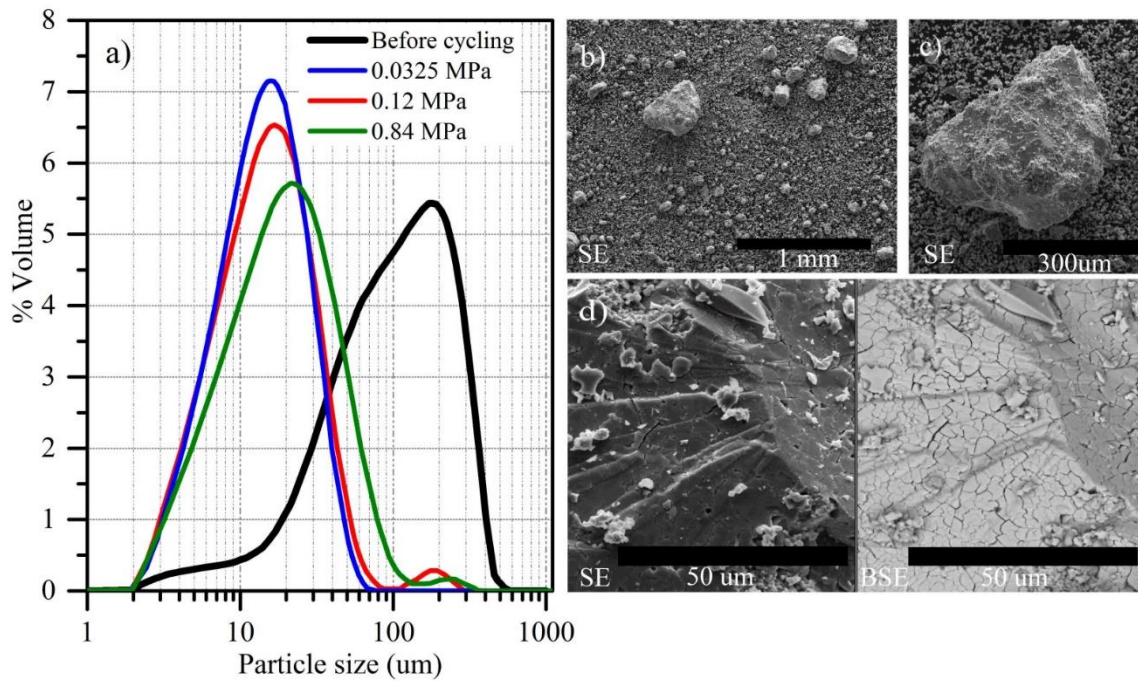
Fig.63. Grain size analysis a) Grain size distribution before and after hydrogenation cycles, b) SE image of grain sizes after hydrogenation with the higher stress sample, c) Zoom of the SE image over a big grain found in the higher stress sample after hydrogenation, d) SE and BSE images showing a fracture zone of the big particle found in the high stress sample [8]

Fig.63a shows a clear reduction in particle size after hydrogenation cycles for the three stresses applied. From an initial particle size of ~200 µm, a reduction by almost a factor of 10 in the particle size takes place due to a decrepitation phenomenon. The main particle size distribution is quite similar for the three stresses applied. However, as it can be evidenced in Fig.63b and c, the greater particles found in the high stress sample (but also in the medium one) are closely related to the smaller peaks of distribution at larger particle sizes.
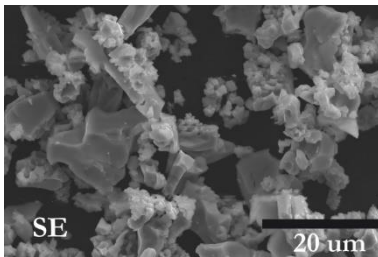
Fig.64. SE image of grain sizes after hydrogenation with the lower stress sample

In contrast, for the lower stress (Fig.64) an agglomeration of particles was evidence but without the partial densification found in the medium and high stress particles. As a result, a bimodal distribution of grains is created during hydrogenation cycles [7]. Likewise, something very important to highlight is the fact that these bigger grains are fractured in smaller fragments, but these fragments remained agglomerated during the hydrogenation cycling process, as evidenced in Fig.63d. Additionally, this phenomenon seems to be enhanced when high mechanical stress is applied, as if higher mechanical pressure was preventing particles from separation, and therefore the big particles become an assembly of smaller fragmented grains that remain nearly at the same place and position relative to each other.

Furthermore, the size distributions follow an increase tendency, where these distributions get broader as the stress is higher (lower > medium > high). This may be due to the presence of stronger agglomerates with intermediate sizes induced by the larger stress applied [7, 10].

4.3.3. Porosity evolution in the hydride bed

The volume evolution of the powder bed is mostly a question of rearrangement [7]. The rearrangement of the powder bed in the test cell may be analyzed through the study of the total volume evolution while swelling or shrinking is occurring. This volume (V_{bed}) is the addition of the volume of the particles ($V_{particles}$) and the porous volume ($V_{porosity}$) in the cell. Therefore, as the volume of the grain is changing during hydrogenation stages, an analysis of the variation in the porosity (ε) during the cycles may help to understand how the particles tend to rearrange in the test cell. The porosity can be defined as the volume of pores compared to the total volume occupied by the stack:

$$\varepsilon = \frac{V_{porosity}}{V_{bed}} = 1 - \frac{V_{particles}}{V_{bed}} \qquad (37)$$

Where $V_{particles}$ depends on a theoretical law of evolution of the swelling (S) that takes into account the crystallographic change after the hydrogenation stages [7]:

$$V_{particles} = V_0*(1+S) \qquad (38)$$

S can be obtained empirically from the following expression:

$$S = \left(\frac{V_{hd} - V_0}{V_0 * Wt_h}\right)*Wt_i \qquad (39)$$

$$V_0 = \frac{m}{\rho} \qquad (40)$$

Where Wt_i is the weight percentage of hydrogen in the alloy during the desorption stage or the absorption one and Wt_h is the weight percentage of hydrogen in the alloy at the beta phase, at 20 bar in Fig.58.), Vo is the initial volume of the sample at each stress applied [7, 13], which considers the mass in the test cell (Table 16) and the density before hydrogenation. V_{hd} in Eq.39 is the volume in the hydrogenated state and was estimated using the density of the alloy after cycles of hydrogenation, as measured by XRPD and shown in Fig.36 section 3.2.3. of chapter 3. Furthermore, since both, the dehydrogenated and the hydrogenated compounds crystallize in the same phase (Fig.31 and Fig.36 of chapter 3), the theoretical swelling evolution of all the samples is a single linear evolution law, where the density evolution from the initial stage and the actual hydrogenated stage is the main parameter to be considered. Hence, the theoretical swelling (S) for the three stresses applied, has been calculated at absorption (20 bar) and for the samples without hydrogen, generating the following equations for this material:

$$S = 0.0784*Wt_i \qquad (41)$$

As a result, Fig.65 presents the evolution of the porosity at the three different stresses applied during all the cycles measured.
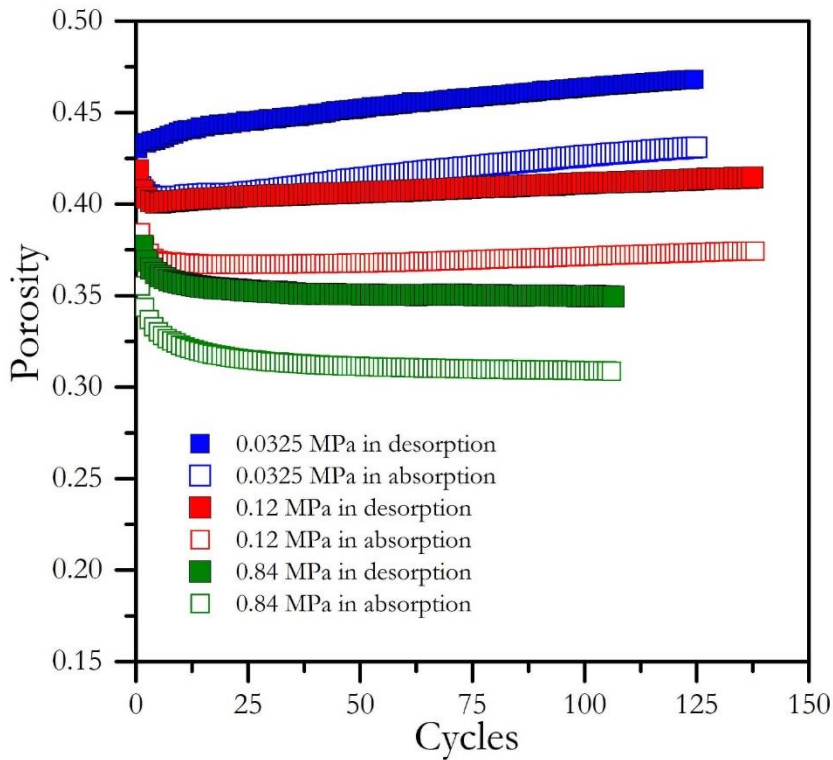
Fig.65. Porosity evolution at the three stress levels applied [8]

The porosity given in Fig.65 follows a similar trend than the one already discussed for the volume in Fig.61. However, some interesting aspects should be highlighted.

Firstly, these curves evidence that whatever the stress applied, the variation of porosity is the same between absorption and desorption. There is a decrease of porosity during absorption, and an increase during desorption. The volume increase of the grains during absorption is partly going to the free volume between particles, causing a decrease of porosity. When the particles shrinks during the subsequent desorption, some of the volume occupied by the particles becomes available to constitute porous volume, so the porosity increases again [7, 10, 13].

A larger stress applied implies a smaller initial porosity, due to a better initial particle arrangement. It can also be remark that the variation of porosity between hydrided and un-hydrided state is higher for higher applied stresses, as if the applied stress compels a better use of the available space in the free volume (i.e. the porosity), and therefore as cycles continues, the volume change of the particles is transferred gradually to the porous volume, in particular for higher stresses. This behavior is somehow remarkable, since for higher stresses, this free available volume (i.e. porosity) is lower than the one for lower stresses.

This fact can be ascertained by calculating the volume variations of the volume partition, as described before:

$$V_{bed} = V_{particles} + V_{porosity} \qquad (42)$$

The volume variation is divided by the mass of the sample to be able to compare the samples between each other:

$$\frac{\overline{\Delta Vr_{bed}}}{m} = \frac{\overline{\Delta Vr_{particles}}}{m} - \frac{\overline{\Delta Vr_{porosity}}}{m} \qquad (43)$$

90
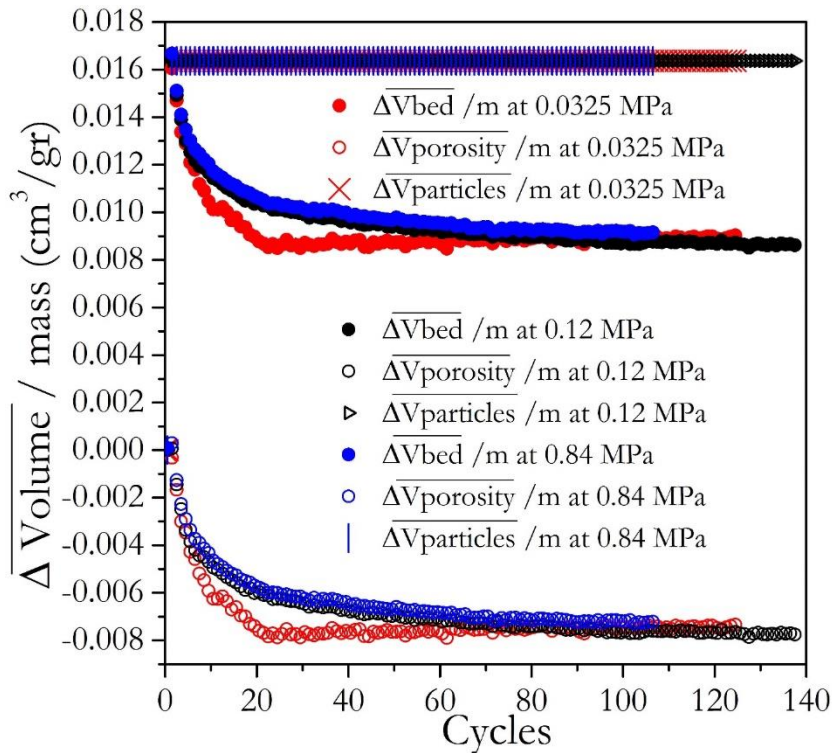
Fig.66. Partition of the volume variations per initial mass of the three samples during desorption cycles.

Eq. 43 was change (negative term in the porous volume variation) in order to present clearer the results of this partition in Fig. 66, where interesting results are shown. It can be observed that there is no volume variation of porosity for the first cycles in all the applied stresses. All the volume variation of the particles is converted to the volume variation of the global powder bed, as if the media was not compressible. Then the volume variation of the particles turns more and more into porous volume variation ($\overline{\Delta Vr_{porosity}}$). The evolution is fast at the beginning, then it slows down toward an asymptotic value. At the end, the variation of porosity nearly rejoins the variation of the powder bed, so that nearly half of the volume variation of the particles is absorbed in the volume between particles (i.e. the porosity). One thing to highlight is that the evolution of the volume variation of porosity is much faster for the lower applied stress, as if in the unconstraint case, the equilibrium of the partitions is reached faster.

4.4. Discussion

In general, the global behavior of a hydride powder bed during absorption and desorption of hydrogen cycling under an axial applied stress reveals that the volume of the samples reached different bulk densities after a certain amount of cycles, and this depends on the stress. For the larger stress, the bulk density of the sample is higher than for lower stresses. Compared to an initial bulk density (Table 16.), the sample exhibits a lower density for the lower stress, a quite similar density for the medium stress and a higher density for the higher applied stress. This can be seen clearly in Fig.67.
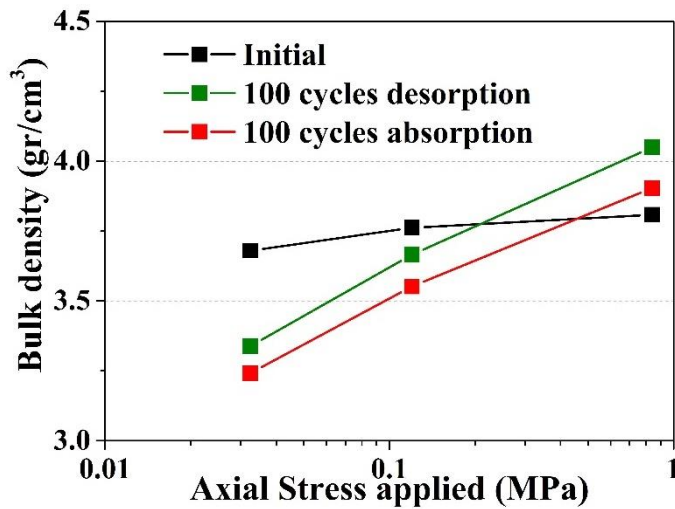
Fig.67. Effect of the axial stress applied in the bulk density of the powder bed at different hydrogenation stages: Initial (before hydrogenation) and after 100 cycles of H_2 absorption and desorption.

It has also been observed that the volume evolution is faster during the first 25 cycles, mainly due to the rapid decrepitation of the initial particles. Besides, it has been noticed that for higher applied stress levels, the particle distribution after cycling is broader than for lower stresses, and that big fragmented initial particles preserve their assembly from being fully shattered, as if small decrepitated fragments were all stick together, even though they are separated by fissures.

To interpret those behaviors, some typical granular media behavior can be mentioned. First, a granular media submitted to a stress or a movement tends to rearrange and depending on its initial state this granular media tends to densify or de-densify [14] (when de-densification occurs, the phenomenon is called dilatancy). Secondly, when particles tend to be small, the Van des Walls contact forces plays a more important role in the packing ability. For smaller particles and a given applied stress, the density of the powder packed bed is lower than for bigger particles. A non-negligible effect of the Van der Walls forces is commonly considered for particles under 10μm size, but this depends on the nature and morphology of the granular medium [15]. Thirdly, a bimodal or multimodal distribution of a powder bed will tend to be denser than a monomodal arrangement of particles [7]. It is important to remark, that this particle distribution can be spatially affected by segregation, as observed by Okumura et al. [3, 12]. Also, since the measurements of the present work were done on the global volume of the hydride sample, this phenomenon could not be evaluated. As a result, even though it is supposed that the phenomenological explanations exposed hereafter are still valid, the influence of segregation on these interpretations should be studied in deep by a further dedicated work.

Fourthly, mechanical stress may affect the particle integrity. In this study, the stress level is very low, but one could at least expect an effect on the particle integrity, or a destructive effect, i.e. a separation of the fragments of particles on the already fragmented particles, particularly for high stresses. This is not what was observed, on the contrary, for the high stress, the grain size analysis tends to show more big particles than for low stresses. This may be explained by the fact that for high applied stresses, the arrangement of particles is better (i.e. as observed the porosity is lower), so that the grains are better nested within the powder bed, (i.e. the big fragmented particles surrounded by smaller ones). Therefore, the stress is more uniformly distributed on the surface of these big particles, preventing them from being split away. This effect is also improved by the fact that the big particles made of smaller fragments, which kept their initial shapes and position, have some cohesion because of the Van der Wall sticking forces [14].

Fig. 68. Particles after hydrogenation experiment. Inset figure in red frame is a zoom of agglomerated particles

This cohesion effect can also be supported by the observed tendency in all the hydrogenated AB₂-type alloys after a regular P-c-I, where the decrepitated material tends to agglomerate at the bottom of the vessel (Fig.68), especially if is a vertical one. Considering this, an horizontal vessel design have a greater advantage since gravity will not aid to the segregation of decrepitated particles [16].

Also, the reduction in the reversible capacity of the hydride can be attributed to a localized agglomeration of the alloy at the bottom of the container, due to this rearrangement effect at the bottom of the vessel as hydrogenation cycles increases. Nevertheless, this localized agglomeration does not become densification up to a critical packing fraction promoted by the axial stress applied [4].

Thus, the higher density observed for the higher applied stress may be explained by the more pronounced multimodal state of the particles sizes observed for higher applied stresses. Likewise, this can be explained by the higher applied stress itself, as it has been recalled previously, that applying a stress on a granular media is conducting to higher density of the powder bed.

Those two effects lead to the same conclusion: the higher the stress, the higher is the density of the breathing granular media, where each level of applied stress correspond to a density, as plotted in Fig.67. To confirm these conclusions, and particularly determine which part of the densification can be attributed to the multimodal effect, and which part is attributed to the natural tendency of the granular medium to densify under stress, some modelling by the discrete element method could be used as initiated in [5]. This method permits to artificially block one mechanism versus another and observe the effect it has on densification.

It has also been observed that the density seems to evolve toward a steady value, even if not reached completely for all the values of applied stresses in this study.

Concerning the final density state of the granular media under a certain applied stress, there may be a kind of equilibrium between the movement forced by the particle during the swelling and shrinking cycling stages and the axial applied stress. For the constantly generated disorder brought by the breathing phenomenon of each grain, the applied stress will somehow contain this movement at a certain level. The higher the stress, the higher the movement is contained, and the higher is the equilibrium density.

Fig.67 evidence the density obtained during 100 cycles, where a steady state has not been reached for all the stress levels, but at least the density values can be compared for this particular state. It was observed that according to the mechanical stress applied, the final density will end up to a lower or higher value compared to the initial value. A higher stress applied is conducting to a higher densification. The results obtained in this study are showing a threshold on the applied stress, leading to a densification or de-densification compared to the initial density. This was not observed for the results obtained by B. Charlas et al. [7], where only densification was observed, nor the result of Matsushita et al. [11], where only de-densification was observed. For the particular powder and the particular stresses applied

in this study, both regimes have been observed and the threshold exists. This threshold may exist as well for the results of Charlas et al. or Matsushita et al. but the explored conditions did not permit to evidence it. Specifically, for the medium stress sample in desorption, a safety factor due to the packing fraction in hydrogenated state was calculated to be ~65%, in other words, an initial packing fraction of 58% (0.12 MPa) will not cause densification as evidenced in Fig.67. Also for these values, an average porosity of 0.4 can be evidence, which will be taken as an input for simulations. The difference of behavior observed between different kinds of hydrides is probably linked to the particles morphology and nature, and this work confirms that there is not a universal breathing behavior.

Finally, as a perspective to future works, it would be interesting to study the influence of the initial state, for instance by pre-densifying the sample before starting to cycle, in order to observe if the sample´s density converge toward the same equilibrium point, or if there is a history influence of the initial applied stress.

4.5. Achievements and partial conclusions

1. New inner parts of the hydride breathing test cell (COMEDHY) has been designed, constructed and set up to successfully measure the effect that several stresses on the mechanical properties of hydrides can have with small quantities of material.

2. The AB_2-type hydride breathing measurements under several applied stresses has revealed that depending on the stress level, densification or de-densification can occur compared to the initial non- decrepitated state. This alloy generates an increase of the volume and porosity after several hydrogenation cycles for a low and medium axial stresses, while for a high stress the hydride powder bed globally shrinks. It seems that a kind of equilibrium is installing between the applied stress and the cyclic breathing movement of the powder bed, once the decrepitation effect is reduced after a few tens of cycles. This equilibrium corresponds to a particular density and is much lower for the low stress level.

3. At early stage of cycling, the volume variation of the grains is fully transferred to the global volume variation, i.e. the powder bed level, and then, a part of this grain volume variation is transferred to the porosity. At the end, porosity is taking nearly half of the grain volume variation, independently of the applied stress. All of these goes along with the fact that the porosity is always higher in the desorbed state.

4. The volume and porous evolutions are linked to the decrepitation and rearrangement mechanisms. The decrepitation process reduced greatly the size of the particles. However, higher axial stresses contain bigger agglomerates, which seems to be small decrepitated particles not fully separated from its initial non-decrepitated grain. This broaden the grain size distribution and increases the densification of the powder bed.

5. Important parameters for the simulation such as the safety factor due to hydrogenated packing fraction with a value of ~65% and the evolution of the porosity with an approximate value of 0.4 were determined properly.

6. The use of a horizontal reactor design will help to reduce the agglomeration and possible densification with hydrogenation cycling

4.6. References

[1] M. V. Lototskyy, V. A. Yartys, B. G. Pollet, and R. C. Bowman, "Metal hydride hydrogen compressors: A review," *Int. J. Hydrog. Energy*, vol. 39, no. 11, pp. 5818–5851, Apr. 2014.

[2] M. M. H. Bhuiya, A. Kumar, and K. J. Kim, "Metal hydrides in engineering systems, processes, and devices: A review of non-storage applications," *Int. J. Hydrog. Energy*, vol. 40, no. 5, pp. 2231–2247, Feb. 2015.

[3] M. Okumura *et al.*, "Investigation of wall stress development and packing ratio distribution in the metal hydride reactor," *Int. J. Hydrog. Energy*, vol. 37, no. 8, pp. 6686–6693, Apr. 2012.

[4] K. Nasako, Y. Ito, N. Hiro, and M. Osumi, "Stress on a reaction vessel by the swelling of a hydrogen absorbing alloy," *J. Alloys Compd.*, vol. 264, no. 1, pp. 271–276, 1998.

[5] B. Charlas, F. Kneib, O. Gillia, D. Imbault, and P. Doremus, "A tool for modelling the breathing of hydride powder in its container while cyclically absorbing and desorbing hydrogen," *Int. J. Hydrog. Energy*, vol. 40, no. 5, pp. 2283–2294, Feb. 2015.

[6] F. Qin, "Pulverization, expansion of La0.6Y0.4Ni4.8Mn0.2 during hydrogen absorption–desorption cycles and their influences in thin-wall reactors," *Int. J. Hydrog. Energy*, vol. 33, no. 2, pp. 709–717, Jan. 2008.

[7] B. Charlas, O. Gillia, P. Doremus, and D. Imbault, "Experimental investigation of the swelling/shrinkage of a hydride bed in a cell during hydrogen absorption/desorption cycles," *Int. J. Hydrog. Energy*, vol. 37, no. 21, pp. 16031–16041, Nov. 2012.

[8] A. R. Galvis Escobar, A. Chaise, V. Iosub, B. Salque, J. F. Fernandez, and O. Gillia, "Stress effect on the swelling/shrinking behavior of an AB2 alloy during hydrogenation cycles," *Int. J. Hydrog. Energy*, vol. 42, no. 35, pp. 22422–22431, Aug. 2017.

[9] J. W. Leachman, R. T. Jacobsen, S. G. Penoncello, and E. W. Lemmon, "Fundamental Equations of State for Parahydrogen, Normal Hydrogen, and Orthohydrogen," *J. Phys. Chem. Ref. Data*, vol. 38, no. 3, pp. 721–748, Sep. 2009.

[10] B. Charlas, A. Chaise, O. Gillia, P. Doremus, and D. Imbault, "Investigation of hydride powder bed swelling and shrinking during hydrogen absorption/desorption cycles under different compressive stresses," *J. Alloys Compd.*, vol. 580, pp. S149–S152, Dec. 2013.

[11] M. Matsushita, M. Monde, and Y. Mitsutake, "Experimental formula for estimating porosity in a metal hydride packed bed," *Int. J. Hydrog. Energy*, vol. 38, no. 17, pp. 7056–7064, Jun. 2013.

[12] M. Okumura, A. Ikado, Y. Saito, H. Aoki, T. Miura, and Y. Kawakami, "Pulverization mechanism of hydrogen storage alloys on microscale packing structure," *Int. J. Hydrog. Energy*, vol. 37, no. 14, pp. 10715–10723, Jul. 2012.

[13] B. Salque *et al.*, "Measure of the hydride breathing while cyclically absorbing and desorbing hydrogen," *J. Alloys Compd.*, vol. 645, pp. S353–S356, Oct. 2015.

[14] P. R. Brewin, Ed., *Modelling of powder die compaction*. London: Springer, 2008.

[15] Visser J, "Van der Waals and other cohesive forces affecting powder fluidization," *Powder Technol.*, vol. 58, no. 1, pp. 1–10, 1989.

[16] C. Na Ranong *et al.*, "Concept, Design and Manufacture of a Prototype Hydrogen Storage Tank Based on Sodium Alanate," *Chem. Eng. Technol.*, vol. 32, no. 8, pp. 1154–1163, Aug. 2009.

Chapter 5. Thermodynamic simulations: A semi-empirical approach to the design of the MHHC system

5.1. Introduction

Several approaches have been followed to enhance MHHC performances [1]. As mentioned in chapter 1, simulations are particularly useful to predict and design hydrogen sorption systems such as Metal Hydride (MH) tanks and MHHC [2, 3]. To design a proper MHHC, an initial thermodynamic approach was implemented in Matlab®. The study was developed in different stages. First, the influence of several real H_2 gas EOS in the determination of a P-c-I, as well as, the effect of experimental thermodynamic features of the alloys (i.e. sloping plateau, hysteresis) were analyzed to select and validate the respective models used. Then, an algorithm that considers the selected thermodynamic models and real H_2 gas EOS is implemented to define and optimize some parameters of the MHHC system (i.e., volume and alloy mass of each stage) to deliver the greatest quantity of hydrogen compressed at the highest compression ratio. Finally, a second algorithm was developed to study the behavior of a three stage MHHC, based on the previous design and some real data from an experimental system that will be deeply discussed in the last chapter of this work. In all the simulations, just the AB_2-type alloys were employed, considering the results and analysis done in chapter 3.

5.2. Validation of the models
5.2.1. H_2 gas EOS

First, as described in chapter 2, due to a good agreement with experimental data and simplicity in the model equation, the Joubert EOS [4] was selected between other H_2 gas real EOS to be implemented in the algorithm. An additional validation was done between this model and the ideal one, considering just the determination of the P-c-I curves as a validation parameter. In Fig.69, a comparison between the determination of a P_h (B9) and a P_l (BN1-2-5) alloy has been performed with the two EOS.
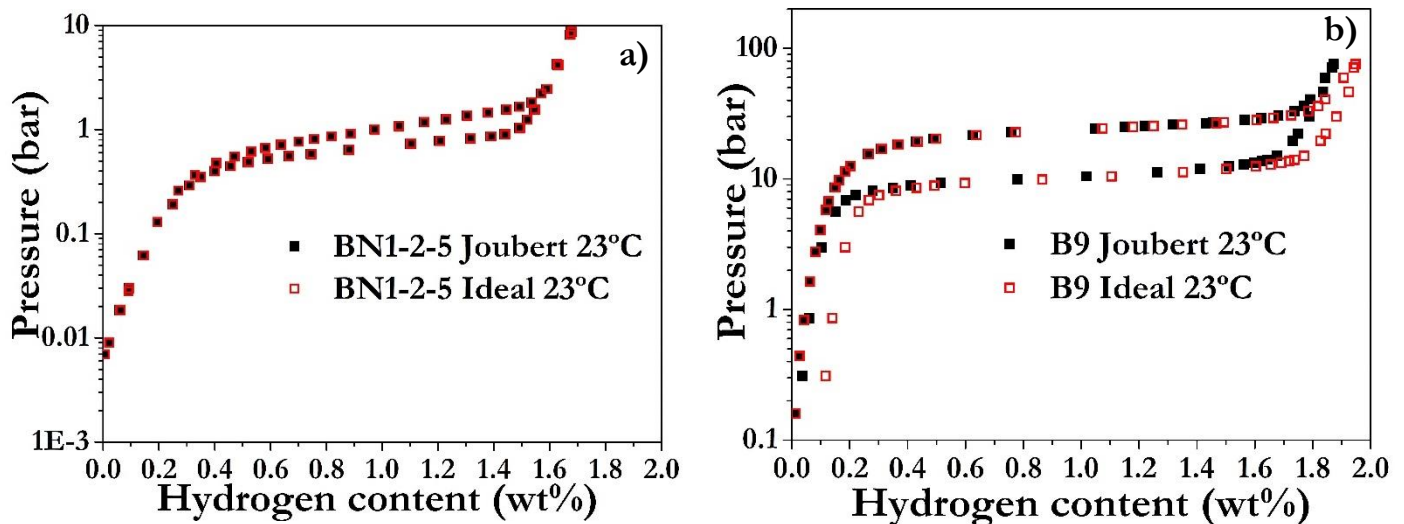
Fig.69. Comparison between ideal EOS and Joubert EOS in a low and high pressure alloy, a) BN1-2-5, b) B9

As observed in Fig.69, the ideal H_2 gas EOS increases the error in the determination of the P-c-I curves, especially at higher P_{eq} (Fig.69b). Since the P-c-I´s are an important input of the thermodynamic simulations, using the proper model is a key fact. Then, having the Joubert EOS and the Fang-Zhou model [5] selected and discussed in section 2.4.2 of chapter 2, the next step was to analyze the difference between using a thermodynamic model that considers the experimental features of the P-c-I curves and one that does not.

5.2.2. Effect of the sloping plateau and hysteresis in a first stage MHHC

In former studies [1] the importance of using the experimental features of the P-c-I curves has been schematically analyzed, however, approximations like flat plateau and no hysteresis were not directly compared with thermodynamic experimental features of real alloys. Through this analysis, the effect of implementing the experimental features of the P-c-I curves instead of "ideal" approximations will be described, considering the operation of a first stage MHHC with the BN1-1 alloy studied in chapter 3. The parameter to be enhance were the CR and the H_2 moles compressed (n_c) to a V_{ext}. In Fig.70, a scheme of the steps followed to develop the study can be observe. In the scheme, the steps followed represents the following: a-b) there is an initial pressure (P_{in}) that will achieve a full β_{min} composition in the hydride at a $T_l=296$ K (23°C) and when this composition is reached the valve is close to isolate VSt1, c) heat is impose to the system to dehydrogenate the alloy at a $T_h=353$ K (80°C) with the connection valve between VSt1 and V_{ext} close, d) The valve is open, there is an expansion of gas to V_{ext} and the T_h remains, e) the valve is close and VSt1 cools down to T_l.
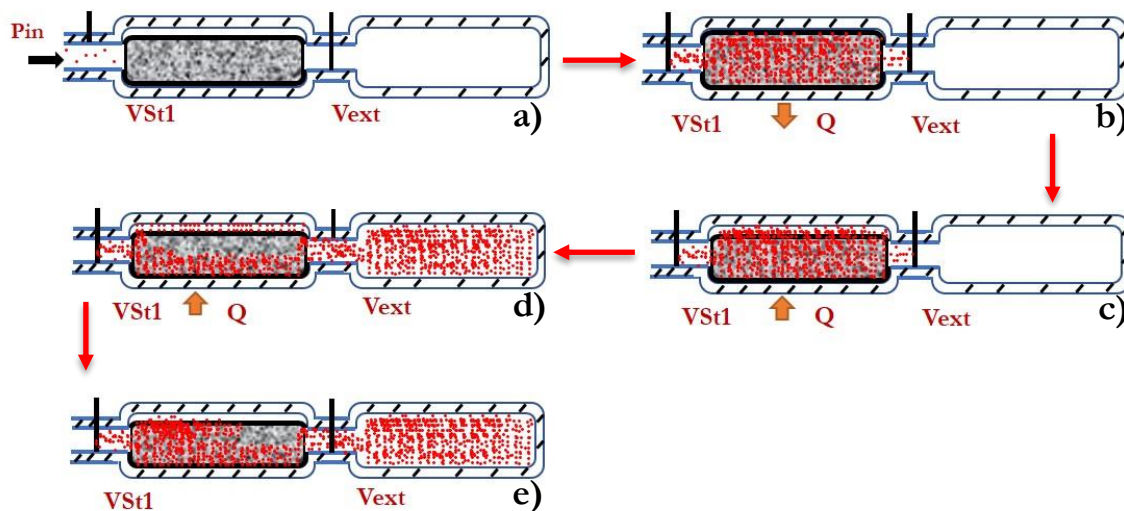
Fig.70. Scheme of the steps follow to evaluate the effect of experimental thermodynamic features in a first stage MHHC, a-e are explained in the text

Also, for the simulations some assumptions and procedures were taken:
1. Two extreme cases were evaluated: one closer to reality with sloping plateau and hysteresis and a second one more "ideal" with flat plateau and no hysteresis.
2. A 58% of hydrogenated packing fraction is used. This study was performed before the mechanical properties analysis presented in chapter 4.
3. The flat plateau curve was generated by assuming that the mid-concentration point at the plateau zone was the same for sloping and flat plateau curves
4. Both curves have the same thermodynamic properties (enthalpy and entropy), and approximately the same reversible capacity
5. The initial pressure has to be different for the two models, $P_{in}=4$ bar for sloping plateau, and $P_{in}=1.5$ bar for flat plateau. In both cases the selected pressure is the one that allows to achieve the β_{min} composition
6. A stablished constant VSt1= 30 cm^3 and its related mass of 98.3 gr taking into account the hydrogenated packing fraction selected.
7. The effect of V_{ext} on the results of the simulation was analyzed.

Then, the Fang-Zhou model coefficients (Eq. 16, chapter 2) found with the fit of the experimental (realistic) and flat plateau curves at 23 and 80°C can be seen in Table 17. Also,

in Fig.71 the O.P. of each stage described in the scheme of Fig.70 can be seen for the experimental and flat plateau curves.

Table 17. Coefficients found with the Fang-Zhou thermodynamic model. ΔH and ΔS in kJ/mol and J/k mol, respectively.

	Experimental				Flat plateau			
	x_1	x_2	x_3	x_4	x_1	x_2	x_3	x_4
α_abs	6.85E-5	1.064	-4000	-21.95	3.50E-3	1.022	-100	-12.15
β_abs	0.57	0.1	-1000	-23	0.87	0.082	-150	-17.4
α_des	2.10E-3	1.145	1E-8	-13.3	1.00E-2	0.9	1E-8	-11.25
β_des	0.49	0.208	2E-7	-12.5	0.83	0.127	2E-7	-11.6
	ΔH	ΔS	fs	k	ΔH	ΔS	fs	k
Plateau_abs	26.51	91	2.42	-1.25E-2	26.51	91	0	0
Plateau_des	28.66	93.5	2.03	-1E-7	28.66	93.5	0	0
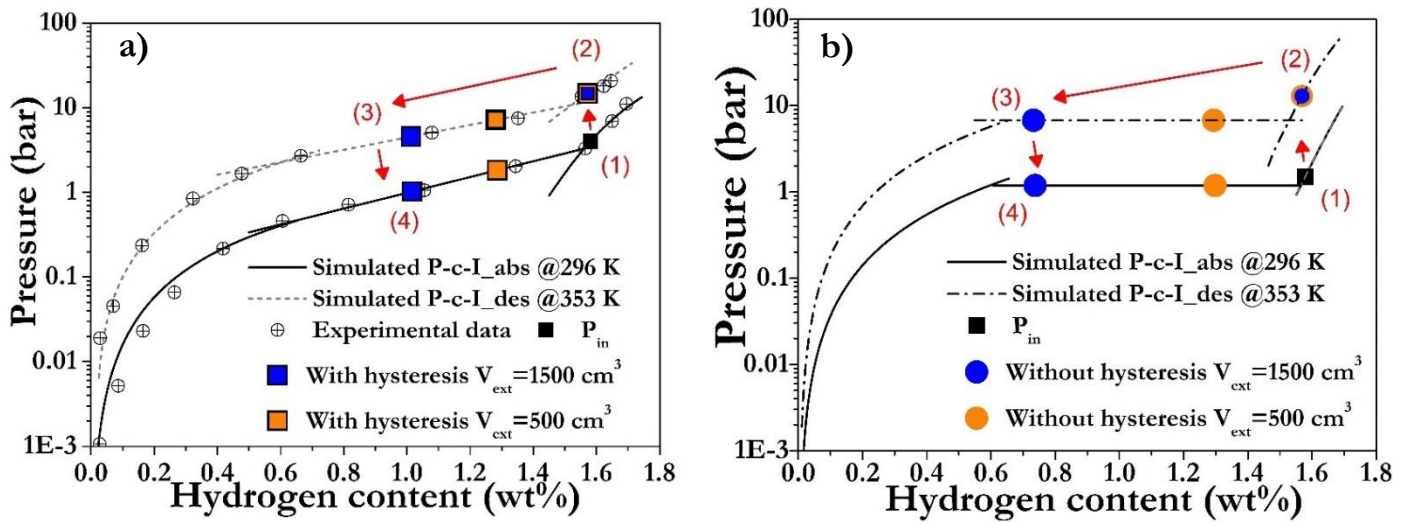
Fig.71. Simulation of a first stage MHHC between absorption (abs) at 23°C (296 K) and desorption (des) at 80°C (353 K), a) with sloping plateau and hysteresis, b) with flat plateau and no hysteresis

Fig.71 exhibit the O.P. of the steps mentioned for two different V_{ext} values. It can be seen clearly that the quantity of hydrogen desorbed is less for the realistic case as compared to the flat plateau one. Also, the P_{in} is lower in the case of a flat plateau because the pressure to achieve $β_{min}$ is also lower in contrast to the real experimental situation. Then, in Fig.72 the results of the CR and n_c for different V_{ext} can be observed.
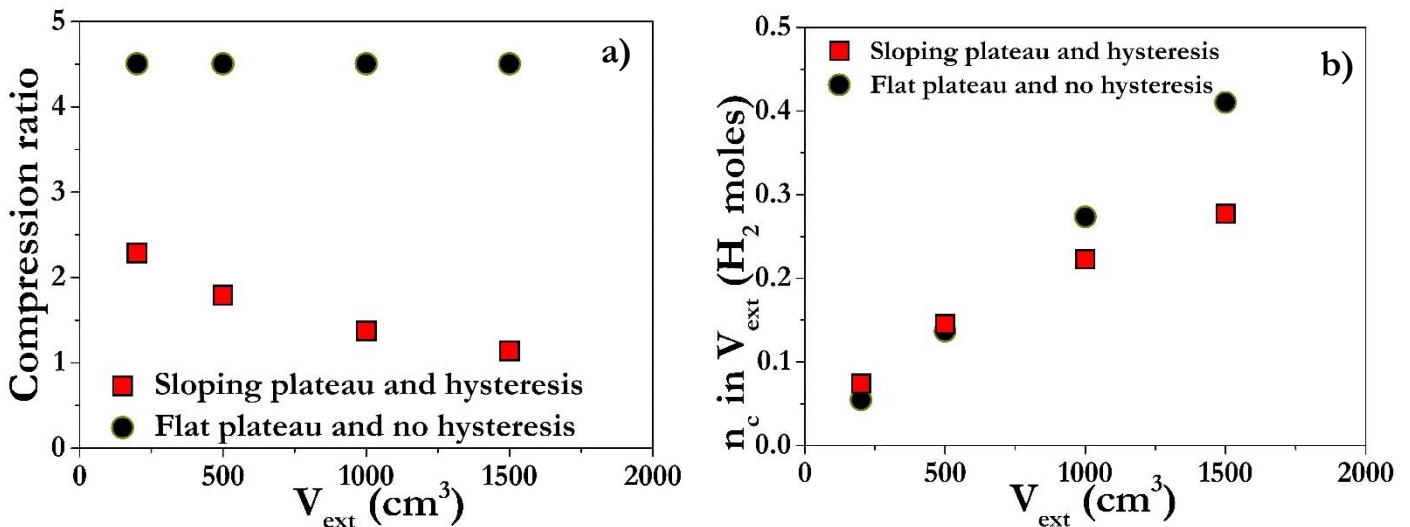
Fig.72. Main results comparison between the two extreme cases of analysis (sloping plateau-hysteresis and flat plateau-no hysteresis) at different V_{ext} values, a) CR, b) n_c.

Several aspects can be analyzed from the results obtained. First, the CR for the flat plateau-no hysteresis case show a constant tendency for all the V_{ext} evaluated, while for the sloping plateau the CR decreases as the external volume increases. This effect can be mainly explain by two facts: first, the change between the P_{in} and the final pressure at T_h is high in the case without hysteresis (black symbols in Fig.72a, higher CR), since the absorption and desorption pressures are the same in the plateau region, and second, a sloping plateau produces that the pressure at T_h changes with composition (red symbols in Fig.72a, lower CR), i.e. larger V_{ext} means less composition in the hydride and subsequent reduced final pressure, while for the flat plateau such pressure remains constant.

A similar tendency can be explain for n_c (Fig.72b), where as V_{ext} increases, a linear tendency is follow by the flat plateau-no hysteresis model (black symbols in Fig.72b), while for the sloping plateau one (red symbols in Fig.72b) this tendency decreases with higher external volumes, due to a higher decrease of pressure at T_h with lower H_2 desorption (Fig.71a) that clearly reduces the quantity of moles that can be compressed in comparison with the moles that can be desorb at the same pressure (Fig.71b), like in the case of a flat plateau.

In resume, this analysis validates and highlights the need of realistic P-c-I models that account the experimental features of this curves for simulation of MHHC to get closer to reality, not only in thermodynamic simulations but also in a future heat and mass transfer modelling. Once, the H_2 gas EOS and P-c-I model have been validated, then the design of the three stage MHHC is performed as described in the following section

5.3. Design of an MHHC through thermodynamic simulations

Considering the methodology explained in chapter 2, the design of a three stage MHHC was developed. The alloys used were the BN1-2-5, BN2 and B9 as P_l, P_m and P_h alloys, respectively. Then, the Fang-Zhou model was implemented to find the respective coefficients of each zone in the P-c-I curves and with them simulate at different temperatures the behavior of the alloys in each stage. In Table 18, the coefficients found for each alloy with the Fang-Zhou model can be seen.

Table 18. Coefficients found with the Fang-Zhou thermodynamic model for the three alloys. ΔH and ΔS in kJ/mol and J/k mol, respectively.

|	BN1-2-5				BN2				B9			
	x_1	x_2	x_3	x_4	x_1	x_2	x_3	x_4	x_1	x_2	x_3	x_4
α_abs	0.006	1.117	916.7901	-10.306	0.0050	0.7709	-731.73	-10.894	0,0029	1,235	-46,44	-5,30
β_abs	0.847	0.0898	-749.946	-15.723	0.8215	0.0988	-85.10	-15.082	0,816	-0,013	4073,1	135,05
α_des	0.008	0.918	158.946	-11.255	0.0101	0.7560	-785.41	-8.972	0,0019	1,040	-128,75	-8,331
β_des	0.937	0.077	-766.89	-15.611	0.8704	0.070	-210.06	-20.736	0,9226	0,093	-60,50	-13,219
	ΔH	ΔS	fs	k	ΔH	ΔS	fs	k	ΔH	ΔS	fs	k
Plateau_abs	27.7	93.8	0.996	-0.0026	23.6	93.4	0.673	-9.73E-5	18.9	90,4	0,354	-4E-4
Plateau_des	31.8	104.1	0.682	-5.87E-5	28.1	104.7	0.691	5.36E-4	26.5	109,2	0,377	-0,0012

The values of the enthalpy and entropy in absorption and desorption found with the program are close to the experimental ones described in chapter 3 (BN1-2-5: ΔH_{abs}=28(2), ΔS_{abs}=96(2), ΔH_{des}=33(1), ΔS_{des}=107.8(0.1); BN2: ΔH_{abs}=24(1), ΔS_{abs}=94(1), ΔH_{des}=29(1), ΔS_{des}=108(3); B9: ΔH_{abs}=19.3(0.5), ΔS_{abs}=91.3(0.2), ΔH_{des}=27(1), ΔS_{des}=110(2)), ΔH and ΔS in kJ/mol and J/k mol, respectively. The fit obtained with the coefficients found, is implemented at the three experimental temperatures used for the experimental P-c-I determination and can be seen in Fig.73 for the three selected alloys (red (23ºC), orange (50ºC) and black (80ºC) lines in Fig.73).
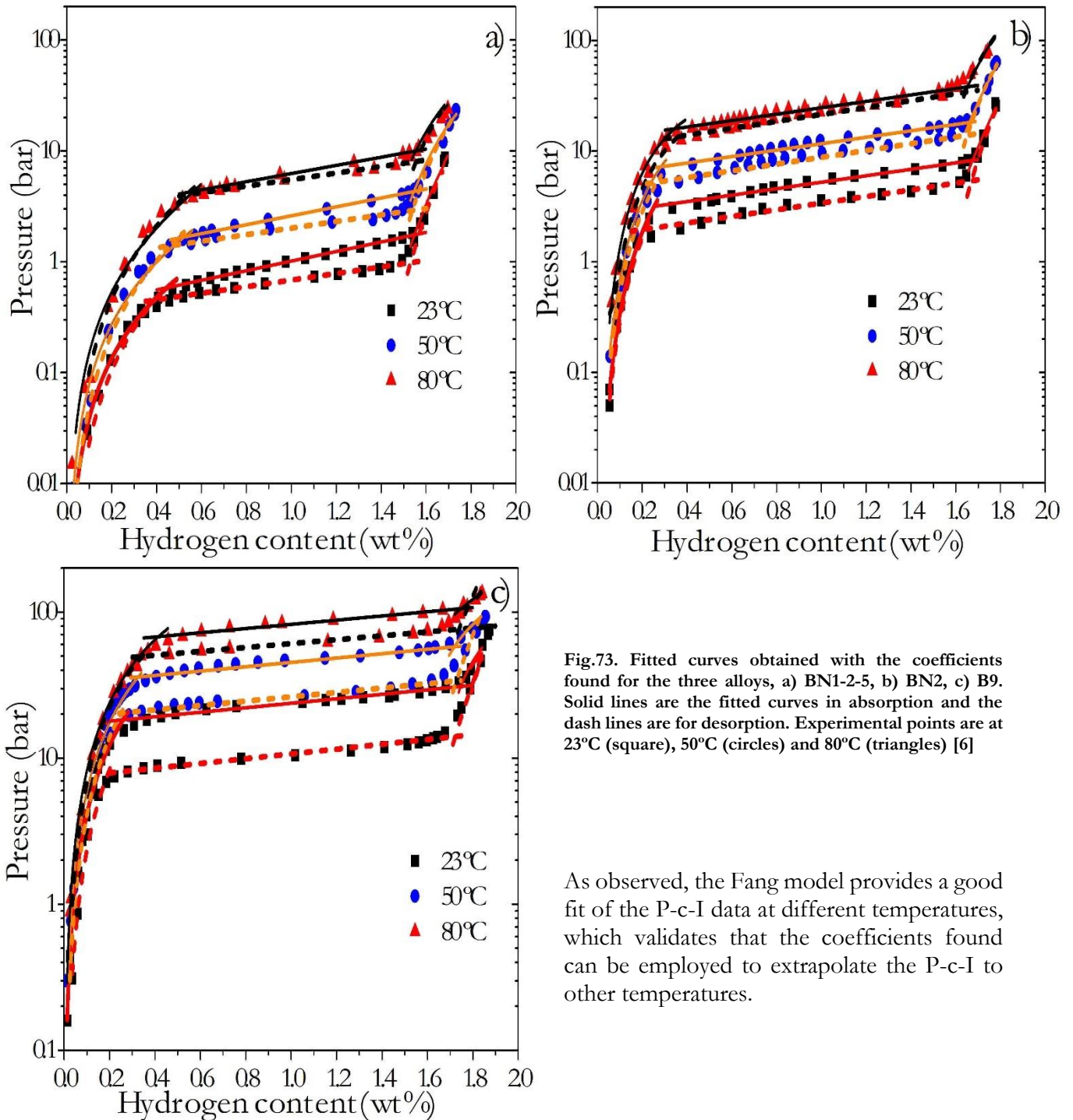
Fig.73. Fitted curves obtained with the coefficients found for the three alloys, a) BN1-2-5, b) BN2, c) B9. Solid lines are the fitted curves in absorption and the dash lines are for desorption. Experimental points are at 23ºC (square), 50ºC (circles) and 80ºC (triangles) [6]

As observed, the Fang model provides a good fit of the P-c-I data at different temperatures, which validates that the coefficients found can be employed to extrapolate the P-c-I to other temperatures.

Furthermore, with the coefficients found and validated, the thermodynamic simulation between the three stages of a MHHC system was performed and can be seen in Fig.74. The figure shows the O.P. for absorption (solid squares) at 23ºC and desorption (solid circles) at a given T_h that fulfills the operational conditions described in chapter 2 (Table 7). The T_h obtained and shown in the figure was initially 110 °C for the three stages, this value was the result of considering that the algorithm had to find a P_{des} at T_h that is higher than the P_{abs} in the following stage. The P-c-I absorption curves at 23°C are experimental data (open symbols) of all the alloys. P-c-I desorption curves at T_h are simulations using the Fang-Zhou model at the temperature where the operation conditions are satisfied. The initial pressure was fix at P_{in}=1.99 bar to generate the β_{min} composition in the P_l alloy, thus creating the initial

103

O.P. of the system. The dot lines with arrows indicate the thermodynamic path followed by the MHHC.
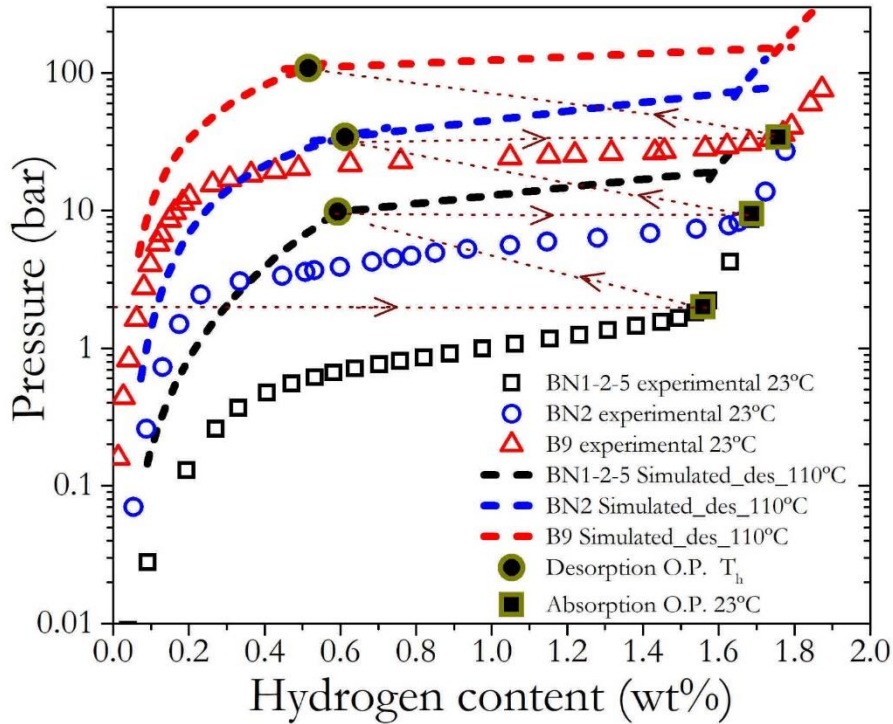
Fig.74. Thermodynamic simulation of the three stage MHHC. The solid squared points are the absorption O.P. for each stage. The solid circle points indicate the desorption O.P. The open symbols are the experimental data of each alloy at 23ºC, while the dash lines are the simulations of the P-c-I zones at 110ºC. The dot lines with arrows indicate the path followed by the three stage MHHC [6].

Several aspects of this simulation should be discussed. The reversible capacity of each stage is comprised between β_{min} at RT and α_{max} at T_h. It should notice that α_{max} increases and β_{min} decreases with temperature, so that the higher T_h, the lower is the reversible capacity [7]. For the first two stages, the T_h should be above a certain value so that the desorption pressure of the initial stage is higher than the absorption pressure of the following stage. For instance, for $T_h1 = 110ºC$, the desorption pressure attains 9.6 bar, which is higher than the β_{min} absorption pressure at 23 °C of the second stage: 9.5 bar. Likewise, the same T_h value for the second stage releases hydrogen at 34.1 bar, which is higher than the 33.9 bar of absorption pressure in the third stage at 23ºC. At these conditions, and, fixing also $T_h3 = 110$ °C, the reversible capacity for BN1-2-5, BN2 and B9 alloys are 0.97, 1.07 and 1.2 wt%, respectively, with a final output system pressure of 108.2 bar.

Furthermore, it should be considered that the desorption O.P. of the third stage influences the total CR and n_c of the system. To validate the influence of the T_h3 temperature in these performances, three temperatures were analyzed: 110ºC, 120ºC and 132ºC. Table 19 present the main results achieved with the different temperatures studied.

Table 19. Main parameters achieved with the T_h3 variation [6]

T_h3 (ºC)	P_{des} (bar)	Reversible capacity (wt.%)	CR
110	108.2	1.2	54.3
120	137.7	1.15	69.1
132	183.2	0.98	92

As the T_h3 temperature rises, the CR gradually increases from 54.3 to 92, considering that P_{des} is an increasing function of temperature. The n_c depends mainly on two parameters of

the design, the reversible capacity and the P_{des} of the third stage, which are largely dependent on temperature and have a different effect on n_c. The first one decreases due to the shrinking of the two-phase $\alpha+\beta$ miscibility gap on approaching the critical temperature (Fig.74) [7], leading to a modest decrease in the moles compressed. On the other hand, the P_{des} increases exponentially with temperature, allowing for an increase in n_c as shown in Fig.75. Furthermore, besides the third stage temperature T_h3, the V_{ext} to which the hydrogen gas is compressed, is of critical importance as it determinates to a large extent the n_c of the system. This is evidenced in Fig.75, showing that this magnitude linearly depends on the V_{ext}.
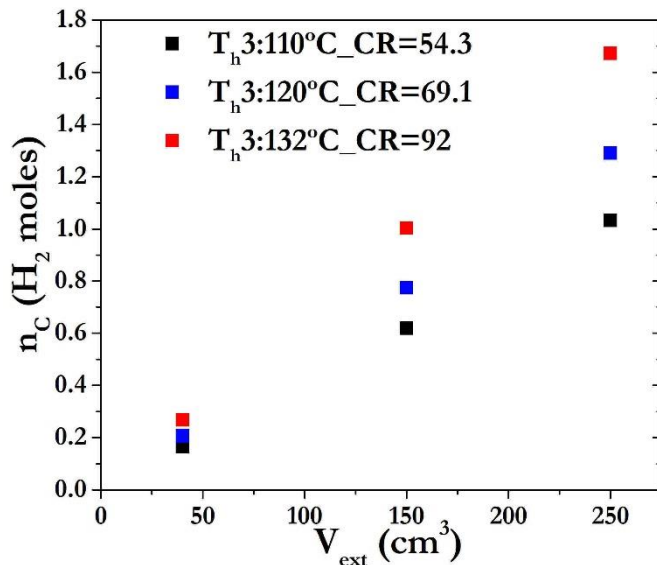
Fig.75. n_c as a function of the V_{ext} for three T_h3 desorption temperatures. Adapted from [6]

As expected, the best CR (92) and the highest amount of n_c (1.672 mol H_2) were achieved at the highest desorption temperature (132ºC) and the largest V_{ext} (250 cm^3) studied. The enhancement of both performances benefit from the exponential grow of the plateau pressure with temperature even if the reversible capacity is reduced. Therefore, on increasing T_h3 both the CR of the system and n_c increase. Indeed, the used methodology constraints the O.P. in the first and second stages, but let free the values of several relevant important parameters of the third stage like the T_h3 and V_{ext}, already discussed. More relevant, the m and VSt of all stages are determined, leading to the best operational characteristics of the compressor.
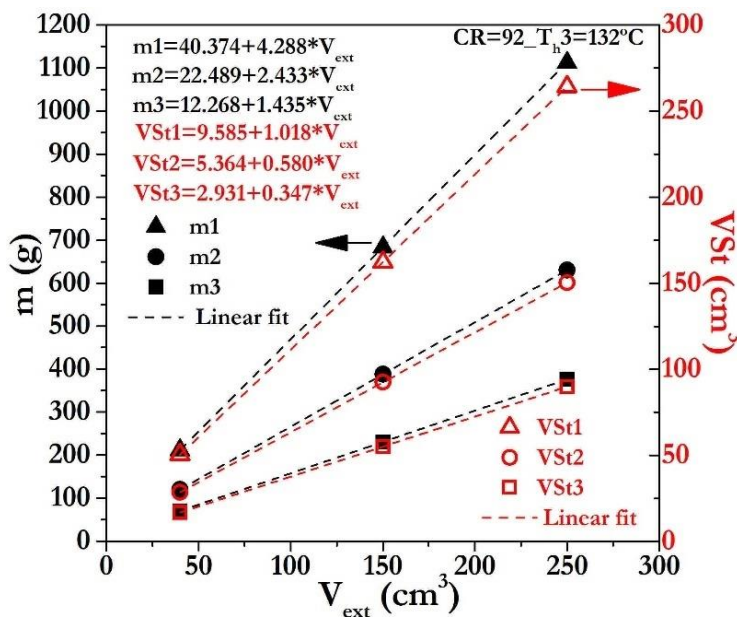
Fig.76. Dependence of alloy mass (left-axis) and vessel volume of each stage (right-axis) with V_{ext} for T_h3 = 132ºC. Inset equations stand for the best linear fits. Adapted from [6]

Fig.76 shows the dependence of the alloy mass and vessel volume at each stage on V_{ext} for T_h3 = 132 °C. Both magnitudes can be fitted with linear equations (given in the figure) that depend on V_{ext}. The optimum alloy masses scale is approximately in the ratio 3:2:1 for the first, second and third stages, respectively. The link between these parameters derive from the thermodynamic simulations shown in Fig.74. The given linear fits can be extrapolated to any

external vessel volume at the given operation conditions. A summary of the optimized operating parameters of the three stage MHHC system are displayed in Table 20.

Table 20. Summary of the operating system parameters found during the simulation

Stage	P_{abs} (bar) // RT (ºC)	P_{des} (bar) // T_h (ºC)	Reversible capacity (wt.%)	m (g) // VSt (cm³) At V_{ext} (cm³)		
				40	150	250
1	1.99 // 23	9.6 // 110	0.97	212 // 50.3	684 // 162	1112 // 264
2	9.5 // 23	34.1 // 110	1.07	120 // 28.6	388 // 92	631 // 150
3	33.9 // 23	183 // 132	0.98	70.5 // 16.8	230 // 55.3	376 // 89.8

Alloy masses and stage volumes given in table 20 result from the optimization of thermodynamic parameters (e.g. compression ratio and desorption temperature) of the third stage. Nevertheless, a further kinetic analysis will be needed to better optimize the system operation and design to attain the highest efficiency and see the real effect of the driving force that has been diminished through this analysis [1]. Also, it is not straightforward to compare our simulation results to previous works because they are very sensitive to system design (volumes and masses of alloys) and operation temperatures. However, for similar temperatures of operation, between RT and 130ºC, CR values between 3 and 75 have been reported for other MHHC prototypes [1]. The results obtained in this thesis are at the top of this range.

The results of this thermodynamic approach differ in several aspects from those in the selection program described in chapter 2. First, the nominal composition of the alloys could not be exactly obtained after their synthesis due to the volatility of the raw materials, as well as to the intrinsic tendency of $TiMn_2$-type compounds to yield chemical inhomogeneity. This proves that simulations will be more precise when they are based in experimental data from real materials. Second, absorption pressures at each stage using real experimental data were observed to differ from those predicted for the ideal ones in the first approach. For instance, for the BN1-2-5 alloy, the experimental absorption pressure at 23ºC and β_{min} is higher (1.99 bar) than that predicted by the first approach (1.4 bar). Analogous deviations are found for BN2 and B9 alloys. This variation results from the sloping nature of the plateau pressure which is not considered in the ideal Van´t Hoff plots [1, 8]. Indeed, the increase in the real absorption pressure at each stage requires a correlated increase in the desorption temperature of the previous one. As compared to an ideal thermodynamic model with flat plateau, the realistic one gives rise to a substantial increase (between 30 and 50ºC, depending on the stage) in the desorption temperatures, thus affecting to the total energy consumption of the MHHC. Third, as concerns hysteresis effects, their influence on the operational parameters is lower than that induced by the sloping plateau. In fact, the hysteresis tends to be reduced when increasing the temperature [9]. Fourth, the realistic simulation considers the dependence of the α_{max} and β_{min} phase limits with the temperature. As the $\alpha+\beta$ region shrinks, the reversible capacity decreases, leading to the necessity of increasing the alloy mass at each compression stage. As a last remark, it is worth noting that even if the evidenced realistic features induced significant changes in the operation conditions of the system, the selection of the three initial alloys by the first approach remains valid. This results from the fact that thermodynamic correlations between the pairs of materials designated remain roughly the same.

5.4. Thermodynamic simulations of a three stage MHHC

In chapter 6 the assembly and operation of a real MHHC system will be presented. It is of high interest to predict the functionality of the system by using the algorithm implemented in this chapter. Therefore, in this section an approximation to the real operability of a three stage MHHC system will be performed considering the real experiments developed in the MHHC measurement system. The alloys employed for these real experiments are the BNIC (St1), BN2IC (St2) and BIC (St3), which are slightly different in their thermodynamics than the BN1-2-5, BN2 and B9 employed for the initial design presented in the previous section.

The masses and VSt employed are the real ones (chapter 6), which have the singularity that are close in value for the three stages, i.e. m1≈m2≈m3 and VSt1≈VSt2≈VSt3, differing from the design done in the latest section, which designated a corresponding approximate ratio of 3:2:1 for the masses and volumes, e.g. 3m1:m3. This election has the negative point that it would not be possible to fully charge St3 from St1 in just one step. As positive aspects, the 1:1:1 ratio was a simpler technical approach for the building of the compressor, and also simplified some very relevant aspects of the design like the implementation of heating or cooling methods. In all the simulations a T_h of 120ºC was implemented for the three stages. As mentioned above, several hydrogenation cycles (designated by a color and numbers) need to be performed to fill completely the St3 with a St1 hydrogenated to its O.P. (β_{min} composition). First, in Fig. 77 a full operation (from St1 to St3) of the system was simulated to observe that with a single full charge of St1 the following stages could be partially charge, i.e. to a low hydrogen concentration in each P-c-I. Each full operation will be stated as cycle.
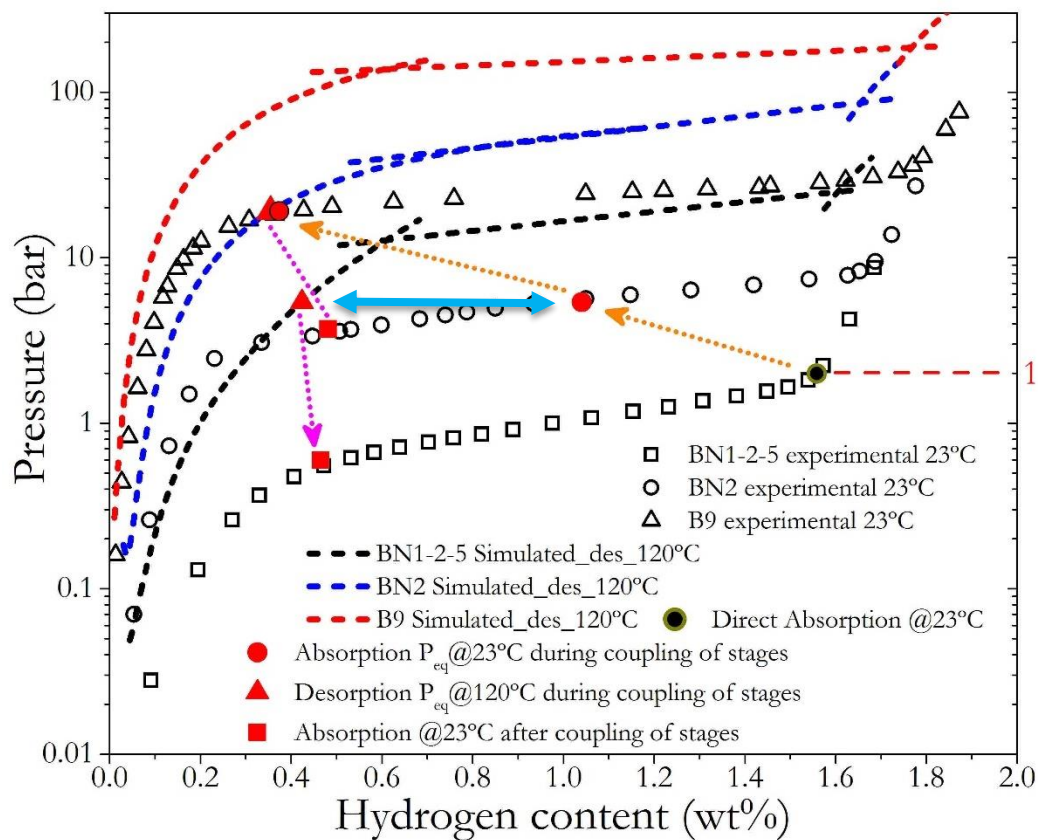
Fig.77. Simulation first cycle approximation of the real operability in the three stage MHHC measurement system. Orange dot arrows indicate the absorption path. Magenta dot arrows indicate the reabsorption at 23ºC path after the coupling of the respective stages. Light blue arrow indicates the equilibrium O.P. during the coupling of the stages.

The initial O.P. of the system is the P_{in} (1.99 bar) to achieve the β_{min} composition for the BN1-2-5 alloy at 23ºC (black and green circle). Then, there is a rise of temperature to T_h (120ºC) and the stages stay coupled until a P_{eq} is obtained simultaneously (light blue arrow pointing the two coupling O.P.) between the desorption of the St1 alloy at 120ºC (filled red triangle over black dash line) and the absorption of the St2 alloy at 23ºC (filled red circles over BN2 experimental points). Then, the valve closes and the hydride in St1 reabsorbs at 23ºC (filled red square over BN1-2-5 experimental points and magenta dot arrow). Next, the same procedure happens between St2 and St3, an increase of temperature to T_h (120ºC) and stage-coupling occurs obtaining a simultaneous P_{eq} between the desorption of the St2 alloy at 120ºC (filled red triangle over blue dash line) and the absorption of the St3 alloy at 23ºC (filled red circle over B9 experimental points). Finally, the valve closes and the hydride in St2 reabsorbs at 23ºC (filled red square over BN2 experimental points and magenta dot line). The orange dash arrow evidence the hydrogenation path described.

Fig. 78 described the full simulation of the MHHC system operation comprising several cycles. Some clarifications are needed to understand the figure properly. The initial O.P. at P_{in} of each cycle at 23ºC are the black and green circles. Other O.P. shown in Fig. 78 will be the absorption ones, before (circles) and after (squares) the coupling of the stages. Three main cycles were simulated, the first two (red (1) and orange (2)) hydrogenate completely the St1 and continue until St3, and a third cycle hydrogenate St2 directly to fulfil the β_{min} composition and resemble the procedure used in the real experiment performed and explained in the following chapter. The final desorption O.P. in St3 at 120ºC (magenta triangle) will determine the final CR of the system. However, the compressed moles were not found considering that the St3 is not couple to any other external volume, like in the former design (V_{ext}), and thus the final moles compressed would be those desorbed from the hydride in the St3 volume.
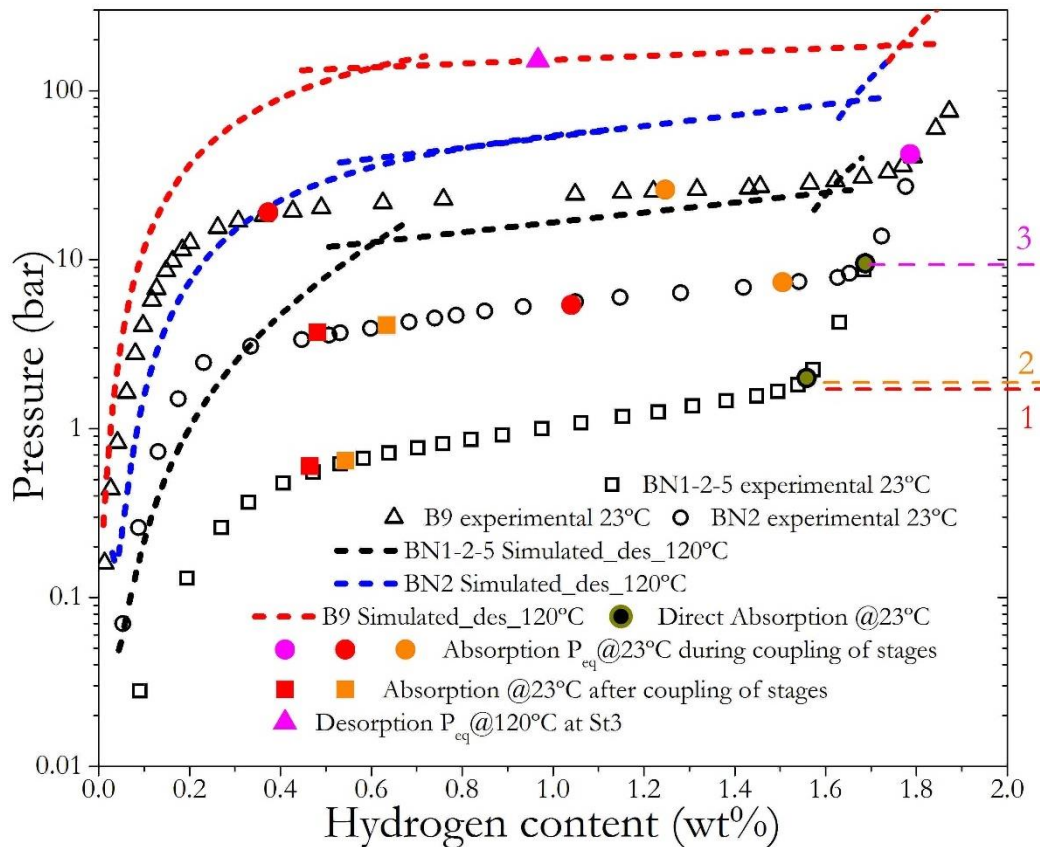
Fig.78. Analysis of the hydrogenation in a three stage MHHC experiment through the implementation of simulations

It can be seen in Fig.78 that the number of cycles in order to hydrogenate St3 to the β_{min} composition is at least three, considering that the quantity of alloy is almost the same for the three alloys. At the end of the cycles, a P_{des} of 151.2 bar was obtained. The CR found between the final P_{des} and the $P_{abs}=1.99$ bar in St1 is of 75.9, which is higher than the CR (69.1) found in the previous simulation (section 5.3). This can be explained partially by considering that for the St3, the O.P.$_{des}$ obtained in this simulation is larger than in the previous case (section 5.3) where it was fixed by the constrains defined (Table 7 in chapter 2), resulting in different CR values.

In resume, during all the phases described, the algorithm implemented has aided to design and understand the behavior of the three stage MHHC system successfully. Many beneficial aspects can be highlighted. The algorithm allows to predict the functionality of the systems at different operational conditions, for instance an important fact to evidence is the study of the system behavior at different temperatures from which there is not experimental data, i.e. the extrapolation at different temperatures of the P-c-I curves. Also, the possibility to simulate any material with experimental P-c-I data available, even in cases where P-c-I curves are determined at few temperatures, i.e. determined at least at two different temperatures. The operation of the system can be tested or simulated considering different approaches to design and/or evaluate the behavior of the system, for instance: 1. determine the pressures and hydrogen compositions of the system at different temperatures and/or alloys, 2. configure the system to specific parameters, e.g. obtained a final or initial pressure and its related stages features (alloys, volumes), 3. Optimize the operational parameters to obtain an enhance system. An extension of the functionality of the algorithm can also be applied to study other operational configurations like a continue operation, and the implementation of indistinctive number of stages.

5.5. Achievements and partial conclusions

1. The determination of P-c-I with ideal EOS generate great errors, especially at higher pressures. The use of the Joubert EOS describes accurately the real behavior of the H_2 gas in a MHHC system.

2. A thermodynamic algorithm has been developed to study the behavior of a MHHC system and design it properly. The model uses experimental thermodynamic data and real equation of state for H_2 gas to provide a more precise simulation of the MHHC operation parameters. This model allows to determine the optimal operational temperature, alloy mass and vessel volume at each stage. The program has the facility to implement different methodologies to study the behavior of MHHC systems under different conditions, i.e. analyze the effect of the sloping plateau and hysteresis in the final single stage compression.

3. The use of a non-experimental P-c-I model (no hysteresis and flat plateau) for the simulation of MHHC systems can produce large errors in key parameters such as the compression ratio and/or the number of moles compressed. Higher and constant CR as well as larger number of H_2-moles compressed are obtained with this non-experimental model. The need of a realistic P-c-I model (sloping plateau, hysteresis and dependence of $\alpha+\beta$ miscibility gap with temperature) is evident to approach simulations to reality and to achieve optimal values of the operational parameters in a MHHC system.

4. The implementation of the algorithm provides different advantages. It allows the study of the system behavior at different temperatures from which there is no experimental data and simulate any material with experimental P-c-I data available, even in cases where P-c-I curves

are determined at few temperatures. Also, it allows to study the behavior of different parameters in the operation of a MHHC system and optimize the operational parameters to obtain an enhance system.

5.6. References

[1]   M. V. Lototskyy, V. A. Yartys, B. G. Pollet, and R. C. Bowman, "Metal hydride hydrogen compressors: A review," *Int. J. Hydrog. Energy*, vol. 39, no. 11, pp. 5818–5851, Apr. 2014.

[2]   Z. Dehouche, N. Grimard, F. Laurencelle, J. Goyette, and T. K. Bose, "Hydride alloys properties investigations for hydrogen sorption compressor," *J. Alloys Compd.*, vol. 399, no. 1–2, pp. 224–236, Aug. 2005.

[3]   V. A. Yartys *et al.*, "Metal hydride hydrogen compression: recent advances and future prospects," *Appl. Phys. A*, vol. 122, no. 4, Apr. 2016.

[4]   J.-M. Joubert, "A Calphad-type equation of state for hydrogen gas and its application to the assessment of Rh–H system," *Int. J. Hydrog. Energy*, vol. 35, no. 5, pp. 2104–2111, Mar. 2010.

[5]   Fang, S., Zhou, Z., Zhang, J., Yao, M., Feng, F., and Northwood, D.O., "The application of mathematical models to the calculation of selected hydrogen storage properties (formation enthalpy and hysteresis) of AB2-type alloys," *Int. J. Hydrog. Energy*, vol. 25, no. 2, pp. 143–149, 2000.

[6]   A. R. Galvis E, F. Leardini, J. R. Ares, F. Cuevas, and J. F. Fernandez, "Simulation and design of a three-stage metal hydride hydrogen compressor based on experimental thermodynamic data," *Int. J. Hydrog. Energy*, Mar. 2018.

[7]   G. Sandrock, "Hydrogen-metal systems," in *Hydrogen Energy System*, Springer, 1995, pp. 135–166.

[8]   A. R. Galvis E., F. Leardini, J. Bodega, J. R. Ares, and J. F. Fernandez, "Realistic simulation in a single stage hydrogen compressor based on AB2 alloys," *Int. J. Hydrog. Energy*, vol. 41, no. 23, pp. 9780–9788, Jun. 2016.

[9]   S. Qian and D. O. Northwood, "Hysteresis in metal-hydrogen systems: a critical review of the experimental observations and theoretical models," *Int. J. Hydrog. Energy*, vol. 13, no. 1, pp. 25–35, 1988.

Chapter 6. Assembly, set up and operation of the Sieverts-type MHHC measurement system.

6.1. Introduction

This chapter is divided in two main objectives. First, a Sieverts-type MHHC test system is assembled and set up to measure a three-stage compressor system between vacuum to 250 bar. For the Sieverts apparatus, the volumes were calibrated by two methods and the thermal management procedure was set up for the operational ranges of temperature designed. Then, the entire MHHC system was set in operation and a further analysis of the complete compression process was accomplished together with a comparison of the experimental results obtained and the simulations performed in chapter 5.

6.2. Design, assembly and set up of the MHHC test system

In Fig.79 the main scheme of the system and an isometric assembly of the design done with Autodesk-Inventor® can be seen.
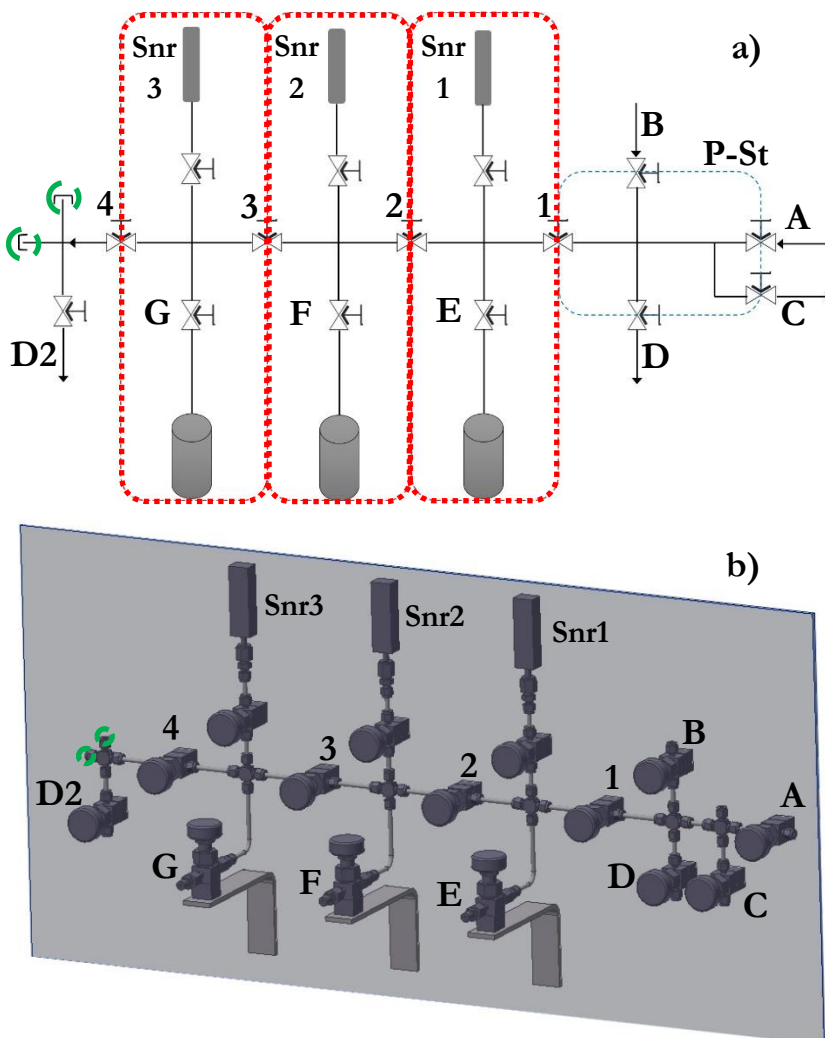
Fig.79. Design of the Sieverts-type MHHC measurement system, a) scheme, b) isometric assembly

In the scheme (Fig.79 a) it can be seen that in a pre-stage section (P-St, dash blue circle) the control of all the gases (A: H_2, B: Ar), in and out (D: atmosphere and C: vacuum), takes place. Then, the compression stages start (dash red circles, where 1, 2 and 3 stand for the beginning of the first, second and third stage, respectively). A final valve (4) defines the outlet of the compressed gas at the third stage to a V_{ext} that can be place at the end of the system (dash green circles) or to the atmosphere (D2). The volumes of each stage (Fig.79b) are delimited by the inlet and outlet valves (e.g. 1 and 2), the connection valves (E, F, G) to the reactors with the alloys and a pressure sensors (Snr) at the top.

Also, the volumes for each stage were designed and assembled trying to reduce the dead volume at each stage. The technical specifications of the MKS pressure sensors employed at each stage can be seen in Table 21. The numbers of each sensor correspond with the stage number where is employed.

Table 21. Specification of the pressure sensors assembled in the system

	MKS sensor type	Specifications
Snr1 and Snr2	Micro –baratron® 870B-13 High pressure	Range: 1000 psi Precision: 1% of the reading Span: 0.04% of reading/°C Overpressure limit: 1.2*1000= 1200 psi = 82 bar
Snr3	Micro –baratron® 870B-33 High pressure	Range: 3000 psi Precision: 1% of the reading Span: 0.04% of reading/°C Overpressure limit: 1.2*3000= 3600 psi =248 bar

The whole system was assembled using commercial parts of Swagelok®. Once the assembly was done, the leak test was performed. For this purpose and also to record the data in situ, a program in Labview® was developed. A leakage test recorded and a printed screen of the recording program can be seen in Fig.80. In addition, St3 was leak-tested during its operation at high pressure up to 120 bar.
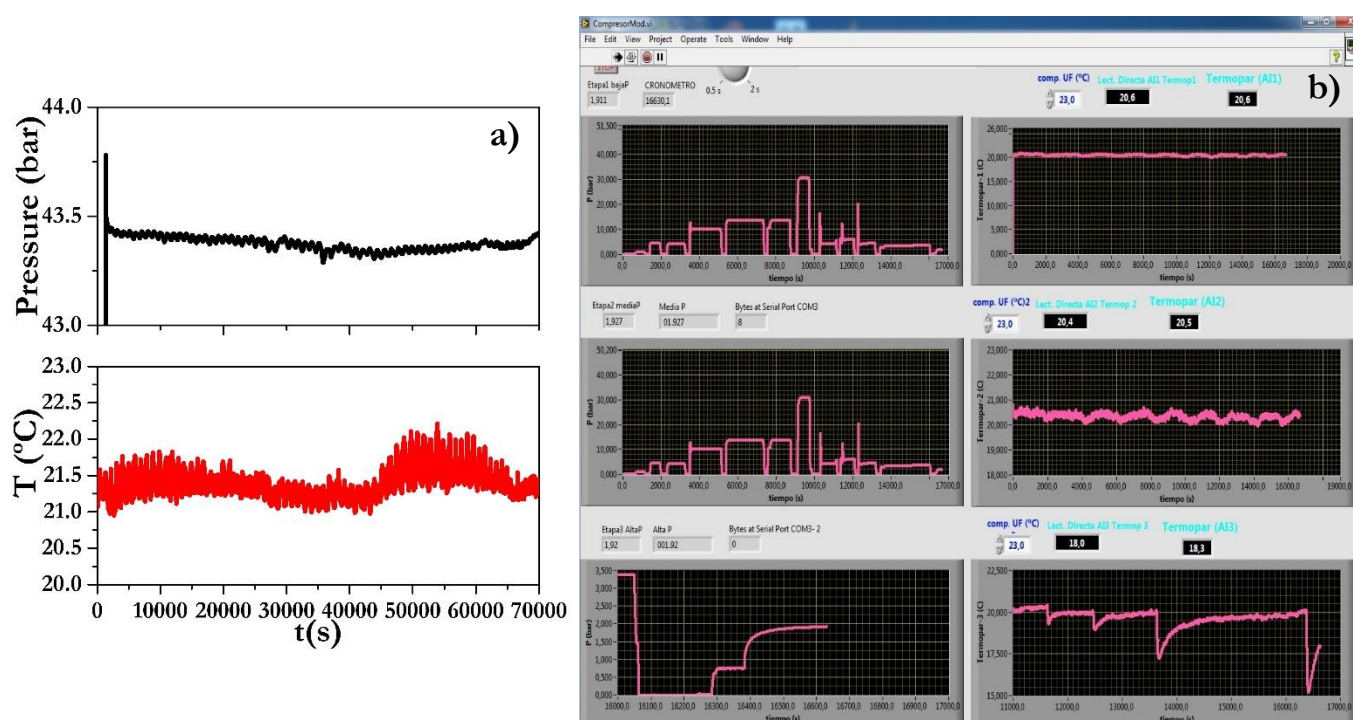
Fig.80. Leaks evaluation, a)pressure and temperature measured in all the system (pre-stage and the 3 stages), b) data adquisition program developed, where the left column (3 rows) are the pressures vs time curves in each stage and the right column (3 rows) are the respective temperatures vs time curves.

Once the Sieverts was leak free, a calibration of the volumes of the system was done. For this, a two step method was applied. First, Ar gas was introduced to the whole system with a flowmeter for ≈1 minute and with a flow of 30 SCCM. From this parameters a number of moles were found that together with the measured pressure, allows to obtain the total volume of the system. Then, the rest of the volumes were found by Ar expansions. All of these measurements were done trying to reduce the relative error to less than 5%, specially in the compressor stages. However, in the case of the P-St area (Fig.79a) this error is higher, but with lesser importance, since all the real measurements are perform in the compressor stages. The calibrated volumes of all the system and their errors can be observed in Table 22. Also the real system assemble with alloys in the reactor vessels can be seen in Fig.81.

Table 22. Calibrated volumes of the Sieverts-type MHHC test bench

VP-St	VSt1	VSt2	VSt3	VSystem
10.8(1.4)	11.40(0.25)	11.39(0.25)	11.45(0.25)	45.05(0.85)

114
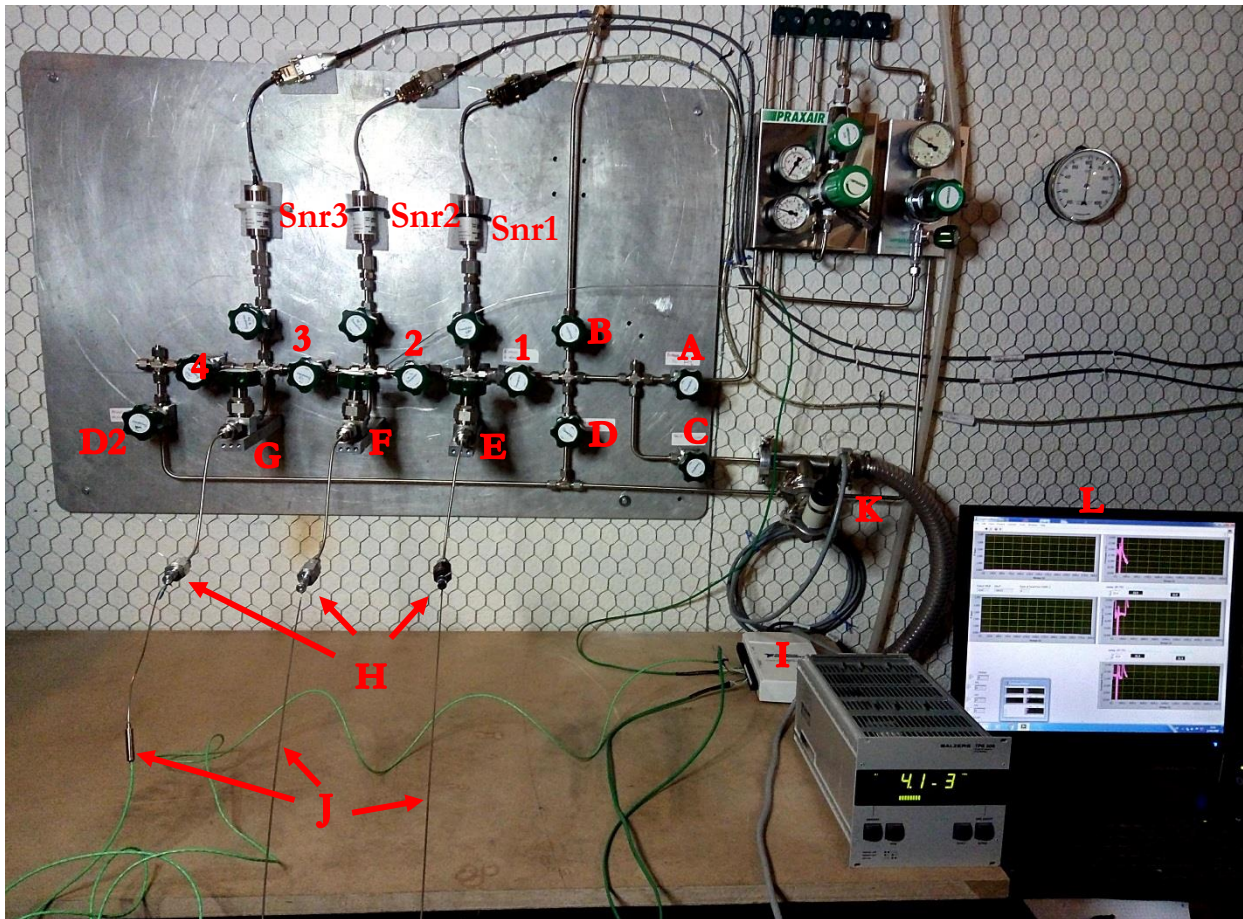
Fig.81. Real system assembly. Most of the letters and numbers in the picture were described previously with the scheme and isometric representation. H. Reactors with the alloys to re-calibrate the volumes, I. Data acquisition card for the temperature through the reading of the thermocouples (J) that are in direct contact with the reactor, K. Pirani® Vacuum sensor, L. Data acquisition program.

To validate the calibration of the volumes, samples of the hydrides measured previously in different Sieverts-type systems were used. Specifically the B9 (0.553(1) g), BN2 (0.653(1)g) samples were use in the second (with a free volume, $V_{fr}2=4.0(1)$ cm^3) and third ($V_{fr}3=4.1(1)$ cm^3) stages to validate if the volume calibration was suitable. In Fig.82 the comparison between the samples measured previously in other systems and the ones measured in the MHHC test system can be seen.
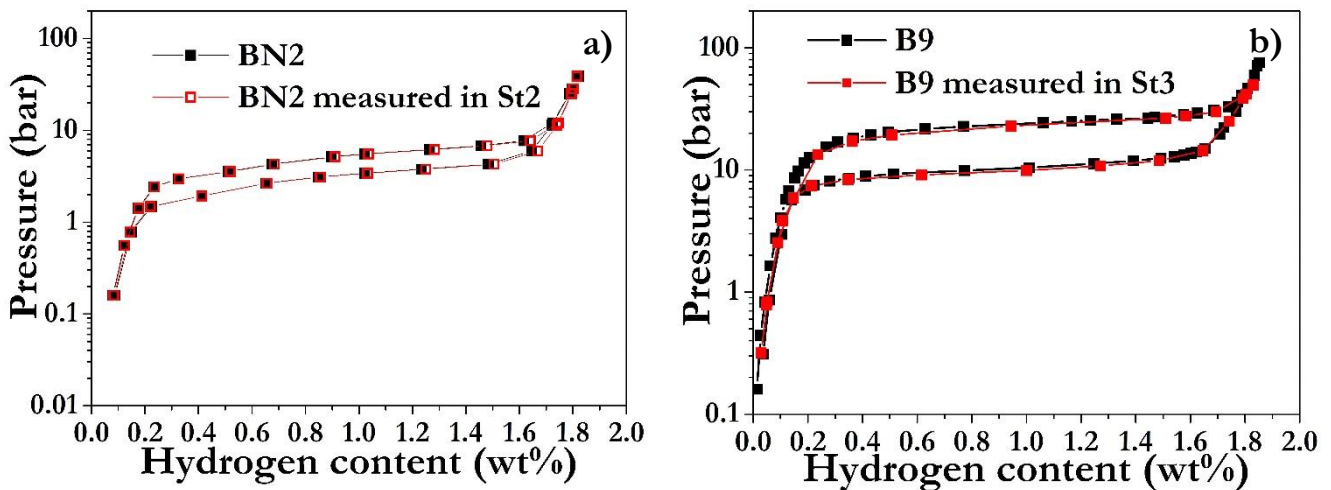
Fig.82. Validation of the system volume calibration with a P-c-I comparison, a) BN2 measured in VSt2, b) B9 measured in VSt3

As observed in Fig.82, the initial calibrated volume (Table 22) is precise enough to replicate a P-c-I mesaured in a different Sieverts-type reactor with a lower error, like the one described in Chapter 3. The highest accumulated error in this system is of 0.032 wt%. Also, the first stage was not re-calibrated considering the accuracy of the results obtained in the other two stages. Other effects accounted were the thermalization of the gas (as described in chapter 2), and the dead volume of the valves in the determination of the P-c-I, considering the moles involve in these volumes during the calculations.

6.2.1. Thermal management system

Fig.83. Complete MHHC test system, A. Sieverts-type MHHC test system, B. circulating bath system, C. Thermal bath vessel and D. heating control unit. Inset pictures are a zoom of the thermal bath (up) and the thermocoax surrounding the reactor (bottom)

On the other hand, once the hydrogenation system was fully operated, the second most important part for the proper operation of the MHHC is the thermal system, which basically needs to have three main functions, keep the temperature constant during the experiment, reduce the thermal shifts during absorption-desorption stages (i.e. the rapid increase of temperature due to the exothermic reaction in the absorption step and a reduction in temperature that takes place due to the expansion of the gas between stages (coupling first-second or second-third), and then, heat the hydrides to increase the temperature while they desorb. Considering these operational requests, the thermal management systems consists of a cooling system and a heating system. Their characteristics are as follow:

The cooling system (Fig.83 B and C) was employed to reduce the temperature rise in the absorption. For this porpuse, the reactor that contains the sample is completely inmerse in an open recipient with deionized water at RT (upper inset picture in Fig.83). The system function basically as an isothermal bath but with a fast control flux of the cooling fluid (i.e. hot water going in (red arrow) and cold one going out (blue arrow) from the circulating bath system and the recipient with the reactor) that guaranties that the temperature set (RT) remains almost constant and in the case of a great temperature peak, the dissipation and stabilization of this temperature would be rapid. The specifications of the circulating bath system can be seen in Table 23.

Table 23. Main operational specifications of the cooling and heating systems employed

Cooling system	Heating system
*Polyscience® 9106AA2E Refrigerated/Heated 6L circulating bath *Temperature range: -10ºC to 150ºC (depending on the operating fluid) *Temperature stability: 0.05ºC *Pump speeds: low 9 L/min -high 15 L/min *Input power of 200 W to achieve a T_l=20-23ºC	*Themocoax of with 1mm of diameter and cover with an Inconel 600 that can reach up to 1000ºC. *K type thermocuple *PMA KS 40-1® Universal PID Temperature Controller: -Single loop controller that provides simple 2-point (on/off) control, continuous PID control, or 3-point stepping control -Scan time 100 ms *Input power of 120 W to achieve a Th=150ºC (~96W to get 120ºC)

Then, the heating system consist of a thermocoax element (lower inset picture in Fig.83) that is rounded around the reactor and heats it up to the pre-design temperature of desorption. To achieve this temperature a Proportional-derivative-integral (PDI) control unit (Fig.83. D) inputs the proper power with the aid of a thermocouple attached to the vessel, without generating a great damping effect so that the time to attain this parameters is the lowest possible, also, when a reduction in the objective temperature is generated, the control unit corrects the value promtly. Then, to maintain this temperature the reactor was wrapped with an aluminium foil.

6.3. Experimental measurements of the three stage MHHC system

For the final assembly of the MHHC, the materials selected (BNIC, BN2IC and BIC) were synthesized in higher quantities (≈110g in total for each type) by induction melting as described in chapter 2. Then the samples were milled at air, sieved in particles of sizes between 150 μm and 1.2 mm and poured in the reactors with the geometry evidence in Fig.84. The quantity of mass in each vessel (Table 24) was calculated using the same geometry for the three reactors (horizontal tube), which consider the design of the heating system selected (thermocoax around the tube), the possibility of densification due to a gravity effect (e.g. horizontal instead of vertical vessels) [1, 2], and also, a lower hydrogenated packing fraction (63%) than the one used in the simulations [1]. Additionally, a 1:1:1 ratio was a simpler technical approach for the building of the compressor, and also simplifies some very relevant aspects of the design like the implementation of heating or cooling methods. However, a negative aspect is the necessity of hydrogenate in several cycles to fully charge the last stage of the MHHC.

Table 24. Mass and free volume of each stage

	St1	St2	St3
Mass (g)	11.010(1)	11.070(1)	10.700(1)
Volume (cm³)	4.5(1)	4.6(1)	4.6(2)
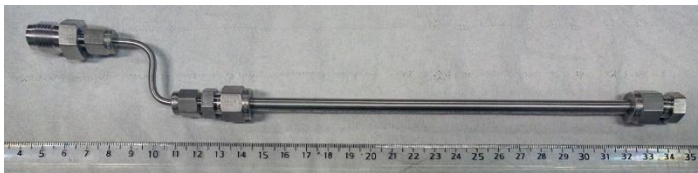
Fig.84. Reactor used for the MHHC experiments in the three stages. Main reactor is a Swagelok® tube that has an outer diameter of 6.25mm and a thickness of 0.889 mm

Then, the reactors were couple to the test system with a filter of 0.5 μm in between and their respective free volumes were calibrated with Ar expansions. The values can be observed in Table 24. Also, each thermocoax element was put around the respective reactor and connected to the corresponding thermal control unit.

The activation of the samples was performed in more than one step for the P_m and P_h alloys, since the mass quantity in each stage is larger than in the samples measured before (B9 and BN2) and thus to fully activate it, a larger quantity of moles would be necessary due to a restriction in the volume and inlet pressure of the system. In Fig.85. the activation of all the alloys can be seen. Specifically, in Fig.85a the raw data of a specific activation in each alloy can be seen, while in Fig.85b the validation of these activation with the P-c-I is evidenced.
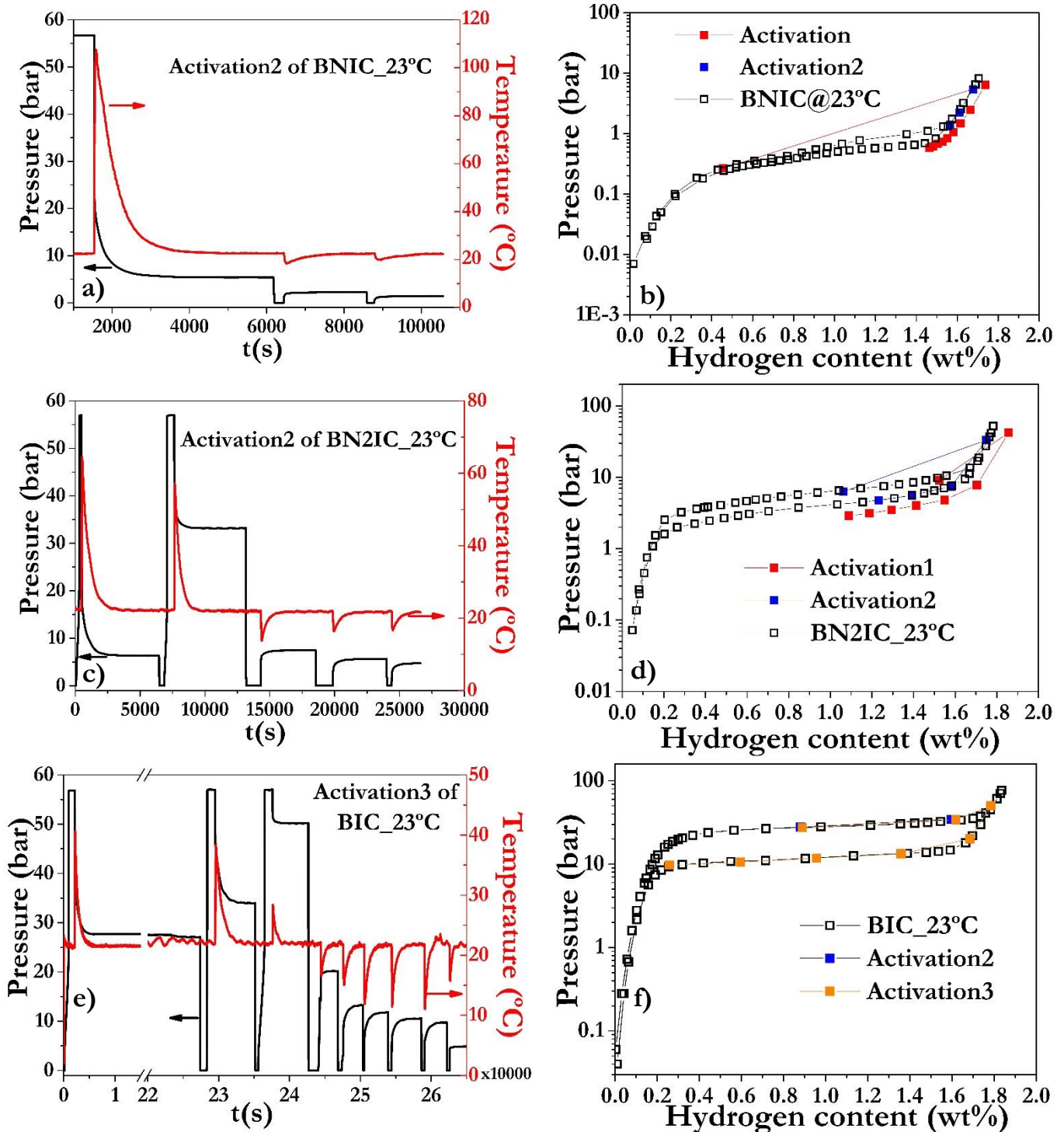
Fig.85. Activation of the three alloys at each stage of compression at 23ºC, a,c,d) raw data of pressure (black) and temperature (red) in a specific activation experiment, b) BNIC, d) BN2IC, f) BIC. In e) the time is multiplied by 10000

First, due to a large quantity of mass and high hydrogenation P_{eq} at RT, the BIC sample had to be fully activated after lowering the temperature of the sample to 10ºC (not shown in

Fig.85 e and f), and putting a direct constant pressure of 60 bar (the maximum pressure achievable in the laboratory), which did not allow to determine the hydrogen concentration in the alloy and thus the real activation was read after the second activation cycle (Fig.85 f). The P_l and P_m alloys did not exhibit this activation issue at RT. Then, it was concluded that all samples were activated properly after three cycles.

An important feature observed in Fig.85 is the very large thermal excursion in all the samples due to a higher quantity of the mass, which generates a longer stabilization time and justify the implementation of a cooling management system that could lessen these effects and stabilize them faster, as desired. The experiments shown in Fig.85, were done without the cooling system and therefore, the stabilization time was very long, taking several minutes or hours (Fig.85a), which confirms that the kinetics of the system is mostly determined by heat transfer, i.e. the removal of heat in this hydrogenation stage, and that a thermal management system is needed to improve the kinetics of the entire MHHC. In Fig.86a, it can be clearly seen a reduction of the temperature peak for the BNIC alloy compared to the temperature peak observed in Fig.85a, for the same alloy. This is due to the implementation of the circulating thermal bath, which specifically reduces the peak intensity (delta of temperature) from ~84(1) °C to ~18(1)°C and the stabilization temperature time of the system from 4538 s (~1.26 hours) to approximately 80 s (~0.02 hours). This variation in the temperature also have an effect in the pressure, which for this case reduces the absorption time from the same 4538 s (~1.26 hours) without thermal bath to 530 s (~0.147 hours) with this system. The heating system was tested at different temperatures to quantify its ability to perform the control of the temperature inside certain limits and over time. As can be seen in (Fig.86b) the temperature is kept constant in a range of ±1 to 1.5 °C and that it is stable through time.
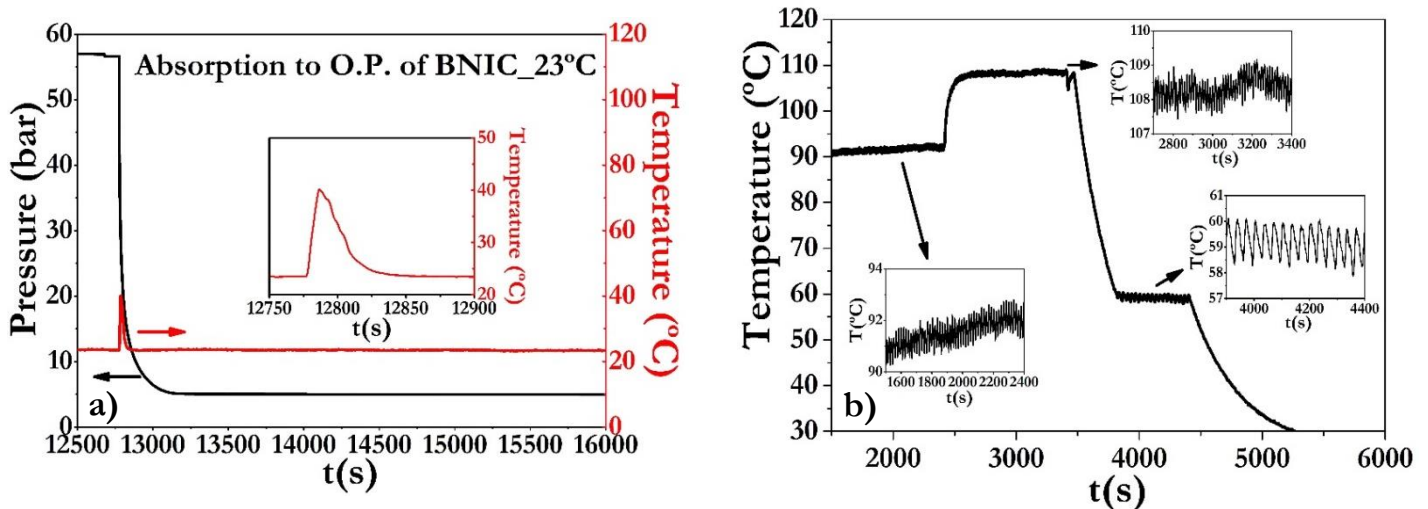
Fig.86. Thermal management system test, a) circulating thermal bath control (right red axis is the temperature), b) heating system control at different test temperatures

With all the system tested, and, the samples activated and prepared for hydrogenation cycles, the compression experiment with all the stages was performed.

6.3.1 Three stage MHHC system experiment

The whole experiment took several hydrogenation steps (cycles), considering that the mass of the alloys in each reactor is close to each other, and, according to the simulation design (chapter 5) these masses should have a ratio approximately of 3:2:1 to follow the O.P. designed for the first, second and third stages, respectively. In Fig.87 the entire experiment (left) and the tracking of the absorption points in each alloy at 23°C (right) can be observed.
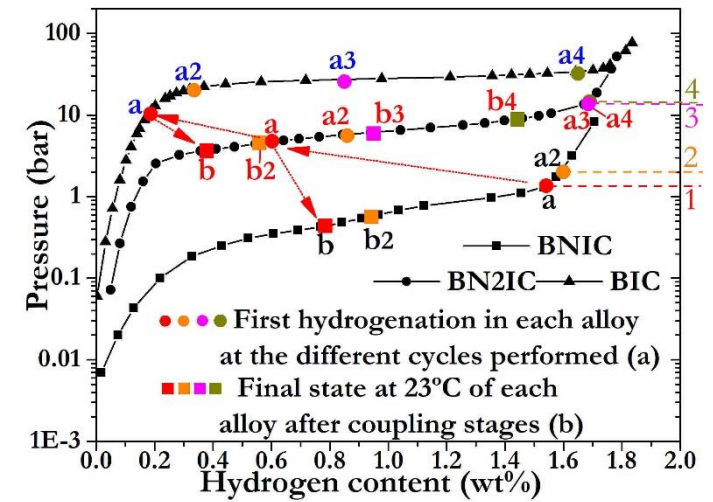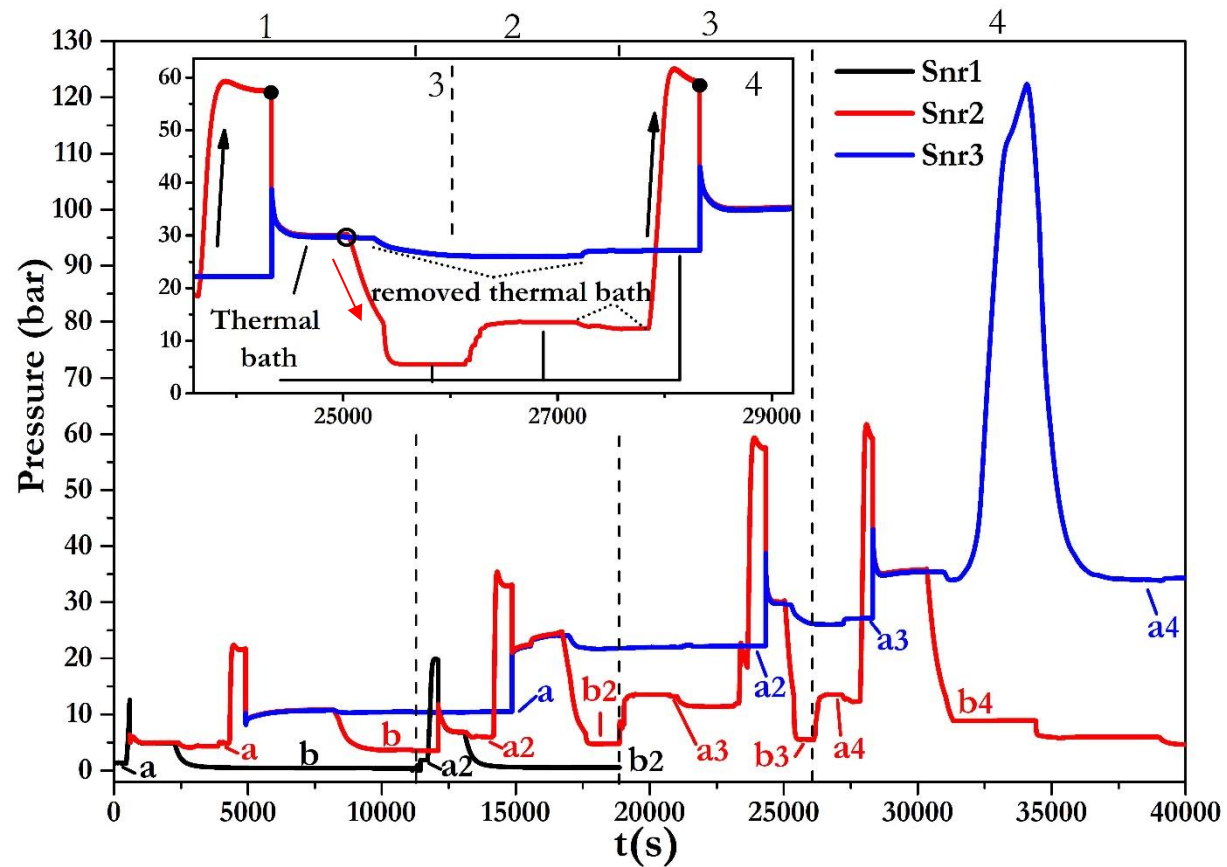
Fig.87. Experiment resume of the operation and behavior of the three stage MHHC measurement system (left) and its followed path in the absorption P-c-I curves at 23ºC (right). Inset graph with black frame is a zoom between the 3 and 4 cycles.

Due to the complexity of the operation, a detailed explanation of the steps followed will be given.

Each stage has a sensor that will follow the evolution of the experiment, Snr1 (black line), Snr2 (red line), Snr3 (blue line). In the absorption stage of all the alloys, the cooling system is employed to maintain 23°C. The equilibrium state of each stage during these absorption processes are indicated by filled circles in Fig.87 right, and, 'a' labels for first (black), second (red) and third (blue) stages, respectively. Also, the final points (reabsorption) after the coupling of the stages in each alloy are obtained at 23°C using the cooling system (filled squares in Fig.87 right, and, 'b' labels for first (black), second (red) and third (blue) stages, respectively), i.e. the absorption points after the transfer of hydrogen from the first to second stage and from the second to third stage, respectively. Note that a 'b' label stand for a partially discharged alloy (i.e. reabsorption at 23°C after the coupling of the stages) while 'a' label stand for a partially charged alloy.

The entire process for the first cycle (1) is defined by red arrows connecting the path followed in Fig.87 right. For this cycle, an inlet pressure in the first stage (black 'a' label in Fig.87) hydrogenates continuously this alloy to the β_{min} composition (Fig.87 right) with the cooling system maintaining 23°C. Then, sensible heat is applied, with the heating system, up to a temperature of 120°C (black arrows in the black-frame inset graph), increasing the pressure in the first stage, while in parallel, the second stage is with the thermal bath at 23°C. Once, the temperature is stabilized in the first stage, the coupling with the second stage is made and a drop of pressure is evident due to the expansion of the gas and the simultaneous absorption of the second hydride, which follow a tendency until a stabilization pressure point is achieved and the valve is close separating the two stages.

From this point on, the heating system is set-off, the temperature drops and the pressure follows the same trend (red arrow in black-frame inset graph), simultaneously, the thermal bath in the second stage is removed (black-frame inset graph) in order to put it in the first stage and observe the final point at 23°C after the coupling (black 'b' label in Fig.87), which generates a sudden pressure drop in St2 due to a fall in the temperature caused when the water left in the reactor got in contact with the air of the room. The cooling system is then returned to the second stage to measure the absorption value at 23°C (red 'a' label in Fig.87). Next, the thermal bath is employed in the third stage and sensible heat is applied to the second one up to a temperature of 120°C, and like before, when the T_h stabilized the coupling of the second and third stages was done until the pressure steadied and a further closing of the valve is performed, repeating then the turning-off of the heating system and finally interchanging the thermal bath between the second and third stages to measure the final and initial absorption points at 23°C (red 'b' and blue 'a' labels), respectively. This process is repeated in the second cycle.

After two full cycles of absorption (numbers and dashed lines in Fig.87 left) the stages were in equilibrium at 23°C in points 'b2' (labels in black at St1 and red at St2), and 'a2' (blue label in St3), as can be seen in Fig.87 right.

It is interesting to analyze the process in which two stages are connected. In Fig.87 left (black frame inset figure) the first coupling of St2 and St3 can be observed. Once the stages are brought into contact there is a transient time in which the pressure equilibrated, followed by a variation of pressure until it reaches stabilization. Note that this situation is not an equilibrium one as we are putting into contact to reservoirs at different temperatures and then some thermalization of the gas is expected during this time. Also, we assume that once

the pressure remains constant both alloys have reach equilibrium. It must be emphasized that in order to obtain the equilibrium points in Fig.87 right, the P-c-I of the material must be known as there is no direct way to know the partition of hydrogen moles between the alloys.

After the two initial full charging cycles described, the second stage was hydrogenated directly to the β_{min} hydride composition, without considering the first stage, to take into account just the number of cycles to hydrogenate the third stage while the second one was at its O.P. Two additional cycles were needed, (3 and 4 sections separated with dash vertical lines in Fig.87 left, and, 3 (pink) and 4 (green) numbers on the P-c-I in Fig.87 right) to achieve the β_{min} composition in the third hydride and finally observed the outcome pressure of the system at T_h. Also, as described for the first and second cycles, the final absorption composition after the coupling of the second (red b3 and b4) and third stages (blue b3 and b4) is done at 23°C with the cooling system.

Finally, a T_h of 120°C was slowly applied to St3 in order to record the pressure that can be attained with the MHHC. A pressure value of 122 bar was obtained in the isolated third stage, i.e. with the connection valve to the second stage close and without an expansion to a V_{ext}.

6.4. Discussion

The design, assembly and set-up of the three stage MHHC measurement system fulfill all the requirements to perform the three stage MHHC system experiment, considering the calibration of all the volumes with the validation of all the comparable thermodynamic measurements done, and also the thermal management systems setting with low errors and thermal stabilization times.

Considering that the P_{in} was 1.44 bar and the final pressure achieved at 120°C was of 122 bar, a final CR=84.7 of the system was achieved, slightly higher than the one simulated in chapter 5 with a similar alloy and temperature (CR= 75.9 @120°C). This result points out that the main objective of the work which was to be able to design and construct a MHHC based on AB_2-type alloys has been achieved and therefore validates the several approaches follow on this work, in particular it validates the algorithms implemented for the simulations.

The complete operation of the system (accounting the cycles used) can take place in less than few hours, which is not too long, considering that the system is not automatic and the operation requires some time to fix the right conditions for the absorption – desorption in all the stages, i.e. set the cooling and heating system as described for each condition evaluated.

Some features of the thermal management of the MHHC are relevant to highlight. There is a fast response of the thermal management systems during the coupling of the stages. This is mainly due to the design of the reactors that have a low thermal resistance by an increment of the heat exchange area (long tube) and a reduction of the heat exchange distances (low thickness and small diameter) [3] that aids to reduce the thermal losses due to a faster conduction of the heat from the thermal system (cooling and heating) to the inner parts of the compressor, i.e. hydride and H_2 gas [3, 4]. For instance, when the second and third stages are connected in the first cycle (red arrow in Fig.88 a and b) there is an increase of temperature in the third stage that is reduced fast by the cooling system (T_l3 in Fig.88). Also, since there is an expansion of the gas to the third stage, the pressurized H_2 in the second stage at T_h will lower its temperature due to the endothermic nature of the dehydrogenation reaction that takes place during the destabilization of the hydride with a pressure difference

[5]. This decrease in temperature is abated by the heating system with an increase in the temperature (blue arrow Fig.88b) that regulates this decrease and settle it to the T_h temperature.
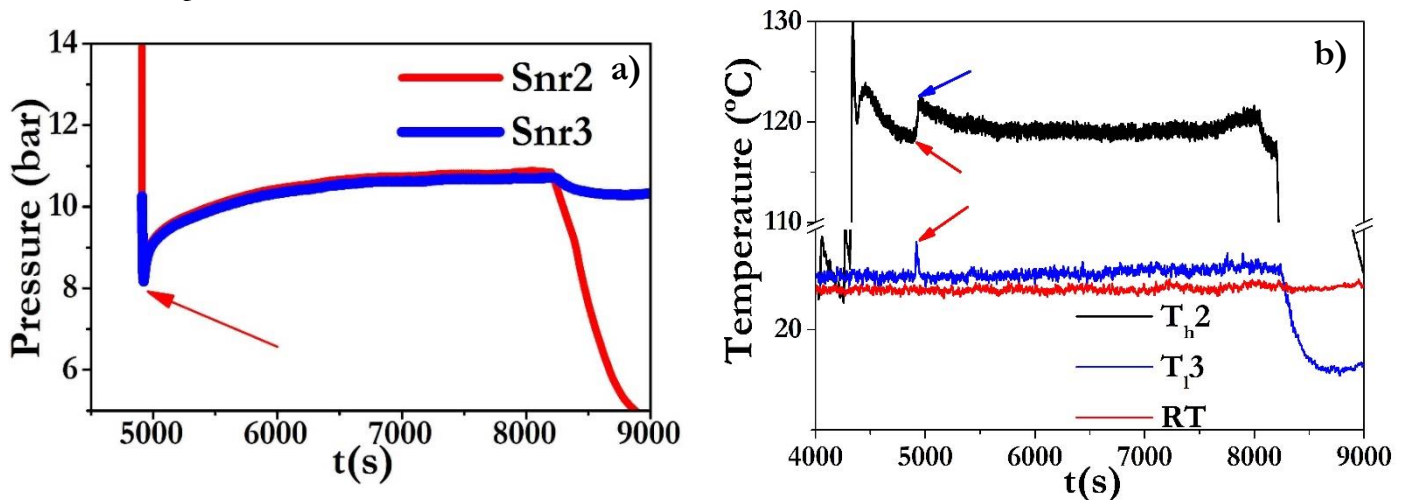
Fig.88 Coupling between the second and third stages in the first cycle, a) Zoom of the pressure area, b) temperature variation in St2 (Snr2, desorption at T_h2) and St3 (Snr3, absorption at T_l3). Red arrow indicates the coupling of the two stages

Though the response of the thermal system is fast, some transient effects are evident in the system, especially in the coupling of the stages. For instance, in the same coupling situation between the second and third stages (red arrow Fig.88a) a thermalization of the gas takes place and can be seen clearly in the increasing pressure behavior while the H_2 temperature measured in the surroundings of the system tends to stabilize (after blue arrow in Fig.88b), which is mostly due to two effects: a higher temperature rise during the absorption process in the third stage that heats up more the H_2 gas than with a lower exothermic reaction, increasing the time to lower the gas temperature to an effective temperature between the two reactors and the rest of the stage volumes, and, the fact that a great volume of the system is at RT without any thermal management system that could aid to stabilize the gas temperature faster. Also, this transient effect can be clearly seen when the coupling valve is closed and the gas pressure tend to balance faster to the temperature applied in each stage, i.e. 23ºC in St3 and 120ºC in St2, considering that there is no more gas temperature regulation between the two main temperature sources and the RT (22ºC) at which the rest of the stage volumes are.

The simplicity of the system gives the opportunity to easily extrapolate to a more complex MHHC system, i.e. a tube bundle, which can aid to increase the productivity of the system without complex changes in the thermal management system.

6.5. Achievements and partial conclusions

1. An experimental Sieverts-type system has been successfully built and set-up to measure and test the functionality of a three stage MHHC system. The ranges of temperatures and pressures that can be measure goes from RT to 400ºC and from vacuum to 250 bar, respectively.

2. The three stages for the MHHC system has been prepared with the alloys selected and characterized through the previous chapters, where the geometry designed has been applied considering the results obtained through the whole study of the alloys, specifically, the porosity evolution, the reduction of the heat resistance and the hydrogenated packing

fraction. Also, the simple geometry of the reactors aided to employ the thermal management system properly for an accurate control and measurement.

3. The MHHC system has been tested, giving several outcomes. A final experimental CR of 84.7 has been achieved at 120ºC in the system. This value can be considered at the top of similar MHHC systems in literature. Also, the simulation of the experimental MHHC behavior approached to these CR value with a similar alloy and temperature. The implementation of the AB$_2$-type alloys evidence that the time response during coupling of the stages is very fast, considering the intrinsic kinetics of these alloys and the thermal management employed. Also, the thermal control helps to abate the temperature excursions generated during the absorption and desorption processes.

4. The simple geometry applied and validated in this study resembles a more complex and habitual system like a tube bundle geometry design. Hence, an extrapolation of the current system to a bundle one can be easily implemented and could increase the productivity of the system.

6.6. References

[1]   A. R. Galvis Escobar, A. Chaise, V. Iosub, B. Salque, J. F. Fernandez, and O. Gillia, "Stress effect on the swelling/shrinking behavior of an AB2 alloy during hydrogenation cycles," *Int. J. Hydrog. Energy*, vol. 42, no. 35, pp. 22422–22431, Aug. 2017.

[2]   C. Na Ranong *et al.*, "Concept, Design and Manufacture of a Prototype Hydrogen Storage Tank Based on Sodium Alanate," *Chem. Eng. Technol.*, vol. 32, no. 8, pp. 1154–1163, Aug. 2009.

[3]   M. V. Lototskyy, V. A. Yartys, B. G. Pollet, and R. C. Bowman, "Metal hydride hydrogen compressors: A review," *Int. J. Hydrog. Energy*, vol. 39, no. 11, pp. 5818–5851, Apr. 2014.

[4]   V. A. Yartys *et al.*, "Metal hydride hydrogen compression: recent advances and future prospects," *Appl. Phys. A*, vol. 122, no. 4, Apr. 2016.

[5]   E. I. Gkanas *et al.*, "Numerical study on a two-stage Metal Hydride Hydrogen Compression system," *J. Alloys Compd.*, vol. 645, pp. S18–S22, Oct. 2015.

Final achievements, conclusions and derivative future work

Several parameters have a significant effect on the performance of MHHC. The hydride alloys that are used in each stage have a direct effect on the performance of the compressor, especially for the CR and H_2 rate, depending on their thermodynamics and intrinsic kinetics. The heat management (in all of its arrangements) is essential to account for sensible heating of the system and the change in P_{eq} due to the exothermic/endothermic reaction of the hydride in absorption/desorption, respectively. Also, the poor thermal conductivity of the MH bed should be improved, and/or, a reduction of the thermal resistance of the system should be considered, where in the latter an optimized aspect ratio can be a close solution to enhance the performance. The dead volume of the system is important since the higher the it is, the lower quantity of hydrogen can be store and compress afterwards, as a result, it would be better a lower dead volume of plumbing parts of the system and a higher the quantity of MH in the tank. However, if also the thermal resistance of the reactor is reduced by decreasing the diameter and wall thickness, then an integrity issue in the vessel can be attained. Thus, the optimized quantity of hydride in the container is a key parameter to consider.

In resume, the main targets to attain with MHHC systems are:
- a high compression ratio (small slope of the isotherms, low hysteresis and appropriate thermodynamics of the metal-hydrogen system);
- high productivity and efficiency (low number of compressions steps, fast kinetics of hydrogen exchange, efficient heat transfer, low transient heat losses);
- long and reliable operation (high cycle stability of metal hydride materials at the operating conditions, efficient system design).

Along this thesis, several of the parameters to enhance a MHHC system were studied. To attain this purpose, the main achievements done and conclusions obtained were the following:

Achievements

1. A basic selection program was developed based on defined operational MHHC parameters and basic thermodynamics obtained from literature. The program analyzed a data base assembled from over 200 hydrides to select a combination of three hydrides, considering operational and thermodynamic parameters.

2. New inner parts of the hydride breathing test cell (COMEDHY) has been designed, constructed and set up to successfully measure the effect that several stresses on the mechanical properties of hydrides can have with small quantities of material.

3. A thermodynamic algorithm has been developed to study the behavior of a MHHC system and design it properly. The model uses experimental thermodynamic data and real equation of state for H_2 gas to provide a more precise simulation of the MHHC operation parameters. This model allows to determine the optimal operational temperature, alloy mass and vessel volume at each stage. The program has the facility to implement different methodologies to study the behavior of MHHC systems under different conditions, i.e. analyze the effect of the sloping plateau and hysteresis in the final single stage compression.

4. An experimental Sieverts-type system has been successfully built and set-up to measure and test the functionality of a three stage MHHC system. The ranges of temperatures and pressures that can be measure goes from RT to 400ºC and from vacuum to 250 bar,

respectively. The use of a horizontal reactor design will help to reduce the agglomeration and possible densification with hydrogenation cycling

5. The three stages for the MHHC system has been prepared with the alloys selected and characterized through the previous chapters, where the geometry designed has been applied considering the results obtained through the whole study of the alloys, specifically, the porosity evolution, the reduction of the heat resistance and the hydrogenated packing fraction. Also, the simple geometry of the reactors aid to employ the thermal management system properly for an accurate control and measurement.

Conclusions

1. The main outcome of the materials selection program was a combination of three AB_2-type alloys for the system and an alternative option for the first stage with an AB_5-type alloy. Both combinations fulfill the constraints stablished.

2. The synthesis process have a great influence in the initial homogenization of AB_2-type alloys, and therefore, a better cooling control should be implemented to enhance the homogeneity

3. Thermal homogenization of the main phase in the AB_2-type alloys is difficult and will not change properly thermodynamic features like sloping plateau and hysteresis, on the contrary, if the process is not well implemented it can degenerate the properties obtained due to a further loss of Mn during the process. On the other hand, an annealing process in AB_5-type alloys worked perfectly generating a homogenization of the main phase in the alloy.

4. From the experimental characterization results it was observed that the AB_2-type alloys studied exhibit several relevant properties for an MHHC system:
*All of the alloys exhibit a good reversible capacity close to the 2 wt%.
*The reduction of the hysteresis with temperature is an excellent fact that help to increase the compression ratio and therefore its productivity. However, the sloping plateau evident in all of the alloys goes in the opposite direction, though, it is a normal issue in these types of alloys that can be accounted with a proper design of the coupled alloys and the MHHC system at each stage, i.e. through simulations.
*Also, from the kinetic models implemented, it was concluded that these alloys exhibit excellent kinetics that can increase the productivity of the system at each stage.
*These $TiMn_2$-based alloys are suitable to variate their composition and tailor different properties such as structural, morphologic, thermodynamic and kinetic, from which a further design of the different stages of the MHHC can be more accurately performed.
*Although, these materials are not historically suited to resist gas impurities, solutions like zeolites or other types of membranes can be easily couple in the case of a couple application that generates non-purified gas.

5. The AB_5-type alloy have a required lower inlet pressure and like other material of its kind, have a good resistance to gas impurities, which is a good advantage for some applications. Although, the reduction of the reversible capacity, and slower kinetics than AB_2-type alloys make it a less desirable material to be applied in a first stage MHHC.

6. The AB$_2$-type hydride breathing measurements under several applied stresses has revealed that depending on the stress level, densification or de-densification can occur compared to the initial non- decrepitated state. These alloys generate an increase of the volume and porosity after several hydrogenation cycles for a low and medium axial stresses, while for a high stress the hydride powder bed globally shrinks. It seems that a kind of equilibrium is installing between the applied stress and the cyclic breathing movement of the powder bed, once the decrepitation effect is reduced after a few tens of cycles. This equilibrium corresponds to a particular density and is much lower for the low stress level.

7. At early stage of cycling, the volume variation of the grains is fully transferred to the global volume variation, i.e. the powder bed level, and then, a part of this grain volume variation is transferred to the porosity. At the end, porosity is taking nearly half of the grain volume variation, independently of the applied stress. All of these goes along with the fact that the porosity is always higher in the desorbed state.

8. The volume and porous evolutions are linked to the decrepitation and rearrangement mechanisms. The decrepitation process reduced greatly the size of the particles. However, higher axial stresses contain bigger agglomerates, which seems to be small decrepitated particles not fully separated from its initial non-decrepitated grain. This broaden the grain size distribution and increases the densification of the powder bed.

9. Important parameters for the simulation such as the safety factor due to hydrogenated packing fraction with a value of ~65% and the evolution of the porosity with an approximate value of 0.4 were determined properly.

10. The determination of P-c-I with ideal EOS generate great errors, especially at higher pressures. The use of the Joubert EOS describes accurately the real behavior of the H$_2$ gas in a MHHC system.

11. The use of a non-experimental P-c-I model (no hysteresis and flat plateau) for the simulation of MHHC systems can produce large errors in key parameters such as the compression ratio and/or the number of moles compressed. Higher and constant CR as well as larger number of H$_2$-moles compressed are obtained with this non-experimental model. The need of a realistic P-c-I model (sloping plateau, hysteresis and dependence of α+β miscibility gap with temperature) is evident to approach simulations to reality and to achieve optimal values of the operational parameters in a MHHC system.

12. The implementation of the algorithm provides different advantages. It allows the study of the system behavior at different temperatures from which there is no experimental data and simulate any material with experimental P-c-I data available, even in cases where P-c-I curves are determined at few temperatures. Also, it allows to study the behavior of different parameters in the operation of a MHHC system and optimize the operational parameters to obtain an enhance system.

13. The MHHC system has been tested, giving several outcomes. A final experimental CR of 84.7 has been achieved at 120ºC in the system. This value can be considered at the top of similar MHHC systems in literature. Also, the simulation of the experimental MHHC behavior approached to these CR value with a similar alloy and temperature. The implementation of the AB$_2$-type alloys evidence that the time response during coupling of the stages is very fast, considering the intrinsic kinetics of these alloys and the thermal

management employed. Also, the thermal control helps to abate the temperature excursions generated during the absorption and desorption processes.

Future work

During this thesis the implementation of a heat and mass transfer simulation has been in progress, using the experimental data obtained from this work, i.e. the kinetic modelling of the alloys, the heat capacity and thermal conductivity of the materials, the mechanical properties and thermodynamic models already implemented. Nevertheless, this investigation will continue as a future work in order to optimize the geometries and thermal management, considering a more complex geometry like a tube bundle design that resembles the current reactor vessel. Hence, an extrapolation of the current system to a bundle one can be easily implemented and could increase the productivity of the system.

A further coupling of the compressor system to a H_2 photo-electrochemical cell will be tested, comparing the AB_2-type and AB_5-type alloys for the first stage. Other configurations of the MHHC system, like a continuous one, can be evaluated.

Varios parámetros tienen un efecto significativo en el rendimiento de un sistema MHHC. Las aleaciones que se utilizan en cada etapa tienen un efecto directo sobre el rendimiento del compresor, especialmente para el ratio de compresión y la velocidad de salida del H_2, que depende de la termodinámica y cinética de estos materiales. El manejo térmico (en todas sus disposiciones) es esencial para tener en cuenta el calentamiento sensible del sistema y el cambio en P_{eq} debido a la reacción exotérmica / endotérmica del hidruro en la absorción / desorción, respectivamente. Además, se debe mejorar la mala conductividad térmica del lecho de hidruro, y/o se debe considerar una reducción de la resistencia térmica del sistema, donde en este último, una relación de aspecto optimizada puede ser una solución cercana para mejorar el rendimiento. El volumen muerto del sistema es importante ya que cuanto más alto es, menor cantidad de hidrógeno puede almacenarse y comprimirse después, como resultado, cuanto menor es el volumen muerto de las partes de la tubería del sistema y cuanto mayor sea la cantidad de material en el tanque, mejor. Sin embargo, si también se reduce la resistencia térmica del reactor disminuyendo el diámetro y el grosor de la pared, entonces se puede tener un problema de integridad en el recipiente. Por lo tanto, la cantidad optimizada de hidruro en el contenedor es un parámetro clave a considerar.

En resumen, los objetivos principales para alcanzar con los sistemas MHHC son:
- una alta relación de compresión (pequeña pendiente de las isotermas, baja histéresis y termodinámica apropiada del sistema metal-hidrógeno);
- alta productividad y eficiencia (bajo número de pasos de compresión, cinética rápida del intercambio de hidrógeno, transferencia de calor eficiente, bajas pérdidas de calor transitorio);
- operación larga y confiable (alta estabilidad de ciclo de materiales de hidruro de metal en las condiciones de operación, diseño eficiente del sistema).

A lo largo de esta tesis, se estudiaron varios de los parámetros para mejorar un sistema MHHC. Para conseguir este propósito, las principales realizaciones y conclusiones obtenidas fueron los siguientes:

Realizaciones

1. Se desarrolló un programa básico de selección de materiales basado en parámetros operacionales definidos para el sistema MHHC y termodinámica básica obtenida de la literatura. El programa analizó una base de datos integrada a partir de más de 200 hidruros para seleccionar una combinación de tres hidruros, considerando parámetros operacionales y termodinámicos.

2. Piezas internas del sistema para medir las propiedades mecánicas de hidruros (COMEDHY) han sido diseñadas, construidas y puestas a punto para medir con éxito el efecto que varios esfuerzos pueden tener en las propiedades mecánicas de los hidruros, utilizando pequeñas cantidades de material.

3. Se ha desarrollado un algoritmo termodinámico para estudiar el comportamiento de los sistemas MHHC y diseñarlo adecuadamente. El modelo usa datos termodinámicos experimentales y una ecuación de estado real para gas H_2, y con esto proporcionar una simulación más precisa de los parámetros de operación del sistema. Este modelo permite determinar la temperatura de operación óptima, la masa de aleación y el volumen del reactor en cada etapa. El programa tiene la capacidad de implementar diferentes metodologías para

estudiar el comportamiento de los sistemas MHHC bajo diferentes condiciones, es decir, analizar el efecto del plateau inclinado y la histéresis en la compresión final de una sola etapa.

4. Se ha construido y puesto a punto con éxito un sistema experimental tipo Sieverts para medir y probar la funcionalidad de un sistema MHHC de tres etapas. Los rangos de temperaturas y presiones que se pueden medir van de temperatura ambiente a 400°C y de vacío a 250 bar, respectivamente. El uso de un diseño de reactor horizontal ayudará a reducir la aglomeración y la posible densificación con ciclos de hidrogenación

5. Las tres etapas del sistema MHHC han sido preparadas con las aleaciones seleccionadas y caracterizadas a través de los capítulos anteriores, donde el diseño de la geometría utilizada se ha aplicado considerando los resultados obtenidos a través del estudio experimental de las aleaciones, específicamente la evolución de la porosidad, la reducción de la resistencia térmica y el factor de empaquetamiento en estado hidrogenado. Además, la geometría simple de los reactores ayuda a emplear el sistema térmico de forma adecuada para un control y medición precisos.

Conclusiones

1. El resultado principal del programa de selección de materiales fue una combinación de tres aleaciones de tipo AB_2 para el sistema y una opción alternativa para la primera etapa con una aleación de tipo AB_5. Ambas combinaciones cumplen con las restricciones establecidas.

2. El proceso de síntesis tiene una gran influencia en la homogeneización inicial de aleaciones de tipo AB_2, y por lo tanto, se debe implementar un mejor control del enfriamiento para mejorar la homogeneidad.

3. La homogeneización térmica de la fase principal en las aleaciones de tipo AB_2 es difícil de obtener y no modifica adecuadamente características termodinámicas como el plateau inclinado y la histéresis, por el contrario, si el proceso no se implementa bien, puede degenerar las propiedades obtenidas debido a una mayor pérdida de Mn durante el proceso. Por otro lado, el proceso de recocido en aleaciones de tipo AB_5 funcionó perfectamente generando una homogeneización de la fase principal en la aleación.

4. A partir de los resultados de la caracterización experimental, se observó que las aleaciones de tipo AB_2 estudiadas exhiben varias propiedades relevantes para un sistema MHHC:
* Todas las aleaciones exhiben una buena capacidad reversible cercana al 2% en peso.
* La reducción de la histéresis con la temperatura es un hecho importante a destacar ya que ayuda a aumentar la relación de compresión y, por lo tanto, su productividad. Sin embargo, el plateau inclinado evidente en todas las aleaciones va en la dirección opuesta, y aunque es un problema normal en estos tipos de aleaciones, puede tenerse en cuenta mediante un diseño adecuado de los materiales acoplados y el sistema MHHC en cada etapa, es decir, a través de simulaciones.
* Además, a partir de los modelos cinéticos implementados, se concluyó que estas aleaciones exhiben una excelente cinética que puede aumentar la productividad del sistema en cada etapa.
* Estas aleaciones basadas en $TiMn_2$ son adecuadas para variar su composición y con esto poder adaptar diferentes propiedades estructurales, morfológicas, termodinámicas y cinéticas, a partir de las cuales se puede realizar un posterior diseño más detallado de las diferentes etapas del MHHC.

* Aunque estos materiales no son históricamente adecuados para resistir impurezas en el gas, soluciones como las zeolitas u otros tipos de membranas se pueden acoplar fácilmente en el caso de una aplicación acoplada que genere gases no purificados.

5. La aleación de tipo AB_5 tiene una presión de entrada baja y, al igual que otros materiales de esta clase, tiene una buena resistencia a las impurezas en el gas, lo que es una ventaja para algunas aplicaciones. Aunque la reducción de la capacidad reversible y la cinética más lenta que las aleaciones de tipo AB_2, lo convierten en un material menos deseable para ser aplicado en una primera etapa de un sistema MHHC.

6. Las medidas de propiedades mecánicas del hidruro tipo AB_2 sometido a varias tensiones aplicadas ha revelado que dependiendo del nivel de esfuerzo, puede producirse densificación o de-densificación en comparación con el estado inicial no decrepitado. Estas aleaciones generan un aumento del volumen y la porosidad después de varios ciclos de hidrogenación para un esfuerzo axial bajo y medio, mientras que para un esfuerzo alto, el lecho de polvo de hidruro se encoge globalmente. Se está generando un equilibrio entre el esfuerzo aplicado y el movimiento cíclico de expansión/contracción de todo el polvo, una vez que el efecto de decrepitación se reduce después de algunas decenas de ciclos. Este equilibrio corresponde a una densidad particular y es mucho menor para el bajo nivel de esfuerzo.

7. En etapas iniciales del ciclado, la variación del volumen de los granos se transfiere completamente a la variación de volumen global, es decir, a todo el lecho de polvo, y luego, una parte de esta variación de volumen de grano se transfiere a la porosidad. Al final, la porosidad está tomando casi la mitad de la variación del volumen del grano, independientemente del estrés aplicado. Todo esto concuerda con el hecho de que la porosidad es siempre mayor en el estado desorbido.

8. La evolución del volumen y la porosidad están vinculadas a los mecanismos de decrepitación y reordenamiento. El proceso de decrepitación redujo en gran medida el tamaño de las partículas. Sin embargo, las tensiones axiales más altas contienen aglomerados más grandes, que parecen ser pequeñas partículas decrepitadas no completamente separadas de su grano inicial no decrepitado. Esto amplía la distribución del tamaño de grano y aumenta la densificación del polvo

9. Se han determinado parámetros importantes para la simulación tales como el factor de empaquetamiento en estado hidrogenado con un valor cercano a 65% y la evolución de la porosidad con un valor aproximado de 0.4.

10. La determinación de las P-c-I con ecuaciones de estado ideal genera grandes errores, especialmente a presiones más altas. El uso de la ecuación de estado de Joubert describe con buena precisión el comportamiento real del gas H_2 en un sistema MHHC.

11. El uso del modelo de P-c-I no experimental (sin histéresis y plateau plano) para la simulación de sistemas MHHC puede producir grandes errores en parámetros clave tales como la relación de compresión y / o el número de moles comprimidos. En este modelo no experimental se obtienen relaciones de compresión más altas y constantes, así como una mayor cantidad de moles de H_2 comprimido. La necesidad de un modelo que incorpore P-c-I realistas (plateau inclinado, histéresis y dependencia de la zona α + β con la temperatura) es evidente para aproximar las simulaciones a la realidad y lograr valores óptimos de los parámetros operacionales en un sistema MHHC.

12. La implementación del algoritmo proporciona diferentes ventajas. Permite estudiar el comportamiento del sistema a distintas temperaturas, a partir de las cuales no hay datos experimentales, y, simular cualquier material con datos experimentales disponibles de P-c-I, incluso en casos donde estas se determinan con pocas temperaturas. Además, permite estudiar el comportamiento de diferentes parámetros en el funcionamiento de un sistema MHHC y optimizar los parámetros operativos para obtener un sistema de mejorado.

13. El sistema MHHC ha sido probado exitosamente, dando varios resultados. Se ha logrado un radio de compresión experimental final de 84.7 a 120°C en el sistema. Este valor se puede considerar en el rango superior de otros sistemas MHHC similares en la literatura. Además, la simulación termodinámica del comportamiento experimental de MHHC logro acercarse a estos valores de ratio de compresión con aleaciones y temperaturas similares. La implementación de las aleaciones de tipo AB_2 evidencia que la respuesta de tiempo durante el acoplamiento de las etapas es muy rápida, considerando la cinética intrínseca de las aleaciones y el sistema térmico empleado. Además, el control térmico ayuda a disminuir los cambios de temperatura generados durante los procesos de absorción y desorción.

Trabajos futuros

Durante el transcurso de esta tesis se han implementado simulaciones de transferencia de calor y masa de manera preliminar, utilizando los datos experimentales obtenidos durante este trabajo, es decir, el modelado de la cinética intrínseca de las aleaciones, la capacidad térmica, la conductividad térmica, las propiedades mecánicas y los modelos termodinámicos ya implementados. Sin embargo, esta investigación continuará como un trabajo futuro para optimizar las geometrías y el manejo térmico, considerando una geometría más compleja como un diseño de carcasa y conjunto tubular que se asemeja al recipiente del reactor actual. Por lo tanto, una extrapolación del sistema actual a uno más complejo se puede implementar fácilmente y podría ayudar a aumentar la productividad del sistema.

Asimismo, se probará un acoplamiento adicional del sistema del compresor a una célula foto-electroquímica para producción de H_2, comparando las aleaciones de tipo AB_2 y tipo AB_5 para la primera etapa. Se pueden evaluar otras configuraciones del sistema MHHC, como un sistema de flujo continuo.

Annexes

ANNEX 1. Combination of materials selected with the selection program. The materials indicated in the table are those selected for the 2 stage, considering 1 (1st column) and 3 (1st row) stage materials

1 Stage / 3 Stage →	Ti$_{0.9}$Zr$_{0.1}$Mn$_{1.4}$V$_{0.2}$Cr$_{0.4}$		Ti$_{0.8}$Zr$_{0.2}$Mn$_{0.8}$CrFe$_{0.2}$	MmNi$_{4.6}$Fe$_{0.4}$	ZrCo$_{1.8}$Al$_{0.2}$
Ti$_{0.9}$Zr$_{0.1}$V$_{0.2}$Mn$_{1.2}$	LmNi$_{4.91}$Sn$_{0.15}$	Zr$_{0.76}$Ti$_{0.24}$Ni$_{1.16}$Mn$_{0.63}$V$_{0.14}$Fe$_{0.18}$	Zr$_{0.76}$Ti$_{0.24}$Ni$_{1.16}$Mn$_{0.63}$V$_{0.14}$Fe$_{0.18}$	Zr$_{0.76}$Ti$_{0.24}$Ni$_{1.16}$Mn$_{0.63}$V$_{0.14}$Fe$_{0.18}$	Ti$_{0.7}$Zr$_{0.3}$Mn$_{1.9}$Mo$_{0.1}$
Zr$_{0.85}$Ti$_{0.15}$Cr$_{0.8}$Fe$_{1.2}$	LmNi$_{4.91}$Sn$_{0.15}$	Zr$_{0.76}$Ti$_{0.24}$Ni$_{1.16}$Mn$_{0.63}$V$_{0.14}$Fe$_{0.18}$	Zr$_{0.76}$Ti$_{0.24}$Ni$_{1.16}$Mn$_{0.63}$V$_{0.14}$Fe$_{0.18}$	Zr$_{0.76}$Ti$_{0.24}$Ni$_{1.16}$Mn$_{0.63}$V$_{0.14}$Fe$_{0.18}$	Ti$_{0.7}$Zr$_{0.3}$Mn$_{1.9}$Mo$_{0.1}$
Zr$_{0.9}$Ti$_{0.1}$Cr$_{0.8}$Fe$_{1.2}$	LmNi$_{4.91}$Sn$_{0.15}$	Zr$_{0.76}$Ti$_{0.24}$Ni$_{1.16}$Mn$_{0.63}$V$_{0.14}$Fe$_{0.18}$	Zr$_{0.76}$Ti$_{0.24}$Ni$_{1.16}$Mn$_{0.63}$V$_{0.14}$Fe$_{0.18}$	Zr$_{0.76}$Ti$_{0.24}$Ni$_{1.16}$Mn$_{0.63}$V$_{0.14}$Fe$_{0.18}$	Zr$_{0.76}$Ti$_{0.24}$Ni$_{1.16}$Mn$_{0.63}$V$_{0.14}$Fe$_{0.18}$
Ti$_{0.9}$Zr$_{0.1}$V$_{0.5}$Mn$_{1.3}$	Ti$_{0.7}$Zr$_{0.3}$Mn$_{1.9}$Mo$_{0.1}$	Ti$_{0.8}$Zr$_{0.2}$Mn$_{1.2}$V$_{0.2}$Cr$_{0.6}$	Zr$_{0.76}$Ti$_{0.24}$Ni$_{1.16}$Mn$_{0.63}$V$_{0.14}$Fe$_{0.18}$	Zr$_{0.76}$Ti$_{0.24}$Ni$_{1.16}$Mn$_{0.63}$V$_{0.14}$Fe$_{0.18}$	Ti$_{0.7}$Zr$_{0.3}$Mn$_{1.9}$Mo$_{0.1}$
Ti$_{0.9}$Zr$_{0.1}$V$_{0.3}$Mn$_{1.3}$	Ti$_{0.7}$Zr$_{0.3}$Mn$_{1.9}$Mo$_{0.1}$	Ti$_{0.8}$Zr$_{0.2}$Mn$_{1.2}$V$_{0.2}$Cr$_{0.6}$	V$_{92.5}$Zr$_{7.5}$	V$_{92.5}$Zr$_{7.5}$	V$_{92.5}$Zr$_{7.5}$
Ti$_{0.8}$Zr$_{0.2}$Mn$_{1.5}$V$_{0.5}$	Zr$_{0.76}$Ti$_{0.24}$Ni$_{1.16}$Mn$_{0.63}$V$_{0.14}$Fe$_{0.18}$	-	V$_{92.5}$Zr$_{7.5}$	V$_{92.5}$Zr$_{7.5}$	V$_{92.5}$Zr$_{7.5}$
Ti$_{0.6}$Zr$_{0.4}$Mn$_{1.4}$Cr$_{0.4}$Cu$_{0.2}$	Zr$_{0.76}$Ti$_{0.24}$Ni$_{1.16}$Mn$_{0.63}$V$_{0.14}$Fe$_{0.18}$	-	V$_{92.5}$Zr$_{7.5}$	-	-
MmNi$_{4.3}$Al$_{0.7}$	Ti$_{0.7}$Zr$_{0.3}$Mn$_{1.9}$Mo$_{0.1}$	Ti$_{0.8}$Zr$_{0.2}$Mn$_{1.2}$V$_{0.2}$Cr$_{0.6}$	Zr$_{0.76}$Ti$_{0.24}$Ni$_{1.16}$Mn$_{0.63}$V$_{0.14}$Fe$_{0.18}$	Zr$_{0.76}$Ti$_{0.24}$Ni$_{1.16}$Mn$_{0.63}$V$_{0.14}$Fe$_{0.18}$	Ti$_{0.7}$Zr$_{0.3}$Mn$_{1.9}$Mo$_{0.1}$
LaNi$_{4.8}$Sn$_{0.2}$	Ti$_{0.7}$Zr$_{0.3}$Mn$_{1.9}$Mo$_{0.1}$	Ti$_{0.8}$Zr$_{0.2}$Mn$_{1.2}$V$_{0.2}$Cr$_{0.6}$	Zr$_{0.76}$Ti$_{0.24}$Ni$_{1.16}$Mn$_{0.63}$V$_{0.14}$Fe$_{0.18}$	Zr$_{0.76}$Ti$_{0.24}$Ni$_{1.16}$Mn$_{0.63}$V$_{0.14}$Fe$_{0.18}$	Ti$_{0.7}$Zr$_{0.3}$Mn$_{1.9}$Mo$_{0.1}$
LaNi$_{4.6}$Si$_{0.4}$	Ti$_{0.7}$Zr$_{0.3}$Mn$_{1.9}$Mo$_{0.1}$	-	Zr$_{0.76}$Ti$_{0.24}$Ni$_{1.16}$Mn$_{0.63}$V$_{0.14}$Fe$_{0.18}$	Zr$_{0.76}$Ti$_{0.24}$Ni$_{1.16}$Mn$_{0.63}$V$_{0.14}$Fe$_{0.18}$	Ti$_{0.7}$Zr$_{0.3}$Mn$_{1.9}$Mo$_{0.1}$
LaNi$_{4.5}$Si$_{0.5}$	Ti$_{0.7}$Zr$_{0.3}$Mn$_{1.9}$Mo$_{0.1}$	Ti$_{0.8}$Zr$_{0.2}$Mn$_{1.2}$V$_{0.2}$Cr$_{0.6}$	Zr$_{0.76}$Ti$_{0.24}$Ni$_{1.16}$Mn$_{0.63}$V$_{0.14}$Fe$_{0.18}$	Zr$_{0.76}$Ti$_{0.24}$Ni$_{1.16}$Mn$_{0.63}$V$_{0.14}$Fe$_{0.18}$	Ti$_{0.7}$Zr$_{0.3}$Mn$_{1.9}$Mo$_{0.1}$
LaNi$_{4.4}$Zn$_{0.6}$	LaNi$_5$	Ti$_{0.45}$Fe$_{0.45}$V$_{0.05}$Mn$_{0.05}$	Ti$_{0.7}$Zr$_{0.3}$Mn$_{1.9}$Mo$_{0.1}$	Ti$_{0.7}$Zr$_{0.3}$Mn$_{1.9}$Mo$_{0.1}$	Ti$_{0.7}$Zr$_{0.3}$Mn$_{1.9}$Mo$_{0.1}$

ANNEX 2. Flux Diagram of the Thermodynamic Algorithm for the three stage MHHC system design
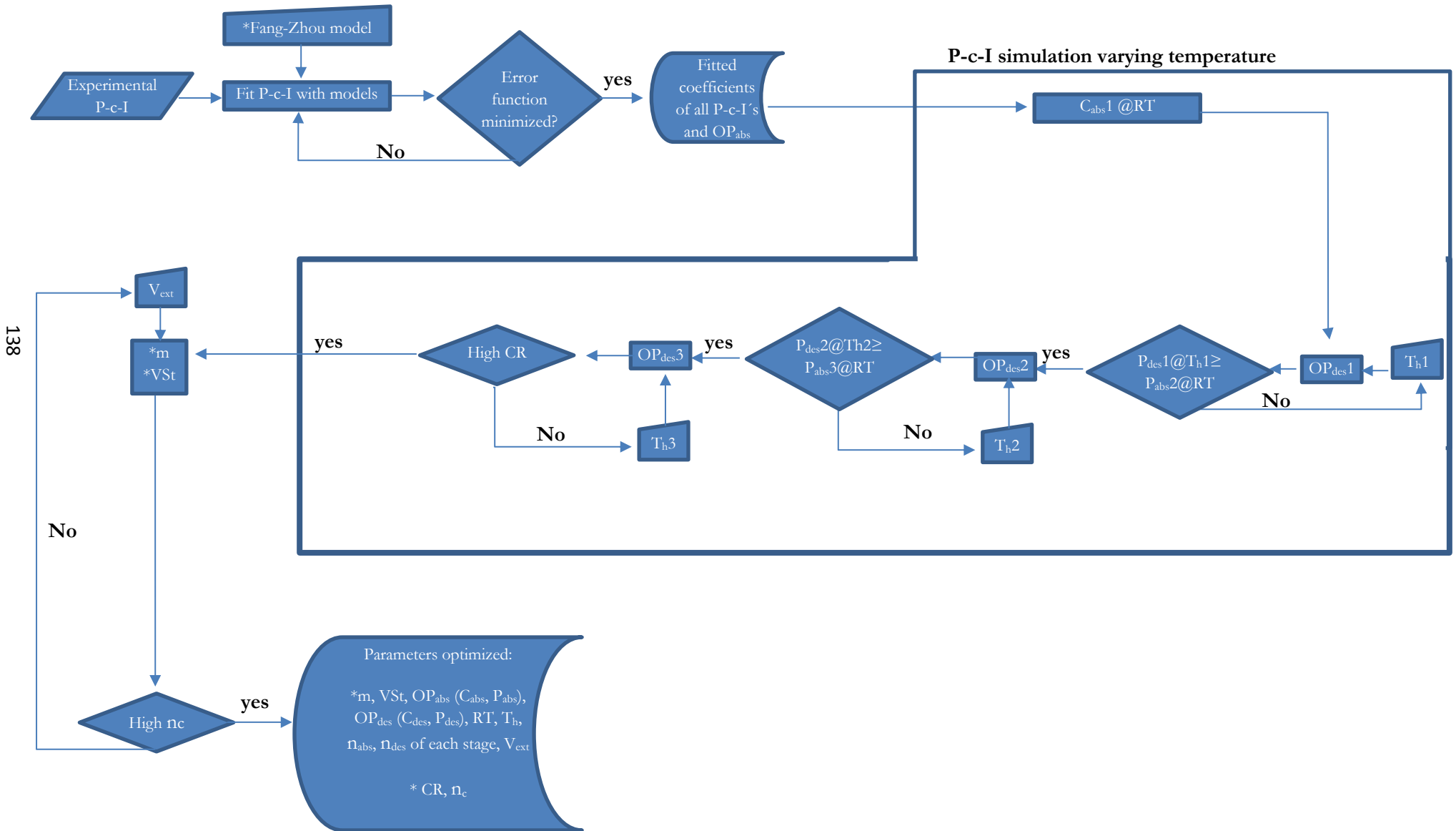
**ANNEX 3. Composition and Rietveld refinement parameters of all the alloys**

|		Light zone (at/f.u.)	Dark zone (at/f.u.)	light-dark average (at/f.u.)	100x (at/f.u.)	Nominal Stoichiometry (at/f.u.)			
BN1-1	Ti	0.89(2)	0.91(1)	0.90(2)	0.89(1)	0.901	a(Å)	V (Å³)	χ²
	Zr	0.11(1)	0.09(1)	0.10(2)	0.11(1)	0.1	4.9160(2)	168.73(2)	1.59
	Mn	1.30(1)	1.18(8)	1.24(9)	1.25(1)	1.339	c(Å)	ρ (g/cm³)	Rb (%)
	V	0.30(2)	0.28(2)	0.29(2)	0.30(1)	0.299	8.0618(5)	6.35(2)	17.2
BN1-2-2	Ti	0.80(1)	0.86(1)	0.83(2)	0.85(1)	0.849	a(Å)	V (Å³)	χ²
	Zr	0.20(1)	0.14(1)	0.17(2)	0.15(1)	0.151	4.9099(1)	168.16(1)	28.9
	Mn	1.52(1)	1.39(1)	1.46(2)	1.39(1)	1.331	c(Å)	ρ (g/cm³)	Rb (%)
	V	0.31(1)	0.31(1)	0.31(2)	0.30(1)	0.3	8.0547(1)	6.48(1)	14.6
BN1-2-3	Ti	0.79(1)	0.86(1)	0.83(2)	0.85(1)	0.849	a(Å)	V (Å³)	χ²
	Zr	0.21(1)	0.14(1)	0.17(2)	0.16(1)	0.151	4.9131(1)	168.45(1)	47.1
	Mn	1.56(1)	1.40(1)	1.48(2)	1.38(1)	1.332	c(Å)	ρ (g/cm³)	Rb (%)
	V	0.3(1)	0.31(1)	0.31(2)	0.29(1)	0.3	8.0580(2)	6.48(1)	16
BN1-2-4	Ti	0.80(1)	0.89(1)	0.85(2)	0.85(1)	0.85	a(Å)	V (Å³)	χ²
	Zr	0.20(1)	0.11(1)	0.15(2)	0.15(1)	0.15	4.9113(1)	168.30(1)	29.6
	Mn	1.51(1)	1.27(1)	1.39(2)	1.37(1)	1.33	c(Å)	ρ (g/cm³)	Rb (%)
	V	0.31(1)	0.32(1)	0.31(2)	0.29(1)	0.3	8.0570(1)	6.48(1)	14.5
BN1-2-5	Ti	0.80(1)	0.87(1)	0.84(2)	0.85(1)	0.85	a(Å)	V (Å³)	χ²
	Zr	0.20(1)	0.13(1)	0.16(2)	0.15(1)	0.15	4.9139(1)	168.56(1)	2.29
	Mn	1.53(1)	1.27(1)	1.40(2)	1.40(1)	1.33	c(Å)	ρ (g/cm³)	Rb (%)
	V	0.30(1)	0.30(1)	0.30(2)	0.31(1)	0.3	8.0629(1)	6.45(1)	10.4
BN125A	Ti	0.80(1)	0.88(1)	0.84(1)	0.85(1)	0.85	a(Å)	V (Å³)	χ²
	Zr	0.20(1)	0.12(1)	0.16(1)	0.15(1)	0.15	4.9134(1)	168.55(1)	6.85
	Mn	1.39(1)	1.42(1)	1.40(1)	1.35(1)	1.33	c(Å)	ρ (g/cm³)	Rb (%)
	V	0.30(1)	0.31(1)	0.31(1)	0.31(1)	0.3	8.0622(1)	6.45(1)	24
BN1-2-6	Ti	--	--	--	0.85(1)	0.85	a(Å)	V (Å³)	χ²
	Zr	--	--	--	0.16(1)	0.15	4.9128(1)	168.45(1)	39
	Mn	--	--	--	1.30(1)	1.328	c(Å)	ρ (g/cm³)	Rb (%)
	V	--	--	--	0.29(1)	0.302	8.0592(1)	6.45(1)	13.7
BNI1	Ti	0.80(1)	0.85(1)	0.83(2)	0.84(1)	0.85	a(Å)	V (Å³)	χ²
	Zr	0.20(1)	0.15(1)	0.18(2)	0.16(1)	0.15	4.9219(1)	169.27(2)	22.5
	Mn	1.35(1)	1.33(1)	1.34(2)	1.29(1)	1.33	c(Å)	ρ (g/cm³)	Rb (%)
	V	0.29(1)	0.31(1)	0.30(2)	0.27(1)	0.3	8.0684(2)	6.45(2)	14.9
BNI2	Ti	0.81(2)	0.88(2)	0.85(4)	0.85(1)	0.849	a(Å)	V (Å³)	χ²
	Zr	0.18(1)	0.12(1)	0.15(2)	0.15(1)	0.15	4.9212(1)	169.25(1)	1.81
	Mn	1.46(1)	1.23(1)	1.35(2)	1.25(1)	1.33	c(Å)	ρ (g/cm³)	Rb (%)
	V	0.31(1)	0.29(1)	0.30(2)	0.28(1)	0.301	8.0696(1)	6.47(1)	13.5
BNIC1	Ti	--	--	--	0.85(1)	0.849	a(Å)	V (Å³)	χ²
	Zr	--	--	--	0.15(1)	0.15	4.9172(2)	168.87(1)	8.09
	Mn	--	--	--	1.39(1)	1.33	c(Å)	ρ (g/cm³)	Rb (%)
	V	--	--	--	0.29(1)	0.3	8.0645(3)	6.43(1)	6.69
BNIC2	Ti	0.82(2)	0.88(3)	0.85(5)	0.85(1)	0.85	a(Å)	V (Å³)	χ²
	Zr	0.18(1)	0.12(1)	0.15(2)	0.15(1)	0.15	4.9164(2)	168.80(1)	21.9
	Mn	1.50(2)	1.28(4)	1.39(6)	1.41(1)	1.33	c(Å)	ρ (g/cm³)	Rb (%)
	V	0.33(1)	0.32(1)	0.33(2)	0.31(1)	0.3	8.0640(3)	6.42(1)	7.83
BN2	Ti	0.73(1)	0.84(1)	0.79(1)	0.80(1)	0.8	a(Å)	V (Å³)	χ²
	Zr	0.27(1)	0.16(1)	0.21(1)	0.20(1)	0.2	4.9030(1)	167.58(1)	3.83
	Mn	1.16(1)	1.19(1)	1.18(1)	1.20(1)	1.2	c(Å)	ρ (g/cm³)	Rb (%)
	Cr	0.62(1)	0.51(1)	0.56(1)	0.56(1)	0.6	8.0470(1)	6.54(1)	10.4
	V	0.17(1)	0.22(1)	0.20(1)	0.20(1)	0.2			
BN2A	Ti	0.74(1)	0.85(1)	0.80(1)	0.80(1)	0.8	a(Å)	V (Å³)	χ²
	Zr	0.26(1)	0.15(1)	0.20(1)	0.20(1)	0.2	4.9035(1)	167.57(1)	3.37
	Mn	1.16(1)	1.20(1)	1.18(1)	1.18(1)	1.2	c(Å)	ρ (g/cm³)	Rb (%)
	Cr	0.58(1)	0.50(1)	0.54(1)	0.55(1)	0.6	8.0475(1)	6.54(1)	24.5
	V	0.18(1)	0.22(1)	0.20(1)	0.20(1)	0.2			
BN2IC	Ti	0.74(1)	0.88(5)	0.81(6)	0.80(1)	0.8	a(Å)	V (Å³)	χ²
	Zr	0.26(2)	0.14(3)	0.19(5)	0.20(1)	0.2	4.9021(1)	167.47(1)	5.58
	Mn	1.17(1)	1.22(2)	1.20(3)	1.28(1)	1.2	c(Å)	ρ (g/cm³)	Rb (%)
	Cr	0.67(1)	0.52(2)	0.60(3)	0.60(1)	0.6	8.0471(1)	6.50(1)	5.10
	V	0.17(1)	0.26(4)	0.21(5)	0.20(1)	0.2			

		Light zone (at/f.u.)	Dark zone (at/f.u.)	light-dark average (at/f.u.)	100x (at/f.u.)	Nominal Stoichiometry (at/f.u.)			
BN2IC2	Ti	--	--	--	0.81(1)	0.8	**a(Å)**	**V (Å³)**	**χ²**
	Zr	--	--	--	0.19(1)	0.2	4.9026(1)	167.49(1)	8.43
	Mn	--	--	--	1.27(1)	1.2	**c(Å)**	**ρ (g/cm³)**	**Rb (%)**
	Cr	--	--	--	0.58(1)	0.605	8.0469(2)	6.51(1)	7.84
	V	--	--	--	0.20(1)	0.2			
B1	Ti	0.88(1)	0.93(1)	0.91(2)	0.91(1)	0.899	**a(Å)**	**V (Å³)**	**χ²**
	Zr	0.12(1)	0.08(1)	0.09(2)	0.09(1)	0.1	4.8844(1)	165.64(1)	1.31
	Mn	1.34(1)	1.36(1)	1.35(2)	1.36(1)	1.399	**c(Å)**	**ρ (g/cm³)**	**Rb (%)**
	Cr	0.47(1)	0.36(1)	0.42(2)	0.40(1)	0.401	8.0169(1)	6.42(1)	16.46
	V	0.18(1)	0.22(1)	0.20(2)	0.20(1)	0.2			
B1-2	Ti	0.88(2)	0.92(2)	0.90(4)	0.89(1)	0.901	**a(Å)**	**V (Å³)**	**χ²**
	Zr	0.11(2)	0.08(1)	0.10(3)	0.11(1)	0.099	4.8793(2)	165.13(1)	1.55
	Mn	1.39(2)	1.46(2)	1.43(4)	1.38(1)	1.401	**c(Å)**	**ρ (g/cm³)**	**Rb (%)**
	Cr	0.41(3)	0.35(2)	0.38(5)	0.38(1)	0.399	8.0089(3)	6.41(1)	18.9
	V	0.18(2)	0.22(2)	0.20(4)	0.20(1)	0.2			
B1-3	Ti	--	--	--	0.89(1)	0.901	**a(Å)**	**V (Å³)**	**χ²**
	Zr	--	--	--	0.11(1)	0.1	4.8757(2)	164.75(1)	1.62
	Mn	--	--	--	1.42(1)	1.403	**c(Å)**	**ρ (g/cm³)**	**Rb (%)**
	Cr	--	--	--	0.38(1)	0.397	8.0025(3)	6.46(1)	17.5
	V	--	--	--	0.20(1)	0.2			
B1-4	Ti	0.87(1)	0.93(2)	0.90(3)	0.91(1)	0.901	**a(Å)**	**V (Å³)**	**χ²**
	Zr	0.13(2)	0.07(1)	0.10(3)	0.09(1)	0.099	4.8761(2)	164.80(1)	1.52
	Mn	1.40(2)	1.49(2)	1.45(4)	1.44(1)	1.4	**c(Å)**	**ρ (g/cm³)**	**Rb (%)**
	Cr	0.41(3)	0.33(4)	0.37(7)	0.37(1)	0.399	8.0037(3)	6.44(1)	24.8
	V	0.18(1)	0.24(4)	0.21(5)	0.21(1)	0.2			
B1-5	Ti	0.88(1)	0.93(1)	0.91(2)	0.898(7)	0.9	**a(Å)**	**V (Å³)**	**χ²**
	Zr	0.12(1)	0.07(1)	0.11(1)	0.101(5)	0.1	4.8752(2)	164.72(1)	1.52
	Mn	1.41(1)	1.50(1)	1.45(1)	1.446(8)	1.401	**c(Å)**	**ρ (g/cm³)**	**Rb (%)**
	Cr	0.45(1)	0.32(1)	0.39(2)	0.379(6)	0.4	8.0024(4)	6.37(1)	20
	V	0.17(1)	0.26(1)	0.22(2)	0.211(5)	0.199			
B1-6	Ti	--	--	--	0.90(1)	0.9	**a(Å)**	**V (Å³)**	**χ²**
	Zr	--	--	--	0.10(1)	0.1	4.8749(2)	164.68(1)	1.78
	Mn	--	--	--	1.45(1)	1.4	**c(Å)**	**ρ (g/cm³)**	**Rb (%)**
	Cr	--	--	--	0.38(1)	0.4	8.0016(3)	6.44(1)	19.6
	V	--	--	--	0.20(1)	0.2			
B3	Ti	0.88(1)	0.94(1)	0.91(2)	0.90(1)	0.897	**a(Å)**	**V (Å³)**	**χ²**
	Zr	0.12(1)	0.06(1)	0.09(2)	0.10(1)	0.1	4.8794(2)	165.10(1)	1.44
	Mn	1.38(1)	1.38(1)	1.38(2)	1.33(1)	1.406	**c(Å)**	**ρ (g/cm³)**	**Rb (%)**
	Cr	0.44(1)	0.31(1)	0.38(2)	0.38(1)	0.399	8.0072(4)	6.44(1)	21.3
	V	0.18(1)	0.24(1)	0.21(2)	0.20(1)	0.198			
B4	Ti	0.88(1)	0.94(1)	0.91(2)	0.904(7)	0.902	**a(Å)**	**V (Å³)**	**χ²**
	Zr	0.12(1)	0.07(1)	0.09(2)	0.095(4)	0.098	4.8809(2)	165.29(1)	1.25
	Mn	1.37(1)	1.44(1)	1.41(2)	1.335(8)	1.399	**c(Å)**	**ρ (g/cm³)**	**Rb (%)**
	Cr	0.45(1)	0.33(1)	0.39(2)	0.392(6)	0.401	8.0116(3)	6.44(1)	22.5
	V	0.17(1)	0.24(1)	0.21(2)	0.203(5)	0.2			
B7	Ti	0.88(1)	0.93(1)	0.90(2)	0.90(1)	0.899	**a(Å)**	**V (Å³)**	**χ²**
	Zr	0.13(1)	0.07(1)	0.10(2)	0.10(1)	0.101	4.8740(1)	164.60(1)	1.33
	Mn	1.40(1)	1.54(1)	1.47(2)	1.45(1)	1.469	**c(Å)**	**ρ (g/cm³)**	**Rb (%)**
	Cr	0.45(1)	0.32(1)	0.38(2)	0.39(1)	0.399	8.0009(1)	6.48(1)	11.9
	V	0.17(1)	0.27(1)	0.22(2)	0.21(1)	0.202			
B8	Ti	0.88(1)	0.94(1)	0.91(2)	0.90(1)	0.901	**a(Å)**	**V (Å³)**	**χ²**
	Zr	0.12(1)	0.06(3)	0.09(4)	0.10(1)	0.099	4.8769(2)	164.88(1)	1.33
	Mn	1.40(2)	1.57(3)	1.49(5)	1.43(1)	1.399	**c(Å)**	**ρ (g/cm³)**	**Rb (%)**
	Cr	0.44(1)	0.30(4)	0.37(5)	0.38(1)	0.401	8.0049(3)	6.47(1)	14.2
	V	0.17(1)	0.28(3)	0.23(5)	0.20(1)	0.201			
B9	Ti	0.88(1)	0.94(1)	0.91(2)	0.90(1)	0.9	**a(Å)**	**V (Å³)**	**χ²**
	Zr	0.12(1)	0.06(1)	0.09(2)	0.10(1)	0.1	4.8828(1)	165.48(1)	1.22
	Mn	1.37(1)	1.38(1)	1.38(2)	1.35(1)	1.4	**c(Å)**	**ρ (g/cm³)**	**Rb (%)**
	Cr	0.44(1)	0.28(1)	0.36(2)	0.35(1)	0.4	8.0143(2)	6.44(1)	12.2
	V	0.18(1)	0.25(1)	0.22(1)	0.20(1)	0.2			

		Light zone (at/f.u.)	Dark zone (at/f.u.)	light-dark average (at/f.u.)	100x (at/f.u.)	Nominal Stoichiometry (at/f.u.)			
B9A	Ti	0.88(1)	0.93(1)	0.91(1)	0.90(1)	0.90	**a(Å)**	**V (Å³)**	**χ²**
	Zr	0.12(1)	0.07(1)	0.09(1)	0.10(1)	0.10	4.8806(1)	165.27(1)	3.93
	Mn	1.36(1)	1.39(1)	1.38(1)	1.37(1)	1.35	**c(Å)**	**ρ (g/cm³)**	**Rb (%)**
	Cr	0.43(1)	0.36(1)	0.39(1)	0.40(1)	0.35	8.0114(1)	6.44(1)	25.9
	V	0.18(1)	0.22(1)	0.20(1)	0.20(1)	0.20			
BI1	Ti	0.87(1)	0.94(1)	0.91(2)	0.90(1)	0.899	**a(Å)**	**V (Å³)**	**χ²**
	Zr	0.13(1)	0.06(1)	0.09(2)	0.10(1)	0.101	4.8815(1)	165.32(1)	52.3
	Mn	1.33(1)	1.34(2)	1.34(3)	1.37(1)	1.339	**c(Å)**	**ρ (g/cm³)**	**Rb (%)**
	Cr	0.45(1)	0.27(3)	0.36(4)	0.40(1)	0.4	8.0110(2)	6.43(1)	14.8
	V	0.17(1)	0.25(2)	0.21(3)	0.21(1)	0.199			
BI2	Ti	0.88(1)	0.94(2)	0.91(2)	0.90(1)	0.901	**a(Å)**	**V (Å³)**	**χ²**
	Zr	0.12(1)	0.06(2)	0.09(4)	0.10(1)	0.099	4.8785(1)	165.04(1)	13.1
	Mn	1.35(1)	1.38(3)	1.37(4)	1.36(1)	1.4	**c(Å)**	**ρ (g/cm³)**	**Rb (%)**
	Cr	0.44(1)	0.27(3)	0.36(4)	0.40(1)	0.4	8.0071(2)	6.43(1)	15.6
	V	0.17(1)	0.25(2)	0.21(3)	0.22(1)	0.2			
BIC	Ti	0.89(1)	0.93(1)	0.91(2)	0.90(1)	0.9	**a(Å)**	**V (Å³)**	**χ²**
	Zr	0.11(1)	0.07(1)	0.09(2)	0.10(1)	0.1	4.8766(1)	164.84(1)	12
	Mn	1.41(1)	1.42(1)	1.42(2)	1.48(1)	1.4	**c(Å)**	**ρ (g/cm³)**	**Rb (%)**
	Cr	0.42(1)	0.31(1)	0.37(2)	0.40(1)	0.4	8.0038(2)	6.44(1)	9.16
	V	0.19(1)	0.25(1)	0.22(2)	0.20(1)	0.2			
BIC2	Ti	0.88(1)	0.93(3)	0.91(4)	0.90(1)	0.9	**a(Å)**	**V (Å³)**	**χ²**
	Zr	0.12(1)	0.07(1)	0.10(2)	0.10(1)	0.1	4.8764(1)	164.83(1)	7.87
	Mn	1.40(1)	1.40(2)	1.40(3)	1.48(1)	1.41	**c(Å)**	**ρ (g/cm³)**	**Rb (%)**
	Cr	0.42(3)	0.31(4)	0.37(7)	0.39(1)	0.4	8.0038(1)	6.44(1)	10.71
	V	0.19(1)	0.24(3)	0.22(4)	0.20(1)	0.206			

	Annealed	**As-cast**				
	Global stoichiometry - 100x (at/f.u.)	Global stoichiometry - 100x (at/f.u.)	Matrix Dark zone (at/f.u.)	Intermediate zone (at/f.u.)	Light zone (at/f.u.)	Nominal Stoichiometry (at/f.u.)
La	1.00(1)	1.00(1)	1.00(1)	1.00(1)	1.00(1)	1
Ni	4.81(3)	4.78(3)	4.94(3)	4.46(1)	3.43(1)	4.8
Sn	0.19(1)	0.22(1)	0.06(1)	0.54(1)	1.57(1)	0.2

ANNEX 4. XRPD of all the measured AB$_2$-type alloys
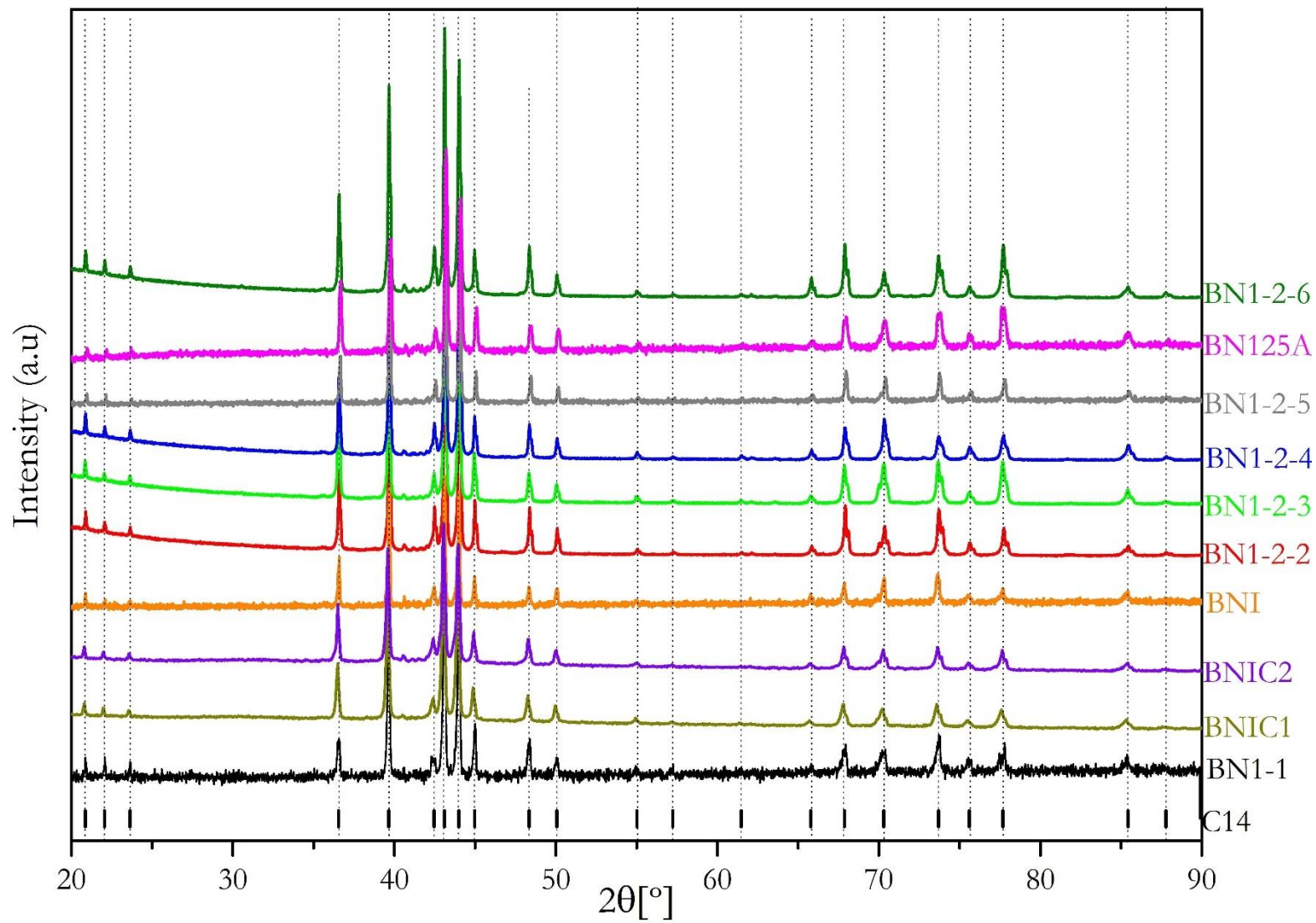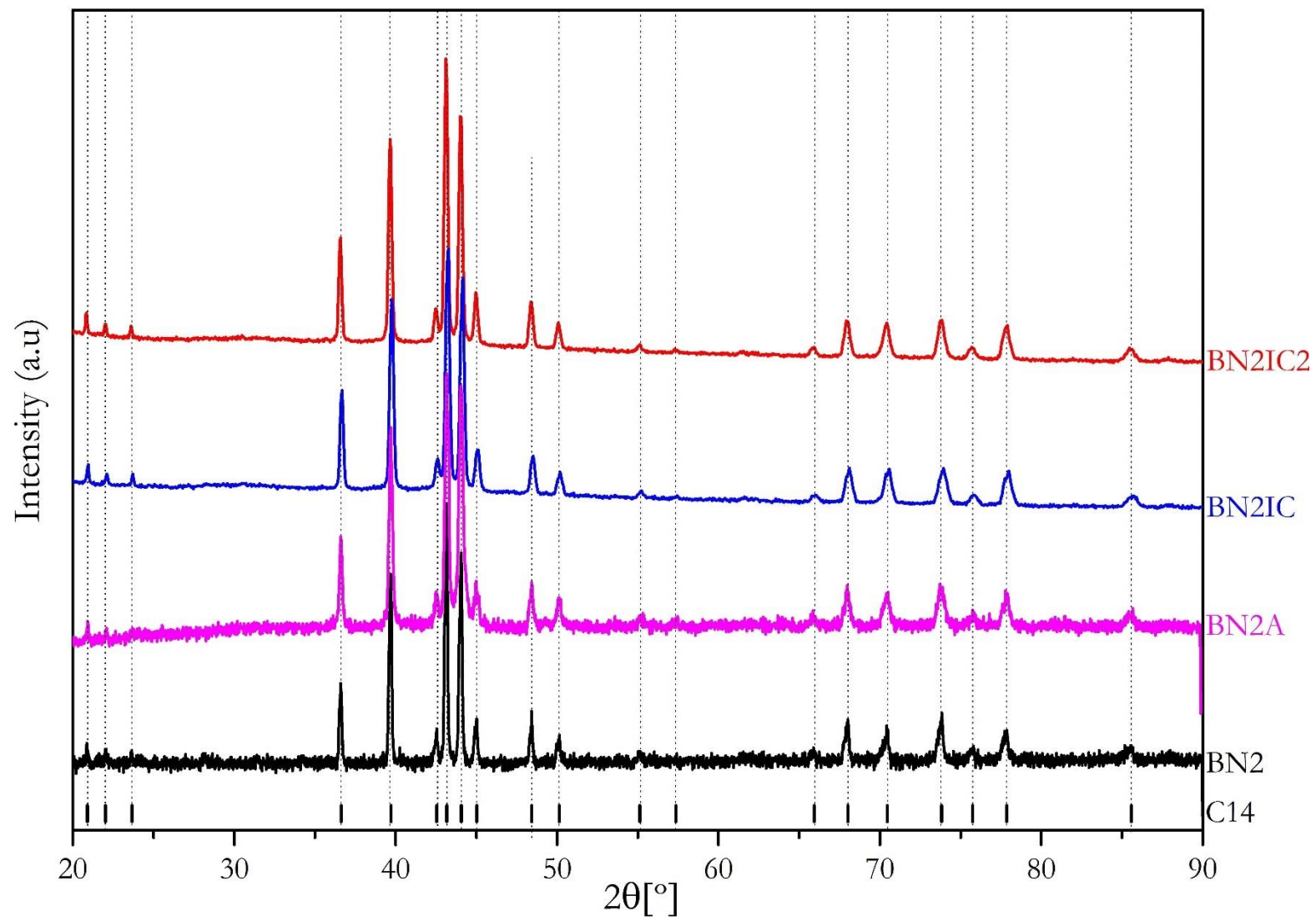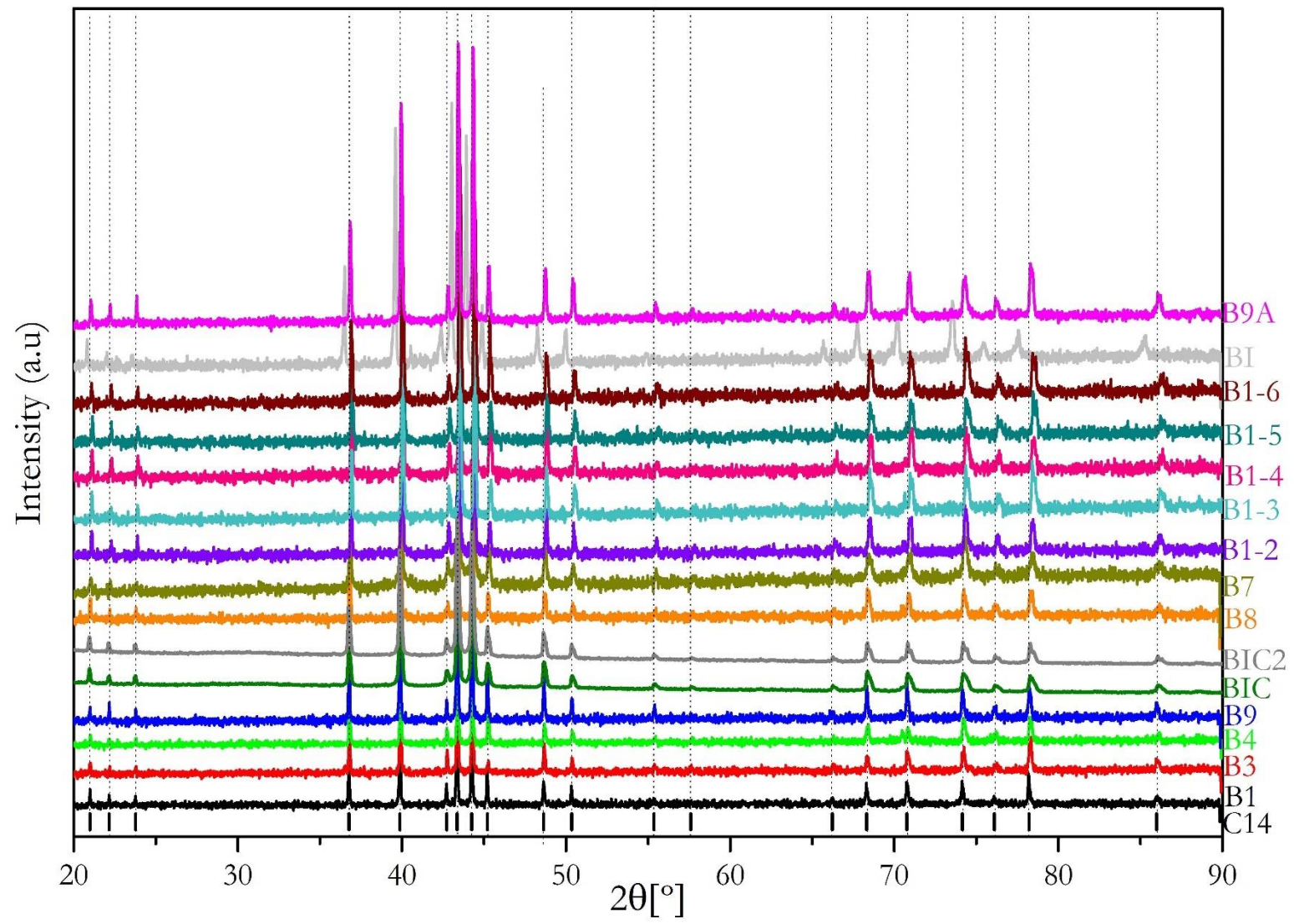
Annex 5. Reacted fraction and driving force models evaluated

The main equations used for the reacted fraction $f(F(\alpha))$ are [Reference 31 of chapter 3]:

Symbol	Model	Equation
D1	One-dimensional diffusion	$(F(\alpha))^2=kt$
D2	Two-dimensional diffusion	$(1-F(\alpha))*\ln(1-F(\alpha))+F(\alpha)=kt$
D3	Three-dimensional diffusion (Jander equation)	$[1-(1-F(\alpha))^{1/3}]^2=kt$
D4	Three-dimensional diffusion (Ginstling-Braunshtein equation)	$1-2*F(\alpha)/3-(1-F(\alpha))^{2/3}=kt$
F1	First-order reaction	$-\ln(1-F(\alpha))=kt$
R2	Two-dimensional phase boundary	$1-(1-F(\alpha))^{1/2}=kt$
R3	Three-dimensional phase boundary	$1-(1-F(\alpha))^{1/3}=kt$
Z0	Zero order	$F(\alpha)=kt$
A2	Avrami-Erofe´ev with n=2	$[-\ln(1-F(\alpha))]^{1/2}=kt$
A3	Avrami-Erofe´ev with n=3	$[-\ln(1-F(\alpha))]^{1/3}=kt$

The main equations used for the driving force $(g(P,P_{eq}))$ are [Reference 30 and 33 of chapter 3]:

Symbol	Model	Equation
$g(P,Peq)_1$	Normalized pressure dependence method	Absorption: $(P-P_{eq})/P_{eq}$
		Desorption: $(P_{eq}-P)/P_{eq}$
$g(P,Peq)_2$	Pressure dependence related to a diffusion process	Absorption: $\ln(P/P_{eq})$
		Desorption: $\ln(P_{eq}/P)$
$g(P,Peq)_3$	Pressure dependence related to a phase transformation process	Absorption: $1-(P_{eq}/P)^{1/2}$
		Desorption: $1-(P/P_{eq})^{1/2}$

Papers published during the thesis:

[1]A. R. Galvis E, F. Leardini, J. R. Ares, F. Cuevas, and J. F. Fernandez, "Simulation and design of a three-stage metal hydride hydrogen compressor based on experimental thermodynamic data," *Int. J. Hydrog. Energy*, Mar. 2018.

[2]A. R. Galvis Escobar, A. Chaise, V. Iosub, B. Salque, J. F. Fernandez, and O. Gillia, "Stress effect on the swelling/shrinking behavior of an AB2 alloy during hydrogenation cycles," *Int. J. Hydrog. Energy*, vol. 42, no. 35, pp. 22422–22431, Aug. 2017.

[3]A. R. Galvis E., F. Leardini, J. Bodega, J. R. Ares, and J. F. Fernandez, "Realistic simulation in a single stage hydrogen compressor based on AB2 alloys," *Int. J. Hydrog. Energy*, vol. 41, no. 23, pp. 9780–9788, Jun. 2016.

Congresses and seminars:

*Poster presentation of the work *Simulation and design of a three-stage metal hydride hydrogen compressor based on experimental thermodynamic data*, in the Multifunctionality of metal hydrides for energy storage – developments and perspectives (e-MRS2017 fall); 18-21 September 2017, Warsaw, Poland.

*Presented the seminar *Hydride compressors: basic insights and progress*, given at the INSTITUT DE CHIMIE ET DES MATERIAUX PARIS-EST- UMR 7182, from the CNRS and the Universitaté Paris-Est, France. 27 october 2016.

*Oral presentation of the work *Stress effect on the Swelling / Shrinking behavior of an AB₂ alloy during hydrogenation cycles*, in the The 15th International Symposium on Metal-Hydrogen Systems (MH2016); 7-12 August 2016, Interlaken, Suiza

*Poster presentation of the work *Realistic thermodynamic features in a metal hydride compressor simulation*, in the Hydrides as Energy Materials (HydEM2016); 1-3 June 2016, Aarhus, Denmark

*Oral presentation of the work *H₂ real gas effect simulation in a non-continuous single stage AB₂ compressor*, in the mESC-IS 2015, International Symposium on Materials for Energy Storage and Conversion; 7-9 September 2015, Ankara, Turquía

Research stays:

* INSTITUT DE CHIMIE ET DES MATERIAUX PARIS-EST- UMR 7182, from the CNRS and the Universitaté Paris-Est, France. November-december 2017. Synthesis of AB₂-type alloys in great quantities and their characterization. Paper in development from the work done in the research stay

* INSTITUT DE CHIMIE ET DES MATERIAUX PARIS-EST- UMR 7182, from the CNRS and the Universitaté Paris-Est, France. September-november 2016. Thermodynamic and kinetic characterizaton of AB₂-type alloys. Paper published from the work done in the research stay

* Commissariat à l'énergie atomique et aux énergies alternatives (CEA) of Grenoble, France. July-August 2015. Hydrides Mechanical properties measurements. Paper published from the work done in the research stay

Other recognitions:

*Best Poster at the Multifunctionality of metal hydrides for energy storage – developments and perspectives (e-MRS2017 fall), with the work *Simulation and design of a three-stage metal hydride hydrogen compressor based on experimental thermodynamic data*

Final acknowledgment:
To all the institutions that helped and/or collaborated with the development of this thesis, thank you a lot.